Dissertation zur Erlangung des naturwissenschaftlichen Doktorgrades
der Julius-Maximilians-Universität Würzburg

Detection of a plasmon-polariton quantum wave packet by coherent 2D nanoscopy

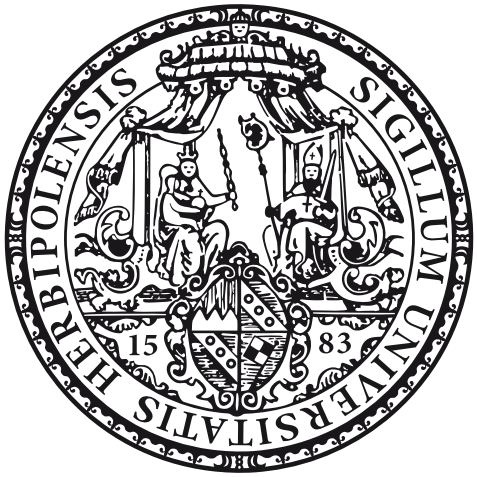

vorgelegt von
Sebastian Pres

aus
Fritzlar

Würzburg, 2023

Eingereicht am: 01.03.2023 bei der Fakultät für Physik und Astronomie

Gutachter der Dissertation:

1. Gutachter: Prof. Dr. Tobias Brixner

2. Gutachter: Prof. Dr. Bert Hecht

3. Gutachter:

Mitglieder des Prüfungskomitees:

Vorsitzender: Prof. Dr. Thomas Trefzger

1. Prüfer: Prof. Dr. Tobias Brixner

2. Prüfer: Prof. Dr. Bert Hecht

3. Prüfer: Prof. Dr. Adriana Pálffy-Buß

Tag des Promotionskolloquiums: 06.12.2023

Doktorurkunden ausgehändigt am: .....

Every word has consequences.
Every silence, too.

Sartre, 1945
Les Temps Modernes

Zusammenfassung

Plasmonische Nanostrukturen gelten als vielversprechende Kanditaten für wesentliche Bestandteile integrierter Quantentechnologien, da sie in der Lage sind, breitbandige elektromagnetische Felder auf der Nanoskala effizient zu lokalisieren. Durch die spektral breitbandige optische Anregung kann das so erzeugte lokale Nahfeld als räumliche Überlagerung von spektral verschiedenen Plasmon-Polariton Moden aufgefasst und daher als klassisches Wellenpaket beschrieben werden. Da Plasmon-Polaritonen wiederum nichtklassische Lichtzustände übertragen und erhalten können, stellt sich allerdings die spannende Frage, inwieweit man sie als quantenmechanische Wellenpakete, sprich eine Superposition von unterschiedlichen Quantenzuständen, beschreiben muss.

Doch wie lässt sich der Quantenzustand solcher Plasmon-Polaritonen untersuchen, charakterisieren und schließlich manipulieren? Bislang beruhte die Untersuchung bei Raumtemperatur vollständig auf der Analyse der quantenoptischen Eigenschaften der entsprechenden ein- und ausgehenden Fernfeld-Photonenmoden. Diese Methoden erlauben allerdings bisher nur eine eher indirekte Untersuchung des Plasmonen-Polaritonen-Quantenzustands mittels Überführung in Photonen. Darüber hinaus mangelt es diesen indirekten Methoden an räumlicher Auflösung und sie bieten daher keinen Zugang zum Plasmonen-Polaritonen-Quantenzustand am Ort der Nanostruktur. Die spektroskopische Methode der kohärenten 2D-Nanoskopie bietet allerdings die Möglichkeit, den Plasmon-Polariton-Quantenzustand *sowohl* im Hilbert-Raum *als auch* im Raum- und Zeitbereich zu verfolgen, wodurch eine vollständige Charakterisierung des Plasmon-Polaritons möglich ist.

In dieser Arbeit wird ein vielseitiger experimenteller Aufbau zur kohärenten zweidimensionalen (2D)-Nanoskopie vorgestellt, der spektrale Durchstimmbarkeit und Femtosekunden-Zeitauflösung mit räumlicher Auflösung auf der Nanometerskala durch den Nachweis optisch angeregter nichtlinear-emittierter Elektronen mittels Photoemissionselektronenmikroskopie (PEEM) kombiniert. Die optische Anregung durch amplituden- und phasengeformte, systematisch modifizierte und interferometrisch stabile Multipulssequenzen wird realisiert und über Fouriertransformierte Spektrale Interferenz (FTSI) charakterisiert. Diese lineare Technik ermöglicht eine effiziente Datenerfassung parallel zu einem gleichzeitig durchgeführten Experiment. Die vollständige Rekonstruktion des elektrischen Feldes jeder erzeugten Multipulssequenz wird verwendet, um die Auswirkung nicht-idealer Pulssequenzen auf die zweidimensionalen Spektraldaten von populationsbasierten multidimensionalen Spektroskopiemethoden, wie beispielsweise der in dieser Arbeit verwendeten kohärenter 2D-Nanoskopie, zu analysieren. Die Untersuchung der räumlich aufgelösten nichtlinearen Elektronenemissionsausbeute von plasmonischen Gold-Nanoresonatoren durch kohärente 2D-Nanoskopie erfordert eine Quasiteilchen-Behandlung der angesprochenen Plasmon-Polariton-Mode und die Entwicklung eines Quantenmodells, um die plasmonenunterstützte Multiquanten-Elektronenemission

von Nanostrukturen korrekt zu beschreiben. Die gute Übereinstimmung zwischen simulierten und experimentellen Daten ermöglicht es, bestimmte spektrale Merkmale mit Überlagerungen von nicht-benachbarten Plasmon-Polariton-Quantenzuständen, sprich nicht-benachbarter Besetzungszahlzustände des zugrunde liegenden quantisierten, harmonischen Oszillators, in Verbindung zu bringen und so direkt das Plasmon-Polariton--Quantenwellenpaket am Ort der Nanostruktur zu untersuchen.

Dies ist ein notwendiger Schritt, um den Plasmon-Polariton-Quantenzustand lokal zu kontrollieren und zu manipulieren, und somit von allgemeinem Interesse für die Realisierung von quantenoptischen Geräten im Nanomaßstab.

Abstract

Plasmonic nanostructures are considered promising candidates for essential components of integrated quantum technologies because of their ability to efficiently localize broadband electromagnetic fields on the nanoscale. The resulting local near field can be understood as a spatial superposition of spectrally different plasmon-polariton modes due to the spectrally broad optical excitation, and thus can be described as a classical wave packet. Since plasmon polaritons, in turn, can transmit and receive non-classical light states, the exciting question arises to what extent they have to be described as quantum mechanical wave packets, i.e. as a superposition of different quantum states.

But how to probe, characterize and eventually manipulate the quantum state of such plasmon polaritons? Up to now, probing at room temperatures relied completely on analyzing quantum optical properties of the corresponding in-going and out-going far-field photon modes. However, these methods so far only allow a rather indirect investigation of the plasmon-polariton quantum state by means of transfer into photons. Moreover, these indirect methods lack spatial resolution and therefore do not provide on-site access to the plasmon-polariton quantum state. However, since the spectroscopic method of coherent two-dimensional (2D) nanoscopy offers the capability to follow the plasmon-polariton quantum state *both* in Hilbert space *and* in space and time domain a complete characterization of the plasmon polariton is possible.

In this thesis a versatile coherent 2D nanoscopy setup is presented combining spectral tunability and femtosecond time resolution with spatial resolution on the nanometer scale due to the detection of optically excited nonlinear emitted electrons via photoemission electron microscopy (PEEM). Optical excitation by amplitude- and phase-shaped, systematically-modified and interferometric-stable multipulse sequences is realized, and characterized via Fourier-transform spectral interferometry (FTSI). This linear technique enables efficient data acquisition in parallel to a simultaneously performed experiment. The full electric-field reconstruction of every generated multipulse sequence is used to analyze the effect of non-ideal pulse sequences on the two-dimensional spectral data of population-based multidimensional spectroscopy methods like, e.g., the coherent 2D nanoscopy applied in this thesis. Investigation of the spatially-resolved nonlinear electron emission yield from plasmonic gold nanoresonators by coherent 2D nanoscopy requires a quasi-particle treatment of the addressed plasmon-polariton mode and development of a quantum model to adequately describe the plasmon-assisted multi-quantum electron emission from nanostructures. Good agreement between simulated and experimental data enables to connect certain spectral features to superpositions of non-adjacent plasmon-polariton quantum states, i.e, non-adjacent occupation-number states of the underlying quantized, harmonic oscillator, thus direct probing of the plasmon-polariton quantum wave packet at the location of the nanostructure.

This is a necessary step to locally control and manipulate the plasmon-polariton quantum state and thus of general interest for the realization of nanoscale quantum optical devices.

CONTENTS

PHYSICAL CONSTANTS

Quantity	Symbol	Value	Unit
Vacuum speed of light	c	299.79	$\frac{\text{nm}}{\text{fs}}$
Electron rest mass	m_0	0.511	$\frac{\text{MeV}}{\text{c}^2}$
Electron charge	e	1.6×10^{-19}	C
Planck constant	$\hbar$	0.658	$\text{eV} \cdot \text{fs}$
Boltzmann constant	k_B	8.62×10^{-5}	$\frac{\text{eV}}{\text{K}}$
Vacuum permeability	μ_0	$4\pi \times 10^{-7}$	$\frac{\text{N}}{\text{A}^2}$
Vacuum permittivity	ϵ_0	$\frac{1}{\mu_0 c^2}$	$\frac{\text{F}}{\text{m}}$
Hartree energy	E_H	27.211	eV
	$\hbar$c	197	$\text{eV} \cdot \text{nm}$

All equations presented in this thesis are given in SI units. Note that in some exceptions, e.g., the simulations based on the Lindblad equation, the model parameters applied in each particular simulation are defined in atomic units (a.u.) as emphasized at corresponding positions in the text.

CHAPTER

ONE

INTRODUCTION

Developing integrated quantum technologies on the nanoscale for information processing or sensing requires knowledge about the essential classical and quantum-mechanical parameters used in the underlying descriptive model to characterize the temporal dynamics that produce and influence a certain quantum state of the utilized quantum system upon optical excitation.

In particular, this work addresses the question of how the ultrafast multi-step process of nonlinear electron emission from a gold nanoresonator can be described and made useful as a detection channel to probe the quantum state of a particular system directly at the nanoscale. This is achieved via a coherent multidimensional spectroscopic technique, called coherent two-dimensional (2D) nanoscopy, which is realized, verified, and applied in a new laboratory of the Brixner group in Würzburg during this thesis. This technique allows the acquisition of spatially-resolved nonlinear 2D correlation spectra which provide direct access to the nonlinear local response of the system under study and thus contain information about the relevant parameters characterizing the ultrafast temporal dynamics within the quantum system. In fact the "quantum system" utilized in this thesis, consists of one mode of a nanoresonator which interacts with the electrons of the metal. The optical excitation of this mode emits metal electrons to the vacuum in a nonlinear process. Thus, the relevant parameters describing the temporal dynamics of the coupled system are entangled which makes a direct probing almost impossible. Nevertheless, by modeling the multi-step electron emission process based on the experimentally achieved nonlinear 2D correlation spectra, the relevant classical and quantum-mechanical parameters are identified and disentangled.

The key to discover and disentangle these parameters lies in general in the in-

vestigation of the interaction between a quantum system and other systems, e.g., its environment. Note that due to this interaction, the quantum system and its environment are entangled [8]. Within this entangled system, a quantum state is defined by its wave function which is constructed from a certain superposition of eigenstates, which by themselves define the quantum system in a suitable basis set. Experimentally, every information obtained from the system, e.g., temporal dynamics of a quantum state, results in fact from energy exchange with the system, implying that the optically perturbed quantum system is driven out of thermal equilibrium with its environment. On its way back to thermal equilibrium the system loses energy, i.e., exchanges energy with the environment, which manifests in the classical effect of *dissipation* [8]. Quantification of the dissipation process allows a reconstruction of the temporal quantum-state dynamics, if it is only affected by dissipation. But, even if dissipation is negligible or absent, implying an infinitely long time to reach thermal equilibrium, the conclusion that there is no interaction between the investigated system and its environment is wrong, since both form still an entangled system. In fact, interaction always comes along with *decoherence*, which quantifies the entanglement itself and has to be understood as a pure quantum effect with no classical analogue [8]. In contrast to interaction via energy exchange the interaction can be thought of as an exchange of which-path or which-state information without absorbing any energy from the system. Thus, decoherence may come along with dissipation but does not have to, whereas dissipation always implies the appearance of decoherence [8].

Parametrization of dissipation and decoherence is typically achieved in terms of time scales such as, e.g., the relaxation time scale in case of dissipation. However, even though disentanglement of these time scales using a suitable theoretical model is possible, the actual insight into the underlying physics of the probed system is still dependent on and limited by the applied theoretical model. Nevertheless, determination of the time scale that dominates during the experimental probing process allows to estimate whether quantum phenomena significantly affect the temporal dynamics of the system or not. This becomes clear through Zurek's approximation [9] of the ratio between the *relaxation* (τ_r) and *decoherence* (τ_d) time scales for a massive object described by a coherent superposition of two Gaussian wave packets at different positions being separated by a distance Δx via

$$\frac{\tau_\mathrm{r}}{\tau_\mathrm{d}} \sim \left(\frac{\Delta x}{\lambda_\mathrm{dB}}\right)^2. \tag{1.0.1}$$

Here, the individual object is characterized by its thermal de Broglie wavelength $\lambda_\mathrm{dB} = \frac{\hbar}{\sqrt{2mk_\mathrm{B}T}}$ [10], with Boltzmann constant k_B (defined in the preamble), object mass m and temperature T. Assuming a macroscopic object like, e.g., an ant with

$m = 10$ mg ($\sim 10^{30}$ eV) at room temperature $T = 300$ K. The ant's thermal de Broglie wavelength is much smaller than microscopic length scales, on the order of $\lambda_{\mathrm{dB}} \sim 10^{-22}$ m. Supposing that the coherently superimposed Gaussian wave packets, which describe the ant, exist at locations separated by $\Delta x \sim 1$ cm results in a ratio of $\frac{\tau_{\mathrm{r}}}{\tau_{\mathrm{d}}} \sim 10^{38}$. Zurek concludes that even if the relaxation time τ_{r} would be on the order of the age of the universe, $\sim 10^{17}$ s [11], the quantum coherence would decay on a $\tau_{\mathrm{d}} \sim 10^{-21}$ s time scale. Hence, for macroscopic objects, the dissipation effect of the environment can be completely neglected with respect to the system dynamics on any time scale relevant to decoherence effects and vice versa which explains the absence of quantum phenomena in the macroscopic world. As discussed in this work, the situation changes in microscopic systems on the nanometer length scale. Since the thermal de Broglie wavelength of electrons at room temperature is much larger at $\lambda_{\mathrm{dB}} \sim 1$ nm and the position separation of the coherent superposition is reduced to $\Delta x \sim 10$ nm both time scales are on the same order of magnitude ($\frac{\tau_{\mathrm{r}}}{\tau_{\mathrm{d}}} \sim 10^2$) and consequently affect the system dynamics.

Electronic relaxation processes, which are of particular interest for this work, take in general place on time scales around $1,000-0.1$ fs [12, 13] and require for this reason a femtosecond (1 fs $= 10^{-15}$ s) time-resolution to analyze experimentally electronic relaxation and decoherence dynamics in microscopic systems. Due to the development of femtosecond laser-pulse sources [14, 15] ultrafast laser-spectroscopy techniques [16] offer the required time resolution combined with spectral tunability [17]. These technical achievements established the field of "femtochemistry" [18].

The experimental method of coherent 2D electronic spectroscopy [19–21] uses optical excitation by ultrashort multipulse sequences with systematically scanned temporal inter-pulse delays and offset phases to disentangle the induced temporal dynamics by detecting specific contributions of the *nonlinear* sample response which are related to the relevant time scales. After its initial development for laser excitation in the near-infrared (NIR) [22] and infrared (IR) [23] spectral range the technique has been transferred to the visible (VIS) [24, 25] and ultraviolet (UV) region [26] and has become a standard tool to study the interactions — approachable in the corresponding spectral range — within microscopic sample systems [27]. The obtained information is represented in a 2D correlation spectrum which correlates signal peaks at various pump-pulse (connected to the first inter-pulse delay τ) and probe-pulse energies (connected to the last inter-pulse delay t) depending on the spectral bandwidth of the optical excitation. Temporal evolution of the individual signals in the 2D correlation spectrum is further accessible by detection of several 2D spectra as a function of an additional intermediate inter-pulse delay T.

To analyze the interactions in temporal domain and on nanometer length scales, coherent 2D spectroscopy is combined with the ultra-high spatial resolution of photoemission electron microscopy (PEEM). This combined approach is known as coherent 2D nanoscopy [28]. The experimental setup with its three main components, a dual noncollinear optical parametric amplifier (NOPA) system, a femtosecond spatial light modulator (SLM) pulse shaper and the PEEM, was realized and verified in this work, where the pulse-shaper setup was mainly within my area of responsibility. The combined components are used to perform coherent 2D nanoscopy experiments on various surface systems, especially gold nanoresonators.

Besides utilization of the spectroscopic technique itself, the accuracy of the 2D correlation data considering both experimental imperfections and theoretical assumptions is investigated in this thesis. Even when finite pulse duration is considered in simulations, excitation pulses are often assumed to have "ideal" shapes although it is known that, e.g., chirp in excitation pulses can have an effect on 2D data [29]. Here a performance efficient method based on Fourier-transform spectral interferometry (FTSI) [30] is implemented to characterize every multipulse sequence during a 2D spectroscopy scanning procedure which takes into account both random and systematic variations during the scan.

Optical excitation of gold nanoresonators [31] leads to correlated electron oscillations in the metal which are described as *plasmon polaritons* [32]. The ability of the nanoresonator to efficiently localize broadband electromagnetic radiation on the nanoscale [33, 34] enables performance efficient detection of spatially and temporally resolved plasmon-assisted nonlinear electron emission. Plasmon polaritons have been further shown to transmit and preserve non-classical light states [35] which reveals their clear quantum nature. Both abilities make them an essential ingredient for integrated quantum technologies. Coherent 2D nanoscopy is utilized here to provide access to the plasmon-polariton quantum state, by detecting quantum coherences emerging due to superpositions of adjacent and non-adjacent eigenstates of a plasmon-polariton quasiparticle. Thus, probing of a plasmon-polariton quantum wave packet, meaning a superposition of various eigenstates, directly at the nanostructure at room temperature is achieved which enables characterization of the particular plasmon-polariton quantum state.

The experimental data is reproduced by using quantum dynamical simulations. Within the developed model the plasmon polariton is treated as a quantum harmonic oscillator (QHO) weakly coupled to single-particle excited states in the metal. This fully quantized description is necessary since the established semiclassical approach, commonly applied to study the classical spatio-temporal evolution of plasmon polaritons, fails. The implemented quantum model sheds light on the nonlinear plasmon-assisted electron-emission process and the plasmon polariton itself. It allows further an implementation of relaxation and decoherence time

scales as individual parameters of both quantum-system constituents, the plasmon-polariton and the single-particle excited states, which can be then optimized with respect to the experimental data. This optimization allows to characterize the relevant time scales and transfer processes affecting the dynamics of a certain quantum state. Moreover, the ability to monitor the plasmon-polariton quantum dynamics as a function of space provides a detailed view of the plasmon polariton and will be important for realization of nanoscale quantum optical devices and the interpretation of coupling schemes like, e.g., molecule–resonator coupling.

The thesis is structured as follows: Chapter 2 introduces the reader to the most important theoretical concepts and methods covering the fields of electron emission from metals, plasmonics, multidimensional spectroscopy and modeling the temporal dynamics of open quantum systems. Chapter 3 describes the whole experimental apparatus, which was implemented during this work starting from an empty laboratory. Note that a major project during the build-up phase under my responsibility was the realization of the femtosecond pulse-shaper setup. In Ch. 4 the FTSI method and data processing for multipulse characterization as implemented and performed by me is explained. Further, the systematic analysis of relevant pulse parameters and the effect of deviations on the obtained 2D data is worked out. Chapter 5 covers the performed 2D nanoscopic investigation of the plasmonic nanoresonators and introduces the quantum model of nonlinear plasmon-assisted electron emission developed in a collaborative effort. Finally, Ch. 6 summarizes the results of this thesis.

CHAPTER

TWO

THEORETICAL CONCEPTS

Since this thesis comprises nonlinear optical multidimensional spectroscopy at plasmonic nanostructures detected via PEEM the following sections give an overview over the essential physical concepts used in these fields.

Section 2.1 briefly introduces the most important physical quantities and concepts describing the different electron emission channels in metals which lead to linear and nonlinear electron emission starting with the macroscopic interaction of a free electron gas with electromagnetic fields. In Sec. 2.2 the basic properties of plasmonic nanosystems and the widely used formalism based on their local response to electromagnetic excitation is declared. Section 2.3 explains the theoretical aspects of coherent 2D nanoscopy and introduces important concepts like Liouville pathways and phase cycling. It focuses in particular on simplifications of the established perturbative formalism allowed in strongly-dephasing systems and within this simplified formalism presents as an example, how a single harmonic-oscillator response manifests in a 2D spectrum. The chapter ends with Sec. 2.4 introducing the Lindblad quantum master-equation which enables a non-perturbative approach to simulate the excitation dynamics in open quantum systems as utilized in several chapters of this thesis.

2.1. Basics of electron emission from metals

Electron emission from metals can be described in a simplified scheme as the interaction of free electrons within the metal with electric or electromagnetic fields. Metals contain a large density of free electrons which originate from the valence

electrons of the metal atoms as described below. Their particular labeling *free* is related to the fact that the electrons experience no restoring force from the medium when driven by, e.g., an electromagnetic field [36].

The interaction of free electrons with electromagnetic fields is in general characterized by the frequency dependent complex relative permittivity (or complex dielectric function) $\epsilon_r(\omega) = \epsilon_1(\omega) + i\epsilon_2(\omega)$ which can be described for metals by the Drude-Lorentz model [36]. Its real $\epsilon_1(\omega)$ and complex part $\epsilon_2(\omega)$ are related to the complex refractive index

$$\tilde{n}(\omega) = n(\omega) + i\kappa(\omega) = \sqrt{\epsilon_r(\omega)}, \tag{2.1.1}$$

with refractive index $n(\omega)$ and extinction coefficient $\kappa(\omega)$. The complex refractive index determines the reflectivity R of the medium

$$R = \left|\frac{\tilde{n}(\omega) - 1}{\tilde{n}(\omega) + 1}\right|^2, \tag{2.1.2}$$

and its absorption properties via the absorption coefficient

$$\alpha(\omega) = \frac{2\kappa(\omega)\omega}{c}. \tag{2.1.3}$$

A detailed description of the Drude-Lorentz model, the explicit form of, e.g., the absorption coefficient $\alpha(\omega)$ and its connection to the conductivity of the metal can be found in Ref. [36]. Note that for free-electron metals at optical frequencies most of the excitation energy is re-radiated as a coherent reflection into the vacuum and energy absorption by the metal is obtained via decoherence of collective free-electron excitations by elastic and inelastic processes like, deformation potential (see [37] for definition), impurities and e-e scattering [38].

In general, the phase space of kinetic energies E and particle impulses of the free electron, described by the wave vector $\mathbf{k}$, are determined by its $E(\mathbf{k})$ dispersion relation. For a completely free electron which only possesses kinetic energy this results in the free-electron parabola defined by

$$E(\mathbf{k}) = \frac{\hbar^2\mathbf{k}^2}{2m_0}, \tag{2.1.4}$$

with electron rest mass m_0 (defined in the preamble of this thesis) and electron wave vector $\mathbf{k}$. Since the inter-atomic separation between the atoms in a solid-state medium is approximately the size of the atoms itself, the outer-core atomic orbitals overlap and interact with each other. This leads to an energy broadening of the discrete levels of the free atom into broad bands. Note that the inner-core orbitals do not overlap and thus retain their discrete level structure.

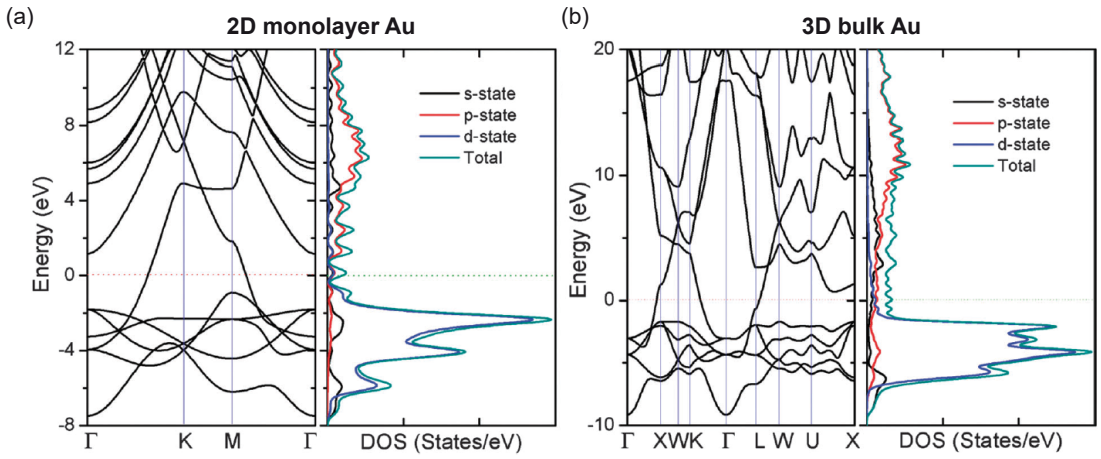

Figure 2.1 – Electronic structures of gold (Au). (a) 2D Au monolayer: $E(\mathbf{k})$ dispersion relation (band structure) (left, black), total density of states (DOS) (right, cyan) and partially DOS (blue, red and black) of the corresponding s-, p-, and d-band, respectively. (b) Band structure for three-dimensional (3D) bulk (fcc) Au and corresponding density of states (DOS) following the same color labeling as in (a). The Fermi energy is located in both cases at 0 eV. The band structure is depicted in the reduced-zone scheme along certain high symmetry points within the Brillouin zone. The symmetry points correspond to certain wave-vector configurations, e.g., $\Gamma \equiv \mathbf{k} = (0, 0, 0)$ depending on the crystal structure. For details see Ref. [36]. Copied with permission from Ref. [39].

Due to the overlapping outer-core atomic orbitals the electrons, located in these orbitals, are assumed to move freely. The electrons located in the outermost orbitals are called "valence electrons". They participate in chemical bonds between atoms and are assigned to a particular band, e.i., the valence band. The remaining ion cores of the atoms form a regular positively charged lattice. The periodic potential of the ion cores leads to a perturbation of the motion of the nearly free valence electrons which modifies their simple $E(\mathbf{k})$ dispersion relation shown in Eq. (2.1.4). As a result of the modified $E(\mathbf{k})$ dispersion relation a lattice specific band structure in k-space is formed. Due to the periodicity of the lattice this band structure can be simplified in a reduced zone scheme as depicted exemplarly for gold (Au) in Fig. 2.1. Detailed description can be found in Ref. [36, 40].

Following Bloch's theorem [41] the electronic states within the bands are assumed to be delocalized and can be described by the following wave function, in general called Bloch function

$$\phi_{\mathbf{k}}(\mathbf{r}) = \frac{1}{\sqrt{V}} u_{\mathbf{k}}(\mathbf{r}) \exp(i\mathbf{k}\cdot\mathbf{r}), \tag{2.1.5}$$

with normalization volume V and envelope function $u_{\mathbf{k}}(\mathbf{r})$ containing the periodicity of the lattice. Each electronic band is related to a different envelope function retaining the character of the original atomic orbitals from which the band was formed, e.g., s-band, p-band or d-band.

The delocalized electron waves move freely in the whole crystal. This delocalization enables collective excitations of many atoms rather than individual atoms which manifests in, e.g., the formation of excitons by delocalized electrons and holes in a semiconductor (Wannier–Mott excitons) or plasmon formation by free electrons in metals or doped semiconductors [36]. Note that the last-mentioned collective excitations will be investigated in detail in Ch. 5.

The number of states within a certain energy range $E \to (E + \mathrm{d}E)$ of a band is expressed in terms of a so-called density of states (DOS) function $g(E)$ which is defined as

$$\text{Number of states} = \int_{E}^{E+\mathrm{d}E} g(E)\mathrm{d}E. \tag{2.1.6}$$

Thus, the DOS describes the distribution of the electronic states within the band. Electrons fill the different bands, up to a characteristic energy called Fermi energy E_{F}. The Fermi energy in metals is situated typically several eV below the vacuum (or ionization) energy E_{Vac}, e.g., about $4.6 - 5.6$ eV in the case of gold [42]. This means that electrons are bound to the material with at least this binding energy, which is commonly also referred to as the work function Φ of the material.

The dominant electron emission processes in the discussed experiments are linear and nonlinear photoemission which are introduced in the subsequent sections.

2.1.1. Linear photoemission

Linear photoemission was first observed in the late 19th century and explained by Albert Einstein in 1905 by the well-known photoelectric effect [43]. After absorption of one photon with energy $E_{\mathrm{ph}} = \hbar\omega$ an electron is emitted only if the photon energy $E_{\mathrm{ph}} = \hbar\omega$ is larger than the work function Φ of the metal.

The most general approach of photoemission is based on Fermi's golden rule. The transition rate w_{fi} for direct photon absorption from an initial N-electron state described by the Bloch function $\Phi_{\mathbf{k}_\mathrm{i}}(\mathbf{r})$ to a final state $\Phi_{\mathbf{k}_\mathrm{f}}(\mathbf{r})$ is therefore obtained by [36, 44]

$$w_{\mathrm{fi}} = \frac{2\pi}{\hbar} |\langle \Phi_{\mathbf{k}_\mathrm{f}}| H_{\mathrm{int}} |\Phi_{\mathbf{k}_\mathrm{i}}\rangle|^2 g(\hbar\omega), \tag{2.1.7}$$

with $g(\hbar\omega)$ being the joint DOS evaluated at the photon energy $\hbar\omega$ of the optical excitation which by itself is described by the light-matter interaction Hamiltonian H_{int} with [45]

$$H_{\mathrm{int}} = \frac{1}{2m}(\mathbf{p} - q\mathbf{A}(\mathbf{r},t))^2 + q\phi(\mathbf{r},t). \tag{2.1.8}$$

Here, $\phi(\mathbf{r},t)$ describes a possibly present scalar potential and $\mathbf{p} = -i\hbar\boldsymbol{\nabla}$ the momentum operator. m is the rest mass of the interacting particle with charge q and $\mathbf{A}(\mathbf{r},t)$ corresponds to the vector potential of the electromagnetic excitation field

$$\mathbf{A}(\mathbf{r},t) = A_0 \boldsymbol{\epsilon} \mathrm{e}^{i(\mathbf{kr}-\omega t)} + \mathrm{c.c.}, \tag{2.1.9}$$

with polarization vector $\boldsymbol{\epsilon}$. In a perturbative treatment for electrons ($q = -e, m = m_0$) as interacting particles, using the Coulomb gauge ($\phi(\mathbf{r},t) = 0$) and neglecting the higher-order term $\mathbf{A}(\mathbf{r},t)^2$, which corresponds to two-photon absorption, H_{int} is further simplified [44]

$$H_{\mathrm{int}} = \frac{e}{m_0}\mathbf{p}\cdot\mathbf{A}, \tag{2.1.10}$$

and the electric and magnetic fields are retrieved from the vector potential by $\mathbf{E}(\mathbf{r},t) = -\partial\mathbf{A}(\mathbf{r},t)/\partial t$ and $\mathbf{B}(\mathbf{r},t) = \boldsymbol{\nabla}\times\mathbf{A}(\mathbf{r},t)$, respectively. Note that the matrix element $\langle \Phi_{\mathbf{k}_\mathrm{f}}| H_{\mathrm{int}} |\Phi_{\mathbf{k}_\mathrm{i}}\rangle$ is closely connected to the electric dipole moment of the transition [36] and that the so far applied final state $\langle \Phi_{\mathbf{k}_\mathrm{f}}|$ reflects the situation that the final electronic state lies within a continuous band which is not true in case of linearly photoemitted electrons. In that more advanced case two important models have been developed.

The process of linear photoemission can be further described in a three-step model [44, 46]. After excitation to a particular "bulk final state" by absorbing a photon, the excited electron propagates to the surface of the sample and is eventually transmitted through the surface and emitted into the vacuum. During the propagation to the surface, energy and momentum redistribution is implemented by elastic and inelastic collisions like, e.g., electron-phonon (e-ph), electron-electron (e-e) or electron-defect (e-d) scattering events.

An alternative one-step model description describes the photoemission process in terms of a single coherent process which contains photon absorption, electron removal and electron detection. This approach requires that in addition to bulk states, surface states, evanescent states, and surface resonances have to be included

in the Hamiltonian [44]. Within this model the photoemission transition takes place between an initial electronic state confined to the solid (a bulk or surface state) and a final vacuum state, which condenses the scattering in the bulk and at the surface, leaking into the solid. These final states are called "time-reversed" or "inverse" LEED-states [46].

Due to the complexity of the one-step model the three-step model is mostly used and has proven to be rather successful [47–49]. For more details, concerning the three-step and one-step model description the reader is referred to Ref. [44, 46].

2.1.2. Nonlinear photoemission

Due to high peak intensities coming along with the invention of short-pulse lasers the nonlinear photoemission regime became experimentally accessible [50, 51]. In a nonlinear photoemission process a certain number of photons N with energy $E_{\mathrm{ph}} = \hbar\omega \ll \Phi$ are absorbed by the same electron of the metal. Since the energy of the photoemitted electron has to be larger than the metal work function Φ, a N-photon emission process is observed only if $N \cdot \hbar\omega > \Phi$.

Ideally, the order N of the photoemission process is determined by characterizing the laser power P or field-amplitude E dependence of the electron emission current $J \sim P^N \sim E^{2N}$ [50, 51]. It is known that this power dependence can be influenced by a variety of effects, e.g., bad signal-to-noise ratio, thermal heating of the electron gas and space-charge effects [52] or even by ultrafast excitation of collective electron modes in layered structures [53].

Nonlinear photoemission proceeds via both incoherent (sequential step-wise process) and coherent (instantaneous one-step process) excitation processes [54–56] which occur within the optical pulse duration on the order of several femtoseconds. Since excited electrons in metals exhibit rapid pure-dephasing times (defined in Eq. (2.1.15)) on the same order of magnitude [38, 57], the distinction between both processes remains experimentally challenging. In this work, excitation pulses with a pulse duration $\Delta t < 20$ fs are utilized and consequently both types of excitation processes have to be taken into account.

Probing nonlinear photoemission as a function of, e.g., a temporal delay between two adjacent ultrashort pulses (double-pulse excitation) enables nonlinear time-resolved photoemission experiments. Time-resolved experiments permit to measure electron scattering times which are related, via their scattering length, to fundamental properties like, e.g., electrical and thermal conductivity [38].

During the N-photon emission process the constituents of coherently excited electron-hole (e-h) pairs scatter and create an incoherent population of hot-electrons and hot-holes. Since the scattering lifetime of hot-electrons τ_{ee} (or hot-holes) is in general proportional to $\tau_{\mathrm{ee}} \sim \frac{1}{(E-E_{\mathrm{F}})^2}$ [58], with $(E - E_{\mathrm{F}})$ corresponding to the

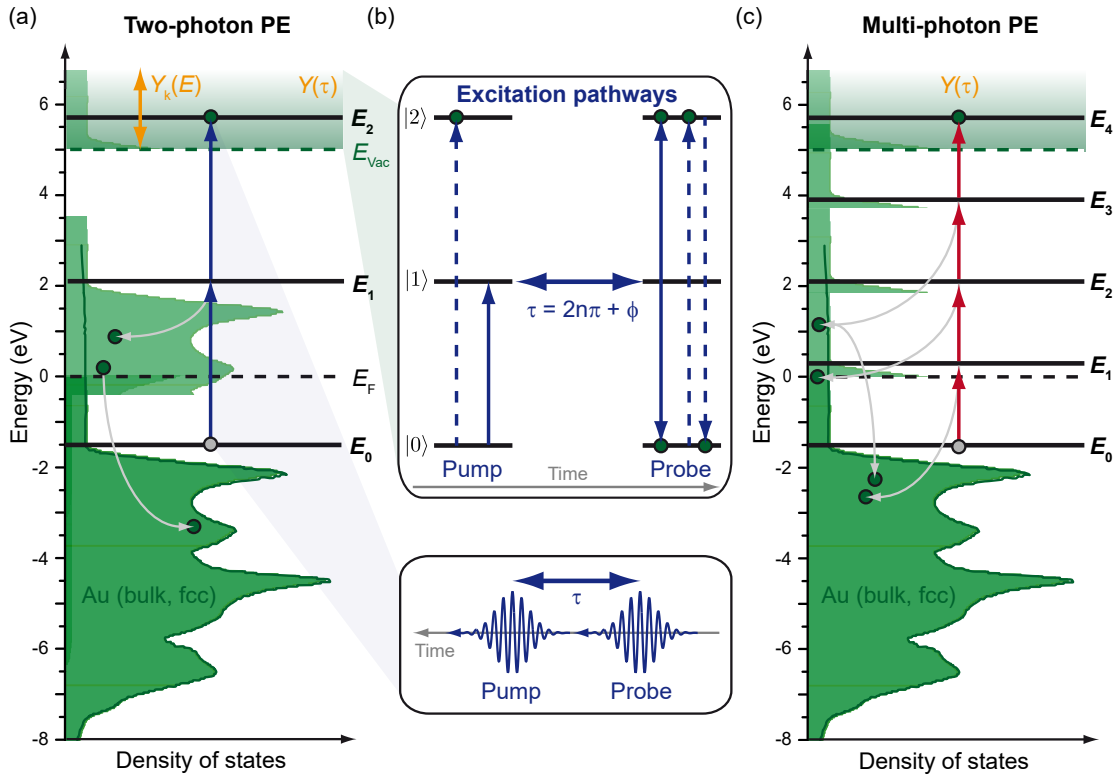

Figure 2.2 – Two-photon photoemission (PE) and multi-photon PE schemes for bulk Au. (a) The occupied density of states (DOS) of bulk Au (fcc) and the non-thermal hot-electron distribution generated by one-photon absorption ($\hbar\omega = 3.5$ eV, blue arrows) are depicted in dark and light green, respectively. Photoemitted electrons in exemplary final state $|2\rangle$ at E_2 are generated by absorption of a second photon delivered either by pump or probe pulse. Detecting the emitted photoelectron yield $Y_{\mathbf{k}_\parallel}(E)$ at certain in-plane electron momentum $\mathbf{k}_\parallel$ as function of kinetic energy enables two-photon PE spectra (orange), whereas the integrated signal as a function of inter-pulse delay $Y(\tau)$ provides two-pulse correlation measurements (orange) yielding information concerning, e.g, the temporal dynamics of the intermediate-states (here, e.g., $|1\rangle$ at E_1). The dominant intermediate-state decay mechanism (e-e-scattering) is depicted (grey arrows). (b) Upper box: Four possible excitation pathways of an exemplary two-photon PE process induced by identical pump and temporally delayed probe pulses (bottom box). Two-photon absorption occurs within an individual pump or probe pulse (up-pointing dashed blue arrows) by instantaneous two-photon absorption or by sequential one-photon absorption (up-pointing blue arrows, only intuitive order shown). If the absorption process is coherent, all four channels interfere constructively (up arrows) or destructively (down arrows) depending on the phase ϕ induced by the delay τ and the decoherence rate (integer factor n due to phase wrapping). (c) Multi-photon PE scheme ($N = 4$) using the same DOS and decay-process labeling as in (a) but with reduced photon energy $\hbar\omega = 1.75$ eV (red arrows). The detected four-photon correlation data contains information concerning the temporal dynamics and induced coherences of multiple intermediate states (here: states at energies E_1, E_2 and E_3). Adapted from Ref. [38].

electron energy E relative to the Fermi energy E_F, typical e-e (or h-h) scattering times are infinite at $E = E_\mathrm{F}$ (electrons at the Fermi surface) and decrease to $\ll 10$ fs for energies of several eV above the E_F. [38]. The short e-e scattering time leads to the fact that the non-thermal electron distribution generated by photoexcitation thermalizes first to a *hot* Fermi-Dirac distribution via e-e scattering, before transferring energy to the lattice via e-ph scattering [59].

Note that the electronic system exhibits a smaller heat capacity than the lattice which results in extremely high electron gas temperatures after femtosecond pulse excitation [60]. Final thermal equilibration of both electron and phonon baths is obtained on a longer time scale (> 100 fs) via e-ph scattering. A more detailed summary concerning the electron dynamics in metals including also surface state effects is found in Ref. [38].

In this work, nonlinear time-resolved photoemission experiments including up to $N = 4$ photons are presented, which will be explained in detail in Sec. 2.3. Here, the reader is firstly introduced to some essential concepts and simplifications of the photoemission process used in time-resolved two-photon-photoemission (2PPE) spectroscopy ($N = 2$), which will be helpful later. The following concepts are based on the explanations of Ref. [38].

The principle of time-resolved 2PPE spectroscopy is exemplarily presented in Fig. 2.2 (a) for electron excitation in bulk gold (calculated DOS of bulk Au (fcc) depicted in green). After excitation of the first ultrafast laser pulse with $\hbar\omega = 3.5$ eV (blue arrow) a non-thermal distribution of electrons (lighter green) and holes is generated. The explicit form of this hot-electron distribution depends on the excitation energy, the explicit transition moments and the joint density of occupied and unoccupied states. Due to the high work function $\Phi = E_\mathrm{Vac} = 4.6 - 5.6$ eV of gold [42], no electron is emitted by single-photon absorption.

In Fig. 2.2 (a), an exemplary nonlinear excitation pathway of electrons at initial energy E_0 below E_F is depicted. A transient population of electrons at intermediate energy E_1 above E_F can be photoemitted by absorbing a second photon from the time-delayed pulse since $E_1 + \hbar\omega > E_\mathrm{Vac}$. The different initial, intermediate, and final states at corresponding energies which are involved in the 2PPE process are labeled by the basis functions $|0\rangle$, $|1\rangle$ and $|2\rangle$, respectively.

Since the emission of the electron from the sample surface to the vacuum in perpendicular direction ($\perp$, with respect to the surface) is not invariant under translation, $\mathbf{k}_\perp$ is not a good observable [61]. Nevertheless, for well-ordered surfaces the crystal potential and lattice periodicity stay constant in parallel direction ($\parallel$, with respect to the surface). This means that for all emitted electrons $\mathbf{k}_\parallel$ is invariant (conserved) and its absolute value is defined by $|\mathbf{k}_\parallel| = \sin(\xi)\sqrt{2m_0 E_\mathrm{kin}/\hbar^2}$

with electron rest mass m_0 and ξ being the electron emission angle between the surface normal and $\mathbf{k}$ [61]. In this way, the detected photoemission current, i.e., the photoemission yield Y, can in general be measured as a function of energy $E(\mathbf{k}_\parallel) = E_{\mathrm{kin}}(\mathbf{k}_\parallel) = E_2(\mathbf{k}_\parallel) - E_{\mathrm{Vac}}$ and in-plane momentum $\mathbf{k}_\parallel$ of the emitted electron to obtain nonlinear kinetic energy electron spectra $Y_{\mathbf{k}_\parallel}(\mathrm{E})$.

For fixed in-plane momentum $\mathbf{k}_\parallel$ this spectrum contains information regarding the hot-electrons situated at, e.g., E_1 since E_1 and $E(\mathbf{k}_\parallel)$ are related by $E_1 = E(\mathbf{k}_\parallel) + \hbar\omega - E_{\mathrm{Vac}}$. Note that E_1 and E_{Vac} are measured relative to E_{F}. By detecting electron spectra at different tuned temporal delay steps $Y_{\mathbf{k}_\parallel}(\mathrm{E}, \tau)$ between pump and probe pulse (see lower box in Fig. 2.2 (b)) the thermalization of the hot-electron population can be investigated [38]. Note that on top of that, by measuring $E(\mathbf{k}_\parallel)$ as a function of electron emission angle ξ dispersion curves can be obtained [61], e.g., $E_1(\mathbf{k}_\parallel)$ based on the exemplarily depicted emission process in Fig. 2.2 (a).

Since in this work, the energy- and $\mathbf{k}_\parallel$-integrated photoemission current is detected as a function of temporal delays between excitation pulses, the integrated photoemission yield as function of the temporal delay $Y(\tau)$ between the two excitation pulses will be considered in particular. This probes electronic relaxation processes via a two-pulse correlation measurement, if both pulses have the same spectrum and parallel polarization. In this case the 2PPE process has four independent excitation-pathways shown in the upper box of Fig. 2.2 (b), whose individual contribution to the two-pulse correlation measurement data depends on the delay τ and the photoinduced electron dynamics.

Due to the high pulse power (large field amplitude) the 2PPE can be generated by two-photon absorption of either the pump (up-pointing blue dashed arrow on the left Fig. 2.2 (b) or probe pulse (up-pointing blue dashed arrow on the right in Fig. 2.2 (b). If the *intermediate-state population lifetime* at energy E_1 is long compared to the delay τ, also sequential one-photon absorption from each pulse contributes to the 2PPE signal, which is depicted in the upper box of Fig. 2.2 (b) for the intuitive ("first-pump-than-probe") excitation pathway (two sequential up-pointing blue arrows). If further the *coherence in the excitation* is significantly shorter than the delay τ, the population dynamics of the hot-electrons will dominate the delay-dependent signal. In case the coherence persists on the time scale of the delay τ, the four excitation channels can interfere (see Fig. 2.2 (b)) constructively (up-pointing arrows) or destructively (down-pointing arrows) depending on the phase ϕ (n labels here an integer factor due to phase wrapping) between pump and probe pulse. Note that in case of the coherent process, also the counter-intuitive order of interaction (first pump-coupling between state $|1\rangle$ and $|2\rangle$ then probe-coupling between state $|0\rangle$ and $|1\rangle$) contributes to the emission signal (Fig. 2.2 (b) shows only intuitive order) [62].

Since the measured nonlinear correlation signal contains not only information concerning the hot-electron population decay times but also on the dephasing times of the induced coherences in the material, a theoretical model beyond the incoherent rate-equation approach is needed to fully describe the measured signal. The simplest model which accounts also for coherent effects is obtained by using optical Bloch equations. These equations describe in general the time evolution of the response of an atomic system, represented by a density matrix, to an external, time-dependent perturbation including coherence effects induced by a multiphoton excitation process [63].

In case of the exemplarily discussed two-pulse correlation experiments depicted in Fig. 2.2 (a) and (b) the response of the system to the external optical perturbation is given in general by the wave function [63]

$$\Psi(t) = \sum_m a_m(t)\phi_m. \tag{2.1.11}$$

$\Psi(t)$ can be written as a linear combination of the basis functions of the unperturbed system ϕ_m and is well known if the time-evolution of the amplitude coefficients $a_m(t)$ is defined. Because of the optical perturbation the coefficients $a_m(t) \sim \mathrm{e}^{-im\omega_\mathrm{l}t}$ contain "fast varying" temporal variations at optical frequencies ω_l. They are replaced by "slowly varying" set of complex coefficients $c_m(t)$ by the transformation

$$a_m(t) = c_m(t)\mathrm{e}^{-im\omega_\mathrm{l}t}. \tag{2.1.12}$$

Within this so-called "rotating frame" the optical Bloch equations are given by

$$\frac{dc_m(t)}{dt} = -i\Delta_m c_m(t) + \frac{i}{2\hbar}\mu_{m,m-1}\tilde{E}^*(t)c_{m-1}(t) + \frac{i}{2\hbar}\mu_{m,m+1}\tilde{E}(t)c_{m+1}(t), \tag{2.1.13}$$

with detuning $\Delta_m = \omega_{0m} - m \cdot \omega_\mathrm{l}$ between the optical excitation, oscillating at central frequency ω_l, and the electronic states $|m\rangle$ with $m \in \{0, 1, 2\}$ (see Fig. 2.2 (a)) and individual transition dipole moments $\mu_{m,m\pm1}$ [63]. Note that the description of the optical excitation via the two-pulse sequence which is in general given by $\tilde{E}(t) = E(t)\cos(\omega_\mathrm{l}t) + E(t-\tau)\cos(\omega_\mathrm{l}(t-\tau))$ with pulse envelopes $E(t)$ and $E(t-\tau)$ is simplified in the rotating frame resulting in $\tilde{E}(t) = E(t) + E(t-\tau)\exp(-i\omega_l\tau)$. From Eq. (2.1.13) the time evolution of the different populations and coherences of the 3-level system excited by a 2-pulse excitation is retrieved by solving $3^2 = 9$ coupled differential equations. The respective temporal dynamics can be clearly arranged in a density matrix

$$\rho(t) = \begin{pmatrix} c_0(t)c_0^*(t) & c_0(t)c_1^*(t) & c_0(t)c_2^*(t) \\ c_1(t)c_0^*(t) & c_1(t)c_1^*(t) & c_1(t)c_2^*(t) \\ c_2(t)c_0^*(t) & c_2(t)c_1^*(t) & c_2(t)c_2^*(t) \end{pmatrix}, \tag{2.1.14}$$

in which time-dependent "populations" of the corresponding states $|m\rangle$ are represented by the diagonal elements $\rho_{mm}(t) = c_m(t)c_m^*(t)$ and off-diagonal elements correspond to the time evolution of the "coherences" (also known as "induced polarizations") $\rho_{mn}(t) = c_m(t)c_n^*(t)$, describing the field-induced coupling between the states $|m\rangle$ and $|n\rangle$.

Both populations ρ_{mm} and coherences ρ_{mn} decay by inelastic and elastic scattering which is quantified by the population-relaxation (or energy-relaxation) times T_1^m and the phase-relaxation times T_2^{mn}, respectively. Since phase-relaxation (also called "decoherence" or simply "dephasing") results from both inelastic population decay T_1^m and pure-dephasing T_2^{*mn} due to elastic scattering processes, the corresponding total dephasing rate (inverse total dephasing time T_2^{mn}) is given by [64]

$$\frac{1}{T_2^{mn}} = \frac{1}{2T_1^m} + \frac{1}{T_2^{*mn}}. \tag{2.1.15}$$

A detailed introduction and analysis of this general equation can be found in Ref. [65]. The authors shed light on the physical origin of the individual terms based on quantum mechanical and stochastic models and further discuss critically the interesting implication $T_2 \leq 2T_1$ since $1/T_2^* \geq 0$.

Numerically solving the system of coupled differential equations (see Eq. (2.1.13)) for the time-integrated population of the final state

$$\rho_{22}(\tau) = \int c_2(t)c_2^*(t)dt, \tag{2.1.16}$$

as a function of the inter-pulse delay τ enables simulation of the two-pulse correlation data. Nevertheless, disentanglement of the individual decay times (T_1^m and T_2^{mn}) is still non-trivial and requires a certain decomposition of the measured correlation curve by Fourier-filtering as described in detail in Ref. [38].

Even though the optical Bloch equations establish an intuitive approach of analyzing nonlinear correlation data, they do not give any information about the underlying physical mechanisms that are responsible for the observed dynamics. As pointed out in Ref. [38] decoherence occurs through elastic and inelastic scattering of e-h-pairs with the deformation potential, Fermi sea, impurities or the sample surface, while the decay of the intermediate-state population mainly proceeds due to e-e scattering processes (as depicted schematically in Fig. 2.2 (a)). Hot-electrons may scatter with electrons within the Fermi sea, leading to carrier

multiplication processes as, e.g., secondary hot-electron generation [66]. Further hot-electron decay mechanisms are ballistic transport or diffusion into the bulk [67, 68]. A detailed discussion of coherent and incoherent electron dynamics can be found as well in Ref. [38].

Figure 2.2 (c) schematically depicts the multi-photon photoemission scheme from bulk Au using the same DOS as in (a). Due to the reduced photon energy of $E_{\mathrm{ph}} = \hbar\omega = 1.75$ eV photoemitted electrons can be only generated in a four-photon excitation process resulting in a nonlinearity $N = 4$ of the photoemission. From the two-pulse correlation data based on the detection of the integrated photoemission yield $Y(\tau)$ as a function of temporal delays between the pump and probe pulse τ the temporal dynamics and induced coherences of multiple intermediate states can be retrieved. Here three exemplary intermediate states at energies E_1, E_2 and E_3 are depicted. Note that each intermediate state can decay by several mechanisms as discussed above, e.g., e-e scattering (grey arrows).

Since unraveling of the large amount of included decay times and possible excitation pathways by Fourier-filtering is challenging, in this thesis a coherent multidimensional spectroscopy method is utilized [69] by extending the two-pulse excitation to a multipulse excitation and by using a technique called phase-cycling [70] which in combination allows to selectively filter certain excitation-pathway contributions in the detected signal. The combination of coherent multidimensional spectroscopy with the spatial resolution of PEEM is called 2D nanoscopy [28], whose basic aspects are introduced to the reader in Sec. 2.3.

2.2. Properties of Au plasmonic surface systems

To briefly introduce the reader to the field of plasmonics, the fundamental properties of surface plasmon resonances in Au nanoparticles are first summarized, mainly following the explanations in Ref. [32]. Then a more detailed introduction to localized surface plasmon resonances in plasmonic nanoresonators is presented, as described in Ref. [31], since nanostructured surface systems of such a type are investigated in this thesis. Subsequently, the main aspects of the common formalism to describe the local response of plasmonic system to optical excitation is discussed.

2.2.1. Surface plasmon polaritons

The concept of "plasmons" describes collective free-electron oscillations in metals, which are modeled as bosonic quasiparticle excitations. The collective free-electron oscillation can be viewed, within the Fermi-liquid model, as a negatively charged

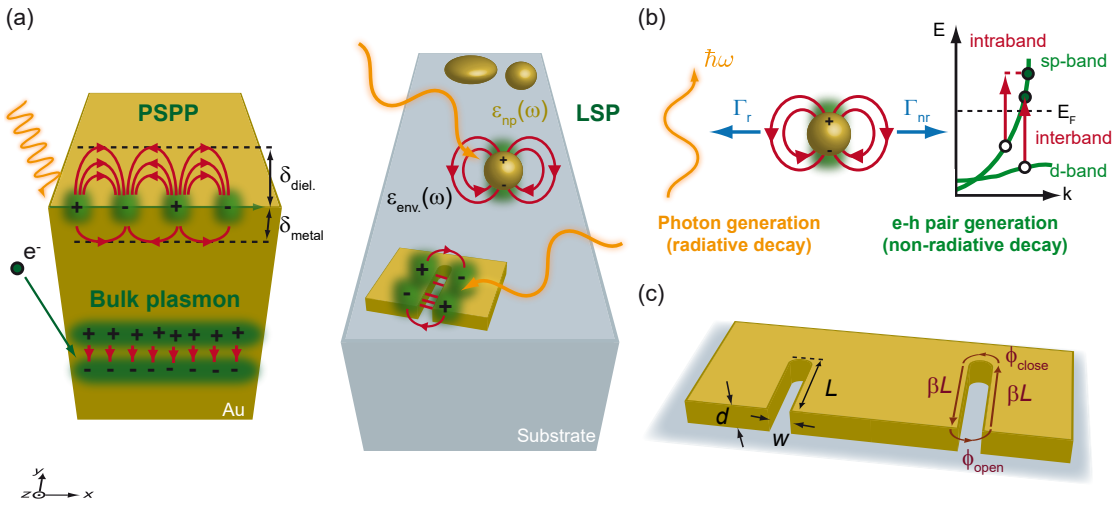

Figure 2.3 – Schematic view and basic properties of plasmonic systems. (a) A temporal snapshot of the, in principle oscillating, electron-gas density (green clouds) with labeled higher (−) and lower (+) electron density and resulting exemplary electrical field lines (red), implying the corresponding local plasmonic near field. Depicted are possible exemplary collective free-electron-gas oscillations in Au (left) which manifests, e.g., as a bulk plasmon excited by inelastic electron scattering (e^-) or optically excited (orange) at the vicinity of the surface as propagating surface-plasmon polariton (PSPP). $\delta_{\text{diel.}}$ and δ_{metal} correspond to the field-penetration depth at the dielectric and metallic surface side (skin-depth), respectively. Plasmonic nanoparticles (right) facilitates the optical excitation of localized surface-plasmon polaritons (LSPs), whose spectrally localized surface-plasmon resonances position depends on the nanoparticle dielectric function $\epsilon_{\text{np}}(\omega)$, size, shape and the dielectric function of the environment $\epsilon_{\text{env.}}(\omega)$. LSP generation in plasmonic resonator systems (bottom system on "Substrate") as investigated in this thesis. (b) Radiative (Γ_{r}) and non-radiative (Γ_{nr}) plasmon-decay mechanisms as explained in the main text. (c) The spectral position of the LSP resonances in plasmonic nanoresonators depends on their geometrical parameters (black), namely the slit waist w, resonator length L and thickness d, and can be described by a Fabry-Pérot model (red) including the open-end and close-end phase-factors ϕ_{open} and ϕ_{close} and the propagation constant β. Adapted from Ref. [31, 32, 71].

electron cloud which is oscillating around its equilibrium position with respect to the positively charged ions of the lattice [33].

Figure 2.3 presents a schematic view of the large variety of plasmonic systems and its basic properties. Plasmons in bulk matter (longitudinal waves), also known as volume or bulk plasmons (depicted in Fig. 2.3 (a), bottom), cannot be directly excited below the metal skin depth δ_{metal} by transversal electromagnetic fields (or-

ange), since the plasmon and photon energy dispersion relation never cross each other [33]. Nevertheless, at the material surface, specific plasmon modes exist and can be excited, e.g., by external electromagnetic fields [72]. First experimental signatures of surface plasmon modes have been achieved by inelastic electron scattering in electron-energy-loss-spectroscopy (EELS) experiments [73–75] and observation of the re-emitted light [76]. A detailed overview concerning excitation of surface plasmon modes by electron beam can be found in Ref. [77].

Coupling of light to the free electron-gas becomes most efficient, if the wave vector of the light is nearly parallel to the surface as for example realized in attenuated total internal reflection configurations [33]. More sophisticated surface plasmon excitation is realized by compensating the mismatch in wave vector between light and surface plasmon via metal-surface structuring by specially designed groove- or hole-gratings [78, 79], random surface roughness, where scattering provides the necessary momentum components [80], using defects [81], specially designed edge-incoupler [82–84] or by strong light focusing [85] or local, point-source-like near-field excitation [86]. These excitations are in general described by Maxwell's equation solved at the vicinity of a surface. The electromagnetic field resulting from the mathematical solution is then referred to as propagating surface-plasmon polariton (PSPP). At this point it should be emphasized that the additional term "polariton" relates to the fact that the plasmonic near field (red field lines in Fig. 2.3 (a)), generated by the optical electromagnetic excitation, is coupled to the excited collective electron oscillations within the material (green clouds in Fig. 2.3 (a)). Visualization of the explicit local plasmonic near fields at 30 nm spatial resolution has been realized by optical near-field scanning techniques, e.g, scanning near-field optical microscopy (SNOM) [87, 88].

Since the size of metallic nanoparticles is comparable to the metal skin depth δ_{metal} and consequently much smaller than the wavelength λ of the optical excitation (see Fig. 2.3 (b)), the excitation light can fully penetrate the metal and build up a polarization by displacing the conduction electrons. Such non-propagating modes are called localized surface-plasmon polaritons (LSPs) [33].

The electron-cloud displacement generates a restoring force, pulling the electrons back to their equilibrium position, which is described theoretically by a mass-on-a-spring damped harmonic oscillator driven by the electromagnetic radiation. The mass is thereby related to the electron density (green clouds in Fig. 2.3) and the spring constant corresponds to the coulombic restoring force between the negative electrons and the positively charged lattice. Within this approach the electron cloud follows the oscillation of the incident electromagnetic field with a phase shift described by a harmonic oscillator model, i.e., it oscillates like a dipole, which underlines the "nanoantenna" character of metallic nanoparticles [89].

Following this theoretical approach allows to determine the resonance condition

of the LSP. The spectral resonance position is labeled by the resonance frequency ω_{LSP} defined at the maximum extinction cross-section $\sigma_{\mathrm{Ext}}(\omega)$ [32]. The general resonance condition, called Fröhlich condition, shows that the LSP is resonantly excited at frequencies ω which satisfy [90, 91]

$$\mathrm{Re}[\epsilon_{\mathrm{np}}(\omega)] \approx -\chi\epsilon_{\mathrm{env}}(\omega). \tag{2.2.1}$$

This condition emphasizes that the spectral position of the extinction peak depends on both the complex dielectric function of the nanoparticle $\epsilon_{\mathrm{np}}(\omega)$ and the dielectric function of the surrounding environment $\epsilon_{\mathrm{env}}(\omega)$ and is further affected by the geometrical size, shape (χ-factor) and composition of the individual nanoparticles [92, 93]. Note that typical Au LSP resonances ω_{LSP} are located in the range from visible (> 500 nm) to near infrared (~ 1200 nm) wavelengths [32]. LSP probing is achieved by measuring the optical extinction by absorption spectroscopy [90, 94], by far-field extinction microscopy [71, 95], EELS [96–98], or cathodo-luminescence [99, 100].

As seen in Eq. (2.2.1), the real part $\mathrm{Re}[\epsilon_{\mathrm{np}}(\omega)]$ of the complex dielectric function is related to the resonance properties of the nanoparticle. In contrast, its imaginary part $\mathrm{Im}[\epsilon_{\mathrm{np}}(\omega)]$ contains information concerning the losses leading to damping of the plasmonic oscillation. The comparison of the imaginary part of the dielectric function $\epsilon(\omega)$ of gold and silver reveals, that Au suffers from higher losses than silver (Ag) in the visible spectral range [32, 101]. The increased losses in gold nanospheres are due to an additional decay channel of the LSP. This decay channel opens in Au because the band-edge frequency, i.e., the frequency at which interband transitions from the occupied 5d valence band to the unoccupied states in the $6\mathrm{s} - 6\mathrm{p}$ conduction band (as seen in Fig. 2.1 and Fig. 2.3 (b)) are allowed, overlaps with the LSP resonance position and therefore supports electron-hole pair generation by LSP decay. For silver this LSP decay channel is prohibited since the band-edge frequency is larger than the LSP resonance frequency, resulting in the decreased losses in silver [102].

The lifetime of an excited plasmon oscillation is expressed by the quality factor Q, whose explicit expression is strongly dependent on the geometry of the considered nanoparticle. Assuming to be in the quasistatic regime [103], i.e, almost homogeneous electric field distribution along the whole nanoparticle volume, which is achieved for nanoparticle sizes much smaller than the wavelength of the optical excitation, the quality factor can be written as [32]

$$Q(\omega) = -\frac{\mathrm{Re}[\epsilon_{\mathrm{np}}(\omega)]}{\mathrm{Im}[\epsilon_{\mathrm{np}}(\omega)]}, \tag{2.2.2}$$

which relates the absorption properties to the losses of the plasmonic resonance.

Directly at the resonance frequency ω_{LSP} the quality factor Q can be further approximated [89]

$$Q \sim \frac{\omega_{\mathrm{LSP}}}{\Delta\omega_{\mathrm{LSP}}}, \tag{2.2.3}$$

with $\Delta\omega_{\mathrm{LSP}}$ describing the full-width at half-maximum (FWHM) of the plasmonic resonance.

Losses lead in general to the decay of the plasmonic oscillation, which determines in case of a single Au nanoparticle the spectral bandwidth, known as the homogeneous linewidth, of the LSP resonance. Using a damped harmonic-oscillator model Ref. [104] shows that the LSP bandwidth is proportional to the total relaxation rate Γ, which is defined by

$$\Gamma = \Gamma_{\mathrm{nr}} + \omega^2 \Gamma_{\mathrm{r}}, \tag{2.2.4}$$

Γ_{nr} corresponds to the non-radiative rate due to electronic relaxation processes, eventually producing heat, and Γ_{r} labels the radiative contribution, which leads to elastically scattered radiation into the far-field. Both contributions are depicted schematically in Fig. 2.3 (b). Note that the radiative-decay contribution gets significantly decreased for smaller resonance frequencies due to the ω^2-term. The non-radiative decay includes multiple dephasing mechanisms like, e.g., e-e scattering, e-p scattering, electron-defects scattering and surface damping effects (details can be found in [32]) which are summarized in a so-called Landau-damping [105].

This Landau-damping mechanism generates electron-hole pairs on a time scale of $1-100$ fs via interband or intraband excitation [106–108] as depicted in Fig. 2.3 (b). The generated e-h pairs thermalize on a 500 fs timescale by e-e scattering to a hot Fermi-Dirac distribution which thermalizes with the lattice by e-p scattering within $1-5$ ps, which is described in detail in [32].

The relative amount of both radiative and non-radiative decay-rate contributions determines the ratio of absorbed versus scattered photons. An experimental [71] and theoretical investigation of nanoparticle dimers [109] reveals, that for nanoparticle-radii below 20 nm non-radiative decay dominates, while for larger radii radiative decay becomes more important. Both decay rates describe a population decay and can at first be connected to the population relaxation time T_1.

In the plasmonic framework the plasmon dephasing time T_2 is in principle related to its population relaxation time T_1 and a possible elastic phase-loss process T_2^* (pure dephasing) [110] by the same equation as given by Eq. (2.1.15). In general the T_2^*-contribution is neglected for plasmonic dephasing times [71, 110]. Nevertheless, the question if the plasmon polarization decay is determined by population decay only is still open and rarely discussed in literature. Note that in fact

such pure-dephasing processes have been reported for image-potential states at metal surfaces [111] and excitons in semiconductor quantum-dot like islands in narrow gallium arsenide (GaAs) quantum wells [112]. In the first case, they were induced by quasi-elastic scattering processes depending on the static order of adsorbate overlayers, while in the second case the coupling to acoustic phonons and the three-dimensional (3D) quantum confinement have been identified as factors enhancing those processes.

The results presented in the subsequent chapters are explained neglecting plasmonic pure-dephasing processes which simplifies the aforementioned relation to

$$\frac{1}{T_2} = \frac{1}{2T_1}, \tag{2.2.5}$$

and directly connects now the total decay rate Γ to the dephasing time T_2, of the coherent electron oscillation

$$\Gamma = \frac{2\hbar}{T_2}, \tag{2.2.6}$$

meaning that a larger bandwidth of the LSP resonance corresponds to a faster loss of coherence. This dephasing time is strongly depending on factors like particle geometry or the environment and varies between $2 - 50$ fs [71, 113].

One additional important property of plasmonic nanoparticles and nanoresonators (introduced in Sec. 2.2.2) is their ability to channel far-field radiation to sub-wavelength dimensions, which amplifies the electromagnetic fields locally by several orders of magnitude [33]. Various approaches exist to describe this phenomenon and the reader is guided to Ref. [32] for review. The local field enhancement factor $f(\mathbf{r}, \omega)$ can be defined as

$$f(\mathbf{r}, \omega) = \frac{|\mathbf{E}_{\mathrm{loc}}(\mathbf{r}, \omega)|}{|\mathbf{E}_0(\mathbf{r}, \omega)|}, \tag{2.2.7}$$

with local electric field $\mathbf{E}_{\mathrm{loc}}(\mathbf{r}, \omega)$ at position $\mathbf{r}$ and incident electric field $\mathbf{E}_0(\mathbf{r}, \omega)$. The achieved $f(\mathbf{r}, \omega)$ differs depending on the explicit plasmonic system between $1 - 10^3$ and may also result at particular positions in $f(\mathbf{r}, \omega) < 1$ because of destructive interference between incident and scattered light [114].

2.2.2. Plasmonic nanoresonators

As introduced in the previous section, plasmonic nanostructures enable precise control of their spectral properties, e.g., resonance frequency ω_{LSP}, quality factor Q, and enable concentration of optical excitation fields into sub-wavelength volumes resulting in strong local electric near fields. These abilities make plasmonic

nanostructures most suitable to investigate strong light-matter coupling in small volumes [115–118] . Their versatility is exhibited by different geometries like, e.g., slots [119–123], bowties [124–126] or nanoholes [127–130] which find broad application, e.g., in the field of biochemical sensing [122, 128–130].

In this thesis, asymmetric open-ended plasmonic nanoslit resonators are investigated, which are fabricated by gallium (Ga) focused-ion-beam (FIB) milling of a chemically synthesized, single-crystalline gold microplate [131, 132]. Each plasmonic nanoresonator features different Fabry-Pérot resonances whose effective resonance wavelengths depend on the geometrical slit properties: width w, length L, and thickness d, as depicted in Fig. 2.3 (c). This enables tuning of the individual resonance frequencies of the respective modes by changing the aspect ration L/w. As shown in Ref. [31], variation of the corresponding nanoresonator length L allows tuning of the various nanoslit resonances through the visible and near infrared spectrum. Note that since the different nanoslits are fabricated from the same microplate, they have the same thickness d.

After optical excitation, standing waves of LSPs are generated within the resonator, which establish various resonant modes. The resonance condition of these modes is described by a Fabry-Pérot model [89]

$$2\beta(\lambda_{\text{eff}}) \cdot L + \phi_{\text{total}}(\lambda_{\text{eff}}) = 2n\pi, \tag{2.2.8}$$

with propagation constant $\beta(\lambda_{\text{eff}})$ depending on the effective mode wavelength λ_{eff} and $\phi_{\text{total}}(\lambda_{\text{eff}}) = \phi_{\text{open}}(\lambda_{\text{eff}}) + \phi_{\text{close}}(\lambda_{\text{eff}})$ labeling the total accumulated phase shift at the open- and closed-end termination (see Fig. 2.3 (c)). Here n describes the order of the corresponding resonance. Note that since the incident radiation penetrates at optical frequencies into the metal the collective electron oscillations is not excited by the wavelength λ of incidence radiation but by a shorter effective wavelength λ_{eff} depending on the material properties. For systems like a plasmonic dipole antenna λ_{eff} can be related to the incident radiation wavelength λ by a linear scaling law [133] whereas for more complicated geometries these relations, the propagation constant and accumulated phase shift have to be obtained by numerical simulations like, e.g., finite-difference time-domain (FDTD) simulations.

For the investigated nanoresonators the following general statements hold: Increasing the aspect ratio L/w leads to a red-shift of the surface plasmon resonances and the emergence of higher-order modes [31]. The emergence of higher-order modes, which are spectrally separated, but present at equal spatial locations within the nanoresonator, enables interference of these modes and emphasizes further the ability of nanoresonators to squeeze multiple resonance to spatially small mode volumes. Chen *et al.* further quantifies experimentally and theoretically that these nanoresonators feature high quality factors Q (see Eq. (2.2.3)) between

$10 - 20$ across a large tuning range due to small radiative losses.

The effective local electrical near field $\mathbf{E}_{\mathrm{loc}}(\mathbf{r},\omega)$ within the plasmonic resonator can be simulated by the FDTD method and is used to describe the resonators far-field response to optical excitation fields as used within a so-called "local response formalism" introduced in the next section. The FDTD method [134, 135] calculates the local electric near field of an object by numerical integration of Maxwell's equation [136] in the time domain on a finite spaced grid (Yee cells). The geometry and material composition of the simulated object and its environmental properties can thereby be freely defined and in this way best adapted to the actual sample system. In this thesis the commercial code of Lumerical FDTD Solutions$^{\mathrm{TM}}$ has been used for numerical simulations.

2.2.3. Basics of the local response formalism

As introduced in Sec. 2.2.2 plasmonic nanoparticles and nanoresonators feature highly localized electric near fields $\mathbf{E}_{\mathrm{loc}}(\mathbf{r},\omega)$ upon optical excitation. The particular near-field distribution for a given optical excitation field $\mathbf{E}(\mathbf{r},\omega)$ is determined by the local response function $\mathbf{R}(\mathbf{r},\omega)$.

Note that the local response function acts on each polarization component $j \in \{\mathrm{p,s}\}$ of the incident electric field $E^{(j)}(\mathbf{r},\omega)$, which means that $\mathbf{R}(\mathbf{r},\omega)$ has in general tensor properties $\mathbf{R}^{(j)}(\mathbf{r},\omega)$. In this thesis linearly polarized excitation fields (adjusted perpendicular to the long nanoresonator axis) are used, which irradiate the plasmonic nanostructure under normal incidence (see Fig. 2.4 (a)). Hence, the description can be reduced to only one electric field component, e.g., $E^{(\mathrm{p})}(\mathbf{r},\omega)$ and a vector of the complex local response function

$$\mathbf{R}^{(\mathrm{p})}(\mathbf{r},\omega) = \begin{pmatrix} \mathrm{R}_x^{(\mathrm{p})}(\mathbf{r},\omega) \\ \mathrm{R}_y^{(\mathrm{p})}(\mathbf{r},\omega) \\ \mathrm{R}_z^{(\mathrm{p})}(\mathbf{r},\omega) \end{pmatrix}, \tag{2.2.9}$$

from which the amplitude and phase of the local near-field components in x-, y- and z-direction are calculated.

As depicted in Fig. 2.4 (a), $\mathbf{E}_{\mathrm{loc}}(\mathbf{r},t)$ can be achieved in time domain by a convolution ("$*$") of the optical excitation $E^{(\mathrm{p})}(\mathbf{r},t)$ and the temporal local response function $\mathbf{R}^{(\mathrm{p})}(\mathbf{r},t)$. Since in spectral domain the local electric field $\mathbf{E}_{\mathrm{loc}}(\mathbf{r},\omega)$ is calculated by simply multiplying the optical excitation $E^{(\mathrm{p})}(\mathbf{r},\omega)$ with the spectral local response function $\mathbf{R}^{(\mathrm{p})}(\mathbf{r},\omega)$, the local electric field is in general calculated first in spectral domain and than transformed to the time domain by inverse Fourier transformation via

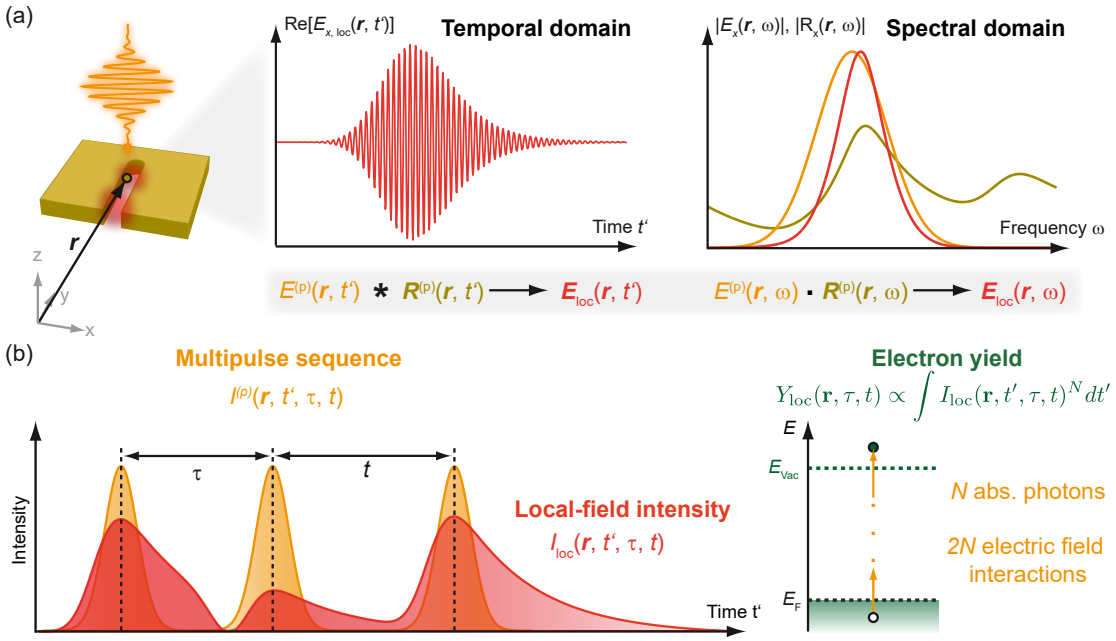

Figure 2.4 – Local response formalism of plasmon-assisted multiphoton photoemission. (a) The local response $\mathbf{R}^{(\mathrm{p})}(\mathbf{r},t')$ at exemplary position $\mathbf{r}$ of a plasmonic nanoresonator due to optical excitation (orange) by $E^{(p)}(\mathbf{r},t')$ results in a local electric near field $\mathbf{E}_{\mathrm{loc}}(\mathbf{r},t')$ (red clouds) within the slit. $\mathbf{E}_{\mathrm{loc}}(\mathbf{r},t')$ (red, x-component of real part is shown only) is determined in the temporal domain by convolution ($*$) of $E^{(p)}(\mathbf{r},t')$ with $\mathbf{R}^{(\mathrm{p})}(\mathbf{r},t')$, whereas in spectral domain $\mathbf{E}_{\mathrm{loc}}(\mathbf{r},\omega)$ (red, x-component of abs. part) is simply calculate by a multiplication ($\cdot$) of $E^{(p)}(\mathbf{r},\omega)$ (orange, abs. part) and $\mathbf{R}^{(\mathrm{p})}(\mathbf{r},\omega)$ (golden, x-component abs. part) and the complete temporal evolution $\mathbf{E}_{\mathrm{loc}}(\mathbf{r},t')$ is generated by inverse Fourier transformation of $\mathbf{E}_{\mathrm{loc}}(\mathbf{r},\omega)$. (b) Principle of the local response formalism applied to optical excitation by a multipulse sequence (orange) with systematically tuned inter-pulse delays τ and t affecting the local field intensity $I_{\mathrm{loc}}(\mathbf{r},t',\tau,t)$ (red). The corresponding nonlinear local electron yield $Y_{\mathrm{loc}}(\mathbf{r},\tau,t)$ (green) is calculated as indicated by assuming an N-th order photoemission process including in total $2N$ field-interactions, distributed along the constituent pulses. Adapted from [137, 138].

$$\mathbf{E}_{\mathrm{loc}}(\mathbf{r},t) = \mathscr{F}^{-1}\Big\{E^{(\mathrm{p})}(\mathbf{r},\omega)\cdot\mathbf{R}^{(\mathrm{p})}(\mathbf{r},\omega)\Big\}. \tag{2.2.10}$$

In this thesis, the spatially-resolved nonlinear electron emission yield $Y_{\mathrm{loc}}(\mathbf{r})$ is analyzed generated by the intense local near fields within a plasmonic nanoresonator upon optical excitation. This so-called "plasmon-assisted nonlinear electron emission yield" was in a first approach treated as a plasmon-assisted multiphoton

photoemission process and therefore calculated based on a model introduced by Merschdorf *et al.* [139], which will be also labeled as the FDTD-approach in this thesis. This model assumes an instantaneous pure-dephasing time T_2^* of the intermediate electronic states motivated by the large bandwidth of available electronic states above the Fermi energy in metals [140]. Even though, for transitions between isolated states coherent effects have been observed [141, 142], in the limit of continuous bands with a constant DOS, coherent effects have been further shown to cancel in time-resolved two-photon photoemission signals [143].

As a result, the local nonlinear electron emission yield $Y_{\mathrm{loc}}(\mathbf{r})$ is being proportional to the temporally integrated N-th power of the local electric near-field intensity $I_{\mathrm{loc}}(\mathbf{r},t)$ via

$$Y_{\mathrm{loc}}(\mathbf{r}) \propto \int_{-\infty}^{\infty} I_{\mathrm{loc}}(\mathbf{r},t)^N \mathrm{d}t$$
$$= \int_{-\infty}^{\infty} \Big(\mathbf{E}^{+}_{\mathrm{loc}}(\mathbf{r},t)\cdot\mathbf{E}^{-}_{\mathrm{loc}}(\mathbf{r},t)\Big)^N \mathrm{d}t = \int_{-\infty}^{\infty} \Big|\mathscr{F}^{-1}\Big\{E^{(\mathrm{p})}(\mathbf{r},\omega)\cdot\mathbf{R}^{(\mathrm{p})}(\mathbf{r},\omega)\Big\}\Big|^{2N}\mathrm{d}t. \tag{2.2.11}$$

Based on the perturbative treatment of the photoemission yield, discussed in the framework of 2D nanoscopy in Sec. 2.3, it should be emphasized here that the number of involved electric excitation-field terms is given by $2N$. This means, that the number of electric-field interactions leading to an emitted electron population is given by twice the number of absorbed photons N. This nonlinearity N of the electron emission process is in general known by, e.g., a separate power-law measurement.

The aforementioned enhancement of the local near field $\mathbf{E}_{\mathrm{loc}}(\mathbf{r},t)$ by plasmonic nanostructures has been shown to be beneficial in nonlinear PEEM experiments [144, 145] and enables in particular to spatially resolved the effective plasmonic mode pattern generated by the highly localized, thus, spatially interfering plasmonic modes. This shows further, that localized plasmonic modes of designed nanostructures can be investigated by nonlinear PEEM within a large-area field of view (calibrated: $\varnothing \sim 120-1$ µm) with sub-diffractional spatial resolution, which is in principle only limited by the de-Broglie wavelength of the detected electrons

$$\lambda_{\text{de-Broglie}} = \frac{2\pi\hbar}{\sqrt{2m_0 E_{\mathrm{kin}}}} \sim 1 \text{ nm}, \tag{2.2.12}$$

with kinetic energy $E_{\mathrm{kin}} = eU_{\mathrm{acc}} \sim 1$ eV. In Sec. 3.4 the different technical and experimental limitations which determine the effective spatial resolution of the used PEEM are discussed.

As briefly introduced in Sec. 2.1.2, the optical excitation with a pulse sequence

with systematically tuned temporal delay facilitates a time-resolved detection of the local electron emission yield $Y(\tau)$, which contains information concerning the radiative and non-radiative inelastic decay processes [137]. Depending on the inter-pulse delay τ and t the effective local-field intensity $I_{\mathrm{loc}}(\mathbf{r}, \tau, t)$ changes, resulting in a delay dependent local emission yield $Y(\mathbf{r}, \tau, t)$ as schematically depicted in Fig. 2.4 (b). Systematic tuning, for each temporal delay step, of the relative offset-phases $\Delta\varphi_{12}$ and $\Delta\varphi_{23}$ between the constituent pulses of the pulse sequence, a technique called phase-cycling [70] (introduced in Sec. 2.3) enables the selective extraction of certain excitation paths from the detected local emission signal $Y(\mathbf{r}, t, \tau, \Delta\varphi_{12}, \Delta\varphi_{23})$ by a 2D spectroscopy experiment.

Besides probing and analyzing the local photoemission yield as a function of certain pulse-sequence parameters, the local yield itself can be used as an increasable feedback parameter which allows to control the optical near fields in the vicinity of a plasmonic nanostructure, e.g., by adaptive polarisation pulse shaping [146]. The combination of the sub-diffractional spectral-resolution of PEEM and the selectivity and femtosecond temporal-resolution of 2D optical spectrosopy results in the coherent 2D nanoscopy method [28], whose main aspects are summarized in the following section.

2.3. Aspects of coherent 2D nanoscopy

The coherent 2D nanoscopy technique was developed in a joint effort [28] and a detailed theoretical description of this technique can be found in Ref. [138, 147]. It is based on the principles of coherent optical multidimensional spectroscopy, a versatile technique for studying ultrafast processes in complex systems. Several different beam geometries have been demonstrated [148]. In the conventional non-collinear phase-matching approach, the nonlinear signal upon optical excitation is detected in form of a coherently emitted field within a four-wave mixing process [20, 21, 149]. Alternatively, population-based multidimensional spectroscopy utilizes incoherent observables like, e.g., fluorescence [150–156], photoelectrons [28, 157, 158], photocurrents [159–162], or photoions [163–165]. Both approaches have been successfully used to investigate, e.g., coherent phenomena in a variety of quantum systems.

Common to all coherent multidimensional optical spectroscopy techniques is the detection of the nonlinear collective system response as a function of temporal delays between ultrashort laser pulses of an optical multipulse excitation sequence. Using two inter-pulse delays τ and t (coherence times) enables one to spectrally resolve both excitation and detection frequencies and reveal correlations between them [20]. The correlations are represented as signal peaks in a complex-valued

2D spectrum, as exemplarily depicted in Fig. 2.5, whose real and imaginary parts are interpreted as absorptive and refractive contributions, respectively [22].

In the subsequent sections the main aspects of coherent 2D nanoscopy are briefly summarized. This technique in particular analyses the local nonlinear photoemission yield upon optical multipulse excitation as a function of systematically tuned relative temporal delays and offset phases between the constituent pulses. The detected local spectroscopic information enables in principle to disentangle the temporal dynamics of the investigated surface system at a particular location in real space.

2.3.1. Density-matrix representation of pure and mixed states

At first the Hermitian density matrix ρ, which is used in this thesis as a synonym for the density operator $\hat{\rho}(t)$ is defined. The density matrix, phenomenologically introduced in Sec. 2.1.2 (see Eq. (2.1.14)), is defined for *pure states* $|\Psi(t)\rangle$ in the basis of energy eigenfunctions $|\phi_i\rangle$ with $i \in \{n, m\}$ by [166]

$$\begin{aligned} \rho^{(\mathrm{pure})}(t) &= |\Psi(t)\rangle \langle\Psi(t)| \\ &= \sum_{n,m} c_n(t) c_m^*(t) \, |\phi_n\rangle \langle\phi_m| = \sum_{n,m} \rho_{nm}(t) \, |\phi_n\rangle \langle\phi_m| \, . \end{aligned} \tag{2.3.1}$$

Note that these eigenfunctions $|\phi_i\rangle$ are represented by vectors which contain numerical elements. These elements are in general 0 and only 1 for the element of the corresponding eigenstate. The particular pure-state density-matrix elements $\rho_{nm}(t) = \langle\phi_n| \, \rho^{(\mathrm{pure})}(t) \, |\phi_m\rangle$ correspond in case of diagonal elements $n = m$ to the probability of finding the system in state n represented by the wave function $|\phi_n\rangle$ and in case of off-diagonal elements $n \neq m$ to coherent superpositions of the two related wave functions $|\phi_n\rangle$ and $|\phi_m\rangle$. Pure states fulfill the following equality which correlates their diagonal with their off-diagonal elements

$$\rho_{nn}(t)\rho_{mm}(t) = |\rho_{nm}(t)|^2. \tag{2.3.2}$$

Further, $\rho^{(\mathrm{pure})}$ obeys the normalization condition

$$\mathrm{Tr}(\rho(t)) = \sum_n \rho_{nn}(t) = \sum_n c_n(t) c_n^*(t) = 1. \tag{2.3.3}$$

The expectation value of a quantum-mechanical operator $\hat{O}(t)$ is determined by $\left\langle \hat{O}(t) \right\rangle = \langle\Psi(t)| \, \hat{O} \, |\Psi(t)\rangle$ and connected to the density matrix via

$$\left\langle \hat{O}(t) \right\rangle = \sum_{n,m} c_n(t) c_m^*(t) \left\langle \phi_m \right| \hat{O} \left| \phi_n \right\rangle = \sum_{n,m} \rho_{nm}(t) \hat{O}_{mn} = \mathrm{Tr}\Big(\rho^{(\mathrm{pure})}(t) \hat{O} \Big). \quad (2.3.4)$$

A further important property of the density matrix of pure states is that its "purity" equals one, meaning that $\mathrm{Tr}(\rho^2(t)) = 1$ for $\rho(t) = \rho^{(\mathrm{pure})}(t)$. Note that pure states are in principle a good description of single quantum systems which are uncoupled from the environment.

But, in a real physical measurement, e.g., due to a limited spatial resolution of the experimental apparatus, the probed system contains a large number of these single quantum systems which couple also to environmental degrees of freedom. Unfortunately, there is no way to write a wave function of statistically averaged quantum systems [167], yet a general description of such ensemble systems is achieved by introducing time-dependent probabilities $P_k(t)$ in the density matrix itself. These weights reflect the statistical mixture of different pure states

$$\left| \Psi_k(t) \right\rangle = \sum_k c_{k,n}(t) \left| \phi_n \right\rangle , \quad (2.3.5)$$

The density matrix of a so called *mixed state* is then determined by summing over all weighted density matrices of the individual single quantum systems k

$$\rho^{(\mathrm{mixed})}(t) = \sum_k P_k(t) \rho_k^{(\mathrm{pure})}(t) = \sum_k P_k(t) \left| \Psi_k(t) \right\rangle \left\langle \Psi_k(t) \right| . \quad (2.3.6)$$

In doing so, the density matrix uses the single quantum-system formalism to describe the behavior of an ensemble consisting of many similar quantum systems by defining a probability distribution of states that these systems can be found in. Since the same normalization conditions $\mathrm{Tr}(\rho(t)) = 1$ holds for the mixed-state density matrix, its real- and positive-valued diagonal elements

$$\rho_{nn}(t) = \left\langle \phi_n \right| \rho^{(\mathrm{mixed})}(t) \left| \phi_n \right\rangle , \quad (2.3.7)$$

are called *populations* referring to the occupation probability of a certain eigenstate n within the ensemble, whereas its complex-valued off-diagonal elements

$$\rho_{nm}(t) = \left\langle \phi_n \right| \rho^{(\mathrm{mixed})}(t) \left| \phi_m \right\rangle , \quad (2.3.8)$$

represent the statistical mixture of coherent superpositions of the individual eigenstate wave functions $|\phi_i\rangle$ with $i \in \{n, m\}$ and are called *coherences*.

Due to the complex-valued nature of these off-diagonal elements they obey the Cauchy-Schwartz inequality

$$\rho_{nn}(t)\rho_{mm}(t) > |\rho_{nm}(t)|^2. \tag{2.3.9}$$

The purity of the mixed-states density matrix is $\mathrm{Tr}(\rho^2(t)) < 1$ for $\rho(t) = \rho^{(\mathrm{mixed})}(t)$ and the expectation value of an operator $\hat{O}(t)$ is calculated by

$$\left\langle \hat{O}(t) \right\rangle = \sum_k P_k(t) \left\langle \Psi_k(t) \right| \hat{O} \left| \Psi_k(t) \right\rangle = \mathrm{Tr}\Big(\rho^{(\mathrm{mixed})}(t)\hat{O}\Big). \tag{2.3.10}$$

Note that the operator hat "ˆ" for quantum-mechanical operators will from now on be omitted in this thesis and only explicitly written if important. An important quantity is the expectation value of the time-independent dipole operator which is defined in the basis of energy eigenstates via

$$d = \sum_{n,m} \mu_{nm} \left| \phi_n \right\rangle \left\langle \phi_m \right|, \tag{2.3.11}$$

with dipole matrix elements μ_{nm}. Its expectation value quantifies the polarization $P(t)$ of the quantum system which is then given by

$$P(t) = \langle d \rangle = \mathrm{Tr}(\rho(t)d), \tag{2.3.12}$$

From now on, we refer to the mixed-state density matrix $\rho^{(\mathrm{mixed})}(t)$ by calling it simply ρ to realize a clear structure of the equations. Note that the time-dependence of ρ will be further only mentioned explicitly in important cases.

The time-evolution of the density matrix is derived from its temporal derivative and using Schrödinger's equation $\frac{\partial|\Psi(t)\rangle}{\partial t} = -\frac{i}{\hbar} H \left|\Psi(t)\right\rangle$ containing the Hamilton operator H, which yields for a density matrix of pure states the Liouville-von Neumann equation

$$\frac{\partial \rho^{(\mathrm{pure})}}{\partial t} = -\frac{i}{\hbar}[H, \rho^{(\mathrm{pure})}]. \tag{2.3.13}$$

In contrast, a mixed-state density matrix contains the time-dependent probabilities which lead by application of the chain-rule to the following time evolution of the individual matrix elements ρ_{nm} [167]

$$\frac{\partial \rho_{nm}}{\partial t} = \sum_k \frac{\partial P_k(t)}{\partial t} c_n(t) c_m^*(t) - \frac{i}{\hbar}[H, \rho]_{nm}. \tag{2.3.14}$$

The last term resembles the Liouville-von Neumann equation while the first term leads to additional dephasing and population relaxation which have been briefly introduced in Eq. (2.1.15).

2.3.2. Liouville-space representation

Dephasing and population relaxation can be handled in a convenient fashion by choosing a representation in Liouville space for the theoretical description. A detailed comparison between the Liouville space description and the more common treatment in Hilbert space can be found in Ref. [166].

The important changes at this point are that the density matrix ρ of a N-level system is represented by a vector $|\rho\rangle\rangle$ with N^2 elements which interacts with superoperators $\mathcal{L}$ with $N^2 \times N^2$ elements. The multiplication of the so-called "Liouville operator" $\mathcal{L}$ with the density-matrix vector $|\rho\rangle\rangle$ replaces the commutator $[H, \rho]$ in Hilbert space. The Liouville-von Neumann equation then reads

$$\frac{\partial|\rho\rangle\rangle}{\partial t} = -\frac{i}{\hbar}\mathcal{L}\,|\rho\rangle\rangle. \tag{2.3.15}$$

In analogy to the Hamilton operator in Hilbert space the Liouville operator is in general given by the sum of the unperturbed operator $\mathcal{L}$ and an interaction operator $\mathcal{L}_{\text{int}}(t)$ describing, e.g., the interaction with a light field $E(t)$ by

$$\mathcal{L}(t) = \mathcal{L} + \mathcal{L}_{\text{int}}(t) = \mathcal{L} - \mathcal{D}E(t). \tag{2.3.16}$$

Here $\mathcal{D}$ corresponds to the time-independent dipole operator in Liouville space. Due to the small perturbation of the light field $E(t)$ on the system, represented by $|\rho\rangle\rangle$, the density matrix can be expanded in a power series with respect to the field interactions n

$$|\rho\rangle\rangle = \sum_n |\rho^{(n)}\rangle\rangle. \tag{2.3.17}$$

As a consequence, the n-th order contribution $|\rho^{(n)}\rangle\rangle$ involves n field interactions and scales therefore with the n-th power of the electric-field amplitude or with the $n/2 = N$ power of the electric-field intensity.

The temporal evolution of the individual contribution $|\rho^{(n)}\rangle\rangle$ contains situations in which the system interacts with the electromagnetic field at *absolute* times t'_i with $i \in \{0, 1, 2, ..., n\}$, which are described by the interaction operators $\mathcal{L}_{\text{int}}(t'_i)$, and situations without interacting with the field, in which the time evolution of the unperturbed system (starting at, e.g., absolute time t'_0) is described by the Liouville-space Greens function $\mathcal{G}(t'_{i+1} - t'_i)$

$$\mathcal{G}(t'_{i+1} - t'_i) = \Theta(t'_{i+1} - t'_i)\exp\left(-\frac{i\mathcal{L}\cdot(t'_{i+1} - t'_i)}{\hbar}\right), \tag{2.3.18}$$

containing the time-independent Liouville operator $\mathcal{L}$ in analogy to the unperturbed system Hamiltonian H_0. $\Theta(t'_{i+1} - t'_i)$ corresponds to the Heaviside step

function. With the individual interaction operators $\mathcal{L}_{\text{int}}(t_i')$ and the corresponding Greens functions $\mathcal{G}(t_{i+1}' - t_i')$ each contribution $|\rho^{(n)}\rangle\rangle$ can be written in Liouville space as described in full detail in [138, 166].

Under the following assumptions the equation is simplified: First that the system is in equilibrium state $|\rho(t_0)\rangle\rangle$ before the first interaction which leads to elimination of the first Greens function $\mathcal{G}(t_1' - t_0')$. In addition, the time variables and integrals are rewritten in terms of *relative* delays, $t_i = t_{i+1}' - t_i'$, *between* the individual interactions instead of the former *absolute* times *of* the interaction t_i'. Implementing the interaction operator $\mathcal{L}_{\text{int}}(t_i') = -\mathcal{D}E(t_i')$ and sending $t_0 \to -\infty$ results then in

$$|\rho^{(n)}(t)\rangle\rangle = \left(\frac{i}{\hbar}\right)^n \int_0^\infty \mathrm{d}t_n \int_0^\infty \mathrm{d}t_{n-1} \ldots \int_0^\infty \mathrm{d}t_1 \, \mathcal{G}(t_n)\mathcal{D}\mathcal{G}(t_{n-1})\mathcal{D}\mathcal{G}(t_1)\mathcal{D}\,|\rho(-\infty)\rangle\rangle \ldots$$
$$\cdot E(t - t_n) \cdot E(t - t_n - t_{n-1}) \cdot \ \ldots \ \cdot E(t - t_n - t_{n-1} \ldots \ - t_1). \tag{2.3.19}$$

Note that here the individual $E(t)$-terms correspond to individual field excitations, meaning that the field of the optically exciting multipulse sequence applied in an experiment enters in *each* of this terms individually.

In Liouville space the expectation value of any operator $\hat{O}$ is given by the scalar product with the density matrix $|\rho\rangle\rangle$ [166]. Using the series expansion of the density matrix Eq. (2.3.17) and the dipole operator d, the influence of the n-th order perturbation of the field $E(t)$ on the n-th order polarization of the system is determined by

$$P^{(n)}(t) = \langle\langle \, d \, |\rho^{(n)}(t)\rangle\rangle, \tag{2.3.20}$$

Of paramount importance is that $P^{(n)}(t)$ features the n-th order polarization response function

$$S^{(n)}(t_n, t_{n-1}, \ \ldots t_1) = \left(\frac{i}{\hbar}\right)^n \langle\langle \, d \, | \, \mathcal{G}(t_n)\mathcal{D}\mathcal{G}(t_{n-1})\mathcal{D} \ldots \mathcal{G}(t_1)\mathcal{D}\,|\rho(-\infty)\rangle\rangle. \tag{2.3.21}$$

This nonlinear response function contains information concerning the correlations between the n electric-field interactions separated by the *relative* delay times $t_n, t_{n-1}, \ \ldots t_1$. Note that the dipole operator d labels here on purpose the operator in vector notation as defined by Eq. (2.3.11) whose dimensions $N \times N$ equals the dimensions of ρ, whereas the dipole operator in Liouville space $\mathcal{D}$ is a matrix with

dimensions $N^2 \times N^2$.

2.3.3. Principles of 2D nanoscopy

In contrast to conventional 2D spectrocopy techniques [168], which detect the coherent radiation emitted based on the excited nonlinear polarization in the sample as described by Eq. (2.3.20), 2D nanoscopy detects the incoherent time-integrated local photoemission yield $Y(\mathbf{r})$. Based on the Liouville-space representation introduced above, the n-th order photoemission yield $Y^{(n)}(\mathbf{r})$ is connected to the n-th order density matrix via [138]

$$Y_m^{(n)}(\mathbf{r}) = \int_{-\infty}^{\infty} \langle\langle mm|\rho^{(n)}(\mathbf{r},t)\rangle\rangle \, \mathrm{d}t. \tag{2.3.22}$$

Following Ref. [138], the final photoemission-step is modeled here indirectly in the sense that the photoemission yield is defined to be identical to the population in the population state $|mm\rangle\rangle$. Since in this model the state $|mm\rangle\rangle$ is located energetically below the vacuum energy, it assumes a direct population transfer from the population state $|mm\rangle\rangle$ to the free-electron state, which is of course a reasonable assumption in case of a particular ionization pulse, which drives the photoemission transition separately from the multipulse sequence probing the n-th order density matrix $|\rho^{(n)}(\mathbf{r},t)\rangle\rangle$. In the plasmon-assisted electron-emission model presented in this thesis the last step is explicitly driven only by the plasmonic system in a unidirectional incoherent process as outlined in Ch. 5, which includes both the dominating plasmonic population-decay mechanisms and the population relaxation in the metal [68].

Note that due to the spatially-resolved yield detection, the density matrix and in this way also the correlation function exhibit an additional dependence on the spatial coordinate $\mathbf{r}$. This results in the following relation of the photoemission probability

$$\begin{aligned} &\langle\langle mm|\rho^{(n)}(\mathbf{r},t)\rangle\rangle = \\ &= \int_0^{\infty} \mathrm{d}t_n \int_0^{\infty} \mathrm{d}t_{n-1} \ldots \int_0^{\infty} \mathrm{d}t_1 \, \mathcal{R}^{(n)}(\mathbf{r}, t_n, t_{n-1}, \ldots t_1) \cdot \\ &E(\mathbf{r}, t - t_n) \cdot E(\mathbf{r}, t - t_n - t_{n-1}) \cdot \ \ldots \ \cdot E(\mathbf{r}, t - t_n - t_{n-1} \ldots - t_1). \end{aligned} \tag{2.3.23}$$

The t_n are here, similar as in Eq. (2.3.21), related to the *relative* delay times.

The fundamental difference between the correlation $\mathcal{R}_m^{(n)}$ and the in Eq. (2.3.21) introduced correlation $S^{(n)}$ lies in the fact, that $\mathcal{R}_m^{(n)}$ leads to an electronic population in the m-th population state as a response to the incident electric field $E(\mathbf{r},t)$, whereas $S^{(n)}$ describes the polarization of the medium after optical excitation. The time- and space-dependent correlation function $\mathcal{R}_m^{(n)}$ is then calculated by

$$\begin{gathered}\mathcal{R}_m^{(n)}(\mathbf{r},t_n,t_{n-1},\ ...\,t_1) = \\ \left(\frac{i}{\hbar}\right)^n \langle\langle mm|\,\mathcal{G}(\mathbf{r},t_n)\mathcal{D}(\mathbf{r})\mathcal{G}(\mathbf{r},t_{n-1})\mathcal{D}(\mathbf{r})\ ...\ \mathcal{G}(\mathbf{r},t_1)\mathcal{D}(\mathbf{r})\,|\rho(-\infty)\rangle\rangle.\end{gathered} \tag{2.3.24}$$

Transformation of this equation into the interaction picture is achieved by implementing the time-dependent dipole operator $\mathcal{D}(\mathbf{r},t)$

$$\mathcal{D}(\mathbf{r},t) = \exp\!\left(\frac{i\mathcal{L}(\mathbf{r})\cdot t}{\hbar}\right)\mathcal{D}(\mathbf{r})\ \exp\!\left(-\frac{i\mathcal{L}(\mathbf{r})\cdot t}{\hbar}\right), \tag{2.3.25}$$

where the temporal propagation of the electronic states is given by the unperturbed Liouville operator $\mathcal{L}(\mathbf{r})$. Note that the instantaneous interaction at $t=0$ simplifies to $\mathcal{D}(\mathbf{r},0)=\mathcal{D}(\mathbf{r})$ [138].

Inserting further, the Liouville-space Greens function as defined in Eq. (2.3.18), which is now also dependent on $\mathbf{r}$ due to the spatial dependence of $\mathcal{L}(\mathbf{r})$, the correlation function exhibits the following form

$$\begin{gathered}\mathcal{R}_m^{(n)}(\mathbf{r},t_n,t_{n-1},\ ...\,t_1) = \left(\frac{i}{\hbar}\right)^n \delta(t_n)\Theta(t_{n-1})\ ...\ \Theta(t_1)\cdot \\ \langle\langle mm|\,\mathcal{D}(\mathbf{r},t_{n-1}+\ ...\ +t_1)\mathcal{D}(\mathbf{r},t_{n-2}+\ ...\ +t_1)\ ...\ \mathcal{D}(\mathbf{r},t_1)\mathcal{D}(\mathbf{r})\,|\rho(-\infty)\rangle\rangle.\end{gathered} \tag{2.3.26}$$

This formulation of the nonlinear response leading to an electronic population in the m-th state further involves the assumption that all decay mechanisms of the final population state during t_n can be described by a simple exponential function with one decay parameter. Ref. [138] points out that temporal integration over t_n results in a photoemission rate, which is proportional to the population directly after the last interaction at t_{n-1}. As a consequence, the exponential decay has been omitted and replaced by the δ-function in Eq. (2.3.26).

Assuming that $|\rho(-\infty)\rangle\rangle$ is in a population state, e.g., the energetic ground state of the system, a single dipole coupling ($n=1$) cannot transfer this population into another population (different diagonal element of the density matrix vector $|\rho(-\infty)\rangle\rangle$). The ground-state population can only be transferred to a coherence

(off-diagonal element of the vector $|\rho(-\infty)\rangle\rangle$).

However, for nonlinear number of field interactions $n > 1$ various possible transitions between density-matrix vector elements have to be considered. The successive transitions between different populations and coherences result in complex excitation pathways. Common graphical representations of this "Liouville pathways", are given by pictorial pathways through the *matrix* of density-matrix vector elements, also known as reduced density-matrix representation, in which the individual elements are represented as combination of Hilbert-states, e.g., $|g\rangle$ (rows) and $\langle g|$ (column) vectors, seen in Fig. 2.5 (b), or by using a double-sided Feynman diagram (DSFD) representation as depicted in Fig. 2.5 (c).

Arrows label in both representations the particular electric-field interactions acting on an energetic multilevel system whose particular structure depends on the investigated sample. The complete set of rules which have to be taken into account while drawing DSFD can be found in Ref. [167]. Note that the sign of each diagram is given by $(-1)^r$, where r corresponds to the number of field interactions on the *right* side, i.e., acting on the bra. This sign of each DSFD multiplied with the sign resulting from the $(i/\hbar)^n$-factor in the correlation function as seen, e.g., in Eq. (2.3.24), where n is here related to the *total* number of field interactions, determines the overall sign of the detected signal response which is preserved only in the purely absorptive 2D spectrum [167].

In Fig. 2.5 (a) an exemplary three-level ladder-system is assumed with electronic ground-state level $|g\rangle$, excited state $|e\rangle$ (with energy $E_e < E_{\mathrm{Vac}}$) and final state $|f\rangle$ ($E_f > E_{\mathrm{Vac}}$), which are energetically separated by $\Delta E \approx \hbar\omega_0$ and resonantly excited by an electric field (orange) containing photons with energy $\hbar\omega_0$. This particular example assumes $n = 4$ interactions of the system with the exciting electric field and detection of the final state population $|mm\rangle\rangle = |ff\rangle\rangle$ which results in probing *only* the correlation function $\mathcal{R}_f^{(4)}$. Note that using an additional high-energetic ionization pulse, enables to transfer also population from low-energy states with $E \ll E_{\mathrm{Vac}}$ as, e.g., $|ee\rangle\rangle$ to the vacuum. In this case, the corresponding correlation functions, e.g., $\mathcal{R}_e^{(4)}$ are as well probed and the corresponding terms, e.g., $\langle\langle ee|\rho^{(4)}(\mathbf{r},t)\rangle\rangle$ are add up in Eq. (2.3.22).

The horizontal (vertical) arrows in the reduced density-matrix representation, shown in Fig. 2.5 (b), indicate a change of a "ket", e.g., $|g\rangle$ ("bra", e.g., $\langle g|$) due to the field interaction, whereas in DSFDs, depicted in Fig. 2.5 (c), the arrows pointing to the diagram increase the corresponding ket or bra, while arrows pointing away from the diagram reduce it. The individual field interactions take place at *relative* times as described in Eq. (2.3.26) and lead to rephasing (red), non-rephasing (blue) and double-coherence (green) signal contributions whose individual DSFDs are presented in Fig. 2.5 (c). Note that mirroring each DSFDs

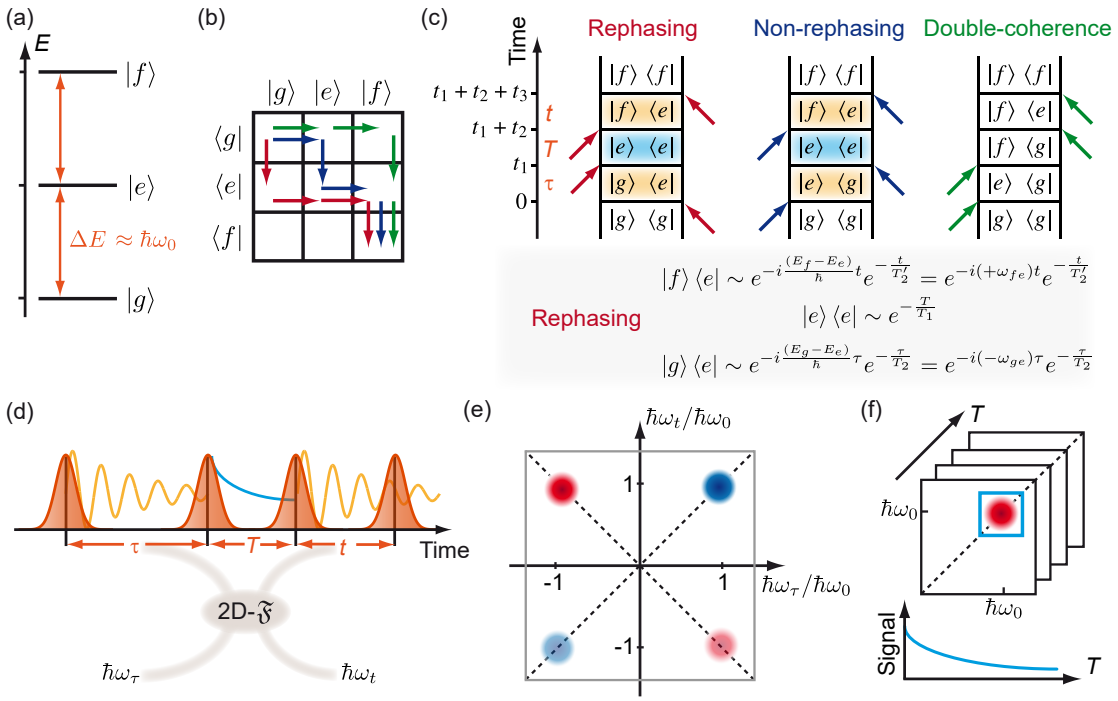

Figure 2.5 – Liouville pathways for an exemplary three-level system. (a) Three-level system with electronic ground state $|g\rangle$, excited state $|e\rangle$ and final state $|f\rangle$ which are energetically spaced by ΔE resonantly driven by photons with energy $\hbar\omega_0$. (b) Reduced density-matrix representation with rephasing (red), non-rephasing (blue) and double-coherence (green) Liouville excitation pathways for the case of $n = 4$ field interactions (colored arrows) corresponding to $\mathcal{R}_f^{(4)}$. (c) Double-sided Feynman diagram (DSFD) of corresponding Liouville pathways with final population in the double-exited state $|f\rangle\langle f|$. The individual field interactions (colored arrows) take place at relative times. Oscillation and dephasing dependence of the main compounds of the rephasing DSFD (grey shade) as measured in the laboratory frame of reference. (d) Systematic tuning of inter-pulse delays τ, t (coherence times) of the optical excitation (orange), e.g., using four-pulse sequences, enables sampling of the oscillation frequencies ω_{ge}, ω_{fe} and dephasing times T_2, T_2' of the individual coherences (yellow). (e) After 2D-Fourier transformation with respect to the coherence times τ, t the rephasing (red) and non-rephasing (blue) signal contributions are visualized in a 2D spectrum at energies $\hbar\omega_\tau, \hbar\omega_t$ corresponding to their oscillation frequencies. (f) Additional tuning of the inter-pulse delay T (waiting time) allows acquisition of multiple 2D spectra as a function of waiting time T. This enables, e.g., monitoring of the population (here: $|e\rangle\langle e|$) decay and thus characterization of the population relaxation time T_1. Partially adapted from Ref. [138].

on the vertical axis results in the complex conjugated pathways yielding the same information.

All three signal contributions are in a coherence (yellow shade) after the first interaction followed by a population (cyan shade) in case of rephasing and non-rephasing signals and in case of a double-coherence of a additional double coherence $|f\rangle\langle g|$. The difference between rephasing and non-rephasing signals becomes clear in the phase evolution of the particular coherence after the first field interaction. The rephasing signal exhibits two coherences $|g\rangle\langle e|$ and $|f\rangle\langle e|$ oscillating in the laboratory frame of reference (see Eq. (2.3.36)) with frequencies $-\omega_{ge}$ and $+\omega_{fe}$, respectively, which have opposite signs (gray shaded area), whereas the two coherences included in the non-rephasing signal oscillate at frequencies of equal signs.

This thesis focuses on the rephasing and non-rephasing signal contributions. To analyze the temporal dynamics of the constituent coherence and population states ultrashort multipulse sequences are used as optical excitation fields as depicted in Fig. 2.5 (d). By systematic tuning of the inter-pulse delays τ, t (coherence times) of the exemplarily shown four-pulse sequence (orange) and assuming one electric field interaction n per constituent pulse the oscillation and dephasing behaviour (yellow) of the corresponding coherence is sampled.

These sampled dynamics are visualized in a two-dimensional (2D) spectrum, schematically depicted in Fig. 2.5 (e), with energy axes $\hbar\omega_\tau$ and $\hbar\omega_t$ after performing a 2D-Fourier transformation. Based on the sign and value of the oscillation frequencies of the sampled coherences, the rephasing (red) and non-rephasing (blue) signal contributions end up in different quadrants of the 2D spectrum. Note that also their complex conjugated counterparts are depicted schematically (shaded red and blue) in their corresponding quadrants. To obtain intuitive energy axes the isolated rephasing signal contribution is commonly plotted in the quadrant of positive energy axes by flipping the $\hbar\omega_\tau$-axis. Isolation of certain signal contributions is discussed in detail in Sec. 2.3.5.

Systematic tuning of the additional inter-pulse delay T (waiting time) "between" the two coherence times τ, t enables generation of 2D spectra as a function of waiting time T as shown in Fig. 2.5 (f). This allows to monitor the temporal dynamics of, e.g., the population $|e\rangle\langle e|$ as in the depicted example (cyan line). Note that in case of the double-coherence signal contribution the double-coherence oscillation at frequency ω_{fg} and its dephasing is sampled by the waiting time T. Several different relaxation dynamics in various sample system have been investigated, e.g., energy transfer [169–181] or exciton dynamics [182–187] while interacting with the local environment.

Ref. [138] shows in a detailed comparison that the correlation functions $S^{(3)}$

and $\mathcal{R}_m^{(4)}$ contain similar possible excitation pathways. This leads to the result that, even though 2D nanoscopy finally detects an incoherent population-based signal (photoemission), coherent spectroscopic information is obtained as well, as commonly featured by optical coherent 2D spectroscopy via detection of the beating between the re-emitted coherent signal superimposed with a reference signal (local oscillator). The same result holds for various population-based multidimensional spectroscopy techniques detecting different incoherent observables like, e.g., fluorescence [150–156], photocurrents [159, 160], or photoions [163, 164]. In all techniques the optical excitation field perturbs the investigated system n times via dipole interaction (seen in Eq. (2.3.20) and Eq. (2.3.23)).

A significant difference between the optical techniques and 2D nanoscopy is the selection of the final population $|mm\rangle\rangle$, which affects the composition of the possible excitation pathways. In coherent optical 2D spectroscopy the last field interaction transfers a coherence, prepared due to the previous field interactions, to a ground state population. In this way, the finally detected signal field is emitted by a *stimulated* emission process in a propagation direction of a defined signal-field wave vector $\mathbf{k}_{\mathrm{sig}}$. On the other hand, in population-based fluorescence 2D spectroscopy the various field interactions have to end in a population which is located energetically above the ground state. The isotropic *spontaneously* emitted fluorescence (no preferential propagation direction) transfers these population to the ground state and therefore do not require an additional field interaction to emit the signal field. Hence, excitation pathways describing processes detected in optical 2D spectroscopy end mostly in the energetic ground-state of the system.

2D nanoscopy features absorption of multiple photons until the final population state $|mm\rangle\rangle$ gets populated. This includes additional boundary-conditions for possible excitation pathways in a 2D nanoscopy experiment.

First, the last state in the corresponding excitation pathway has to be a population, which means that the last field interaction step has to transfer a coherence into a population of the density matrix. Second, in the 2D nanoscopy experiments discussed in this thesis, no particular ionization pulse is applied, which would transfer, in addition to the individual field interactions $E(\mathbf{r}, t)$ driven by the multipulse sequence, the population of the m-th population state to the free-electron state above the vacuum energy. This would affect the introduced equations only in a sense that the energetic position of the m-th population state has to be already above the work function Φ, meaning that the m-th population state has to be thought of as the free-electron state.

Nevertheless, this raises the question of whether the assumption that a mono-exponential decay of the final population state leading to the $\delta(t_n)$ in Eq. (2.3.26) holds in this particular case of an absent ionization pulse.

As described in Ch. 5 a different approach is presented in this thesis for modeling the final electron-emission step which excludes this particular step completely from the power-series expansion Eq. (2.3.23). This approach features a not-dipole-coupled final step based on an undirectional, incoherent and plasmon-driven population transfer. Since this transfer is included in a non-perturbative simulation approach introduced in Sec. 2.4 and discussed in detail in Ch. 5, the debatable assumptions in the theory given by Ref. [138] shall be emphasize here and in the following section.

2.3.4. 2D nanoscopy in strongly dephasing systems

Before describing the separation of certain possible excitation pathways via the phase-cycling technique, let's first focus on additional modifications of Eq. (2.3.26), which have been established in Ref. [138] for metallic systems, due to their short electron dephasing times T_2 (see Eq. (2.1.15)).

The introduced modifications by Strüber *et al.* are based on the local-response approach discussed in Sec. 2.2.3, and simplify the model further in a sense that the photoemission process is dominated by the local-field intensity and not by electronic excitation processes. The modified model indeed shows that 2D nanoscopy enables investigation of collective coherent effects like plasmonic resonances in a metallic environment, characterized by short dephasing times of electronic excitations [138]. Based on the short metallic pure-dephasing times T_2^*, due to large amount of unoccupied electronic states above the Fermi energy [140], and population-relaxation times T_1 in the few-femtosecond regime [68, 188, 189], *instantaneous* dephasing and relaxation is assumed and for this reason the Liouville Green's function describing the temporal dynamics in the electron system in the absence of light perturbation is replaced by a δ-function

$$\mathcal{G}(\mathbf{r}, t) = \delta(t). \tag{2.3.27}$$

Inserting this simplified Green's function in Eq. (2.3.24) leads to the following expression of the n-th order correlation function [138]

$$\begin{aligned} &\mathcal{R}_m^{(n)\ \text{Strongly deph.}}(\mathbf{r}, t_n, t_{n-1},\ \ldots t_1) = \\ &\left(\frac{i}{\hbar}\right)^n \langle\langle mm|\ \Big(\mathcal{D}(\mathbf{r})\Big)^n\ |\rho(-\infty)\rangle\rangle \prod_{k=1}^{n} \delta(t_k). \end{aligned} \tag{2.3.28}$$

Due to the now time-independent interaction part, the population of the equilibrium state $|\rho(-\infty)\rangle\rangle$ is instantaneously transferred in the m-th population state by n dipole interactions, which are all acting on the system at the *same* time since

the delay t_k is set to zero by the δ-function. Note that this simplification eliminates *a priori* any temporal dynamics induced by explicit electronic transitions.

This becomes obvious by implementing $\mathcal{R}_m^{(n)\text{Strongly deph.}}(\mathbf{r}, t_n, t_{n-1}, \ldots t_1)$ in the general equation Eq. (2.3.23) and performing the time integration. This results in

$$\begin{gathered}\langle\langle mm|\rho^{(n)}(\mathbf{r},t)\rangle\rangle = \\ \left(\frac{i}{\hbar}\right)^n \langle\langle mm|\ \Big(\mathcal{D}(\mathbf{r})\Big)^n\ |\rho(-\infty)\rangle\rangle \Big(E(\mathbf{r},t)\Big)^n.\end{gathered} \tag{2.3.29}$$

Strüber *et al.* concentrates then further on the time-dependent part and interprets the field $E(\mathbf{r},t)$ as the momentary local electric-field introduced in Eq. (2.2.10)

$$\langle\langle mm|\rho^{(n)}(\mathbf{r},t)\rangle\rangle \propto \Big(E_{\text{loc}}(\mathbf{r},t)\Big)^n = \Big(E^+_{\text{loc}}(\mathbf{r},t) + E^-_{\text{loc}}(\mathbf{r},t)\Big)^n. \tag{2.3.30}$$

Due to the time-integration over t in the finally detected n-th order photoemission yield highly-oscillating terms vanish and the products in $\Big(E^+_{\text{loc}}(\mathbf{r},t) + E^-_{\text{loc}}(\mathbf{r},t)\Big)^n$ simplify to $\Big(E^+_{\text{loc}}(\mathbf{r},t)E^-_{\text{loc}}(\mathbf{r},t)\Big)^{n/2}$. This reassembles finally the yield as a function of the momentary local intensity $I_{\text{loc}}(\mathbf{r},t)$

$$Y_m^{(n)}(\mathbf{r}) \propto \int_{-\infty}^{\infty} \Big(E^+_{\text{loc}}(\mathbf{r},t)E^-_{\text{loc}}(\mathbf{r},t)\Big)^{n/2}\,\mathrm{d}t = \int_{-\infty}^{\infty} \Big(I_{\text{loc}}(\mathbf{r},t)\Big)^{n/2}\,\mathrm{d}t. \tag{2.3.31}$$

In a last mathematical derivation Ref. [138] explicitly shows, using the time-domain convolution-relation between the spatially homogeneous optical excitation field and the linear local response function

$$\mathbf{E}_{\text{loc}}(\mathbf{r},t) = E(\mathbf{r},t) \circledast \mathbf{R}(\mathbf{r},t) = \int_{-\infty}^{\infty} E(\mathbf{r},t-t')\mathbf{R}(\mathbf{r},t')\,\mathrm{d}t', \tag{2.3.32}$$

that the photoemission probability can be reformulated in terms of the positive and negative frequency components of the optical excitation fields $E^+(t-t')$, $E^-(t-t')$ and a new correlation function $\mathcal{Q}(\mathbf{r},t_1,...,t_n)$

$$\begin{gathered}\langle\langle mm|\rho^{(n)}(\mathbf{r},t)\rangle\rangle \propto \\ \int_{-\infty}^{\infty} \mathrm{d}t_{2n} \ldots \int_{-\infty}^{\infty} \mathrm{d}t_n \ldots \int_{-\infty}^{\infty} \mathrm{d}t_1\, \mathcal{Q}(\mathbf{r},t_1,...,t_n) \prod_{k=1}^{n} E^{\pm}(t - \sum_{i=k}^{n} t_i).\end{gathered} \tag{2.3.33}$$

Note that the limits of integration result from the definition of the individual convolution integrals and the substitution of absolute time variables by *relative*

delays t_i. The new correlation function $\mathcal{Q}(\mathbf{r}, t_1, ..., t_n)$ contains the product of the local time-domain response functions, as a function of the relative delays

$$\mathcal{Q}(\mathbf{r}, t_1, ..., t_n) = \prod_{k=1}^{n} R(\mathbf{r}, \sum_{i=k}^{n} t_i). \tag{2.3.34}$$

Ref. [138] follows from this relation that in case of instantaneous electronic pure-dephasing and relaxation the local photoemission signal as measured by 2D nanoscopy probes not the material properties, but the local response function via the generated local electric fields. For this reason, the spectroscopic information in the detected signal is in this particular case dominated by the collective excitation in the metal.

Note that in this thesis it will be discussed in Chapter 5 that plasmon-assisted nonlinear electron emission can be indeed successfully described using a full quantum model including electronic-state pure-dephasing and population-relaxation properties.

2.3.5. The phase-cycling technique

As seen in Fig. 2.5, optical excitation of the sample system triggers multiple possible Liouville pathways through the density matrix which by itself represents the entire system. These pathways lead to different signal contributions and certain spectroscopic features in the measured 2D spectrum whose individual analysis allows characterization of covered populations and coherences. In this paragraph the reader is introduced into the extraction of *particular signal contributions* out of the whole spectroscopic information contained in the detected n-th order photoemission yield by a technique called phase cycling [70].

This technique is established in this thesis by using optical excitation by three-pulse sequences $E(t') = E^+(t') + E^-(t') = 2\mathrm{Re}[E^+(t')]$ with systematically tuned delays τ, t and inter-pulse offset phases $\Delta\varphi_{12} = \varphi_2 - \varphi_1, \Delta\varphi_{13} = \varphi_3 - \varphi_1$ defined with respect to the first pulse

$$\begin{aligned} E^+(t', \tau, t, \Delta\varphi_{12}, \Delta\varphi_{13}, \gamma_{\mathrm{Ref}}) &= E_1(t')\mathrm{e}^{i\omega_0 t'} \\ &+ E_2(t'-\tau)\mathrm{e}^{i\omega_0 t' - i\omega_0\gamma_{\mathrm{Ref}}\tau - i\Delta\varphi_{12}} \\ &+ E_3(t'-\tau-t)\mathrm{e}^{i\omega_0 t' - i\omega_0\gamma_{\mathrm{Ref}}(\tau+t) - i\Delta\varphi_{13}}. \end{aligned} \tag{2.3.35}$$

Note that here t' corresponds to the time variable because t already labels the temporal delay between the second and third pulse and $E^-(t')$ is the complex-conjugated of $E^+(t')$. Further is the central frequency of the optical excitation

labeled by ω_0 and the individual envelope functions, e.g., $E_2(t'-\tau)$ are idealized as Gaussian functions, e.g., $E_2(t'-\tau) = \frac{E_0}{2}\exp\left(-2\ln(2)\frac{(t'-\tau)^2}{\Delta t^2}\right)$, with FWHM pulse duration Δt of the corresponding intensity profile. In the following discussion the envelope functions are further idealized by using δ-functions, e.g., $E_2(t'-\tau) = \delta_2(t'-\tau)$.

The dimensionless factor γ_{Ref} defines here the reference frequency of the particular frame of reference

$$\omega_{\mathrm{Ref}} = (1-\gamma_{\mathrm{Ref}})\omega_0, \tag{2.3.36}$$

and can in principle vary between $\gamma_{\mathrm{Ref}} = 0$, where the measurement is performed in the fully rotating frame, rotating at the central frequency ω_0 of the exciting pulse train, and $\gamma_{\mathrm{Ref}} = 1$, corresponding to the laboratory frame where $\omega_{\mathrm{Ref}} = 0$ [190]. Since the sampled signal contributions at oscillation frequency ω oscillate in the particular frame at the difference frequency $\omega - \omega_{\mathrm{Ref}}$, a smaller frequency sampling rate is sufficient in the fully rotating frame, which enables larger time steps $\delta t_{\max} = \pi/|\omega - \omega_{\mathrm{Ref}}|_{\max}$ of the systematically tuned delays τ, t to sample the oscillation of the signal contribution [191]. Since the relative phase offsets $\Delta\varphi_{12}, \Delta\varphi_{13}$ are independent of the γ-factor, it does not affect the following discussion and is therefore set here to $\gamma_{\mathrm{Ref}} = 0$. Note that from now on the γ-factor is simply referred to as γ.

In coherent optical 2D spectroscopy using a noncollinear optical excitation-scheme the selection of distinct spectroscopic signal contributions is achieved by detecting only the emitted signal contribution satisfying a certain phase-matching condition. The different phase-matching conditions are defined by combinations of the individual wave vectors $\mathbf{k}_i$ of the involved i single-pulse electric excitation fields [148]. Since this selection procedure requires coherence of the emitted response signal, it is not applicable for population-based 2D spectroscopy techniques like, e.g., fluorescence-based techniques or 2D nanoscopy. In case of the latter the detected photoemission signal is incoherent and does not contain any momentum information which is unaffected by the surface and therefore directly related to the optical excitation fields. Further, the implemented pulse-shaper based 2D nanoscopy setup requires a collinear excitation scheme and accordingly all single-pulse excitation fields exhibit the same wave vector $\mathbf{k}$.

In contrast to the coherently-detected approach exploiting the individual dependence of the coherently emitted signal contributions on the wave-vector combination, it has been shown, even for these signals [192, 193], that certain signal contributions can be also distinguished using their individual dependence on the relative offset phases, i.e., $\Delta\varphi_{12}, \Delta\varphi_{13}$, between the constituent pulses of the excitation sequence. Even for incoherent detection signals the full coherent information

is retrieved following this offset-phase approach as shown by Warren and coworkers [69, 194].

A theoretical description of the phase-cycling technique was given by Tan *et al.* [70]. The principle of phase cycling states that a specific signal can be reconstructed by a linear combination of signals which have been obtained under identical experimental conditions but changed relative phases of the excitation pulse sequence. The individual signal contributions are than extracted by a certain set of integer-valued phase-cycling coefficients (α, β, γ) which fulfill the following conditions [70]

$$\begin{aligned} \alpha + \beta + \gamma &= 0, \\ |\alpha| + |\beta| + |\gamma| &\leq n, \end{aligned} \tag{2.3.37}$$

where n labels the n-th order contribution and thus the number of field interactions. The first condition shows that the coefficient α is already determined by β and γ due to $\alpha = -\beta - \gamma$, which reduces the set of independent coefficients. Note that this reflects the phase-referencing to the first pulse as introduced already by the parametrization of the relative offset phases. This set of coefficients is unique for a particular signal contribution as long as sufficient relative phase combinations have been measured.

To obtain now a partial signal contribution $\tilde{Y}^{(n)}(\mathbf{r}, \tau, t, \beta, \gamma)$ with respect to the coefficients β and γ, the detected n-th order electron yield $Y^{(n)}(\mathbf{r}, \tau, t, \Delta\varphi_{12}, \Delta\varphi_{13})$ has to be integrated over the whole phase space of the relative phase offsets [70]

$$\begin{aligned} &\tilde{Y}^{(n)}(\mathbf{r}, \tau, t, \beta, \gamma) = \\ &\frac{1}{4\pi^2} \int_0^{2\pi} \int_0^{2\pi} Y^{(n)}(\mathbf{r}, \tau, t, \Delta\varphi_{12}, \Delta\varphi_{13}) \mathrm{e}^{-i(\beta\Delta\varphi_{12} + \gamma\Delta\varphi_{13})} \, \mathrm{d}\Delta\varphi_{12} \mathrm{d}\Delta\varphi_{13}. \end{aligned} \tag{2.3.38}$$

Since $Y^{(n)}(\mathbf{r}, \tau, t, \Delta\varphi_{12}, \Delta\varphi_{13})$ cannot be experimentally measured for each relative offset phase value of the phase space, the phase space is sampled in discrete steps $\Delta\varphi_{12} = 2\pi/L$ and $\Delta\varphi_{13} = 2\pi/M$ and consequently the integral is replaced by a discrete sum with $L \times M$ sampling points which results in

$$\begin{aligned} &\tilde{Y}^{(n)}(\mathbf{r}, \tau, t, \beta, \gamma) = \\ &\frac{1}{LM} \sum_{m=0}^{M-1} \sum_{l=0}^{L-1} Y^{(n)}(\mathbf{r}, \tau, t, l \cdot \Delta\varphi_{12}, m \cdot \Delta\varphi_{13}) \mathrm{e}^{-i(\beta l \Delta\varphi_{12} + \gamma m \Delta\varphi_{13})}. \end{aligned} \tag{2.3.39}$$

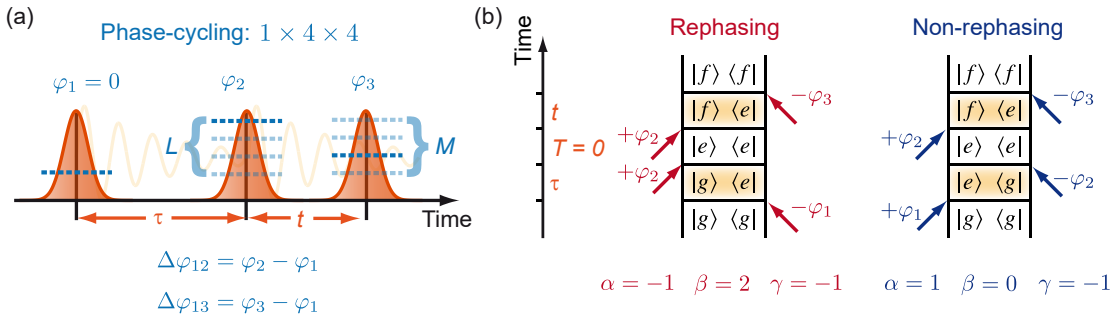

Figure 2.6 – Isolation of rephasing and non-rephasing signal contributions by 1×4×4 phase-cycling. (a) Schematic three-pulse sequence with highlighted phase-cycling scheme and offset phases φ_1, φ_2 and φ_3 (light blue) to isolate exemplary rephasing and non-rephasing signal contributions assuming the three-level system as defined in Fig. 2.5 (a). (b) Characteristic phase signatures $-\varphi_1+2\varphi_2-\varphi_3$ and $\varphi_1-\varphi_3$ to isolate the rephasing (red) or non-rephasing (blue) signal contributions, respectively, out of the measured dataset containing 16 single measurements, acquired with the 16 different offset-phase combinations applied to the exciting three-pulse sequence. Each phase signature corresponds to the depicted phase-cycling coefficients α, β and γ as introduced in the main text. Note that the waiting time $T = 0$. For this reason, the second and third field interaction have to take place both within the pulse duration of the second pulse due to the necessary offset phase φ_2. In case of the non-rephasing contribution this particular phase signature cancels since $\varphi_2 - \varphi_2 = 0$.

Note that the exponential function acts as a weight of the detected electron yield $Y^{(n)}(\mathbf{r}, \tau, t, l \cdot \Delta\varphi_{12}, m \cdot \Delta\varphi_{13})$ at each of the sampling points l, m. This weight depends on the chosen phase-cycling coefficients β, γ and enhances $Y^{(n)}(\mathbf{r}, \tau, t, l \cdot \Delta\varphi_{12}, m \cdot \Delta\varphi_{13})$ at sampling points which contribute to the extracted signal contribution $\tilde{Y}^{(n)}(\mathbf{r}, \tau, t, \beta, \gamma)$, and in turn suppresses the signal at non-contributing sampling points. Due to the discrete Fourier transformation in Eq. (2.3.39) with periodicity given by the number of sampling points L, M, aliased signals can remain after a $1 \times M \times L$ phase cycling experiment. This means, that phase-cycling cannot distinguish between signal contributions $\tilde{Y}^{(n)}(\mathbf{r}, \tau, t, \beta, \gamma)$ and contributions at $\tilde{Y}^{(n)}(\mathbf{r}, \tau, t, \beta + pL, \gamma + qM)$ with integers p and q. Nevertheless, by choosing the appropriate phase-cycling scheme aliased signals can be suppressed. Details can be found in Ref. [70].

In this thesis primarily the $1 \times 4 \times 4$ phase-cycling scheme is applied. It has been shown [70] that this phase-cycling allows to measure simultaneously the rephasing, also known as "photon-echo", the third-order 2Q-2D and 1Q-2Q signal contributions by just one single set of experiments. Assuming $n = 4$ field interactions

and optical excitation by three-pulse sequences as depicted in Fig. 2.6 (a) these contributions are obtained without contamination from aliasing signals. Ref. [194] showed further that additional signal distributions like transient-grating and reverse transient-grating, the latter is in this thesis referred to as the non-rephasing signal contribution, are isolated by the same set of experiments by using the corresponding phase-cycling coefficients α, β and γ.

The phase-cycling coefficients of the rephasing (photon-echo) contribution (red) are $\alpha = -1, \beta = 2$ and $\gamma = -1$ leading to the phase signature $-\varphi_1 + 2\varphi_2 - \varphi_3$ as depicted in Fig. 2.6 (b). Due to the fact that in this work photoemitted electrons are used as detection signal and in case of the applied pulse-excitation scheme, the boundary condition that the last interaction has to end in the population state $|f\rangle\langle f|$ has to be taken into account in addition to Eq. (2.3.37). As a result, the depicted rephasing DSFD is the only possible contribution to the detected signal for $n = 4$ field interactions (and its complex conjugated version). This is already not the case for the non-rephasing (reverse transient-grating) contribution (blue) shown in Fig. 2.6 (b) as explained in detail in the end of Sec. 2.3.6.

Based on the phase-cycling coefficient conditions in Eq. (2.3.37) the situation changes for the rephasing contribution at increased number of field interactions $n > 4$. Then multiple possible DSFD can be drawn which end in $|f\rangle\langle f|$. In general, all these possible Feynman-diagrams add up with diagram-specific weights in the isolated signal contribution. In our particular example (see Fig. 2.5 (a)) they all appear at the same spectral position in the 2D spectrum due to the equal oscillation frequency of the individual coherences.

Beyond that, based on the second condition in Eq. (2.3.37), additional multi-quantum signals appear in the 2D spectrum as described in detail in Ch. 5. The name "multi-quantum signals" results from the fact that these contributions exhibit coherences which oscillate at multiples of their fundamental oscillation frequency. This usually leads to modifications of the time increment of the tuned inter-pulse delays of the excitation pulse sequences to sample these high-frequency oscillations properly [155]. In Ch. 5 these multi-quantum contributions are observed without modification of the time increment and explained by back-folding of these under-sampled multi-quantum signals to the correctly sampled 2D spectrum. Note that these additional contributions can be either suppressed using a higher phase-cycling scheme to isolate the contribution of interest as shown in App. A or they serve as additional source of information and can be included in the theoretical modeling as done in Ch. 5.

2.3.6. Single harmonic-oscillator response in a strongly dephasing system

An explicit derivation of the 2D nanoscopic information generated by a single harmonic oscillator in a *strongly dephasing* system for $n = 4$ field interactions is modeled by an exponentially decaying oscillation as local time-domain response [138]

$$R^{+}(t) = \Theta(t)\mathrm{e}^{-i\omega_{\mathrm{Lo}}t-\gamma_{\mathrm{Lo}}t}. \tag{2.3.40}$$

Assuming a weak influence of the damping on the resonance frequency $\omega_{\mathrm{Lo}} \gg \gamma_{\mathrm{Lo}}$ [138], this time-domain response corresponds to the spectral response of a Lorentzian oscillator with central frequency ω_{Lo} and spectral width γ_{Lo}. Note that the assumption of weak damping does not necessarily hold in plasmonic systems which feature small Q-factors and multiple loss mechanisms leading to damping. If $\omega_{\mathrm{Lo}} \approx \gamma_{\mathrm{Lo}}$ the single harmonic-oscillator response cannot be longer described by a symmetric Lorentzian due to an arising asymmetric offset.

Nevertheless, substituting Eq. (2.3.40) in Eq. (2.3.34) together with the optical excitation pulse sequences with appropriate phase-cycling scheme as defined in Eq. (2.3.35) leads after Fourier transformation along both temporal delay axes to the following partial signal contribution $\tilde{Y}^{(4)}(\omega_\tau, \omega_t, \beta, \gamma)$ (see [138] for detailed calculation)

$$\begin{aligned}\tilde{Y}^{(4)}(\omega_\tau, \omega_t, \beta, \gamma) \propto & \frac{1}{i[-(\beta+\gamma)(\omega_{\mathrm{Lo}}-\omega_0)-\omega_\tau]+(4-|\beta|-|\gamma|)\gamma_{\mathrm{Lo}}} \\ & \cdot\frac{1}{i[-\gamma(\omega_{\mathrm{Lo}}-\omega_0)-\omega_t]+(4-|\gamma|)\gamma_{\mathrm{Lo}}} \quad + \quad \text{c.c.} \ .\end{aligned} \tag{2.3.41}$$

Note that the neglected dependence on the local coordinate $\mathbf{r}$ results from the spatially homogeneous time-domain response which is in general a strong idealization of real plasmonic nanostructures.

A 2D spectrum depicts commonly either the real part, imaginary part or the absolute value of $\tilde{Y}^{(4)}(\omega_\tau, \omega_t, \beta, \gamma)$. The spectrocopic features of the two-dimensional line shape of, e.g., the absolute value $|\tilde{Y}^{(4)}(\omega_\tau, \omega_t, \beta, \gamma)|$ are quantified, based on Eq. (2.3.41), by its spectral position along the $\omega_{\tau,t}$-axes and the corresponding spectral widths $\gamma_{\tau,t}$ which depend on the chosen phase-cycling coefficients α, β and γ. The corresponding signal contributions are located along the ω_τ-axis around the central frequency $\omega_\tau = \alpha(\omega_{\mathrm{Lo}} - \omega_0)$ with spectral width $\gamma_\tau = |\alpha|\gamma_{\mathrm{Lo}}$ using the conditions in Eq. (2.3.37). Along the ω_t-axis the central frequency is

given by $\omega_t = -\gamma(\omega_{\mathrm{Lo}} - \omega_0)$ and an increased spectral width $\gamma_t = (|\alpha| + |\beta|)\gamma_{\mathrm{Lo}}$ compared to the spectral width γ_τ. As a consequence, using a single harmonic-oscillator response and assuming a *strongly dephasing system* results in an asymmetric line shape of the phase-cycled signal contributions in the 2D spectrum. Note that 2D nanoscopy in strongly dephasing systems as theoretically described by Ref. [138] cannot distinguish between certain electronic excitation pathways by definition, see Eq. (2.3.28), but allows a distinction of certain photoemission signals $\tilde{Y}^{(n)}(\mathbf{r}, \omega_\tau, \omega_t, \beta, \gamma)$ which are generated by an interference of particular local electric fields Eq. (2.3.31). Nevertheless, the same nomenclature of the individual signals as introduced in Sec. 2.3.5 is employed to emphasize the number of interactions. For the rephasing contribution Eq. (2.3.41) results in

$$\tilde{Y}^{(4)}(\omega_\tau, \omega_t, 2, -1) \propto \frac{1}{i[-(\omega_{\mathrm{Lo}} - \omega_0) - \omega_\tau] + \gamma_{\mathrm{Lo}}} \cdot \frac{1}{i[(\omega_{\mathrm{Lo}} - \omega_0) - \omega_t] + 3\gamma_{\mathrm{Lo}}} \quad + \quad c.c. \ . \tag{2.3.42}$$

Thus, the signal peak of, e.g., the absolute value $|\tilde{Y}^{(4)}(\omega_\tau, \omega_t, 2, -1)|$ is located on the diagonal of the upper left quadrant of the 2D spectrum at ω_τ-axis around the negative frequency $\omega_\tau = -(\omega_{\mathrm{Lo}} - \omega_0)$ and at ω_t-axis around the positive frequency $\omega_t = (\omega_{\mathrm{Lo}} - \omega_0)$. Note that ω_0 corresponds here to the reference-frame frequency ω_{Ref} in the fully rotating frame ($\gamma_{\mathrm{Ref}} = 0$), as described by Eq. (2.3.36). This means that the signal contribution oscillates in the laboratory frame ($\gamma_{\mathrm{Ref}} = 1$) around the resonance frequency $\pm\omega_{\mathrm{Lo}}$ of the harmonic oscillator. Due to the 1:3 ratio of the spectral widths γ_τ and γ_t the peak's two-dimensional line shape is broadened along the ω_t-axis which reflects a factor 3 faster decay of the time-domain signal along the t-axis.

Further contributions as, e.g., the third-order double quantum coherence 2Q-2D ($\alpha = 2, \beta = -1, \gamma = -1$) are analyzed theoretically in Ref. [138] and are located, in contrast to the rephasing contribution, at an off-diagonal spectral position. Note that both the rephasing and 2Q-2D signals result from interactions with all three constituent pulses of the excitation pulse sequence. Consequently, they cannot be obtained by two-pulse experiments like, e.g., interferometric autocorrelation as introduced in Sec. 2.1.2. On the other hand, two-pulse signals, which require only $n = 2$ field interactions, can be extracted from the acquired dataset of 16 single measurements. For example the reverse transient grating signal [195], which is called in this thesis "non-rephasing" signal contribution ($\alpha = 1, \beta = 0, \gamma = -1$).

In our exemplary level system described in Fig. 2.5 (a) only the population in the final state $|f\rangle$ serves as detection signal since $E_f > E_{\mathrm{Vac}}$. For this reason, the non-

rephasing signal distribution has to end in the population of the final state $|f\rangle\langle f|$. This is only possible including at least $n = 4$ field interactions, which results in the fact that the two missing field interactions have to occur without affecting the phase signature of the signal contribution. Hence, the two field interactions have to take place within one excitation pulse and have to cancel each other in the phase signature, i.e., have opposite sign as depicted in Fig. 2.6 (b). Since the two counteracting field interactions can in principle occur in either of the three pulses of the excitation sequence (DSFD in Fig. 2.6 (b) reflects only interaction during the second pulse) these three possible contributions are add up in the corresponding partial photoemission yield $\tilde{Y}^{(4)}(\mathbf{r}, \omega_\tau, \omega_t, 0, -1)$ [138]. As a result, the overall line shape of $\tilde{Y}^{(4)}(\mathbf{r}, \omega_\tau, \omega_t, 0, -1)$ is then influenced by these three combinations and given by [138]

$$\begin{aligned}\tilde{Y}^{(4)}(\mathbf{r}, \omega_\tau, \omega_t, 0, -1) \propto \\ \frac{1}{i[(\omega_{\mathrm{Lo}} - \omega_0) - \omega_\tau] + \gamma_{\mathrm{Lo}} + 2\gamma_{\mathrm{Lo}}} \cdot \frac{1}{i[(\omega_{\mathrm{Lo}} - \omega_0) - \omega_t] + 3\gamma_{\mathrm{Lo}} - 2\gamma_{\mathrm{Lo}}} \\ +2 \cdot \frac{1}{i[(\omega_{\mathrm{Lo}} - \omega_0) - \omega_\tau] + \gamma_{\mathrm{Lo}}} \cdot \frac{1}{i[(\omega_{\mathrm{Lo}} - \omega_0) - \omega_t] + 3\gamma_{\mathrm{Lo}}} \\ + \frac{1}{i[(\omega_{\mathrm{Lo}} - \omega_0) - \omega_\tau] + \gamma_{\mathrm{Lo}} - 2\gamma_{\mathrm{Lo}}} \cdot \frac{1}{i[(\omega_{\mathrm{Lo}} - \omega_0) - \omega_t] + 3\gamma_{\mathrm{Lo}} + 2\gamma_{\mathrm{Lo}}} \quad + \quad c.c. \ .\end{aligned} \tag{2.3.43}$$

All three combinations oscillate at positive frequencies $\omega_\tau = \omega_t = (\omega_{\mathrm{Lo}} - \omega_0)$ and result in one effective signal peak located in the upper right quadrant of the 2D spectrum. The summation of the individual spectral widths for the corresponding frequency axis generates an effective width, where the ratio between the two effective widths γ_τ and γ_t is given by a non-integer value [138]. Note further that the factor 2 in the second summand Eq. (2.3.43) reflects the different statistical weights of the individual contributions as described in detail in [138].

In summary, different possible signal contributions affect the line shape in the 2D spectrum and have to be taken into account in cases where $|\alpha| + |\beta| + |\gamma| < n$. This effect becomes also important, as mentioned before, for rephasing signal contributions at high orders of nonlinearity $N = n/2$ and is omnipresent in this thesis for example in Ch. 5 and App. A. Here a nonlinearity around $N = 4$ of the detected photoemission yield suggests at least $n = 8$ field interactions. At this high nonlinearity of the emission process the isolated signal contributions by the $1 \times 4 \times 4$ phase-cycling scheme contain in addition to the intended rephasing signal

$\alpha = -1, \beta = 2$ and $\gamma = -1$, two multi-quantum contributions with phase-cycling coefficients $\alpha = 3, \beta = -2, \gamma = -1$ and $\alpha = -1, \beta = -2, \gamma = 3$, which turned out to be non-rephasing contributions for the modeled level system introduced in Ch. 5.

2.4. Modeling full excitation dynamics in open quantum systems

The previously discussed theoretical treatment to describe the nonlinear excitation dynamics in quantum systems is based on a weak perturbation of the investigated quantum system by the exciting electric fields. In this limit, the density-matrix operator ρ, representing the population states and coherences of the system can be expanded in a power series with respect to the field interactions n as described in Eq. (2.3.17) and the temporal evolution of certain orders $\rho^{(n)}(t)$ can be investigated by measuring a coherent observable, e.i., the n-th order polarization $P^{(n)}(t)$ defined in Eq. (2.3.20) or incoherent observables like, e.g., the nonlinear photoemission yield $Y_m^{(n)}(t)$ as introduced in Eq. (2.3.22). In this section a different non-perturbative approach is briefly introduced, which models the temporal excitation dynamics of the full density-matrix operator ρ by numerical integration of the Lindblad quantum master-equation. Quantum system specific applications of this approach and associated simulation results are described at corresponding positions in Ch. 4 and Ch. 5.

The Lindblad quantum master-equation [196] is a Markovian master-equation and includes the treatment of dephasing processes like population relaxation (dissipation) and pure dephasing (decoherence). A didactic mathematical derivation of this equation can be found in Ref. [197]. Following this approach the Born-Markov master-equation is derived by using the Liouville-von Neumann equation Eq. (2.3.13) and considering that the density-matrix operator ρ_{SB} is related to a "sample" quantum system S, mathematically described in a Hilbert space $\mathcal{H}_S$, and coupled to another quantum system B, called bath, in $\mathcal{H}_B$, which takes the environment of the quantum system into account. Consequently, ρ_{SB} is defined in the tensor-product space $\mathcal{H}_S \otimes \mathcal{H}_B$.

Two important approximations are made during the derivation of the Born-Markov equation [8]: Firstly, the *Born approximation*, which states that the system-bath coupling is sufficiently weak and that the bath is large, meaning that changes in the density-matrix operator of the pure bath ρ_B can be neglected and the system-bath states can be described by at all times t

$$\rho_{SB}(t) \approx \rho_S(t) \otimes \rho_B. \tag{2.4.1}$$

Secondly, the *Markov approximation*, allows to neglect "memory effects" of the environment in a sense that any self-correlation within the bath system created by the coupling to the quantum system decays rapidly compared to the characteristic timescale of noticeable changes in the states of $\rho_S(t)$. Applying both approximations and using a description in the interaction picture enables one to write the master equation only in terms of the *reduced density operator* $\rho_S(t)$ and the initial state of the bath and eliminates further any effects of $\rho_S(t)$ on $\rho_S(t')$ evaluated at earlier times $t' < t$ [8].

The Lindblad quantum master-equation arises from the requirement that the reduced density matrix stays positive for any pure state $|\Psi\rangle$ at all times t

$$\langle\Psi|\,\rho_S(t)\,|\Psi\rangle \geq 0, \tag{2.4.2}$$

and enables an interpretation of the elements $\langle\Psi|\,\rho_S(t)\,|\Psi\rangle$ as occupation probabilities [8]. Note that the transformation from the Born-Markov master-equation to the Lindblad master-equation involves a third important assumption, the *rotating-wave approximation* [198]. It is justified when the characteristic timescale for evolution of the sample quantum system τ_S is short compared to the relaxation timescale of the system. The final Lindblad quantum master-equation can be written in the diagonal form [197]

$$\frac{\partial\rho_S(t)}{\partial t} = -\frac{i}{\hbar}\Big[H_S, \rho_S(t)\Big] + \sum_k \gamma_k\Big(\mathcal{L}_k\rho_S(t)\mathcal{L}_k^\dagger - \frac{1}{2}\mathcal{L}_k^\dagger\mathcal{L}_k\rho(t) - \frac{1}{2}\rho(t)\mathcal{L}_k^\dagger\mathcal{L}_k\Big), \tag{2.4.3}$$

with Hamiltonian H_S of the "sample" quantum system and the Lindblad operators $\mathcal{L}_k$ labeling various processes k with rate constants γ_k.

The first term on the right-hand side is equivalent to the Liouville-von Neumann equation. It is called the "Liouvillian" and describes the unitary evolution of the quantum system represented by $\rho_S(t)$. The second term on the right-hand side is called "Lindbladian" and emerges in the derivation when the bath system is traced out. Note that in this thesis, the individual terms of the Lindbladian are referred to as "Lindblad terms". They describe the non-unitary evolution of $\rho_S(t)$.

The main difference between unitary and non-unitary dynamics is that unitary processes are reversible whereas non-unitary processes are not. Therefore, dephasing processes like population relaxation and pure dephasing are predestined to be described by the Lindbladian. The particularly modeled process depends then on the explicit construction of the constituent Lindblad operators $\mathcal{L}_k$. To describe

dephasing processes, the $\mathcal{L}_k$ have to be non-Hermitian, meaning that $\mathcal{L}_k \neq \mathcal{L}_k^\dagger$. In case of $\mathcal{L}_k$ being Hermitian ($\mathcal{L}_k = \mathcal{L}_k^\dagger$) Eq. (2.4.3) can be used to describe a measurement process, for example see [197]. The applied definitions to model population relaxation and pure dephasing for the individual quantum systems are given explicitly in the corresponding chapters, e.g, Ch. 5. Note that in Ch. 5 the final unidirectional photoemission step is modeled as well using a modified Lindblad operator in the Lindbladian.

Here, the principle structure of the Lindblad operators is presented using an exemplary two-level system with ground state $|1\rangle = \left(\begin{smallmatrix}1\\0\end{smallmatrix}\right)$ and excited state $|2\rangle = \left(\begin{smallmatrix}0\\1\end{smallmatrix}\right)$. Hence, the density matrix operator is given by $\rho_S(t) = \left(\begin{smallmatrix}\rho_{11} & \rho_{12}\\ \rho_{21} & \rho_{22}\end{smallmatrix}\right)$. The population relaxation process is generated by the Lindblad operator $\mathcal{L}^{\text{pop}} = |1\rangle\langle 2|$ and the corresponding rate $\gamma^{\text{pop}} = \frac{1}{T_1}$. This can be seen by substituting $\mathcal{L}^{\text{pop}}$ in the Lindbladian and calculate it explicitly for each element of $\rho_{nm} = \langle n|\,\rho_S(t)\,|m\rangle$. Neglecting for the moment the Liouvillian in Eq. (2.4.3) a single exemplary population-relaxation process results in

$$\frac{\partial}{\partial t}\begin{pmatrix}\rho_{11} & \rho_{12}\\ \rho_{21} & \rho_{22}\end{pmatrix} = \begin{pmatrix}\frac{\rho_{22}}{T_1} & -\frac{\rho_{12}}{2T_1}\\ -\frac{\rho_{21}}{2T_1} & -\frac{\rho_{22}}{T_1}\end{pmatrix}. \tag{2.4.4}$$

For a single pure-dephasing process characterized by the rate $\gamma^{\text{dep}} = \frac{1}{T_2^*}$ and Lindblad operator $\mathcal{L}^{\text{dep}} = |1\rangle\langle 1| + |2\rangle\langle 2|$ the same calculation leads to

$$\frac{\partial}{\partial t}\begin{pmatrix}\rho_{11} & \rho_{12}\\ \rho_{21} & \rho_{22}\end{pmatrix} = \begin{pmatrix}0 & -\frac{\rho_{12}}{T_2^*}\\ -\frac{\rho_{21}}{T_2^*} & 0\end{pmatrix}. \tag{2.4.5}$$

Note that by this operator construction, the Lindblad operators exhibit the expected behaviour, namely that population relaxation induces in addition to the population-state decay also a decay of the coherences and that pure dephasing only induces a decay of the off-diagonal elements of $\rho_S(t)$. To simulate the excitation dynamics of $\rho_S(t)$ for the particularly defined quantum system, Eq. (2.4.3) is numerically integrated using a Runge-Kutta-4 method by a software package for MATLAB (Quantum Dynamical Toolbox) [199, 200]

After having introduced the reader to the main theoretical concepts related to the different physical fields and methods covered by the subsequent work, the next chapter covers the used experimental apparatus which has been assembled in the course of this thesis.

CHAPTER

THREE

EXPERIMENTAL METHODS

In solids and on surfaces, strong interactions of the system with the environment typically lead to fast coherence decay. As a consequence, the observation of coherence phenomena on surfaces requires femtosecond time resolution, which is offered by ultrafast laser spectroscopy techniques. Another major challenge in disentangling the dynamics of nanostructured materials aside from the required temporal resolution, is the limited spatial resolution due to the optical diffraction limit. A solution is offered by time-resolved photoemission electron microscopy (TR-PEEM) that combines ultrafast optical excitation and high-resolution photoelectron imaging capabilities. This method is suited for the investigation of dynamical phenomena on the nanometer length and femtosecond time scale.

The following chapter describes the experimental setup used during this work for time-resolved photoemission electron microscopy experiments with aberration correction enabling 3 nm spatial resolution and sub-20 fs temporal resolution. The temporal resolution is realized by the development of a widely tunable ($215 - 970$ nm) NOPA at 1 MHz repetition rate. The full versatility of the setup is described in detail in Ref. [1] and the following sections focus here on the experimental components which are used to perform the coherent 2D nanoscopy experiments discussed in Ch. 5. Thereby the descriptions given in Ref. [1] are used and extended as indicated in the preface of this thesis.

The chapter is structured as follows: Section 3.1 introduces the reader to the whole experimental setup followed by detailed discussions of certain setup components, e.i., the laser system in Sec. 3.2, the pulse-shaper setup in Sec. 3.3 and the PEEM in Sec. 3.4, which have been implemented and characterized during

this thesis and are essential for the subsequently discussed measurements. Finally, Sec. 3.5 summarizes the results.

3.1. The coherent 2D nanoscopy setup

An overview scheme of the complete setup is shown in Fig. 3.1. A two-branch NOPA of a custom design, developed and built in the group of Prof. E. Riedle at the LMU Munich [201], is pumped by an Ytterbium (Yb)-doped fiber laser (Amplitude Systèmes, Tangerine HP) at central wavelength of 1030 nm, pulse energy of 35 µJ, and $\sim$ 320 fs pulse duration at 1 MHz repetition rate. A half-wave plate in combination with a thin-film polarizer splits off a portion of the output beam and the resulting 20 µJ pulses pump the NOPA with two parallel amplification beamlines, generating tunable output pulses in the range of $400 - 670$ nm [202] and $630 - 970$ nm [203], while simultaneous operation of the two branches is possible (blue and red lines in Fig. 3.1, respectively). Broadband output pulses of $300 - 600$ nJ are routinely compressed to sub-20 fs with separate prism compressors for each NOPA beamline. Frequency doubling in a $50 - 60$ µm thin and appropriately oriented β-BaB_2O_4 (BBO) crystal of either NOPA beamline results in $\sim$ 30 nJ pulses with a photon energy of up to 5.8 eV (corresponding to 215 nm), indicated as a purple line in Fig. 3.1 for one NOPA output. In combination, the laser system offers gap-less wavelength tunability ranging from the ultraviolet (UV) to the near-infrared (NIR) at 1 MHz repetition rate. The simultaneous operation of the two NOPA beamlines enables time-resolved two-color pump–probe experiments, e.g., for resonant sample excitation with a pump pulse in the visible and subsequent photoemission with an UV probe pulse while the wavelength of either pulse may be chosen independently.

To perform interferometric time-resolved photoemission experiments, phase-coherent pairs of time-delayed pump pulses can be generated with an actively phase-stabilized Mach–Zehnder interferometer in the range of $440 - 970$ nm. For the experiments discussed in this thesis a liquid-crystal display (LCD)-based SLM in $4f$-geometry is implemented and used to generate tailored optical fields with simultaneous control of amplitude and phase [204, 205]. To ensure a horizontal polarization at the LCD-SLM a polarizer (P) (Thorlabs, LPVIS050-MP2) at the beam input is used. The femtosecond pulse is spectrally decomposed by a transmittive volume phase holographic grating (VPHG) (Wasatch Photonics, 938 l/mm) and focused by a cylindrical protected silver mirror (CM) (Hellma Optics, R = -600 mm). The dual-layer 640-pixel LCD-SLM (Jenoptik, SLM-S640d USB) is directly placed in the Fourier plane and enables spectral phase control of each spectral component. Due to the symmetric pulse-shaper geometry the shaped

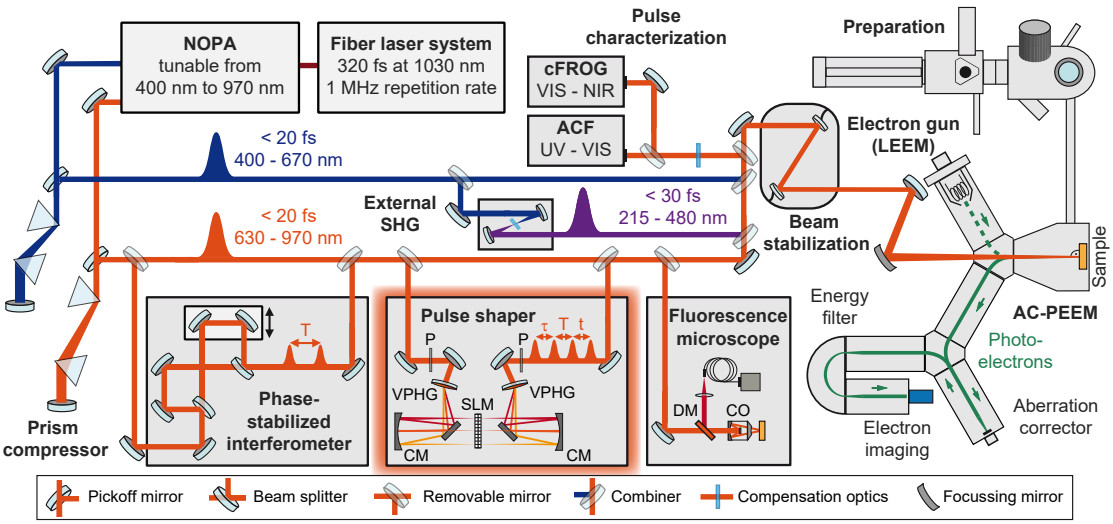

Figure 3.1 – Experimental setup for time-resolved photoemission electron microscopy (TR-PEEM). The noncollinear optical parametric amplifier (NOPA) pumped with Yb-doped fiber laser radiation renders broadband tunable pulses at 1 MHz repetition rate. Simultaneous emission of two independent output beams (red and blue solid lines) is possible and pulses are compressed with corresponding prism compressors to typically sub-20 fs. Second-harmonic generation (SHG) generates ultraviolet radiation with pulse energies up to 5.8 eV for efficient photoemission at low nonlinearity. A Mach–Zehnder-type interferometer with active stabilization generates phase-coherent excitation pulse pairs with time delay T and a pulse shaper based on a liquid-crystal display (LCD) spatial light modulator (SLM) and volume phase holographic gratings (VPHGs) enables tailored optical fields with full amplitude and phase control. Excitation pulse trains covering the range of $600 - 800$ nm are available for multidimensional spectroscopy. NOPA output pulses are combined and guided to the aberration corrector (AC) electron microscope via an active beam stabilization or, alternatively, to the pulse characterization setup consisting of autocorrelators (ACF) and collinear second-harmonic generation (SHG)-frequency-resolved optical gating (FROG) (labeled here as "cFROG"). Electrons photoemitted from the sample (green) are guided, energy-filtered and imaged with high spatial resolution down to 3 nm. The system is complemented with a two-part preparation and characterization ultra-high vacuum (UHV) chamber, an electron gun for low-energy electron microscopy (LEEM) as well as a scanning fluorescence microscope with a Cassegrain-type reflective objective (CO) to minimize dispersion, a dichroic mirror (DM) for signal filtering, and fluorescence lock-in detection with an avalanche photodiode. Reproduced from Ref. [1], with the permission of AIP Publishing.

spectral components are reassembled and amplitude- and phase-shaped pulse sequences (e.g. four-pulse sequence with time delays τ, T, t) are generated behind

the second horizontal P (Thorlabs, LPVIS050-MP2) and guided to the PEEM. In comparison to conventional LCD-SLM pulse shapers that are designed for a fixed input laser spectrum, the pulse shaper in our setup is covering a spectral region ranging from 600 to 800 nm which enables pulse shaping of tunable NOPA output pulses with corresponding spectral components.

Both NOPA output beamlines are combined with a wavelength-adapted dichroic mirror (Laseroptik GmbH) and are guided to the PEEM. A commercial active beam stabilization (TEM Messtechnik GmbH, Aligna 4D) corrects for vibrational instabilities between the optical table and the ultra-high vacuum (UHV) chamber of the PEEM. Sample illumination is possible in normal incidence (90°) or under gracing incidence (16°) to the sample surface (not shown in Fig. 3.1) through fused-silica viewports of 1.5 mm thickness (Torr Scientific Ltd., VPZ16Q-LN) flanged to the electron microscope UHV chamber. For laser pulse characterization in the VIS and NIR, the beam is guided to a commercial autocorrelator setup (ACF) in combination with collinear frequency-resolved optical gating (cFROG) (APE GmbH, pulseCheck). UV pulse duration measurements are performed with an autocorrelator of custom design, built by the Riedle group, based on bulk-material two-photon absorption. The packaged unit is based on the demonstrations by Ref. [206]. For dispersion matching, pulse propagation lengths and transmissive optics (bright blue element) in the characterization beam path resemble the PEEM experimental conditions.

For metallic and molecular thin-film preparation and characterization, an additional two-part UHV preparation chamber is attached to the main PEEM chamber. Further, a self-constructed scanning fluorescence microscope with an all-reflective objective complements the PEEM setup for correlative space- and time-resolved experiments, sample pre-characterization, and comparative (2D) spectroscopy evaluation with complementary (fluorescence) observables as for example discussed in Ref. [207].

3.2. Femtosecond single-pulse preparation

The construction of the decoupled two-branch NOPA system is based on the concept introduced by Bradler and Riedle [202] and differs from previous implementations with lower pump pulse energies [17, 208]. In the presented setup a novel concept reducing two-photon-absorption-induced heating in the BBO crystals is applied in order to avoid pulse energy instabilities [201].

Since a detailed construction description of the implemented NOPA system is found in Ref. [1], this section will be focused on the important spectral and temporal properties of the delivered pulses after pre-compression by the corresponding

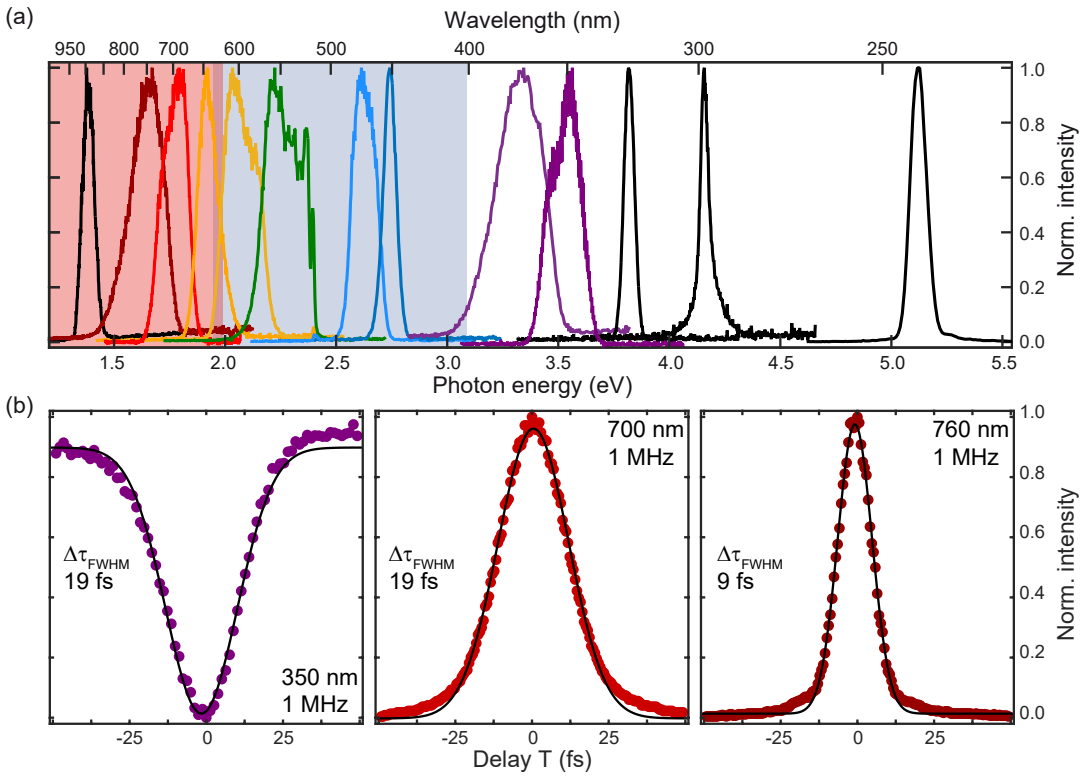

Figure 3.2 – Spectral and temporal single-pulse generation capability of the decoupled two-branch noncollinear optical parametric amplifier (NOPA). Exemplary NOPA output spectra ranging from the near-infrared (NIR) to the ultraviolet (UV) spectral region. Color shading illustrates the tuning ranges of the NOPA branches seeded by the 1ω supercontinuum generation (SCG) (red) and the 2ω SCG (blue). Second-harmonic generation (SHG) of either output extends the tunability down to the UV. Output pulse durations are characterized with noncollinear intensity autocorrelation (b) using two-photon absorption in the UV around 350 nm and using SHG in the visible (VIS) and NIR, exemplarily shown around 700 nm and 760 nm. Adapted from Ref. [1], with the permission of AIP Publishing.

prism-compressor. Figure 3.2 (a) depicts exemplary output spectra of the individual NOPA branches. The difference between the two branches is the frequency range of the generated whitelight spectrum and the frequency of the amplification pulse. Both are spatially superimposed in the individual NOPA crystal under the respective phase-matching and noncollinearity angle conditions [17] to generate the depicted spectra (red and blue shading, respectively).

The red branch is seeded with a continuous whitelight spectrum, generated by supercontinuum generation (SCG) in a Yttrium-aluminium-garnet (YAG) crystal

pumped by the fundamental (1ω) of a small part of the 1030 nm pump radiation and superimposed with a high-energy amplification pulse resulting from the main part of the frequency-doubled pump radiation (515 nm). The blue branch, on the other hand, is seeded with a whitelight continuum pumped by a small part of the frequency-doubled (2ω) 1030 nm pump radiation and exhibits for that reason higher energetic spectral components [202]. These spectral components are amplified in the NOPA crystal by superimposing a high-energy amplification pulse generated by the frequency-tripled pump radiation (343 nm).

With an additional second-harmonic generation (SHG) step of both NOPA outputs the tunability is extended to the UV which effectively enables the source to deliver broadband pulses covering a range from $215 - 970$ nm central wavelength.

The compressibility of pulses with a pair of Brewster-angle fused-silica prisms to sub-20 fs across the tuning range is depicted in Fig. 3.2 (b) for central wavelength $\lambda_0 = 350$ nm, $\lambda_0 = 700$ nm and $\lambda_0 = 760$ nm (from left to right). Note that the sub-20 fs pulse duration of the frequency-doubled UV pulse shown (350 nm) was obtained by pre-compressing the fundamental pulse at $\lambda_0 = 700$ nm central wavelength with the prism compressor [209].

3.3. Femtosecond pulse train generation by SLM pulse shaping

One particular task of this thesis was the construction and implementation of a SLM-based pulse shaper to enable simultaneous amplitude- and phase-shaping of ultrahort pulses generated by the presented NOPA system. The pulse shaper is designed for pulses with spectral components between $600 - 800$ nm to cover a particular tunability-range of the 1ω-branch of the NOPA.

The different technical realizations of ultrafast pulse shaping (e.g., based on acousto-optical modulators) are summarized and compared in Ref. [204, 205, 210]. Compared to the other realizations, the SLM-based approach features an increased optical throughput, which is necessary for the planed multiphoton photoemission experiments, and a compatibility with the high repetition rate (1 MHz) of the laser system. A typical drawback of the SLM-based approach is its inherently slow setting time due to the voltage-controlled alignment of the liquid-crystal molecules. This means that only slow changes of the applied amplitude- and phase-shaping on a $\sim$ 300 ms timescale are realized. However, since spatially resolved electron detection at small fields of view (e.g. 5 µm) requires integration times ranging from a 100 ms to a 10 s timescale, the SLM setting time is not the most significant contribution to the overall measurement time.

3.3.1. Basic concepts of SLM-based indirect amplitude- and phase-shaping

The pulse-shaper setup and its optical components have already been discussed in the beginning of this section and in Ref. [1]. The following section gives first a brief introduction to the basic concept of SLM-based indirect amplitude- and phase pulse shaping, following mainly Ref. [205]. Then the construction and alignment of the setup is quantitatively analyzed by reference on two particular verification measurements, i.e., validation of the $4f$-line alignment and a focus characterization in the Fourier plane. Additionally, the determined calibration curves for the control of the individual SLM-pixel are presented, characterized and optimized to ensure a correct amplitude- and phase-shaping. The main specifications of the constructed pulse shaper are summarized and listed in tabular form in App. B.

Due to the limited speed of electronics and a femtosecond pulse duration, direct shaping of amplitude and phase in time domain has not been achieved, yet. Nevertheless, indirect shaping of the temporal amplitude and phase is accessible by modifying the amplitude and phase in *spectral domain*. Therefore, the spectral amplitude $A(\omega)$ and phase $\varphi(\omega)$ have to be controlled separately for each spectral component of the pulse. This is achieved by the pixelated dual-layer liquid-crystal display (640 pixel each) acting as a spatial light modulator mask which is placed directly in the Fourier plane of a zero-dispersion grating compressor [211].

The zero-dispersion grating compressor consists of two volume phase holographic gratings (VPHGs) and two cylindrical mirrors (CMs) (Fig. 3.1) which are arranged in a $4f$-geometry, and form a so called zero-dispersion- or $4f$-line. The first VPHG introduces angular dispersion to the incoming pulse leading to angular separation of the constituent spectral components. This angular dispersion is compensated by the first CM which results in parallel propagation and spatial separation of the individual spectral components. The CM further focuses each spectral component along the axis parallel to the pixel arrangement of the SLM. The second CM and VPHG lead to recombination of the spectral components after being modified in the Fourier plane.

Based on the grating equation (grating constant $1/d$ with $[d] = \mathrm{mm}/l$ and $l =$ number of lines, angle of incidence θ_{AOI}) and the focal length f of the cylindrical mirrors the spatial position x_n of a particular spectral component ω_n in the Fourier plane is given in linear approximation by

$$x_n = \alpha\omega_n, \tag{3.3.1}$$

with α as the linear spatial-calibration coefficient given by the $4f$-line geometry

using a Taylor-expansion at the central wavelength λ_0 of the SLM [205, 212]

$$\alpha = \frac{\lambda_0^2 f}{2\pi c d \cos(\theta_{\mathrm{AOD}}(\lambda_0))}, \tag{3.3.2}$$

and c being the speed of light as defined in the preamble of this thesis. Note that the linear coefficient α allows only a simplified determination of the spatial dispersion of the laser spectrum in the Fourier plane. In general, the exact spatial-calibration equation as given in Ref. [205, 212] has to be used.

Assuming that the focus spot sizes w_{FP} (Gaussian beam waist) of the individual spectral components in the Fourier plane satisfy $w_{\mathrm{FP}} \ll \delta x$, both, the grating diffraction and the size of the individual SLM pixel δx define the frequency resolution $\delta\omega$ of each SLM pixel and consequently the overall performance values like, e.g., the temporal shaping window T. Suppose that the laser spectrum is linearly dispersed, the frequency resolution can be approximated by $\delta\omega \approx \delta x/\alpha$.

The temporal shaping window T_1 defines the maximum time window available for pulse shaping. Besides the shaped pulse sequence, various copies m appear at distance T_m in the temporal domain with decreased intensity [213]. To avoid significant impact of these pulse copies the introduced *total* delay has to be much smaller than the temporal shaping window T_1 which is defined in general by

$$T_m = \frac{2\pi m}{\delta\omega}. \tag{3.3.3}$$

Provided that a linear dispersion along the Fourier plane holds, T can also be expressed as

$$T_m \approx \frac{2\pi m}{\delta x}\alpha = \frac{m}{\delta x}\frac{f\lambda_0^2}{cd\cos(\theta_{\mathrm{AOD}}(\lambda_0))}. \tag{3.3.4}$$

The temporal shaping window is further closely related to the spatio-temporal coupling velocity v_{stc}, quantifying the amount of spatio-temporal coupling of the $4f$-line, which is defined by

$$v_{\mathrm{stc}} = \frac{cd\cos(\theta_{\mathrm{AOI}})}{\lambda_0}. \tag{3.3.5}$$

This relation can be seen using Gaussian beam optics to calculate the waist w_{FP} of an individual spectral component (here exemplary λ_0) in the Fourier plane which results in

$$w_{\mathrm{FP}} = \frac{\cos(\theta_{\mathrm{AOI}})}{\cos(\theta_{\mathrm{AOD}}(\lambda_0))}\frac{f\lambda_0}{\pi w_{\mathrm{in}}}. \tag{3.3.6}$$

Putting Eq. (3.3.6) in Eq. (3.3.4) leads to

$$T_m \approx \frac{m}{\delta x}\frac{\lambda_0 w_{\mathrm{FP}} \pi w_{\mathrm{in}}}{cd\cos(\theta_{\mathrm{AOI}})} = m\frac{w_{\mathrm{FP}}}{\delta x}\frac{\pi w_{\mathrm{in}}}{v_{\mathrm{stc}}}. \tag{3.3.7}$$

Spatio-temporal coupling is inherent to all programmable pulse shapers and cannot be avoided, since it is related to the fact, that the modification of a spectral component ω in the Fourier plane always leads to a modification of its propagation direction k_ω. The negative effect of spatio-temporal coupling becomes clear if the incoming pulse is simply shifted in time by applying a linear spectral phase via the SLM. Due to the simultaneous shaping of ω and k_ω the shift is not only applied in time-domain, as intended, but also in spatial domain along the transverse direction [205]. The effect can be in general minimized by ensuring a small v_{stc}, as seen in Eq. (3.3.5). Here a grating constant $1/d = 935$ l/mm and angle of incidence (AOI) at the VPHG of $\theta_{\mathrm{AOI}} = 19.04°$ has been chosen resulting in $v_{\mathrm{stc}} = 4.3 \times 10^{-4}$ mm/fs (see App. B for technical specifications). Further, a negligible spatio-temporal coupling is verified, if pure spectral-phase shaping leads to no change in the transmitted spectral amplitude, which can be easily monitored on a spectrometer.

The spatio-temporal coupling velocity v_{stc} also affects the spatial tilt of the pulse during the shaping process. A detailed investigation of this effect and how the SLM pixelation in general effects the shaped pulse is discussed in Ref. [214–216]. As described in Ref. [212] the pulse gets tilted away from its propagation axis (z-axis) along the direction of the pixelation (x-axis) by a tilt angle ϑ defined as

$$\vartheta = \arctan\left(\frac{v_{\mathrm{stc}}}{c}\right). \tag{3.3.8}$$

This "tilted pulse shape" leads to spatial chirp of the shaped output pulse depending on its input beam size and pulse duration. To minimize the spatial chirp a larger input beam size is beneficial. Note that the input beam size is limited by the height of the SLM pixels ($\delta y = 10$ mm).

One SLM layer consist of 640 individually voltage programmable pixels [217]. Each pixel is composed of a thin layer of nematic liquid crystals (thickness $d_{\mathrm{LC}} = 10$ µm) placed between two adjacent transparent indium tin oxide (ITO) layers surrounded by two parallel glass substrates (thickness $d_{\mathrm{glass}} \sim 1.5$ mm each). The liquid crystals take the form of small oblate rods which are homogeneously oriented due to a thin alignment layer. If no external voltage is applied, the long rod-axes is oriented parallel to the glass substrate which defines the orientation-axis of the SLM layer. An external electric field can be applied via the ITO layer to each pixel by setting a voltage value U which leads to a reproducible alignment of the liquid

crystals in the electric field within the pixel. This modification of the medium's birefringence affects polarized light and imprints an additional voltage controllable phase

$$\phi(\omega, U) = \frac{\omega \Delta n(\omega, U) d_{\mathrm{LC}}}{c}, \tag{3.3.9}$$

to the spectral phase of the incoming pulse. Note that $\Delta n(\omega, U)$ corresponds here to the refractive-index difference between the slow and fast axes of the birefringend liquid-crystal layer. For that reason, the accumulated static phase due to the glass layers cancels out [217].

To perform independent amplitude- and phase-shaping two separately controllable SLM layer are necessary whose orientation axes are $+45°$ and $-45°$ with respect to the horizontal axis (x). Both layers are directly connected via an optical adhesive and covered at the outsides with an appropriate anti-reflection (AR) coating which is optimized in the spectral range of $500 - 1000$ nm for the present setup. A first polarizer with horizontal transmission axis ensures horizontal polarization of the incoming pulse in the Fourier plane and a second polarizer, placed in the same transmission configuration at the output of the pulse shaper, enables amplitude shaping (see Fig. 3.1). The effect of the dual-layer SLM on the electric field of the incoming femtosecond pulse $E_{\mathrm{in}}(\omega)$ can be described by a complex spectral transfer function $M(\omega)$ formalism

$$E_{\mathrm{out}}(\omega) = M(\omega) \cdot E_{\mathrm{in}}(\omega), \tag{3.3.10}$$

with

$$M(\omega) = \cos\Big(\frac{\phi_1(\omega, U_1) - \phi_2(\omega, U_2)}{2}\Big) \cdot \exp\Big[i\Big(\frac{\phi_1(\omega, U_1) + \phi_2(\omega, U_2)}{2}\Big)\Big]. \tag{3.3.11}$$

The spectral SLM phases $\phi_1(\omega, U_1)$ and $\phi_2(\omega, U_2)$ of layer 1 and layer 2 contribute to the amplitude modulation $A(\omega, U_1, U_2)$ as

$$A(\omega, U_1, U_2) = \cos\Big(\frac{\phi_1(\omega, U_1) - \phi_2(\omega, U_2)}{2}\Big), \tag{3.3.12}$$

and to the phase modulation $\varphi(\omega, U_1, U_2)$ via

$$\varphi(\omega, U_1, U_2) = \frac{\phi_1(\omega, U_1) + \phi_2(\omega, U_2)}{2}. \tag{3.3.13}$$

As a consequence, pure amplitude shaping is achieved under the condition that $\phi_1(\omega, U_1) = -\phi_2(\omega, U_2)$ and pure phase modulation requires $\phi_1(\omega, U_1) = \phi_2(\omega, U_2)$.

The operating principle of the mask-transfer function $M(\omega)$ is exemplarily demonstrated for the generation of a double pulse with delay τ from a single bandwidth limited ($\varphi(t) = \varphi(\omega) = 0$) incoming Gaussian pulse $E_{\text{in}}(\omega) = e^{-(\omega-\omega_0)^2/\Delta^2}$. The shaped double pulse sequence is fully described by

$$E_{\text{out}}(\omega) = \frac{1}{2}E_{\text{in}}(\omega) + \frac{1}{2}E_{\text{in}}(\omega)e^{-i\omega\tau} = M(\omega) \cdot E_{\text{in}}(\omega), \tag{3.3.14}$$

and $M(\omega)$ results to be

$$M(\omega) = \frac{1}{2}(1 + e^{-i\omega\tau}). \tag{3.3.15}$$

In general, the complex mask-transfer function can be separated in amplitude-$A(\omega)$ and phase-modulation $\varphi(\omega)$ by the polar representation $A(\omega)\cdot e^{i\varphi(\omega)}$. Solving now for $A(\omega)$ and $\varphi(\omega)$ yields

$$A(\omega) = |M(\omega)| = \sqrt{M(\omega)M^*(\omega)} = \cos\left(\frac{\omega\tau}{2}\right), \tag{3.3.16}$$

and

$$\varphi(\omega) = \arctan\left(\frac{\text{Im}[M(\omega)]}{\text{Re}[M(\omega)]}\right) = \frac{-\omega\tau}{2}. \tag{3.3.17}$$

Using now Eq. (3.3.12) and Eq. (3.3.13) the SLM phases $\phi_1(\omega, U_1)$ and $\phi_2(\omega, U_2)$ for each spectral component ω can be calculated with respect to the conditions given by Eq. (3.3.16) and Eq. (3.3.17) and established by sending the corresponding voltages U_1 and U_2 to the individual pixels of the particular layer. Note that generating a double pulse requires only a cosine-shaped spectral amplitude modulation, whose oscillation frequency is proportional to the pulse delay τ, and a linear spectral phase modulation, whose slope yields information concerning the sign and value of τ.

3.3.2. Alignment of the 4*f*-setup

The $4f$-line is built up using a commercial white-light fiber laser (SuperK COMPACT, NKT) as coherent illumination source. It delivers unpolarized laser pulses with a pulse duration of < 2 ns at a repetition rate tunable between 1 Hz $-$ 20 kHz and features a broad and rather uniform spectrum between $450 - 2400$ nm. The total output power in the visible spectral range ($450 - 850$ nm) is > 20 mW. In front of the pulse-shaper setup the spectrum is cut in short wavelength range by a longpass filter (510 nm cutting edge, ASAHI) to suppress radiation < 430 nm,

which would damage the liquid crystals of the SLM. Furthermore, the broad infrared part of the spectrum was removed by two highly reflective bandpass mirrors (HR $600-850$ nm, Eksma) so that only the reflected part of the spectrum is used for alignment, yielding a smooth spectrum from $510-900$ nm. The beam diameter was increased by a $1:4$ lens telescope to match the estimated beam diameter of the NOPA output beam and properly collimated. The generated beam profile was monitored by a beam profiler (SP904 BGS, Ophir) and the vertical and horizontal beam waist is characterized ($2\omega_{\text{vert.}} = 3$ mm, $2\omega_{\text{hor.}} = 2.8$ mm).

The first grating (VPHG, Wasatch Photonics) is rotated along the vertical axis to maximize the transmitted power in the first order of diffraction. The positions and angles of the first folding mirror and the first cylindrical mirror are adjusted to compensate the angular dispersion introduced by the grating and to achieve a well collimated and spectrally-dispersed ("rainbow-like") beam at height and width of the liquid crystal layer of the SLM. Using narrow bandpass filters (600 nm, 700 nm or 800 nm with FWHM = 10 nm, Thorlabs) the white-light spectrum is furthermore spectrally filtered which allows a precise mirror adjustment to align, e.g., the central wavelength ($\lambda_c = 700$ nm) of the spectral SLM transmission window ($600-800$ nm) to the center of the SLM pixel array. Note that at this point, a beam dump with a horizontal slit at the height and width of the real SLM pixel array instead of the actual SLM is implemented in the Fourier plane. In addition to compensating for angular dispersion, the cylindrical mirror ($f = -300$ mm) focuses each spectral component along the pixelation axis (x). Since this focusing occurs along the axis of the spectral beam dispersion it cannot be well observed with the white-light laser and is investigated in detail later in this section with a monochromatic helium-neon (HeNe) laser.

Accordingly, the second cylindrical mirror ($f = -300$ mm) is placed in a $2f$ distance, with respect to the first, and the second folding mirror guides the spectral components to the second grating which finally recombines the spectral components. To fine tune the distances between the constituent optics of the $4f$-line, the recombined beam is aligned to a commercial intensity autocorrelator (pulseCheck, APE), further referred to as the "APE".

The fine adjustment of the $4f$-line is done with pre-compressed pulses from the NOPA output as seen in Fig. 3.3. The pulse length Δt of the input pulse (additional 2 mm Fused Silica glass inserted to take into account the accumulated dispersion due to the glass substrates of both gratings for the output pulse) is first characterized by a noncollinear intensity autocorrelation

$$S_{\text{intACF}}(\tau) = \int_{-\infty}^{\infty} I(t)I(t+\tau)\mathrm{d}t. \tag{3.3.18}$$

To generate a detection signal proportional to the intensity product of the two

pulses a nonlinear signal process is required. The APE is adjusted to measures the signal generated by SHG in a thin BBO crystal as a function of pulse delay τ in a noncollinear excitation geometry [211]. Note that the appropriate BBO crystal dependents on the spectral range and pulse length of the input pulse. Assuming a Gaussian-shaped spectrum the pulse duration can be directly determined from the FWHM of the autocorrelation function (ACF) via

$$\Delta t = \frac{\Delta t_{\mathrm{intACF}}}{1.414}. \tag{3.3.19}$$

Using the same characterization at the output of the pulse shaper allows to monitor the pulse duration Δt of the pulse after passing through the $4f$-line and in this way to optimize the distances firstly between second grating and second cylindrical mirror and secondly between both cylindrical mirrors, while keeping the distance between second cylindrical mirror and second grating constant. The distance between the first grating and the first cylindrical mirror is fixed because it serves as the reference distance of the $4f$-line and has been precisely adjusted previously by compensating the angular dispersion of the first grating and to avoid movement of the focus position generated by the first cylindrical mirror.

The measured noncollinear intensity ACF of the optimized $4f$-line is fitted by a Gaussian to quantify the pulse duration. The results are shown in Fig. 3.3. Figure 3.3 (a) characterizes the pulse duration of the input NOPA pulse ($\lambda_0 = 700$ nm) (top) to be $\Delta t_{\mathrm{In}} = 42.8 \pm 0.3$ fs and the output pulse (bottom) $\Delta t_{\mathrm{Out}} = 46.2 \pm 0.3$ fs. This agreement of input and output pulse duration validates the correct alignment of the $4f$-line. In Fig. 3.3 (b) the two polarizers are implemented at the input and output of the pulse shaper and the $4f$-line optimization is repeated at blue shifted central wavelength of the NOPA output ($\lambda_0 = 650$ nm). Note that the optimized output pulse duration $\Delta t_{\mathrm{Out}} = 54.4 \pm 0.1$ fs is significantly increased compared to the input pulse duration of $\Delta t_{\mathrm{In}} = 32.7 \pm 0.1$ fs. Since the output pulse duration could not be further reduced by additional fine-tuning of the $4f$-line, this mismatch might result from the fact that the accumulated dispersion of both thin-film polarizers is not taken into account in the pulse duration characterization measurement of the input pulse Fig. 3.3 (b, top). Both polarizers are based on embedded prolate ellipsoid nanoparticles in sodium-silicate glass (individual thickness 260 ± 50 µm).

3.3.3. Pixel-to-wavelength calibration of the SLM

After the alignment of the $4f$-line the dual-layer SLM was implemented in the Fourier plane as depicted in Fig. 3.1. To generate a precise pixel-to-wavelength calibration curve the white-light laser spectrum, covering the spectral window ($600 - 800$ nm) is monitored on a fiber-coupled (Avantes, $250 - 2500$ nm, FC-UVIR200-

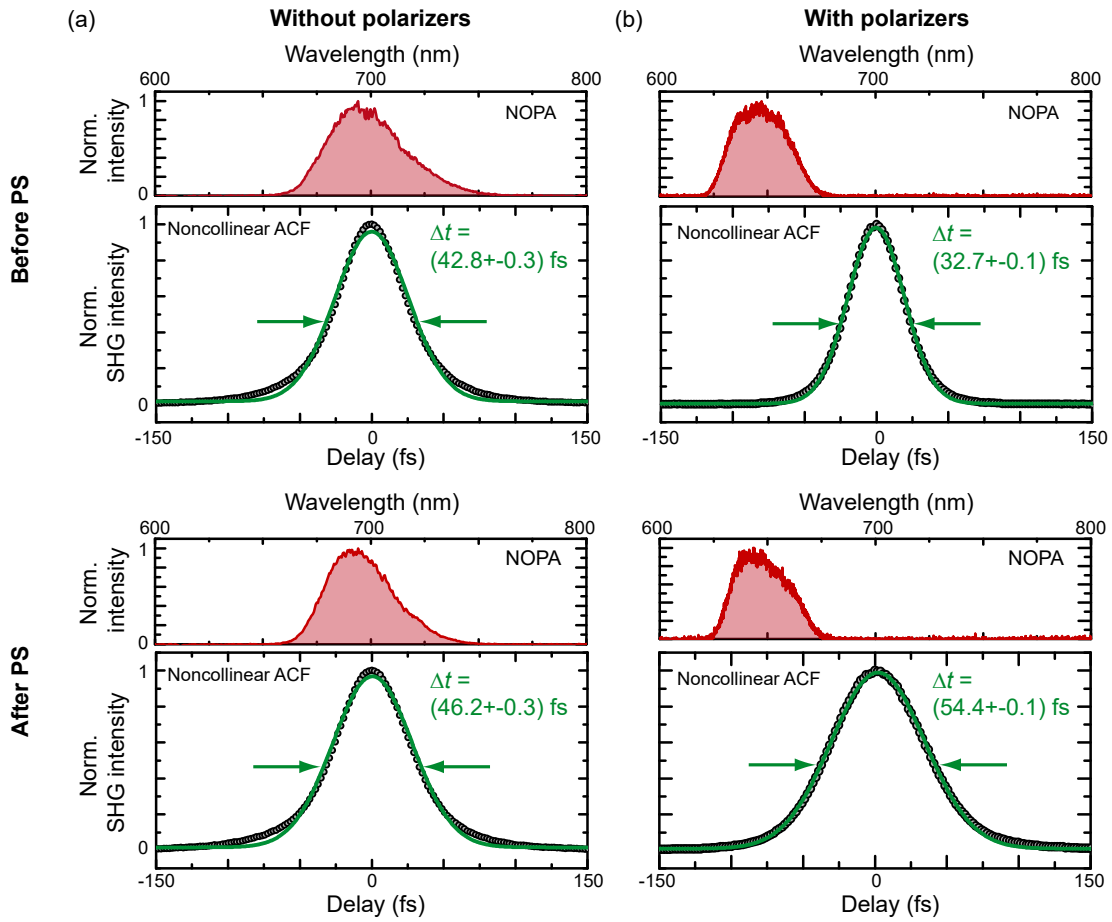

Figure 3.3 – Verification of correct $4f$-line alignment by noncollinear intensity autocorrelation function (ACF) of NOPA pulses. (a) NOPA spectrum (red) and non-collinear intensity ACF (black circles) measured in front of the pulse shaper (PS) (top) and after passing through the $4f$-line (bottom). The pulse duration Δt is calculated from the FWHM of the corresponding Gaussian fits (green). The good agreement of both pulse durations shows a sufficiently well aligned $4f$-line. (b) shows the same characterization with implemented polarizers at the pulse-shaper input and output. The optimized pulse duration Δt of the output pulse (bottom) is increased compared to the input pulse (top) and could not be further reduced by fine-tuning the distances in the $4f$-line.

USB2), irradiance-corrected spectrometer (Avantes, $600-800$ nm, AvaSpec-ULS-3648) with 0.11 nm spectral resolution.

To assign the different spectral components of the white-light spectrum to their corresponding SLM pixels every 10th pixel is set to maximum transmission, while

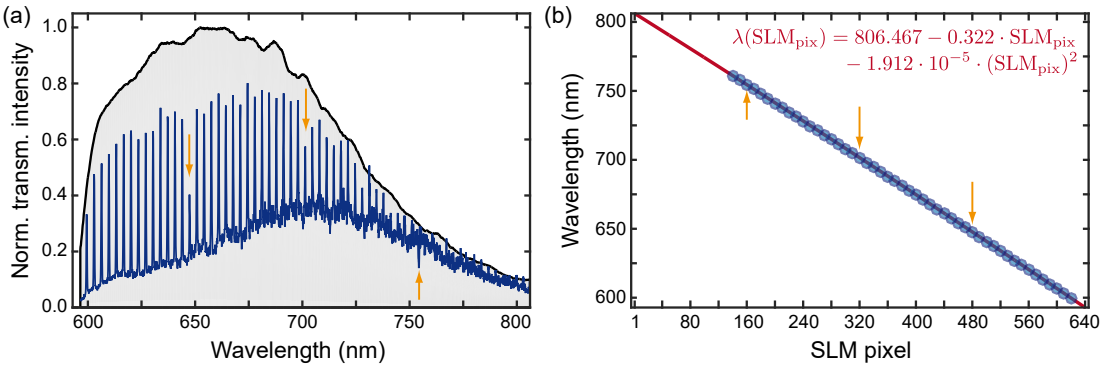

Figure 3.4 – SLM pixel to wavelength calibration with white-light laser. (a) Full transmission (grey) and amplitude modulated (dark blue) white-light laser spectrum. The narrow transmission peaks result from every 10th SLM pixel with maximum transmission, whereas the remaining SLM pixels are set to a voltage corresponding to minimum transmission. (b) Determining the spectral-peak positions by a peak-finder algorithm allows an assignment between the individual maximum transmission SLM pixels and their corresponding spectral component (blue circle). The orange arrows label, so called "special pixel", to establish a unique assignment of the pixels. A quadratic polynomial fitting (red line) generates the final pixel-to-wavelength calibration curve even for spectral ranges with bad peak visibility.

the remaining pixels are set to a voltage value corresponding to minimal transmission. The monitored unmodulated (grey) and amplitude modulated white-light spectrum (dark blue) are depicted in Fig. 3.4 (a). The amplitude modulated spectrum exhibits many narrow peaks at the spectral positions of the maximum transmission pixels. To generate an unambiguous assignment of the pixel number, three, so called "special pixels", are used (orange arrows in Fig. 3.4) at particular transmission values T ($\mathrm{SLM_{pix}} = 160 \Rightarrow T = 10$ %, $\mathrm{SLM_{pix}} = 320 \Rightarrow T = 60$ % and $\mathrm{SLM_{pix}} = 480 \Rightarrow T = 25$ %).

The spectral position of each peak is determined by a peak-finder algorithm and plotted as a function of the number of the known maximum transmission pixels as depicted in Fig. 3.4 (b). Fitting the data by a quadratic polynomial (see red line and insert in Fig. 3.4 (b)) generates the pixel-to-wavelength calibration for all SLM pixels. The fact that the transmitted intensity is nonzero for the minimal transmission pixels is explained by the frequency dependence of the voltage controllable phase as seen in Eq. (3.3.9) resulting in a $1/\lambda$-dependence. The required total π-phase shift, e.g., $\phi_1 = -\pi/2$ and $\phi_2 = +\pi/2$ for pure amplitude modulation to change a pixel from maximum to minimum transmission (see Eq. (3.3.12)) depends non-linearly on λ. Since the applied minimum transmission voltage is

adapted for each spectral component following a linear function, deviations from zero transmission are expected. Nevertheless, due to the polynomial fitting a good calibration curve is created even for the $750 - 800$ nm spectral range with bad transmission peak visibility.

Note that these pixel-to-wavelength calibration is one core element of correct pulse shaping and for this reason holds as an alignment feedback for incoupling of different light sources to the pulse-shaper setup, e.g., NOPA pulses with varying spectral components as seen in Fig. 3.3. One prerequisite for a correctly coupled source is that all spectral components hit their corresponding pixels based on the pixel-to-wavelength calibration curve. The deviation has to be smaller than the nm/pixel-resolution resulting from the slope of the linear term of the fitted calibration curve ($\delta_{\text{pix}} = 0.322$ nm/pixel).

The imperfections coming along with the pixelation of the SLM like, e.g., discrete sampling, pixel gaps, and the pixel boundaries have been investigated and illustrated in Ref. [216]. They emphasize in particular that if the linear dispersion term of the pixel-to-wavelength calibration is incorrect pulses are not shifted accurately to the specified time delays and in case of an incorrect or neglected nonlinear term the pulse will be chirped if delayed to larger times.

3.3.4. Focusing of the spectral components on the SLM pixels

The focusing of the individual spectral components by the cylindrical mirror on the corresponding SLM pixel in the Fourier plane is exemplarily verified. Due to the cylindrical symmetry of the mirror the focusing appears along the axis which coincides with the direction of dispersion of the spectral components. Consequently, the transverse focus size of individual spectral components cannot be separately determined using the white-light laser source.

Instead, a monochromatic HeNe laser with well defined emission wavelength of the $3s_2 - 2p_4$ transition $\lambda_{\text{HeNe}} = 632.82$ nm is used. The beam diameter of the HeNe laser is increased by a $1:3$ lens telescope to match again the estimated beam diameter of the NOPA beam and is properly collimated. As described for the white-light laser, the vertical and horizontal beam waists are characterized ($2\omega_{\text{vert.}} = 4.4$ mm, $2\omega_{\text{hor.}} = 4.3$ mm). The HeNe laser is coupled into the pulse-shaper setup and aligned taking into account that the narrow 632.82 nm component is focused on the corresponding pixel defined by the pixel-to-wavelength calibration.

Figure 3.5 (a, top) depicts a schematic front view of the SLM layer. The grey and colored rectangles represent the individual pixels with a size in y-direction of 10 mm and x-direction of 97 µm. Note the 3 µm gap between each pixel. The HeNe laser beam (elliptical red spot) propagates in z-direction and its elliptical

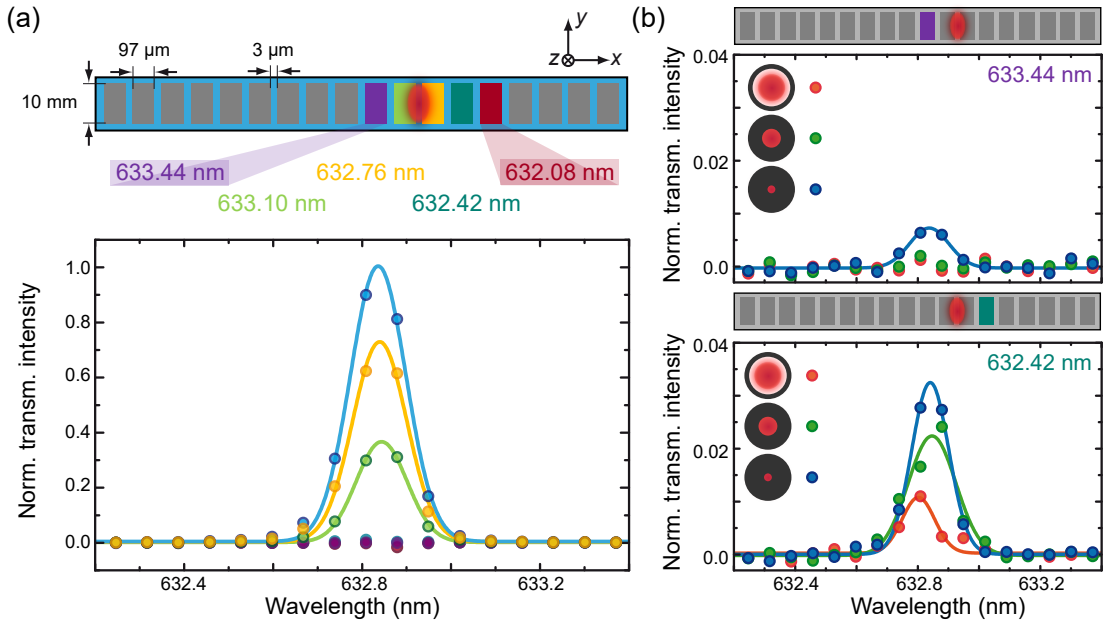

Figure 3.5 – Validation of focusing in Fourier plane with HeNe laser. (a, top) schematically depicts the not-to-scale front view of the SLM pixel array. Certain pixels (colored rectangles) are set one after another to maximum transmission while the remaining pixels (grey) are set to minimal transmission and the transmitted intensity of the spectral component of the HeNe laser ($\lambda_{\mathrm{HeNe}} = 632.82$ nm, red spot) is monitored on a spectrometer (a, bottom). The full transmitted intensity (all pixels at maximum transmission) (blue circle) together with the transmitted intensity of single pixel 522 (green circle) and pixel 523 (yellow circle) are quantified by Gaussian fits (corresponding lines, see Tab. 3.1 for results). (b) quantifies the intensity leakage into the surrounding pixels 521 (purple) and 524 (dark cyan) at three different configurations open (red), half closed (green) and closed (blue) of a one inch aperture placed in the collimated HeNe laser beam. Again visible transmission is quantified by Gaussian fits (corresponding lines).

shape results from the focusing of the cylindrical mirror in x-direction. Due to the pixel-to-wavelength calibration curve (see Fig. 3.4 (b)) the spectral component 632.82 nm is located between pixel 522 (light green) and pixel 523 (yellow).

Note that adjacent emission lines exist, namely $3s_2 - 2p_3$ at $\lambda = 635.2$ nm and $3s_2 - 2p_5$ at $\lambda = 629.4$ nm, which are much weaker in intensity [218] and moreover assigned to SLM pixels outside of the investigated pixel region.

In general, the focus size of each spectral component along the x-direction should be much smaller than the individual SLM pixel width of 97 µm to minimize intensity leakage of the corresponding spectral component into adjacent pixels. This intensity leakage would lead to an unwanted spectral phase contribution of the ad-

	λ_0 (nm)	A	Δ_{FWHM} (nm)	$I_{\mathrm{transm.}}$ (%)
Full transm. *	632.84	1	0.15	100
633.10 nm *	632.84	0.73	0.14	71
632.76 nm *	632.84	0.37	0.13	34
633.44 nm ***	632.84	0.0075	0.15	0.8
632.42 nm *	632.80	0.011	0.12	0.9
632.42 nm **	632.85	0.023	0.18	2.8
632.42 nm ***	632.84	0.032	0.14	3.2

* 1' aperture open
** 1' aperture half closed
*** 1' aperture closed

Table 3.1 – Fitting results with respect to the full transmission spectrum. Top three rows correspond to the Gaussian fits depicted in Fig. 3.5 (a) and labeled correspondingly to the spectral component of the full transmission pixel. The fourth row shows the fit results of Fig. 3.5 (b, top) and the last three rows of Fig. 3.5 (b, bottom), respectively. The asterisks label the state of an one inch aperture ($\varnothing = 25.4$ mm) placed in the collimated HeNe laser beam.

jacent pixels to the wanted spectral phase value $\varphi(\omega_{\mathrm{n}})$, with ω_{n} being the spectral component assigned to pixel n, resulting in incorrect pulse shaping.

Fig. 3.5 (a, bottom) depicts the transmitted intensity of the HeNe laser beam at full transmission of all pixels (blue), and at certain pixels (colored) set to maximum transmission measured on a spectrometer, while the remaining pixels (grey) are set to minimum transmission. The two SLM pixels covered by the spectral component of the HeNe laser (yellow and green) show a distinct transmission line while the other surrounding pixel (purple, dark cyan and dark red) reveal no significant transmission. To quantify the amount of transmission the transmission lines are fitted by a Gaussian function

$$f(\lambda) = A \cdot e^{-\frac{(\lambda-\lambda_0)^2}{2\sigma^2}} + b, \tag{3.3.20}$$

to determine the maximum value A and the width $\Delta_{\mathrm{FWHM}} = 2\sqrt{2\ln(2)}\sigma$ of the transmission line. From these values the transmitted spectrally integrated intensity $I_{\mathrm{transm.}}$ is calculated since $I_{\mathrm{transm.}} = A\Delta_{\mathrm{FWHM}}\sqrt{\pi/4\ln(2)}$. The results are depicted in relation to the full transmission spectrum (blue) in Tab. 3.1 and the small background parameterized by b is neglected.

The analysis shows, that ~ 71 % of the full transmission of the spectral HeNe-laser component is transmitted if only pixel 523 ($\lambda = 632.76$ nm) is set to max-

imal transmission, and ~ 34 % if only pixel 522 ($\lambda = 633.10$ nm) is set to maximum transmission, which validates, that the HeNe-laser component of $\lambda_{\mathrm{HeNe}} = 632.82$ nm is focused between both pixels as expected from the pixel-to-wavelength calibration curve. The fact that the sum of both percentages is larger than 100 % reflects the presence of the 3 µm gap between the two pixels. Since the gap transmission is not controlled by the voltage it is always > 0 as defined by Fresnel equations [219].

A detailed investigation of the intensity leakage into the surrounding pixels 521 ($\lambda = 633.44$ nm) and 524 ($\lambda = 632.42$ nm) is presented in Fig. 3.5 (b) and the individual fitting results are summarized in Tab. 3.1. The plotted three data sets for each pixel correspond to three different states of a one inch aperture ($\varnothing = 25.4$ mm) which was placed in the collimated HeNe laser beam close to the input of the pulse shaper (PS) to decrease the beam size and to introduce far-field diffraction. Both manipulations will slightly increase the focus size of the HeNe laser in the Fourier plane.

As depicted in Fig. 3.5 (b, top) the intensity leakage into pixel 521 (purple) is only observed for a closed aperture (blue circles) which reduces the collimated beam size to $\varnothing = 1 - 2$ mm and introduces strong far-field diffraction. In this case the intensity leakage is less than 1 %. In case of pixel 524 (dark cyan) the intensity leakage is less than 1 % in the open aperture configuration and increases at closed aperture to about 3 %. Assuming an ideal Gaussian-like intensity beam profile this is explained by the fact that the focused spectral component covers pixel 523 (yellow) more, which is assured by the results presented in Fig. 3.5 (a).

Hence, the assembled setup sufficiently focuses the spectral components along the small pixel axis and minimizes the intensity leakage into surrounding pixels to be less than 1 % in the open aperture configuration, which is the normal operating configuration of the pulse shaper.

3.3.5. Voltage-to-phase calibration

The applied voltage-controllable phase $\phi(\omega_n, U)$ for each SLM layer depends linearly on the shaped spectral component ω_n focused to the nth pixel, as indicated by Eq. (3.3.9). To determine which explicit phase ϕ is generated for each voltage U at a particular pixel an additional voltage-to-phase calibration is experimentally generated, following the explanations of the SLM's technical documentation [217]. These calibration curves contain also effects based on the pixel and voltage dependent optical anisotropy $\Delta n(\omega, U)$ and possible pixel-dependent changes of the SLM layer thickness d_{LC} due to manufacturing or alignment.

Therefore, the transmitted intensity T for each spectral component ω_n is measured on a spectrometer as function of the corresponding SLM layer voltage.

$$T(\omega_n, U_1, U_2) = \cos^2\Big(\frac{\phi_1(\omega_n, U_1) - \phi_2(\omega_n, U_2)}{2}\Big)$$
$$= \frac{1}{2}[1 + \cos(\phi_1(\omega_n, U_1) - \phi_2(\omega_n, U_2))]. \quad (3.3.21)$$

The SLM is used in "Low Voltage Mode" meaning that the voltage at each pixel is varied between $0 - 5$ V with 6 kHz AC. The resolution is 12bit and thus the individual SLM pixel voltage is applied between $0 - 5$ V by 4096 voltage counts (Vc). To minimize the influence of the not-calibrated layer during acquisition of the voltage-to-phase calibration curve of the layer to be calibrated, the voltage of the not-calibrated layer is set to 4096 Vc (5 V). This means as well that both layers are calibrated individually. From each generated transmission map the individual phases $\phi_1(\omega_n, U_1)$ and $\phi_2(\omega_n, U_2)$ can be extracted for each layer by

$$\phi_1(\omega_n, U_1) = \phi_2(U_{\max}) \pm \arccos(2 \cdot T(U_1, U_{\max}) - 1)$$
$$\phi_2(\omega_n, U_2) = \phi_1(U_{\max}) \pm \arccos(2 \cdot T(U_{\max}, U_2) - 1). \quad (3.3.22)$$

Since a constant phase-offset like $\phi_1(U_{\max})$ or $\phi_2(U_{\max})$ does not affect the light waves, it does not affect the whole calibration and can be neglected.

Figure 3.6 depicts the measured transmission maps $T(\lambda_n, U_1, U_{\max})$ for Layer 1 in (a) and $T(\lambda_n, U_{\max}, U_2)$ for Layer 2 in (b) with $U_{\max} = 4096$ Vc, respectively. The voltage counts are varied by a step size of 2 Vc along the x-axis and along the y-axis the transmitted spectrum of the white-light laser is monitored for each varied voltage step. The map depicts the modulation of the transmission (white labels maximum transmission, while black corresponds to a transmission minimum) for each spectral component λ_n as function of the applied voltage counts (Vc).

The blue spectrum on the left side of the map in (a) is a cut along Vc = 2500 and reveals significant oscillatory modulation along the wavelength axis. The full resolution spectrum (thin blue line) is smoothed to emphasize these oscillations and plotted in addition as a thick blue line. The wavelength-dependent modulation of the transmission is created by interference between the original spectral component and a small part of it which is back-reflected at particular interfaces due to a change in refractive index.

Two such interfaces form a resonator with a resonance condition which depends on the distance l between the two interfaces and the transmitting spectral component λ. This leads to constructive and destructive modulation of the transmitted intensity. This situation is commonly utilized in Fabry-Pérot interferometers and

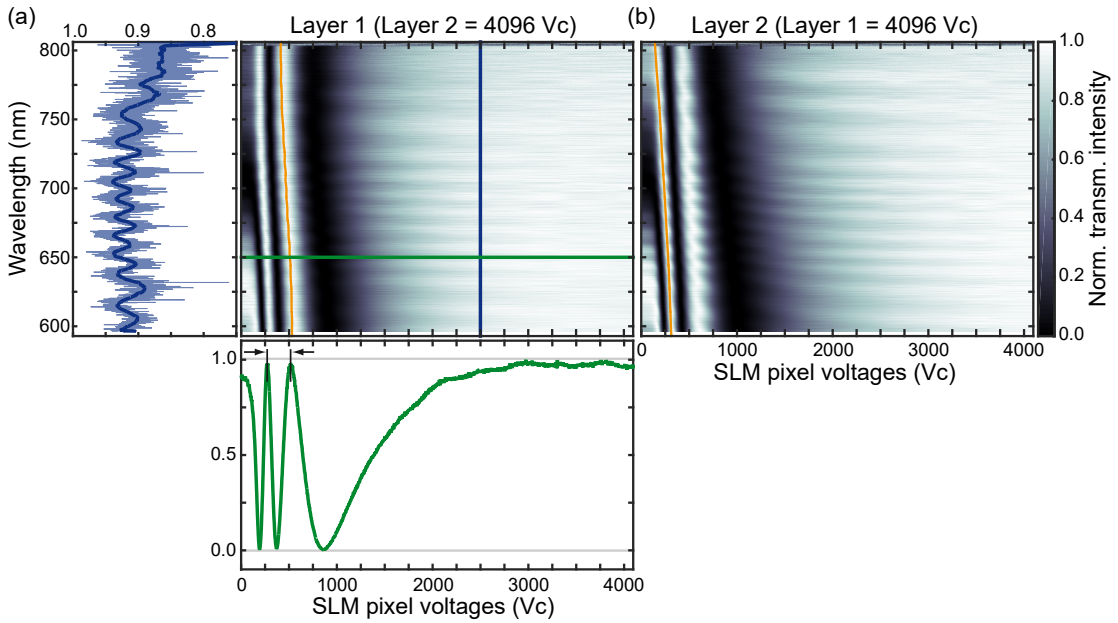

Figure 3.6 – Pixel and SLM voltage dependent transmission maps for voltage-to-phase calibration. (a) Transmission map for the tuned SLM voltage of Layer 1, while Layer 2 is set to a fixed voltage of 4096 Vc. Extracted transmission spectrum at Vc = 2500 (blue) exhibits slight oscillatory transmission modulations along the wavelength axis. The monitored transmission modulation as a function of SLM pixel voltage (green) allows to recreate the applied phase $\phi_1(U_1)$ for each SLM pixel (here: spectral component $\lambda = 650$ nm) by an iterative algorithm. The orange line labels the defined zero-phase voltage curve, the pixel-individual reference point, corresponding to no applied phase. (b) depicts the transmission map for tuned SLM voltage of Layer 2, while Layer 1 is set to 4096 Vc and the zero-phase voltage curve (orange line) defined for Layer 2.

is therefore called here "Fabry-Pérot effect". In a SLM, this effect is usually minimized by design, e.g., by using anti-reflection coatings or by avoiding interfaces with strong refractive index change. In the implemented SLM a significant change of refractive index is not avoidable for the interfaces glass ($n_{\mathrm{glass}} = 1.53$) to the transparent electrode (ITO, $n_{\mathrm{ITO}} = 1.86$ at $\lambda = 660$ nm) and transparent electrode to liquid crystal layer ($n_{\mathrm{LC,\,e}} = 1.74$, $n_{\mathrm{LC,\,o}} = 1.51$ at $\lambda = 633$ nm) and vice versa [217].

From the depicted oscillations the free-spectral-range (FSR) of the resonator is estimated to be $\Delta\lambda_{\mathrm{FSR}} \sim 20$ nm at $\lambda = 660$ nm. The resonator length l can be evaluated via $l = \lambda^2/2n\Delta\lambda_{\mathrm{FSR}}$ and leads to $l \sim 6 - 7$ µm with $n_{\mathrm{LC,\,o}} = 1.51$ being

the refractive index of the ordinary (o) axis of the liquid-crystal layer. The estimated l is smaller than the actual total liquid-crystal layer thickness $d_{\mathrm{LC}} = 10$ µm, which already includes the unknown thickness of the transparent electrodes. As a result, the Fabry-Pérot modulation is predominately introduced by the resonator formed by the two ITO − LC interfaces.

In Ch. 4 the explicitly shaped pulse sequences are reconstructed which allows a direct verification that unwanted pre- or post-pulses generated by the Fabry-Pérot effect do not significantly contaminate the shaped pulse sequences. Furthermore, for the identified resonator the normal incidence reflectance R at the first interface is only about $R = (1.51 - 1.86)^2/(1.51 + 1.86)^2 \sim 1$ %.

The green cut along the voltage direction below the transmission map in Fig. 3.6 (a) depicts the transmission modulation for a individual pixel corresponding to the spectral component $\lambda = 650$ nm. Since the transmission T for a particular SLM pixel of a single layer is given by

$$T(U) = T_0 \cdot \cos^2\Big(\frac{\phi(U)}{2} \pm k\pi\Big), \tag{3.3.23}$$

with U being the tuned layer voltage and $k \in \mathbb{N}_0$. The applied phase $\phi(U)$ can be recovered by inversion via

$$\phi(U) = 2k\pi \pm 2\arccos\sqrt{\frac{T(U)}{T_0}}. \tag{3.3.24}$$

From Eq. (3.3.24) it is clear that the difference in voltage between two adjacent transmission maxima (see black arrows in Fig. 3.6 (a)) corresponds to an additional phase range of 2π. The phase extraction for each pixel is performed by an iterative algorithm (see Ref. [217] for details). An important detail is that the phase extraction starts at maximum voltage counts. Consequently, it is beneficial if the transmission value at 4096 Vc is determined qualitatively similar for each pixel, i.e., close to its maximum transmission value. Note that a transmission maximum for, e.g., layer 1 appears at voltage counts $U_1 = U_{2,\,\mathrm{fixed}}$ (at least for the here implemented SLM) which is an additional argument why a fixed voltage count setting of layer 2 at $U_{2,\,\mathrm{fixed}} = 4096$ Vc is beneficial during acquisition of the transmission map. The orange line in Fig. 3.6 (a) and (b) labels the so called zero-phase voltage for each pixel and serves as the layer individual point of reference for the applied phase $\phi(U)$, which is explained in detail for the final voltage-to-phase calibration maps (see Fig. 3.7).

Figure 3.6 (b) depicts the acquired transmission map and zero-phase voltage for Layer 2 for completeness and the oscillations along the wavelength axis due to the Fabry-Pérot effect are observed as well.

To generate the final voltage-to-phase calibration curve for each layer, several data post-processing steps are performed to further improve the data quality of the acquired transmission maps. Furthermore, the mapping of the individual spectral components to the corresponding SLM pixel by the wavelength-to-pixel calibration is applied.

The resulting final voltage-to-phase calibration curves are depicted in Fig. 3.7 (a) for Layer 1 and (b) for Layer 2. The color coding of the individual maps represents here the applied phase $\phi_{1,2}(U_{1,2})$ referenced to the zero-phase voltage curve (orange) and the wavelength axis is sampled with respect to the 640 SLM pixels, but still labeled "wavelength" for convenience. Cuts along the SLM pixel voltage (green) and wavelength axis (blue) are at the same positions as in Fig. 3.6 for comparison and the two grey curves in each map mark the chosen possible operating range of each SLM layer.

As seen in the cut along the wavelength direction (dark blue) in Fig. 3.7 (a), the oscillations due to the Fabry-Pèrot effect have been successfully smoothed out. The reason becomes clear in Fig. 3.8. The main differences between the voltage-to-phase calibration curves of SLM layer 1 and 2 are depicted in the individual voltage cuts (green) in Fig. 3.7 (a) and (b), respectively. Both curves are monotonically decreasing for larger SLM pixel voltages to enable an unambiguous assignment between the SLM voltage and the corresponding applied phase. The indicated operating range of each layer (grey dots) is defined excluding voltage counts $<$ 100 Vc and $>$ 2800 Vc to maintain the monotonicity within the operating range and covers more than 4π phase for each pixel of both layers.

The zero-phase reference point (orange dot) is set differently for both layers (see the different transmission maxima Fig. 3.6 (a) and (b)). This adjusted setting is slightly unusual, but the idea is that the phase applied by layer 2 is more frequently generated by significantly smaller pixel voltages than the pixel voltages generating the phase at layer 1. For this SLM, this configuration reduces amplitude-shaping artifacts as compared to the standard procedure in which the zero-phase reference point of layer 1 is set at pixel voltages as close as possible to the zero-phase reference point of layer 2. The amplitude-shaping artifacts become noticeable in the transmission spectrum as a sudden decreased (increased) transmission between two adjacent pixels which generates substantial intensity drops (jumps) for corresponding spectral components inside the transmission spectrum.

3.3.6. Validation of the voltage-to-phase calibration

As a first check of the generated SLM calibration curves a transmission check is performed based on pure amplitude shaping of the transmitted spectrum at certain transmission levels. Following Eq. (3.3.21) and using the pure amplitude-shaping

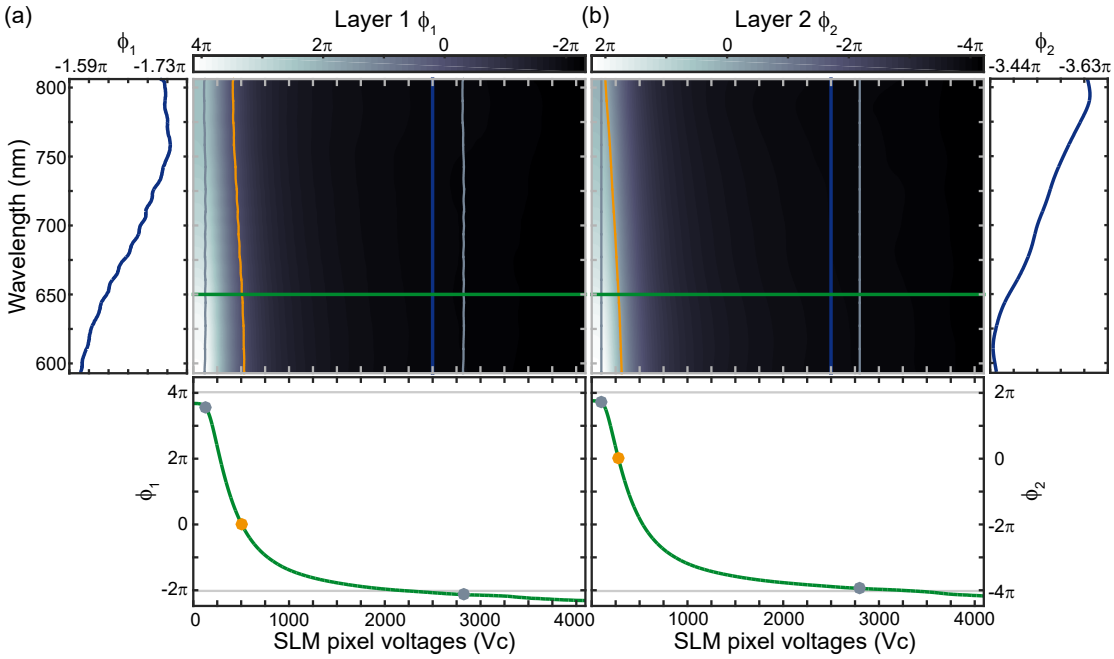

Figure 3.7 – **Final voltage-to-phase calibration curves.** Post-processed calibration curves for layer 1 (a) and layer 2 (b). The color bar labeling the individually applied phases ϕ_1 and ϕ_2 is defined with respect to the corresponding zero-phase voltage curve (orange line). The possible operating range is limited by the two grey vertical curves for each map and covers a 4π-range for each pixel of both layers. Cuts along the wavelength axis (blue) at 2500 Vc are depicted for both layers and selected voltage-to-phase curves (green) for a certain SLM pixel corresponding to $\lambda = 650$ nm are presented to emphasize the differently defined zero-phase reference (orange marker).

condition $\phi_1 = -\phi_2$ the individual phases are set at the layers to modify the overall transmitted intensity of the white-light spectrum as seen in Fig. 3.8 (a) and (b).

In (a) the resulting spectra are depicted using voltage-to-phase calibration curves in which the oscillations along the wavelength axis due to the Fabry-Pérot effect as discussed in Fig. 3.6 are not smoothed out by post-processing. (b) presents the same measurement but using the finally chosen voltage-to-phase calibration curves with smoothed out oscillations as introduced in Fig. 3.7. In both (a) and (b), it is seen that the $T = 100\,\%$ spectrum (orange) matches well with the full transmission spectrum (blue). Note that the full transmission spectrum is generated by initializing the SLM with both layers set to their respective zero-phase voltage curve.

Reducing the transmission from $T = 80\,\%$ (yellow) down to $T = 0\,\%$ (red)

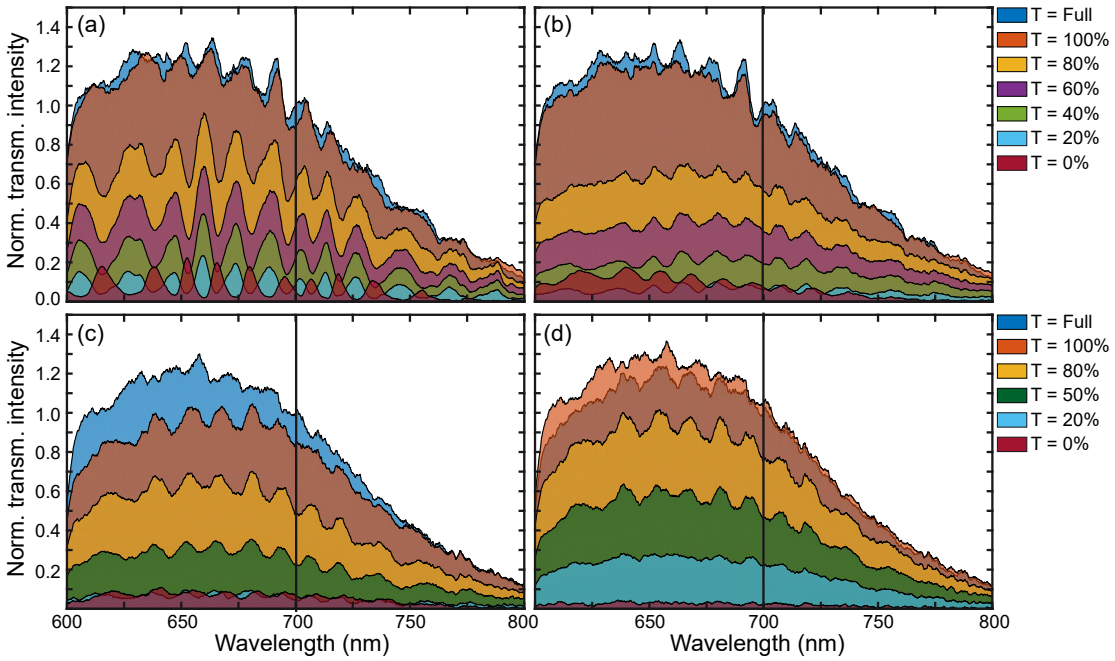

Figure 3.8 – Transmission spectra at modified transmittance by pure amplitude shaping. (a) Using voltage-to-phase calibration curves with no additional smoothing of the oscillatory intensity modulation introduced by the Fabry-Pèrot effect. (b) Using the presented final voltage-to-phase calibration curves with smoothed oscillations (see Fig. 3.7). (c) Using the final voltage-to-phase calibration curves before applying a constant voltage correction. (d) Using the final voltage-to-phase calibration curves after implementation of the constant voltage correction. This leads to a minimized Fabry-Pérot effect and quantitatively correct transmittance values emphasized by normalizing each spectrum to the corresponding full transmission spectrum (blue) at $\lambda = 700$ nm (black line).

decreases indeed step by step the intensity for the whole spectral range for both calibration configurations, but the defined transmittance values are not accurately reproduced. This is emphasized by normalizing each spectrum to the transmitted intensity value of the full transmission spectrum at $\lambda = 700$ nm (black line). Apparently, for a reduced transmittance T, the modulation depth of the oscillatory intensity modulation is increased in (a) as compared to (b). As a result, smoothing of the oscillations along the wavelength direction in the voltage-to-phase calibration minimizes the oscillatory intensity modulation in the transmitted spectrum and is therefore implemented for the SLM control in the used pulse-shaper setup.

To improve the quantitative agreement between the set transmittance T and the

resulting intensity reduction, the voltage-to-phase calibration of the first LCD layer is optimized, similar to the constant voltage correction introduced in Ref. [207], in the following way: The transmission for each LCD pixel is optimized by adding a pixel-dependent voltage offset U_{Offset}(pixel) to the voltage-to-phase calibration curve. For this purpose, the voltage of the first LCD layer is scanned in a range of $\Delta U \sim \pm 50$ Vc around its original voltage-to-phase calibration value U_{Cal}(pixel) $\in \{100, ..., 2800 \text{ Vc}\}$, while the voltage at the second LCD layer is kept constant. For each voltage scan step the transmitted spectrum of the white-light laser source is monitored and the voltage scan is performed twice: first, at a pulse-shaper configuration corresponding to minimum, and second, to maximum, transmission. The voltage offset U_{Offset}(pixel) for optimal minimum and maximum transmission was taken as the average from the two scans and added to the voltage-to-phase calibration of the first layer. Following this procedure, slight calibration inaccuracies are corrected as depicted in Fig. 3.8 (c) and (d). Note that this approach characterizes the spectral intensity as feedback only, not the phase.

In both figures, Fig. 3.8 (c) and (d), the full transmittance spectrum (blue) and certain transmittance spectra at configured transmittance values T are monitored. (c) represents the situation before the voltage offset U_{Offset}(pixel) is applied to the voltage-to-phase calibration as used in Fig. 3.8 (b). As seen in Fig. 3.8 (c) no quantitative agreement of the transmitted spectra and the set transmittance values is observed, which is again emphasized by normalizing the spectra with respect to the full transmission spectrum at $\lambda = 700$ nm (black line). The situation is significantly improved after applying the voltage offset as depicted in Fig. 3.8 (d). Here the transmitted spectrum indeed reproduces the set transmittance values T. The observation that the transmittance of the $T = 100$ % spectrum is slightly larger as the full transmittance spectrum results from the smoothing and normalization of the spectra. The transmittance levels of the additionally depicted spectra at $T = 80$ % (yellow), $T = 50$ % (dark green), $T = 20$ % (bright blue) are precisely achieved for ,e.g. , $\lambda = 700$ nm (black line) and the transmission is minimized for $T = 0$ % (red) as expected for the zero transmittance spectrum.

A summary concerning the most important technical specifications of the implemented pulse-shaper setup is given in App. B.

3.4. Photoemission electron microscope

Figure 3.9 shows the design of the UHV chamber including the PEEM (green shaded, 4×10^{-11} mbar base pressure) and two-part preparation chamber (blue shaded, 5×10^{-10} mbar base pressure). Samples are introduced into the UHV

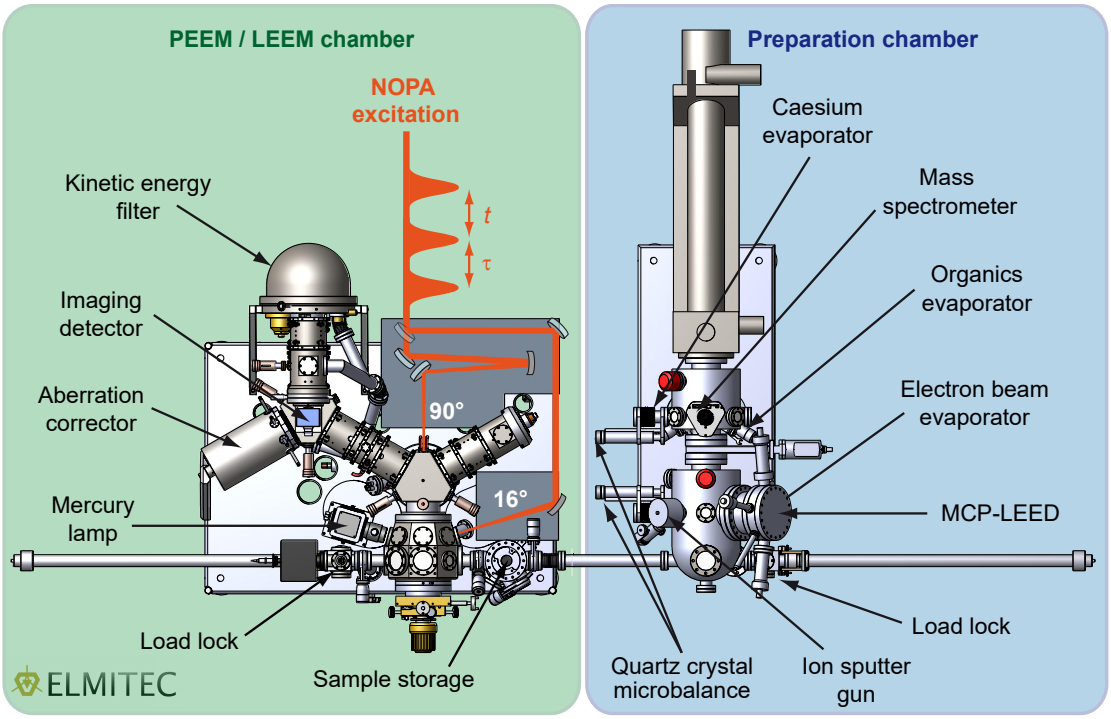

Figure 3.9 – Setup for time-resolved photoemission electron microscopy (PEEM) with nanometer spatial resolution. Design of the UHV chamber for sample preparation (blue shaded) and aberration corrected AC-PEEM (green shaded) with laser beam paths for optical excitation under normal (90° to sample surface) and grazing incidence angle (16°). Adapted from Ref. [1], with the permission of AIP Publishing.

environment via one of two load locks for either direct access to the PEEM or to the preparation chamber. In between there is an additional interconnecting chamber (4×10^{-11} mbar base pressure) with a storage cabinet for five samples.

The electron microscope was developed and manufactured by Elmitec Elektronenmikroskopie GmbH (AC-LEEM III) and combines the two techniques of PEEM and low-energy electron microscopy (LEEM). For the latter, electrons are generated from a Schottky-type field emitter and are guided to the sample. Emitted (PEEM) or reflected (LEEM) electrons are collected by a system of magnetic lenses in the imaging column. Here, a mirror-type aberration corrector (AC) accounts for the principal contributions of spherical and chromatic aberrations introduced mainly by the objective lens [220–222]. A hemispherical imaging energy filter selects electrons by kinetic energy ($\Delta E_{\mathrm{min}} \approx 100$ meV) that are detected with a combination of a chevron-type micro-channel plate (MCP) array with phosphor

screen and a charge-coupled device (CCD) camera.

In combination, the electron microscope offers a variety of application modes: kinetic-energy-selective imaging in real space (AC-PEEM/LEEM mode) and reciprocal space (spatially selective low-energy electron diffraction μ-LEED, photoelectron diffraction or momentum microscopy), as well as direct imaging of the energy filter's dispersive plane (area-selective spectroscopy).

Besides excitation with pulsed laser radiation a continuous-wave mercury (Hg) discharge lamp (LOT QuantumDesign, LSH102) is used for steady-state photoemission microscopy.

The preparation chamber is divided into two parts designated to the preparation of (in-)organic molecular (upper part in Fig. 3.9) and metallic thin films (lower part) using physical vapor deposition techniques. A home-built organic-material effusion cell, a commercial electron-beam evaporator (Focus, EFM 3), and a caesium (Cs) evaporator (Elmitec) are available. The deposition rate is monitored during the evaporation process with quartz-crystal microbalances (Inficon AG, SQM-160). A quadrupole mass spectrometer (Pfeiffer Vacuum GmbH, Prisma plus) monitors residual gas concentrations from 1 to 200 u (unified atomic mass unit).

The quality of long-range ordered surfaces is monitored and controlled with MCP-LEED (Scienta Omicron GmbH, MCP2-LEED) and crystal surfaces are cleaned with an argon (Ar)-ion sputtering gun (Omicron, ISE 5). Cooling of the sample stage is possible in the preparation chamber with liquid nitrogen (LN_2) and in the sample storage cabinet as well as in the electron microscope with liquid helium (He).

The *steady-state spatial resolution* of the AC-PEEM device is demonstrated by the company in Fig. 3.10 (a) using lead (Pb) islands on Si(111) illuminated with the Hg discharge lamp. The resolution is determined by taking an intensity profile (white line) over the spatially resolved PEEM signal (Fig. 3.10 (a), middle) emitted from the rough sample topology and evaluating a steep edge feature according to the $16-84$ % criterion which is discussed in detail in Ref. [223]. Five profiles are evaluated at different locations from which a spatial resolution of 2.6 ± 0.4 nm is determined, while the smallest detected value (right profile in Fig. 3.10 (a)) is 2.1 nm.

As seen in Fig. 3.10 (b), the *minimum length scale* on which characteristic changes in the photoemission yield are determined depends on the sample, e.g., here a plasmonic Au nanoresonator on a silicon-dioxide (SiO_2) substrate, and the applied optical excitation source. Especially for ultrashort laser pulse excitation, space-charge effects [224] might limit the minimum observable length scale. This effect is characterized by recording PEEM images as a function of excita-

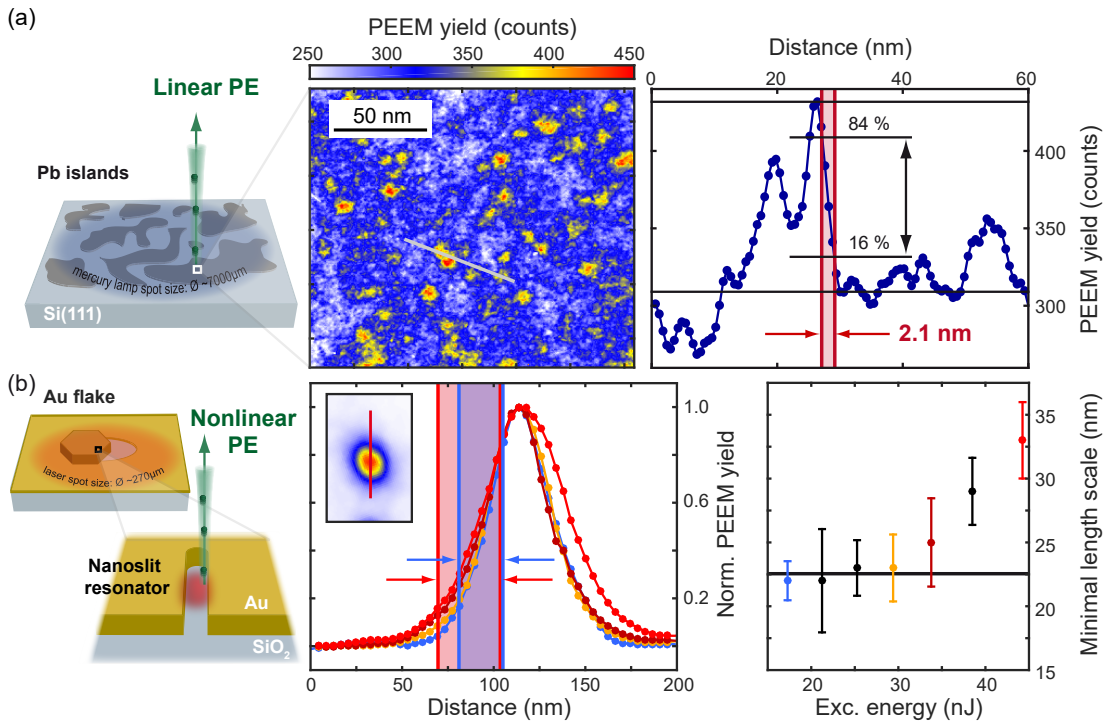

Figure 3.10 – Spatial resolution of the photoemission electron microscope. (a) Steady-state spatially resolved photoemission (PE) image (middle) of lead (Pb) islands on Si(111) (schematically depicted on the left) using continuous-wave illumination light (4.9 eV) of a mercury discharge lamp. The topology profile along the white line is shown on the right with pixelwise photoemission signal (blue dots) and the extracted spatial resolution (red shading). (b) Photoemission yield profiles (middle) of a particular hot spot of a plasmonic gold (Au) slit resonator (schematically depicted on the left) to characterize the minimum length scale (right) on which characteristic changes in the photoemission yield can be determined as a function of the laser excitation energy (660 nm, 19 fs). Adapted from Ref. [1], with the permission of AIP Publishing.

tion pulse energy. Similar to the procedure for retrieving the steady-state spatial resolution, a value characterizing the minimum observed length scale is obtained from the $16-84$ % criterion applied to the image intensity profile of a step-edge feature. Figure 3.10 (b) shows that the minimum length scale upon laser excitation (660 nm, 19 fs) of this particular hot spot from a slit resonator is $\sim$ 22 nm ($<$ 35 nJ) and increases for higher excitation energies up to 35 nm.

Note that in a previous work, a minimum length scale of 12 nm was reported using femtosecond pulse excitation [6]. Here it should be emphasized that the

reported minimum length scale does not directly report the spatial resolution but represents only an upper bound, as the physical properties of electric near-field variation determine the spatial scale of change in the recorded image along with the actual resolution. In general, it is not possible to observe the maximum device resolution with an arbitrary sample upon pulsed laser excitation [222]. Here the determined characteristic changes of the photoemission signal across a minimum length scale of a photoemission hot spot in a plasmonic nanoslit resonator is about 22 nm. This demonstrates that this minimum length scale is in fact determined by a mixture of the underlying physics of the sample and the actual (lower) device resolution of 3 nm. Beyond that, it can not be excluded that the alignment of the PEEM could be further improved resulting in an eventually decreased minimum length scale.

In addition, the PEEM/LEEM system has an energy analyzer for acquiring kinetic energies of electrons [158, 165] in addition to spatial, temporal, k-momentum resolution [225, 226], and (multi-dimensional) optical energy resolution.

3.5. Conclusion

To summarize, this chapter introduces a versatile setup for time-resolved aberration-corrected photoemission electron microscopy (TR-AC-PEEM) that facilitates down to 3 nm spatial resolution in combination with laser excitation by a broadband tunable ($215-970$ nm) sub-20 fs pulsed light source at 1 MHz repetition rate. Further the realization and characterization of the implemented pulse-shaper setup is discussed. Note that the first proof-of-principle 2D nanoscopy experiments with the assembled setup using amplitude- and phase-shaped femtosecond pulses as optical excitation source are presented in App. A.

The full experimental setup enables to measure the spatially resolved incoherent electron yield $Y(\omega_\tau, T, \omega_t, x, y, k, E_{\mathrm{kin}})$ to probe the nonlinear sample coherence on the nanoscale. Using amplitude- and phase-shaped pulse sequences $E(A, \varphi)$ certain contributions to the local nonlinear optical coherence information can be disentangled by the phase-cycling technique. This enables investigation of, e.g., the dominating mechanisms of energy transport in surface systems.

In Ch. 5 the physics behind detected higher-order signals is investigated in detail. Based on the 2D nanoscopy data acquired with the here introduced experimental setup, a quantum model of the nonlinear electron emission process in plasmonic nanoslit resonators is developed. This analysis will shed light on the quantum nature of the localized plasmon polariton in gold nanoslit resonators.

Before presenting these results in detail, let's first focus in the following Ch. 4

on the characterization of the generated multipulse sequences of this particular 2D nanoscopy experiment using the FTSI method. Besides quantification of certain deviations of the actually generated from the ideal multipulse sequences, the possible effect of these deviations on the 2D spectral data is analyzed by utilizing each reconstructed multipulse sequence as optical excitation field in 2D-spectra simulations.

CHAPTER

FOUR

CHARACTERIZATION OF MULTIPULSE SEQUENCES VIA FOURIER-TRANSFORM SPECTRAL INTERFEROMETRY

Coherent 2D electronic spectroscopy has become a standard tool in ultrafast science. Accordingly, it is relevant to consider the accuracy of data considering both experimental imperfections and theoretical assumptions about idealized conditions. Especially since, it is already known that chirped excitation pulses can affect 2D line shapes [29].

This chapter demonstrates a performance-efficient, automated characterization of the full intensity and phase structure of the electric field of each individual multipulse sequence employed during a 2D scanning procedure. Fourier-transform spectral interferometry (FTSI) is employed to quantitatively analyze how the temporal intensity and phase profile varies from scanning step to scanning step and relevant pulse-sequence parameters are extracted. These profiles can be influenced by many independent factors such as power drifts, pulse-shaper imperfections or temperature fluctuations [227] throughout the scanning procedure of a multidimensional spectroscopy experiment. This may lead to both stochastic and systematic deviations of the generated pulse sequence from the expected ideal sequence and in turn have an influence on the retrieved 2D spectra.

Using the characterized fields, 2D spectra are simulated with idealized and real pulse shapes generated from the LCD-based pulse shaper (introduced in Sec. 3.3). This allows us to investigate the impact of any pulse-shape deviations on the 2D spectrum and to implement 2D simulations using the exact pulse shapes instead of commonly used idealized pulse trains consisting of, e.g., infinitely short δ-pulses

or Gaussian-envelope pulses. As exemplary experiments, the fluorescence of a molecular dimer and multiphoton photoemission of a plasmonic nanoslit are considered as detected observables. The deviations induced by pulse-shaping artifacts in the here presented specific case do not distort strongly the population-based multidimensional data.

The characterization procedure itself, as well as the evaluation scripts developed and adapted within the framework of this project, are applicable to other pulses-shaping technologies or excitation geometries, including also pump–probe geometry with multipulse excitation and coherent detection, and allows for accurate consideration of realistic optical excitation fields at all inter-pulse time-delays, even in the pulse-overlapping regime.

After a brief motivation of the field in Sec. 4.1 the experimental implementation is introduced in Sec. 4.2. Note that as a first application the mask-transfer function of the implemented SLM pulse shaper was verified using the spectral interference feedback in App. C. Further, the necessary evaluation steps to reconstruct the full pulse-sequence and the systematic extraction of relevant pulse-sequence parameters is discussed in Sec. 4.3. A systematic analysis of the extracted pulse-sequence is given in Sec. 4.4 and the effect of the full reconstructed pulse-sequence on simulated 2D spectra is studied in Sec. 4.5. The chapter is summarized in Sec. 4.7. The presented results are published in Ref. [2].

4.1. Motivation

In collinear excitation geometries, commonly used in population-based techniques, it is necessary to carry out the pulse delay scanning scheme with systematically and precisely tuned relative phase differences between the pulses as introduced in Sec. 2.3.5. Phase-related pulses have been used already in 1989 to observe and analyze beatings in fluorescence signals [228]. In the multidimensional context, controlling the phases individually allows one to separate various Liouville-space excitation pathways. This procedure, known as phase cycling, has become an essential tool to efficiently extract certain nonlinear signal contributions which are located in a 2D spectrum from the linear signal background [70].

The 2D spectrum in general unravels line-broadening mechanisms, the homogeneous and inhomogeneous linewidths, and the frequency–frequency correlation function [229, 230]. Thus, at this point of the work, the already known effects and imperfections which might affect an interpretation of the spectral features in a measured 2D spectrum should be briefly summarized.

At zero waiting time T, as introduced in Fig. 2.5, homogeneously broadened di-

agonal peaks may be distorted, and one should take care not to confuse this with inhomogeneous broadening [231]. Such peak distortions have negligible effect for $T > 0$ and are of minor relevance for the diagonal broadening of inhomogeneous peaks. Detailed theoretical [232–234] and experimental [235] investigations of signal peak-shape distortions revealed a strong dependence on the excitation beam geometry, phase-matching condition, optical density of the sample, beam overlap region, beam propagation within the sample, and population time T. Especially in noncollinear broadband 2D spectroscopy applications, minimizing cross-peak distortions becomes important and can be achieved with an appropriate geometry [236].

Apart from the "geometric" effects on distortions discussed in the previous paragraph, 2D line shapes are also influenced by the temporal profiles of the applied pulses. In a first experiment, Tian *et al.* employed phase cycling to isolate the 2D photon-echo contribution of electronic transitions in an atomic rubidium vapor [69]. They discussed non-idealities in their acousto-optically based pulse-sequence generation leading to "spurious" pulses, which induced an amplitude modulation with the same phase dependency as the detection signal. This study already indicated that the precise shape of the applied pulse sequence might crucially affect the obtained 2D spectrum and so its interpretation. A systematic theoretical and experimental analysis of the effect of pulse chirp on the shape of 2D electronic spectra has been carried out by the Ogilvie group [29]. They showed, using acousto-optical pulse shaping, that peak-shape asymmetries are introduced if the individual pulses in the experiment exhibit different amounts of chirp. Further, in case that all pulses are similarly chirped, distortions still affect the anti-diagonal symmetry of the signal peak and introduce negative features in the 2D spectrum. In both cases, the introduced asymmetries and negative features in simulated 2D spectra depend on the waiting time T and are the most visible for $T = 0$ fs. They concluded that a careful pulse characterization is absolutely necessary for correct interpretation of frequency-dependent relaxation processes via 2D spectroscopy. A recent investigation of the combined effect of high pulse intensity and chirp on population-based 2D electronic spectroscopy data in atomic rubidium vapor revealed the enhancement and suppression of distinct higher-order signal contributions [237]. Here this analysis is extended further and an automated experimental analysis procedure is presented taking into account that the pulse shapes might additionally vary from scanning step to scanning step.

In addition to pulse shaping using an acousto-optic programmable dispersive filter [238, 239], tailoring of interferometrically stable pulse sequences has been realized by a variety of other techniques and designs [205, 210]. These can be categorized as time-domain [240, 241] or spectral-domain approaches, with the latter mostly employing liquid-crystal-based amplitude and phase shaping [242]

or acousto-optical modulators [243]. Many broadband spectral-domain techniques utilize at least one grating in $4f$-geometry and shape the spectral phase by modulating the refractive index for each spectral component of the femtosecond pulse in the Fourier plane. Using a dual-layer LCD SLM enables independent amplitude and phase shaping of femtosecond laser pulses [204].

Following the LCD-based approach, imperfections in the pulse-sequence generation have been reported and studied in detail like replica pulses as a result of the LCD pixelation [216], spatio-temporal coupling [215, 244, 245], pixel crosstalk or Fabry-Pérot interference effects [207]. Many of these inherent imperfections can be minimized by design, handling or using only a low-voltage working range of the pulse shaper.

One possibility to compensate imperfections due to a non-perfect voltage-to-phase calibration of the individual LCD pixels (a detailed description of the calibration is given in Sec. 3.3 and [210]) is achieved by systematically scanning the voltages of one LCD layer and correcting pixelwise deviations between expected and measured voltage-to-phase dependencies [207]. In this approach, a full correction would include an iterative optimization for every possible phase combination. A non-iterative compensation method for undesired spectral intensity modulations like, e.g., the Fabry-Pérot amplitude modulation effect, was also discussed [246]. In this work by Wittenbecher *et al.*, the voltage dependency of the Fabry-Pérot effect is characterized and reduced by using a two-dimensional look-up table to correct the corresponding voltage values and ensuring that phase shaping is unaffected by this procedure. In both approaches the feedback signals used for compensation or correction have been successive measurements of the spectral intensity of the shaped pulses only, but not their spectral phase.

4.2. Experimental implementation

The here utilized technique is based on analyzing the spectral interference pattern of the shaped pulse sequence and a well-known reference pulse, i.e., FTSI.

4.2.1. Setup

Using the principle of single-channel spectral interferometry [247], FTSI was described by Lepetit *et al.* as a linear technique of phase measurement [30] and enables extracting the relative spectral phase between two pulses. Its experimental implementation and possible error sources have been discussed in detail [248, 249]. The principle is based on the fact that the information about the *relative spectral phase* between reference pulse and shaped pulse sequence is imprinted in the in-

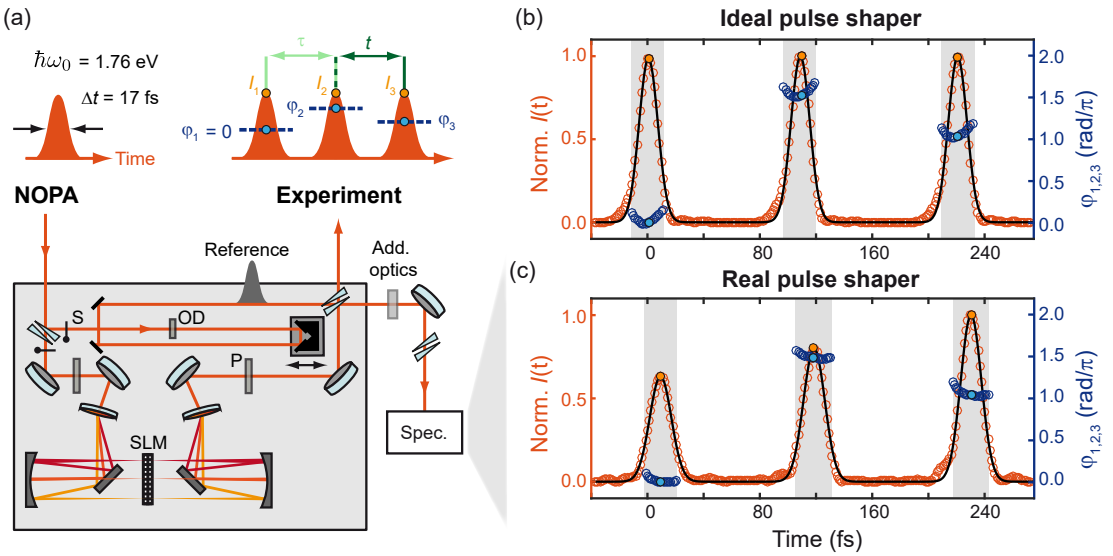

Figure 4.1 – Experimental schematic and exemplary data. (a) Sub-20 fs input pulses (red) from the NOPA are transformed by a SLM-based pulse shaper to generate multipulse sequences for collinear multidimensional spectroscopy experiments. A reference pulse (dark gray) is separated by a thin wedge pair and can be shuttered (S) individually. Its temporal delay and intensity are controlled by a delay stage and neutral density filters (OD) relative to the shaped pulse. The unshaped reference pulse and a small fraction ($\sim$ 3 %) of the experimentally used shaped pulse sequence are spatially recombined after the second thin wedge pair, guided through several additional optics (Add. optics) and spectrally interfere on a spectrometer (Spec.). For each individual pulse sequence the maximum intensity of each sub-pulse $I_{1,2,3}$ (orange), temporal inter-pulse delays τ, t (light and dark green), and intra-pulse phase-offsets $\varphi_{1,2,3}$ (blue) are determined. (b) Temporal intensity profile (red circles) and temporal phase (dark blue circles) for a three-pulse sequence assuming ideal pulse shaping of the input pulse. The intensity maxima $I_{1,2,3}$ (orange circles) and temporal delays τ, t between these maxima are quantified by fitting the intensity profile in the gray shaded windows with a sum of three Gaussian functions (black line). The individual temporal phase offsets are obtained as the phase values at maximum intensity (light blue). (c) Same as in panel (b), but for the experimentally determined real pulse shapes. Adapted with permission from Ref. [2] © Optica Publishing Group.

terference fringe pattern in the spectrum. Since FTSI is based on a non-iterative and linear detection method [30] it is well suited for fast and sensitive pulse characterization of multipulse sequences at low pulse energies and for this reason can be used simultaneously with a nonlinear spectroscopy experiment because only a small portion of the excitation light is required.

As described in Sec. 3.2 a custom-designed NOPA is used to generate sub-20 fs laser pulses with a central wavelength $\lambda_0 = 707$ nm at 1 MHz repetition rate [1]. Before entering the pulse-shaper setup depicted in Fig. 4.1 (a), the laser pulses are pre-compressed by minimizing the second-order dispersion via a prism compressor with two fused-silica prisms which are set up in folded geometry. Only the residual third- and higher-order dispersion is then compensated by the pulse-shaper via pure phase shaping, leaving most of the device capacity for tailoring the individual multipulse sequences via amplitude and phase shaping with the LCD-based pulse shaper (Jenoptik, SLM-S640d USB) [1].

The pixel-to-wavelength calibration, voltage-to-phase calibration and the introduced optimizations are performed using a commercial white-light supercontinuum laser source (NKT, SuperK COMPACT) as described in Sec. 3.3. Due to limited time and computational resources, more sophisticated methods [246] are refrained to minimize pulse-shaper imperfections. Anyway, the purpose of the present work is to characterize the influence of any remaining pulse-shaper imperfections on 2D spectra, not to remove them all, because for other pulse-shaping approaches such correction procedures may not be applicable anyway or lead to different results. Here the focus lies on the accurate characterization of the real pulse shapes in all cases.

Characterization of the shaped pulse sequences in Fig. 4.1 (a) was implemented by FTSI in the following way: A small portion (≈ 3 % energy) of the pulse-shaper input beam is split of with a thin fused-silica wedge pair (Hellma Optics, 1 mm thick edge, 60 arcmin, uncoated) and used as the unshaped reference pulse. The wedge-pair configuration compensates the angular dispersion of the transmitted beam that would occur in a single wedge-pair configuration due to the small inclination (wedge angle) of the rear surface relative to the front surface. Since angular dispersion affects the position of each spectral component in the Fourier plane, it has to be avoided or integrated in the pixel-to-wavelength calibration of the SLM. In addition, a suitable optical density filter (OD = 0.3, Thorlabs, NDUV03A) is implemented in the beam path of the reference pulse to adjust the reference pulse energy such that the spectral intensity is roughly similar to that of an unshaped pulse transmitted through the pulse shaper.

The optical path of the reference pulse is matched to the propagation length of the shaped pulse taking into account the additional temporal retardation induced by the different dispersive media of the two polarizers (P), the two transmission gratings, and both liquid-crystal layers of the SLM. In this way, it is possible to set a temporal delay of around $\tau_{\mathrm{Ref}} \approx 1$ ps between reference pulse and shaped pulse sequence within the travel range of the manual linear micrometer stage (OptoSigma, TSD-601S) featuring the retro-reflector. Temporal delays of this order ensure accurate Fourier filtering during phase reconstruction [205] with respect to

the resolution of the implemented spectrometer. At the second wedge pair, a small part (≈ 3 % energy) of the shaped pulse sequence is recombined with the reference pulse, while the transmitted major part is directed to the PEEM experiment. This arrangement enables the characterization of the shaped pulse sequences used for multidimensional spectroscopy in parallel with the actually performed experiment. As a consequence, each particular time-delay and phase-cycling correlation will be fully characterized.

The reference pulse and shaped pulse sequence are spatially superimposed on a fiber-coupled (Avantes, $250 - 2500$ nm, FC-UVIR200-USB2), irradiance-corrected spectrometer (Avantes, $600 - 800$ nm, AvaSpec-ULS3648) with 0.11 nm spectral resolution and the spectral interference (SI) spectrum is measured. Since the FTSI data processing requires separately measured spectra of the shaped pulse sequence and the reference pulse, the corresponding unwanted beam path is blocked by automated shutters (S) after the first wedge pair when necessary.

Due to its higher pulse energy, the unshaped pulse (Fig. 4.1 (a), upper left) can be well characterized by nonlinear methods, in our case collinear second-harmonic generation (SHG)-frequency-resolved optical gating (FROG) [250]. The characterization in intensity and phase is performed in a commercial collinear SHG-FROG setup (APE, pulseCheck) in the beam path to the experiment. Since the pulse characterization has to be done as accurately as possible at the position of the actual experiment, several additional optics are included on the way to the SHG-FROG setup mimicking the beam path to the experiment. In our particular setup the following additional optics were used: One $\lambda/2$ waveplate (B.Halle, achromatic, $600 - 1200$ nm, RAC 5.2.15 L) for final polarization adjustment, a thin vacuum chamber window (Torr Scientific, 1.5 mm thick, Fused silica), and a single fused-silica wedge (Laser Components, 2 mm thick edge, 15 arcmin, uncoated).

The measured spectrum of the unshaped pulse serves as a constraint for the FROG retrieval algorithm. The retrieved spectral phase is then used to compress the pulse down to $\Delta t = 17$ fs (with a bandwidth-limited pulse duration of $\Delta t_{\mathrm{BWL}} = 15$ fs) by applying the inverted FROG phase to the SLM. Besides that, no phase or amplitude shaping was applied. The compressed pulse at the experiment is finally characterized by an additional SHG-FROG measurement and evaluation. All FROG traces and fitting results of the FROG algorithm for the compressed pulse can be found in Sec. 4.3.

As depicted in Fig. 4.1 (a) the same additional optics (Add. optics) used in the beam path to the SHG-FROG setup are placed in front of the SI spectrometer (Spec.). Since the characterized compressed pulse used in the experiment passes in total two wedge pairs, a third wedge pair was introduced in front of the SI spectrometer to ensure that the pulse at the spectrometer, which travels through the SLM, passes the same amount of glass as the characterized compressed pulse.

The spectral phase characterization of the reference pulse has to be done only once, before the spectral phases of the various shaped sequences can be determined. A direct characterization of the reference pulse via SHG-FROG would be challenging due to its low pulse energy. Since the influence of different propagation length through air on the spectral phase of the compressed pulse is negligible at the spectral range of the pulses ($600 - 800$ nm), the retrieved FROG phase of the compressed pulse utilized in the experiment is an adequate description of the spectral phase of the compressed pulse at the SI spectrometer. The compressed pulse at the SI spectrometer, characterized in that way, enables a spectral-phase characterization of the reference pulse via FTSI, by analyzing the spectral-interference pattern of the spatially superimposed known compressed pulse and the unknown reference pulse (see second step in Sec. 4.3).

As an alternative approach, the spectral phase of the reference pulse can also be reconstructed by characterizing the uncompressed unshaped pulse instead of the compressed shaped pulse by SHG-FROG and using this spectral phase to characterize the spectral phase of the unknown reference pulse by FTSI. However, since the shaped pulse is compressed for generating multipulse sequences in any case, no evaluation step would effectively be saved by this approach.

The additional measurement time associated with the recording of the individual spectra makes up only 11 % of the 67 h overall measurement time. This could in principle be further minimized by shorter integration times, or implementation of parallelized acquisition schemes of the required three spectra per characterized pulse sequence. Note that the expenditure of measurement time for the characterization of the multipulse sequences in a 2D spectroscopy experiment strongly depends on the particular components of the FTSI setup and their arrangement.

4.2.2. Reconstruction of the time-domain structure

FTSI enables the reconstruction of the relative spectral phase $\Delta\varphi(\omega)$ between a reference pulse and an unknown pulse, such as a pulse sequence. If the spectral phase and intensity of the reference pulse are known, the actual spectral phase of the pulse sequence can be calculated. A rigorous description of the details concerning the individual spectral phase reconstruction steps during the FTSI data processing can be found in Sec. 4.3 and follows in general the literature [30, 205].

While this delivers the complete electric field evolution, the aim here is a simplified description that allows analyzing deviations from the ideal case in terms of a limited number of parameters that are meaningful in multidimensional spectroscopy. For a three-pulse experiment (Fig. 4.1 (a), top), these parameters are the two inter-pulse delays, τ, t (light green, dark green), the maximum intensity of each particular pulse, $I_{1,2,3}$ (orange), and the phase offsets that are relevant for

phase cycling, $\varphi_{1,2,3}$ (light blue), describing the zero-order Taylor coefficient (relative to the reference pulse) of the individually Taylor-expanded temporal phase of the particular pulses labeled 1, 2 and 3. These parameters are retrieved in an automated fashion for both the real and ideal pulse sequences in the same manner and then quantitatively compared for each experimental measurement step.

To generate the ideal pulse sequences, the spectral intensity is computed by multiplying the measured spectral intensity of the compressed pulse with the spectral intensity modulation function (the square of Eq. (3.3.12)) sent to the SLM; and the spectral phase is calculated by adding to the spectral phase, retrieved by SHG-FROG of the compressed pulse, to the spectral phase modulation function (Eq. (3.3.13)) sent to the SLM. After inverse Fourier transformation of the corresponding complex-valued electric field, the normalized temporal intensity and phase are obtained.

This ideal (pulse-shaper) pulse sequences exclude any imperfections due the pulse-shaping process itself, i.e, spatio-temporal coupling, adjacent-pixel voltage jumps, layer-to-layer crosstalk, voltage-to-phase calibration inaccuracies, unshaped pixel-gap transmission and pulse-preparation imperfections like, e.g., spatial chirp. Shown in Fig. 4.1 (b) is an example for a pulse sequence from an ideal pulse shaper with the normalized time-domain intensity $I(t)$ (red circles) of a three-pulse sequence at time delays $\tau = 108$ fs, $t = 112$ fs and phase offsets $\varphi_1 = 0$ rad/π, $\varphi_2 = 1.5$ rad/π, $\varphi_3 = 1.0$ rad/π.

As seen in Fig. 4.1 (b), even the pulse sequence from an ideal pulse shaper reveals slight asymmetric temporal pulse shapes as expected, resulting from the non-perfect-Gaussian spectral intensity and uncompensated, residual higher-order spectral phase. Moreover, pulse-preparation imperfections affect also the shape of the extracted temporal phase offsets. Note that in the further discussion the pulse at smallest absolute time is labeled as the first pulse in the pulse sequence and the pulse at largest absolute time as the last pulse.

By fitting the normalized time-domain intensity $I(t)$ with a sum of three Gaussian functions (Fig. 4.1, black line), the inter-pulse delays τ, t (green) and the maximum intensity values $I_{1,2,3}$ (orange circles) of each of the three pulses of the sequence are determined. To optimize the stability of the fitting procedure, the data set was reduced to the gray-shaded regions in Fig. 4.1 (b) by an intensity threshold criterion $I > 0.20 \times I_{\max}$ with $I_{\max} = \max\{I_1, I_2, I_3\}$. From the (relative) zeroth-order Taylor coefficients of the individual temporal phases (dark blue circles), the phase offsets introduced by phase cycling are reconstructed. Further, the uncertainty of the phase offsets, caused by linear, quadratic, or higher-order temporal phase (dark blue circles in Fig. 4.1 (b)), is minimized by defining the phase offset $\varphi_{1,2,3}$ as the temporal phase value at the time of maximum pulse intensity $I_{1,2,3}$ (light blue circles). A detailed discussion of the phase offset extraction

procedure from the temporal phase structure can be found in Sec. 4.3.

In Fig. 4.1 (c) the experimentally characterized field for the same pulse-sequence parameters as the ideal sequence in Fig. 4.1 (b) is presented. For the real pulse-shaper data, the pulse-shape information is evaluated in the same way as for the ideal case, only that the pulse sequence is reconstructed by FTSI from the measured SI spectrum.

Comparing the ideal and the real case reveals that the temporal delays τ, t as well as the phase-offset systematic can be nicely reproduced. In the real pulse-shaper sequence, a global 10 fs temporal shift towards positive times is observed. Since ideal and real pulse-shaper sequences are reconstructed with the same settings, e.g. width and type of window filters, in the evaluation script, this shift could result from a systematic inaccuracy in the linear fitting of τ_{Ref} as described in Sec. 4.3.2. For multidimensional time-resolved spectroscopy, only relative time delays between individual inter-pulse pairs are relevant anyway, and a temporal offset value will not affect the retrieved 2D spectrum. The main difference between both pulse sequences lies in the intensities of individual pulses. The ideal sequence exhibits equal maximum intensities for all three pulses, whereas the real pulse shaper shows a 35 % reduced maximum intensity of the first pulse and a 20 % reduced maximum intensity of the middle pulse compared to the maximum intensity of the last pulse. Discrepancies such as these will be analyzed with our automated procedure for each individual scanning step, leading to a comprehensive analysis of their influence on resulting 2D spectra.

Before presenting in detail how parameters of complex pulse sequences are reconstructed using the presented FTSI approach and systematically analyzed, note that also the measured spectral-interference spectrum itself was used to validate the implemented SLM transfer-function as shown in App. C.

4.3. Pulse-sequence reconstruction and extraction of essential pulse-train parameters

This section describes the different evaluation steps in our experimental routine to reconstruct the spectral and temporal intensity and phase of complex multipulse sequences by FTSI. The extraction of the various amplitude and phase-profiles from the measured set of spectra has been obtained by the LabView virtual instrument (VI) `SI - evaluate dual channel SI_KL v2.0.vi`, which has been verified and modified. The pulse-train parameter determination is performed by `PostProcess_SI_Data_3Pulse_Parallel_ALL.m` in Matlab.

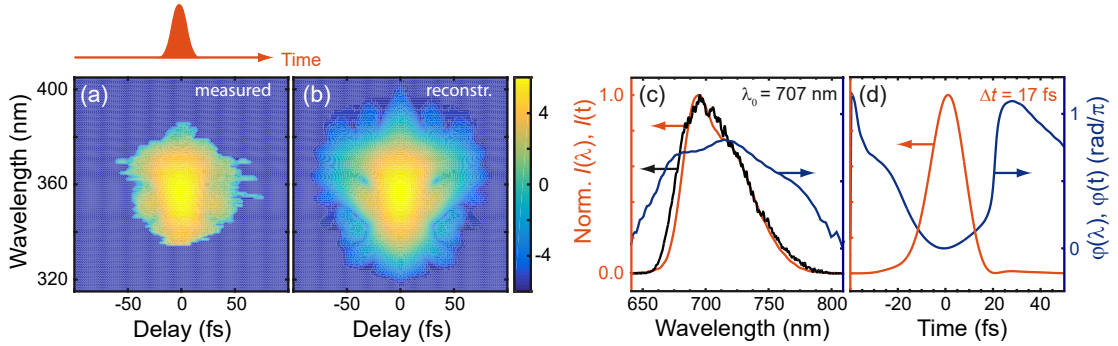

Figure 4.2 – First step: Characterization of compressed single pulse (orange) by SHG-FROG. (a) Measured and (b) reconstructed FROG traces. Nonlinear part of the (c) spectral and (d) temporal phase (blue) and intensity (orange) reconstruction from FROG analysis. The directly measured linear spectrum (black) is shown for comparison and is used as a marginal in the FROG retrieval algorithm. Adapted with permission from Ref. [2] © Optica Publishing Group.

4.3.1. Compressed single-pulse characterization with SHG-FROG

In a first step, the compressed single pulse (orange) is characterized by a commercial SHG-FROG (APE, pulseCheck) as depicted in Fig. 4.2. On its way to the FROG apparatus, this pulse propagates through the same dispersive optics as on its beam path to the experiment (Add. Optics in Fig. 4.1 (a)). The pulse is pre-compressed by a prism compressor and higher-order chirp is minimized by iterative pulse compression with the pulse shaper.

The measured (Fig. 4.2 (a)) and reconstructed (Fig. 4.2 (b)) FROG traces agree well, indicating successful analysis (grid size: 256, minimum FROG error: 0.00367). Shown in Fig. 4.2 (c) is the reconstructed spectral intensity $I(\lambda)$ (orange) and spectral phase $\varphi(\lambda)$ (dark blue) together with an independently measured fundamental spectrum (black), which was used as a marginal in the FROG retrieval algorithm [250], around a central wavelength of $\lambda_0 = 707$ nm. The two spectra agree well, which is a further indication of reliable FROG reconstruction. By 1D-Fourier transformation of the frequency-domain electric field, one obtains the temporal intensity $I(t)$ (orange) and phase $\varphi(t)$ (dark blue), as shown in Fig. 4.2 (d), of the compressed pulse passing through the pulse shaper. The slightly asymmetric intensity spectrum and residual amount of third-order spectral phase lead to a minor post-pulse around 28 fs . The quantified full-width at half-maximum

(FWHM) intensity pulse duration of $\Delta t = 17$ fs is close to the calculated bandwidth limit $\Delta t_{\mathrm{BWL}} = 15$ fs and verifies the successful pulse compression by the combination of prism compressor and pulse shaper.

Note that Fig. 4.2 (c) and (d) determine the remaining spectral and temporal phase (dark blue) of the compressed pulse which is used in the next step to characterize the unknown reference pulse.

4.3.2. Reference-pulse characterization using FTSI

In a second step, as presented in Fig. 4.3, the reference pulse (gray) at fixed time delay $\tau_{\mathrm{Ref}} \approx 1$ ps is characterized by FTSI with the now known single compressed pulse (orange). The parameter τ_{Ref} is set via the manual delay stage in the reference beam path to ensure signal separation in time domain meaning $\tau_{\mathrm{Ref}} > 3\Delta t \approx 50$ fs and a sufficient signal sampling $\tau_{\mathrm{Ref}} < \tau_{\mathrm{max}} = 2\pi/6\delta\omega \approx 2.6$ ps with $\delta\omega \approx 4 \times 10^{-4}$ 1/fs being the resolution of the spectrometer [205].

The reader is cautioned that in this and the following figures all plots are normalized individually after the pulse-sequence reconstruction only to simplify the explanation of the spectral phase reconstruction steps. No normalization is performed during the automated phase reconstruction for the 13456 measurement steps. This ensures that the relative deviations can be analyzed correctly, including comparative intensities between different pulse sequences.

In Fig. 4.3 (a), the measured intensity spectra (integration time: 100 ms , 3 times averaging) are shown. The gray spectrum corresponds to the reference pulse, the orange spectrum to the single compressed pulse and the yellow spectrum to the spatial superposition of both, showing the spectral-interference signal. The oscillatory part is extracted by subtracting the sum of the spectra of the reference, $I_{\mathrm{Ref}}(\lambda)$, and the single compressed pulse, $I_{\mathrm{FROG}}(\lambda)$, from the spectral-interference spectrum. The resulting interference term

$$S(\lambda) = 2\sqrt{I_{\mathrm{Ref}}(\lambda) I_{\mathrm{FROG}}(\lambda)}\cos\Big(\varphi_{\mathrm{Ref}}(\lambda) - \varphi(\lambda) - \frac{2\pi c}{\lambda}\tau_{\mathrm{Ref}}\Big), \tag{4.3.1}$$

is shown in Fig. 4.3 (b). $\varphi_{\mathrm{Ref}}(\lambda)$ describes the "unknown" spectral phase of the reference pulse, $\varphi(\lambda)$ the known spectral phase of the single compressed pulse characterized by FROG in the first step, c is the speed of light and τ_{Ref} corresponds to the delay between reference pulse and compressed single pulse as indicated in Fig. 4.3. Instead of taking the $\arccos(S(\lambda)) \propto \varphi_{\mathrm{Ref}}(\lambda) - \varphi(\lambda) - \frac{2\pi c}{\lambda}\tau_{\mathrm{Ref}}$, the Fourier-transformation approach is applied due to several disadvantages of the $\arccos(S(\lambda))$ method [30].

To avoid numerical errors in the spectral interference oscillations shown in Fig. 4.3 (b), the measured spectra are not resampled or converted from wave-

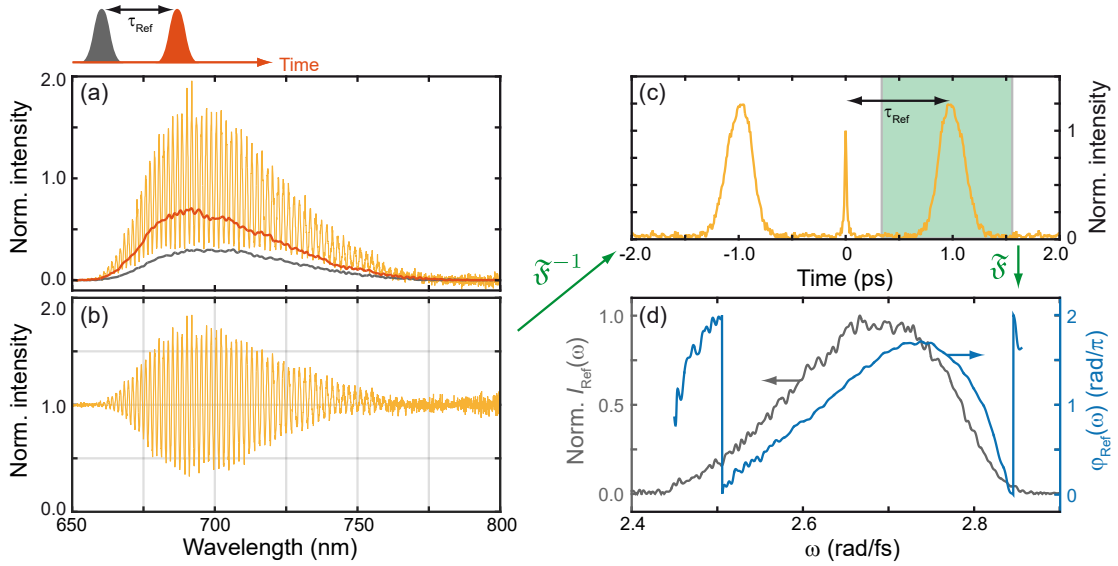

Figure 4.3 – Second step: Characterization of reference pulse (gray) by FTSI with help of the FROG-analyzed compressed single pulse (orange). (a) Spectral interference (yellow) normalized to the sum of reference (gray) and single pulse (orange) spectrum. (b) Extracted spectral interference oscillation. This signal is inverse Fourier-transformed (green arrow) to (c) leading to a dominant peak at τ_{Ref}. This value corresponds to the delay between reference and single pulse. The positive-delay peak is filtered by a rectangular window function (green) and Fourier-transformed back. From the resulting signal $S^{+}(\lambda)$ the spectral phase $\varphi_{\mathrm{Ref}}(\omega)$ (light blue) of the reference pulse is extracted and plotted together with the spectral intensity $I_{\mathrm{Ref}}(\omega)$ (gray) in (d). Adapted with permission from Ref. [2] © Optica Publishing Group.

length to frequency domain before applying an inverse discrete Fourier transformation. This does not affect the performed Fourier-filtering of a certain signal contribution, since the filtered signal is transformed back to its original domain. To construct an intuitive x-axis in the Fourier domain presented in Fig. 4.3 (c) the original wavelength axis of the spectrometer is converted from wavelength to frequency by $\omega_i = 2\pi c/\lambda_i$ where i refers to the individual spectrometer pixel. The time axis in Fig. 4.3 (c) is then calculated by linear interpolation between $\pm\frac{i_{\max}\delta t}{2}$ with time increments $\delta t = 2\pi/(\omega_{\max} - \omega_{\min})$ and total amount of spectrometer pixel $i_{\max} = 3647$. Note that $\omega_{\max}$ and $\omega_{\min}$ correspond here to the maximum and minimum frequency resolved by the spectrometer.

After performing the inverse discrete Fourier transformation (green arrow) the signal contribution around τ_{Ref} is filtered by a rectangular window function (green). The width of the window is chosen broad enough not to clip the signal contribution

around τ_{Ref}. A reported signal-broadening effect due to non-equidistant frequency spacing [249] is negligible in our case because the calibration of spectrometer pixels versus frequency was nearly linear, with a relative maximum deviation of ± 1 % around the central frequency over the whole spectral range of the spectrometer. After Fourier transformation back (green arrow) to the original domain, the filtered complex signal corresponds to

$$S^{+}(\lambda) = \sqrt{I_{\mathrm{Ref}}(\lambda) I_{\mathrm{FROG}}(\lambda)}\, \exp\Big(i\varphi_{\mathrm{Ref}}(\lambda) - i\varphi(\lambda) - i\frac{2\pi c}{\lambda}\tau_{\mathrm{Ref}} \Big). \tag{4.3.2}$$

Hence, the spectral reference phase in spectral domain is given by

$$\varphi_{\mathrm{Ref}}(\omega) = \arg(S^{+}(\omega)) + \varphi(\omega) + \omega\tau_{\mathrm{Ref}}, \tag{4.3.3}$$

$\arg(S^{+}(\omega))$ is obtained by converting $\arg(S^{+}(\lambda))$ from wavelength to frequency and $\varphi(\omega)$ is known from the FROG characterization in the first step.

In most conventional cases of FTSI application the "reference" pulse is known and used to characterize an "unknown" pulse. Indeed, this is the procedure that is followed below to characterize the multipulse sequences. In order to do that, however, the reference pulse itself has to be characterized first, and as a consequence FTSI is used in an "inverted" procedure. This is possible because the "unknown" pulse was characterized via FROG in the first step. The spectral phase $\varphi(\lambda)$ retrieved from FROG characterization (see Fig. 4.2 (c)) is now inserted into Eq. (4.3.3). The phase $\varphi(\lambda)$ is first converted from wavelength to frequency and its frequency increments are resampled to the same frequency increments as those in the measured SI spectrum resulting in $\varphi(\omega)$. The linear phase term $\omega\tau_{\mathrm{Ref}}$ is determined by linear fitting of the extracted spectral phase within the depicted frequency range.

The result obtained by Eq. (4.3.3), namely the spectral reference phase $\varphi_{\mathrm{Ref}}(\omega)$ (light blue), and the separately measured (normalized) reference intensity spectrum $I_{\mathrm{Ref}}(\omega)$ (gray) are depicted in Fig. 4.3 (d). The intensity spectrum is transformed from wavelength to frequency taking into account the Jacobian transformation [251]. In comparison with the compressed single pulse in Fig. 4.2 (c), the reference pulse shows a significantly higher amount of second-order phase which was to be expected because the reference pulse is only pre-compressed by the prism compressor without using the pulse shaper.

4.3.3. Characterization of the individual multipulse sequences using FTSI

Since the reference pulse is characterized at this point, the reconstruction of the the spectral and temporal phase of the shaped multipulse sequences is proceed in a third step presented in Fig. 4.4. Here one particular example of the full series of 13456 spectral-interference spectra is illustrated.

First, it is validated that the reference phase is correctly implemented in the spectral-phase reconstruction method. For this purpose, measurement step #1, in which a single laser pulse (τ, $t = 0$ fs; $\varphi_{1,2,3} = 0$) is created, is separately analyzed. The corresponding reconstructed intensity (orange) and phase (blue) are depicted in Fig. 4.4 (a) in frequency domain and in Fig. 4.4 (b) in time domain for the real, FTSI-reconstructed, pulse (circles) and for the ideal pulse shaper (lines). The reconstruction works correctly if the real pulse shape corresponds to that already determined by SHG-FROG of the single compressed pulse shown Fig. 4.2 (c) and (d).

As seen in Fig. 4.4 (a), the low-frequency edge of the real PS spectral intensity is shifted to higher frequencies compared to the ideal PS whereas the high-frequency edges of both spectra match. The slope of the reconstructed spectral phase corresponds to that of the ideal PS. The gray window in Fig. 4.4 (a) describes the frequency range in which the linear fitting of the reconstructed phase is performed to determine the linear phase factor $\omega\tau_{\mathrm{Ref}}$. Before Fourier transformation to time domain, a six-times zero padding in the spectral-domain data is applied to increase the resolution in the time domain.

Comparing the real PS time reconstruction (circles) to the ideal PS pulse (lines) in Fig. 4.4 (b) reveals a small broadening of the real PS temporal intensity that can be explained by the reduced spectral width of the real PS. Beyond that, no significant deviations in intensity and phase are observed. This leads to the conclusion that the settings in the spectral-interference reconstruction method like Fourier filter-window widths and positions and temporal order between reference and shaped sequence are correctly defined.

In Fig. 4.4 (c-g), the reconstruction of the spectral phase of the shaped pulse $\varphi_{\mathrm{Sh}}(\omega)$ is exemplarily shown, for measurement step #12990, as a basis for further processing.

Note that the related spectral intensity $I_{\mathrm{Sh}}(\omega)$ corresponds to the measured irradiance-corrected spectral intensity of the shaped pulse (with the reference pulse blocked) in case of the real PS. In case of the ideal PS, the spectral intensity retrieved by SHG-FROG of the compressed pulse is used, resampled according to the pixel basis of the pulse shaper and multiplied by the spectral intensity

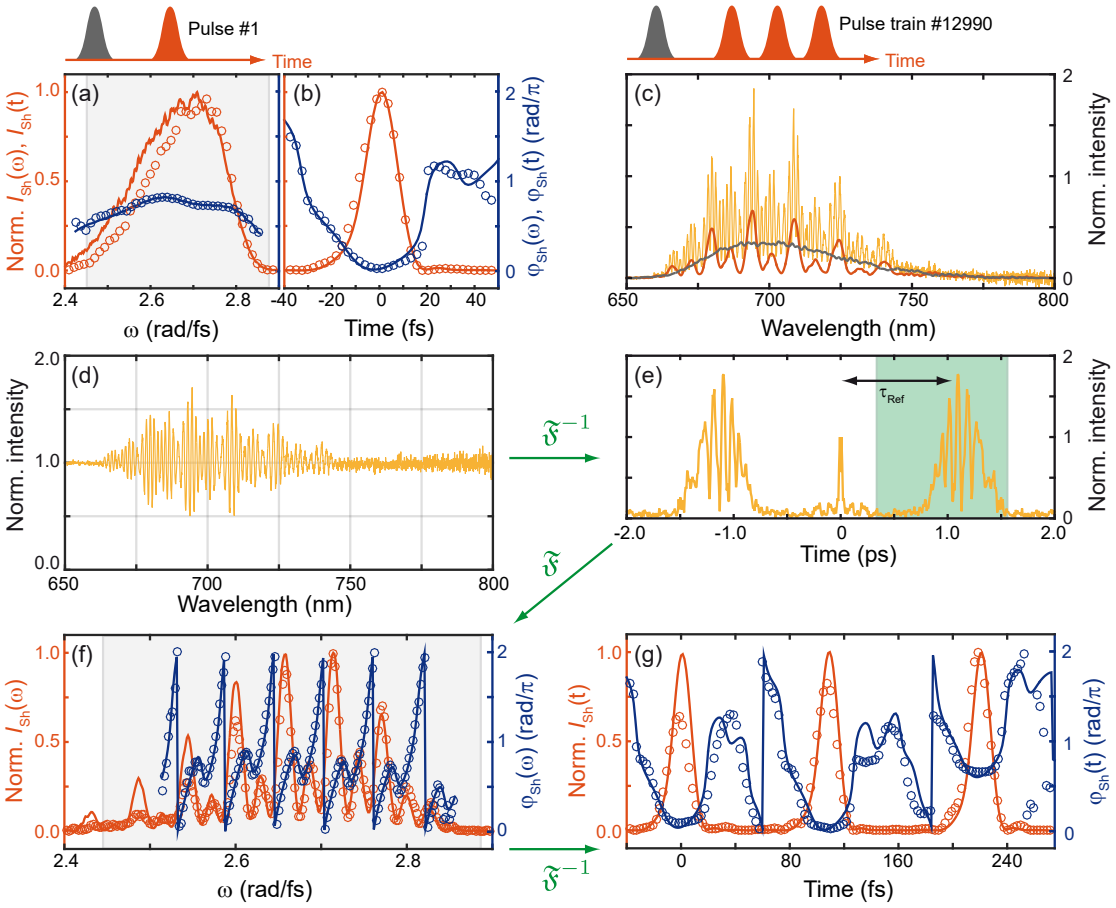

Figure 4.4 – Third step: Automated characterization of 13456 differently shaped pulse sequences. (a) Reconstructed spectral intensity $I_{\mathrm{Sh}}(\omega)$ (orange) and phase $\varphi_{\mathrm{Sh}}(\omega)$ (blue) of the temporally overlapping shaped pulses in measurement step #1 for ideal pulse shaper (lines) and real pulse shaper (circles). (b) Time-domain field after inverse Fourier-transformation (same coding of colors and symbols as in (a). (c–g) Phase-reconstruction steps for an exemplary real pulse shaper sequence (#12990). (c) Measured reference spectrum (gray), shaped spectrum (orange), and spectral-interference spectrum (yellow). (d) Extracted interference term $S(\lambda)$. (e) Signal filtering after inverse discrete Fourier-transformation. The signal around τ_{Ref} is filtered by a rectangular window (green) and Fourier transformed back to the original domain. (f) From this signal, the spectral intensity $I_{\mathrm{Sh}}(\omega)$ (orange) and phase $\varphi_{\mathrm{Sh}}(\omega)$ (blue) are reconstructed for the real pulse shaper (circles) and compared to the corresponding calculated ideal pulse shaper spectral intensity and phase (lines). (g) A final inverse Fourier-transformation reveals the time-domain field (same coding of colors and symbols as in (f)). Adapted with permission from Ref. [2] © Optica Publishing Group.

modulation function that is sent to the pulse shaper while generating the pulse sequence (in this case #12990). The resulting spectrum is then transformed to frequency domain by the Jacobian transformation [251]. The ideal spectral phase is calculated by adding to the resampled spectral phase, retrieved by SHG-FROG of the compressed pulse, the spectral phase modulation function sent to the SLM.

This procedure is automatically applied to all 13456 pulse sequences of the multidimensional spectroscopy experiment discussed in Sec. 4.5. The FTSI reconstruction of general multipulse sequences follows exactly the same steps discussed in Fig. 4.3 for the characterization of the single reference pulse (gray).

Fig. 4.4 (c) depicts the measured (integration time: 100 ms , 3 times averaging, irradiance corrected) reference spectrum (gray), shaped pulse-sequence spectrum (orange), and the superimposed spectral-interference spectrum (yellow). The high-frequency oscillation in the spectral-interference spectrum results from the delay between reference pulse and shaped sequence of $\tau_{\mathrm{Ref}} \approx 1$ ps whereas the superimposed low-frequency oscillation, which is also seen in the shaped spectrum (orange), is related to the specific pulse-sequence delay and phase structure that introduces amplitude modulation via the pulse shaper.

The extracted interference part $S(\lambda)$ shown in Fig. 4.4 (d) is transformed by inverse discrete Fourier-transformation (green arrow). Note that again a calculated time axis is presented for an intuitive understanding of the x-axis as described in detail for the reference-pulse characterization procedure.

The signal contribution around τ_{Ref} is filtered by the same rectangular window function, depicted as green range in Fig. 4.4 (e), as in case of the reference pulse characterization. Since the signal distribution, centered around τ_{Ref}, moves to larger times for increased inter-pulse delays τ, t (compare Fig. 4.4 (c) to Fig. 4.3 (c)), the width of the static window is chosen to cover the whole signal distribution at largest pulse sequence delays. This also takes into account a potential signal-broadening effect [249].

Fourier transforming the filtered signal part back to the original domain gives access to $S^{+}(\lambda)$, and the spectral phase of the shaped sequence $\varphi_{\mathrm{Sh}}(\omega)$ is extracted via

$$\varphi_{\mathrm{Sh}}(\omega) = \arg(S^{+}(\omega) + \varphi_{\mathrm{Ref}}(\omega)) + \omega\tau_{\mathrm{Ref}}. \tag{4.3.4}$$

In contrast to Eq. (4.3.3), now the reference phase is known. The result is plotted in Fig. 4.3 (f) as circles, and the result for the ideal pulse shaper as lines. The (wrapped) spectral phase of the real PS sequence (blue circles) does not show significant deviations with respect to the ideal PS sequence (blue line). The measured intensity spectrum $I_{\mathrm{Sh}}(\omega)$ for real PS (orange circles) and ideal PS (orange line) show slight differences in the maximum intensities, but the spectral position of

the several maxima and minima of the intensity modulation and their individual intensity levels exhibit no significant deviations.

The time-domain structure, depicted in Fig. 4.3 (g), is generated by Fourier transforming (green arrow) the spectral electric field after applying a six-times zero padding. In the real PS sequence, a small global time offset compared to the ideal PS sequence is present. This is due to the determination of the global linear spectral phase $\omega\tau_{\mathrm{Ref}}$ (as described in Eq. (4.3.4)) between the real shaped three-pulse sequence and the reference pulse. The linear fitting is performed on the reconstructed real PS spectral phase within the depicted frequency range (gray range in Fig. 4.3 (f)). In case of the ideal PS the spectral phase is directly calculated based on SHG-FROG as described above.

In general, no pre- or post-pulses are observed at intensity levels $I > 0.05 \cdot I_{\mathrm{max}}$ with I_{max} being the maximum intensity of any of the pulses in the sequence. A deviation of the maximum intensity values of the first two constituent pulses is revealed between real and ideal pulse sequence and discussed in Sec. 4.4. The reconstructed temporal phase discloses almost flat plateaus at different phase values around times of maximum intensity (around 0 fs , 112 fs and 224 fs). The strong increase of $\varphi_{\mathrm{Sh}}(t)$ after the individual plateaus is an indication of residual third-order dispersion leading to the appearance of weak pre-pulses seen in the reconstructed temporal intensity.

4.3.4. Extraction of essential pulse-sequence parameters

In this part, the extraction of pulse-sequence parameters from the time-domain fields is discussed, i.e., starting with the type of information shown in Fig. 4.3 (g), and illustrates the procedure on the example of measurement step #12990 (Fig. 4.5). Here the focus lies on the evaluation of the real PS pulse sequences, but an analogous procedure is carried out for the ideal PS case.

In Fig. 4.5 (a), the intensity $I_{\mathrm{Sh}}(t)$ (red line) and wrapped phase $\varphi_{\mathrm{Sh}}(t)$ (dark blue line) of the reconstructed pulse sequence is depicted as a starting point (obtained by the procedure described in the prefixed sections). To avoid false time-delay evaluations due to weak pre- and post-pulses, the data set is restricted by employing a threshold at 20 % of the maximum intensity, leading to the cut data set (red and blue circles).

As seen in Fig. 4.5 (b), the inter-pulse delays τ, t (light green, dark green) and maximum intensity values $I_{1,2,3}$ (orange marker) are extracted by fitting the cut intensity profile with a sum of three Gaussian functions $f_{\mathrm{TrG}}(t)$ (black),

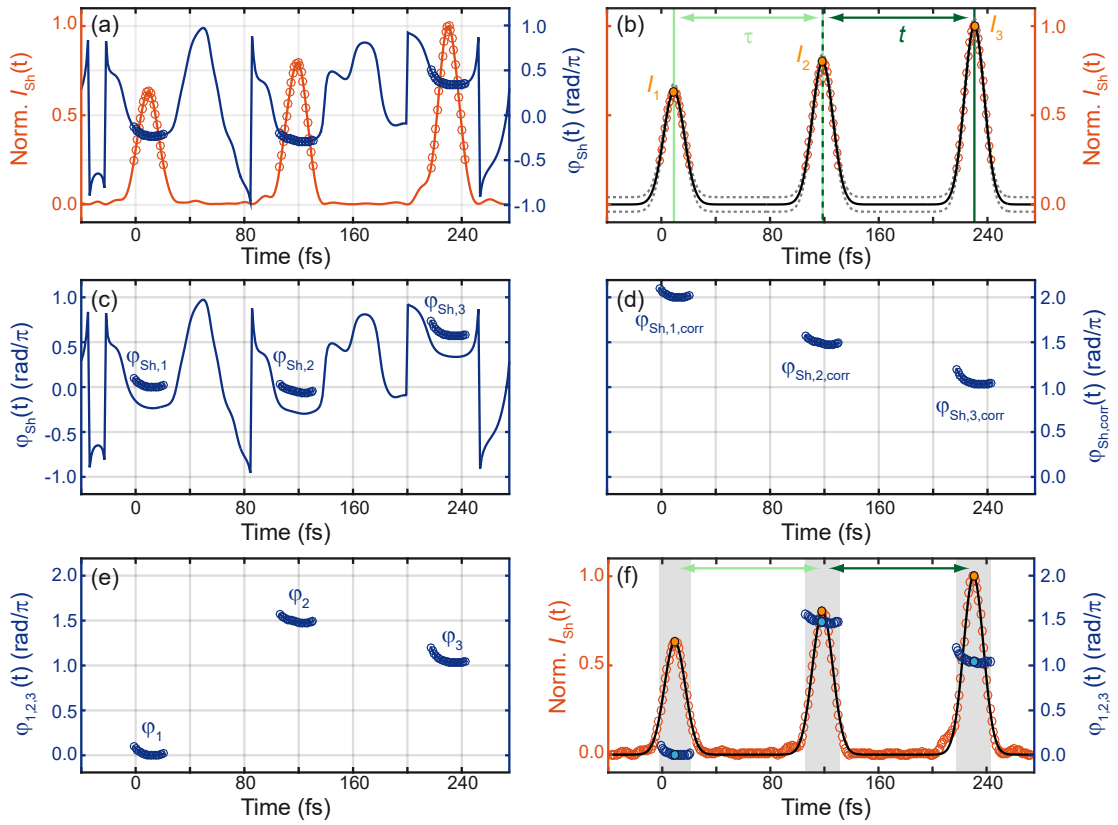

Figure 4.5 – Fourth step: Extraction of pulse-sequence parameters. (a) Reconstructed temporal intensity profile $I_{\mathrm{Sh}}(t)$ (red line) and phase $\varphi_{\mathrm{Sh}}(t)$ (blue line) for a particular three-pulse sequence (#12990). Red circles mark intensity values above 20 % of the maximum intensity. The temporal phase is cut (blue circles) to the same intervals. (b) Experimental data (circles) fitted by a sum of three Gaussian functions (black) and corresponding lower and upper 95 %-confidence bounds (grey dashed lines). The temporal distance between the individual fit maxima defines the delays τ, t (green) and the fit maxima themselves (orange) describe the individual maximum intensity values $I_{1,2,3}$. (c-e) Main post-processing steps to extract the phase offsets $\varphi_{1,2,3}$. (c) Temporal phase $\varphi_{\mathrm{Sh}}(t)$ (blue line) and the three phase cuts (blue circles) after being shifted by a pulse-sequence-specific offset due to referencing of the two pulses at positive times to a zero phase of the first pulse. (d) Corrected temporal phase cuts after removing the delay dependent rotating-frame phase term. (e) Final temporal phase cuts after the last extraction step (see main text). From these phase cuts $\varphi_{1,2,3}(t)$ the phase-cycling step of this pulse sequence is extracted. (f) Summary: $I_{\mathrm{Sh}}(t)$ (red circles) and extracted parameters from the intensity fit (black), namely maximum intensities $I_{1,2,3}$ and delays τ, t. To minimize the phase offset uncertainty due to the not perfectly flat $\varphi_{1,2,3}(t)$, the phase offsets $\varphi_{1,2,3}$ (bright blue) are determined as individual phase-cut value closest to the corresponding $I_{1,2,3}$ (orange). Adapted with permission from Ref. [2] © Optica Publishing Group.

$$f_{\mathrm{TrG}}(t) = I_1 \cdot e^{-4\ln(2)\left(\frac{t-t_1}{\Delta t_1}\right)^2} + I_2 \cdot e^{-4\ln(2)\left(\frac{t-t_2}{\Delta t_2}\right)^2} + I_3 \cdot e^{-4\ln(2)\left(\frac{t-t_3}{\Delta t_3}\right)^2}, \quad (4.3.5)$$

with inter-pulse delays defined as $\tau = t_2 - t_1$, $t = t_3 - t_2$ and individual pulse durations $\Delta t_{1,2,3}$. The gray dashed lines correspond to the lower and upper 95 %-confidence bounds of the fit.

The phase offset values $\varphi_{1,2,3}$ are extracted from the reconstructed temporal phase $\varphi_{\mathrm{Sh}}(t)$ as follows: In a first step, the cut temporal phase is referenced to the first pulse by subtracting from all three temporal phase regimes (blue circles) a global phase offset $\varphi_{\mathrm{Offset}} = \varphi_{\mathrm{Sh}}(t_{\mathrm{Offset}})$, where t_{Offset} is determined by the condition $I(t_{\mathrm{Offset}}) = I_1$. The original uncut temporal phase $\varphi_{\mathrm{Sh}}(t)$ (blue line) and the cut and referenced temporal phases $\varphi_{\mathrm{Sh},1}(t)$, $\varphi_{\mathrm{Sh},2}(t)$ and $\varphi_{\mathrm{Sh},3}(t)$ (blue circles) are depicted in Fig. 4.5 (c).

In a next step, the delay-dependent temporal phase offset, which is imprinted due to the partially rotating frame, is removed from these temporal phases. The benefits of performing a multidimensional spectroscopy experiment in the partially rotating frame are briefly explained in Sec. 4.4. Here the acquired additional temporal phase term is analyzed and how to consider it in the automated evaluation.

For a pulse sequence defined in the fully rotating frame, the individual pulse envelopes are moved in time independently from the underlying carrier oscillation, which remains unchanged, if the inter-pulse time delays τ, t are tuned [190]. To implement this independent control of envelope and carrier oscillation, the pulse shaper generates a delay-dependent phase offset, in addition to the phase-cycling-specific phase offset, depending on the rotating-frame parameter γ which is described in detail by Eq. (2.3.36) in Sec. 2.3.5. In our experiment, γ is set to $\gamma = 0.18$. To remove this additional delay-dependent phase offset from the FTSI data, this term is calculated and added explicitly to the temporal phase of each constituent pulse $\varphi_{\mathrm{Sh},1}(t)$, $\varphi_{\mathrm{Sh},2}(t)$, $\varphi_{\mathrm{Sh},3}(t)$:

$$\varphi_{\mathrm{Sh},1,\mathrm{corr}}(t) = \varphi_{\mathrm{Sh},1}(t), \quad (4.3.6)$$

$$\varphi_{\mathrm{Sh},2,\mathrm{corr}}(t) = \varphi_{\mathrm{Sh},2}(t) + \frac{\omega_0^{'}}{2}(1-\gamma)\cdot\tau, \quad (4.3.7)$$

$$\varphi_{\mathrm{Sh},3,\mathrm{corr}}(t) = \varphi_{\mathrm{Sh},3}(t) + \frac{\omega_0^{'}}{2}(1-\gamma)\cdot(\tau+t). \quad (4.3.8)$$

The delays τ, t used here correspond to the ideal delays and $\omega_0^{'} = \omega_0 + C$ to a modified central frequency with a correction term C, to be explained shortly. The

correct partially rotating-frame offsets depend on the determined central frequency ω_0 of the real pulse sequence, which is calculated by the "center of mass" value in frequency space:

$$\omega_0 = \frac{\sum_i f(\omega_i) \cdot \omega_i}{\sum_i f(\omega_i)}, \tag{4.3.9}$$

with the weighting function $f(\omega_i) = (I(\omega_i) - I_{\min})/I_{\max}$ and spectral components ω_i on the individual spectrometer pixel i. $I(\omega)$ corresponds to the spectral intensity of the unshaped compressed pulse after being transformed by a Jacobi transformation from wavelength to frequency space [251]. The minimum and maximum value of the used spectral intensity in frequency domain is labeled as $I_{\min}$ and $I_{\max}$, respectively. Note that $\omega_0 = 2.6661$ rad/fs, as determined from Eq. (4.3.9), is added by a correction term $C = -0.0029$ rad/fs due to numerical imprecisions in the spectral phase reconstruction process, corresponding to a percentage deviation of the central-frequency of 0.1 %.

In Fig. 4.5 (d) the three temporal phases $\varphi_{\mathrm{Sh},1,\mathrm{corr}}(t)$, $\varphi_{\mathrm{Sh},2,\mathrm{corr}}(t)$, $\varphi_{\mathrm{Sh},3,\mathrm{corr}}(t)$ are displayed after correcting for this partially rotating-frame offset and wrapping the corrected temporal phase values to be in a 0 to 2π range. In a last step, the temporal phases $\varphi_{\mathrm{Sh},1,\mathrm{corr}}(t)$, $\varphi_{\mathrm{Sh},2,\mathrm{corr}}(t)$, $\varphi_{\mathrm{Sh},3,\mathrm{corr}}(t)$ are checked for phase values which are in an interval of 2 ± 0.06 rad/π at the times t of maximum intensity $I_{1,2,3}$ as exemplarily seen for $\varphi_{\mathrm{Sh},1,\mathrm{corr}}(t)$ in Fig. 4.5 (d). If this is the case, the identified temporal phases are wrapped manually by subtracting 2π from the corresponding phase values, here: $\varphi_{\mathrm{Sh},1,\mathrm{corr}}(t)$. The result, seen in Fig. 4.5 (e), shows the temporal phase offsets $\varphi_{1,2,3}(t)$ restoring in this exemplary case phase-cycling step 15 ($\varphi_1 = 0.0$ rad/π, $\varphi_2 = 1.5$ rad/π, $\varphi_3 = 1.0$ rad/π) from the $1 \times 4 \times 4$ phase-cycling scheme.

In Fig. 4.5 (f), the uncut temporal intensity (red circles) together with the extracted parameters are presented. The parameters characterize the reconstructed pulse sequence, namely maximum intensity values $I_{1,2,3}$ (orange circles), inter-pulse delays τ, t (light green, dark green), and the temporal phase offset values $\varphi_{1,2,3}(t)$ (blue circles). For the data analysis presented in Sec. 4.4, the phase offsets $\varphi_{1,2,3}$ (bright blue circles) are defined as the phase values at those times closest to the corresponding maximum intensity values $I_{1,2,3}$.

4.4. Systematic analysis of reconstructed pulse-sequence parameters

So far, a pulse characterization procedure has been introduced and the extraction of physical parameters defining the shaped pulse sequences was exemplarily described. In this section, a systematic comparison between the extracted sequence parameters of the "ideal pulse shaper (PS)" and "real PS" sequences, measured simultaneously to a collinear multidimensional spectroscopy experiment, is demonstrated.

Both inter-pulse time delays τ, t are scanned from 0 to 112 fs and the experiment is performed in a partially rotating frame. This enables us to sample signals at spectral frequencies within the exciting pulse spectrum centered at $\hbar\omega_0 = 1.76$ eV ($\Delta E_{\mathrm{FWHM}} = 0.15$ eV) while using a larger delay increment [153, 252]. In this way, the overall measurement time is reduced. The degree of transformation to the rotating frame is given by the γ parameter, where $\gamma = 0$ corresponds to a fully rotating frame and $\gamma = 1$ to the laboratory frame (see Sec. 2.3.5 for details). In our case, $\gamma = 0.18$ is chosen and the delay increment set to 4 fs to sample signals at spectral frequencies between $0.89 - 1.96$ eV with a resolution of $\delta E = 0.037$ eV [167]. A detailed explanation concerning the sampling range including aliasing effects is given in Sec. 5.8. To extract both rephasing and non-rephasing signal contributions necessary to construct a purely absorptive 2D spectrum, a 16-fold $1 \times 4 \times 4$ phase-cycling scheme is applied [70].

To reconstruct the time-domain structure of all pulse sequences, the intensity spectra of the reference pulse (by blocking the shaped beam), of the current pulse sequence (by blocking the reference beam), and of the superimposed SI spectrum (by opening both shutters) are acquired during each measurement step in an automated fashion. The detailed spectral phase reconstruction steps have been discussed in the previous sections.

Due to the temporal overlap regime of single pulses at inter-pulse delays below 20 fs, and although the FTSI reconstruction works precisely in this range, the sequence parameters can be reliably extracted by fitting only for delays larger than 20 fs. The extracted sequence parameters represent typical three-pulse sequences with τ, $t = 20 - 112$ fs as commonly used in multidimensional spectroscopy experiments. This leads to a data set of 7582 real PS sequences, whose extracted parameters are systematically compared to the ideal PS sequence parameters. The reduced data set corresponds to 56 % of the $29 \times 29 \times 16 = 13456$ different pulse sequences used in the whole experiment. Such a reduction is done here for illustrating in a meaningful and systematic manner the deviations between all real and ideal pulse sequences (see Fig. 4.6). Plotting and comparing the full electric-field

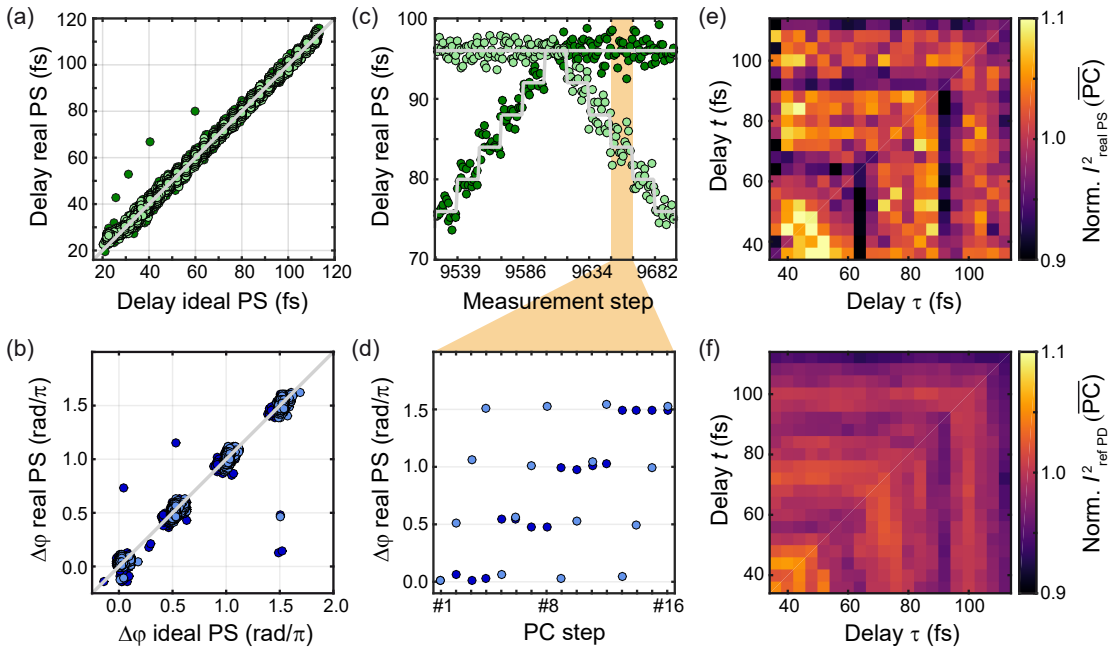

Figure 4.6 – Systematic analysis of reconstructed pulse parameters. (a) Correlation between experimentally determined (real PS) and ideally expected (ideal PS) time delays τ (light green) and t (dark green) for all temporally non-overlapping three-pulse sequences ($\tau, t \geq 24$ fs). The data lining up along the diagonal (gray line) is a sign of good correlation as quantified in the main text. (b) Correlation between experimentally determined (real PS) and ideally expected (ideal PS) relative phases $\Delta\varphi$ of the second ($\Delta\varphi_{12}$, dark blue) and third ($\Delta\varphi_{13}$, light blue) pulse relative to the first one of each sequence. Due to $1 \times 4 \times 4$ phase cycling, the data are clustered around 0 rad/π, 0.5 rad/π, 1.0 rad/π and 1.5 rad/π on the diagonal (gray line). (c) Experimentally determined delays τ (light green) and t (dark green) versus measurement step, exemplarily shown for a subsection out of the full data set. The gray lines show the ideal delay steps. For the 16 measurement steps at constant $\tau = 84$ fs, $t = 96$ fs, highlighted in orange, (d) the experimentally determined relative phases are shown within the 16-step phase-cycling (PC) scheme for the second ($\Delta\varphi_{12}$, dark blue) and third ($\Delta\varphi_{13}$, light blue) pulse, and should ideally fall onto the gray lines. (e) Squared intensity $I^2_{\text{real PS}}$ of the product of the four interacting field amplitudes $\sqrt{I_1} \times \sqrt{I_2} \times \sqrt{I_2} \times \sqrt{I_3} \approx I^2$ of the real pulse sequence for each τ, t delay combination outside of the pulse overlap region. The depicted map is averaged over the 16 phase-cycling steps (PC) and normalized to the mean value of the averaged map, emphasizing deviations. (f) Squared, averaged and normalized linear photodiode signal $I^2_{\text{ref PD}}$ of an unshaped reference pulse measured simultaneously for each measurement step to monitor long-term NOPA intensity drifts. Adapted with permission from Ref. [2] © Optica Publishing Group.

characterization results for several thousand pulse shapes would not have been feasible. However, note that the full characterization results are available, including those for temporally overlapping pulses, and can be used to simulate 2D spectra with real pulse shapes.

In Fig. 4.6 (a) the correlation between the experimentally characterized inter-pulse delays of the real PS sequence and the ideal PS sequence is presented. Both delay values, τ (light green) and t (dark green), accumulate along the diagonal showing very good correlation with Pearson correlation coefficients of $|r|_\tau = 0.99$ and $|r|_t = 0.99$. The four significantly deviating values are due to convergence errors in the automated fitting procedure of the three Gaussian functions and not due to an incorrect pulse sequence shape. Manual fitting of these shapes would remove the error in this plot. Nevertheless, it was decided not to do so here in order to emphasize the fully automated evaluation procedure. Anyway, for accurate simulation of 2D data, the fully characterized and not the fitted fields are employed, such that this deviation is irrelevant.

A similar correlation analysis for the relative inter-pulse phase offset values that are important to validate a correct implementation of the phase-cycling scheme is depicted in Fig. 4.6 (b). For simplicity, this relative inter-pulse phase offset values are in the following referred to as relative phases. Since the phase-cycling phase values are referenced to those of the first pulse in the pulse sequence, the relative phases amount to $\Delta\varphi_{12} = \varphi_2 - \varphi_1$ and $\Delta\varphi_{13} = \varphi_3 - \varphi_1$. Both relative phases, $\Delta\varphi_{12}$ (dark blue) and $\Delta\varphi_{13}$ (light blue), accumulate along the diagonal at 0 rad/π, 0.5 rad/π, 1.0 rad/π, 1.5 rad/π and quantitatively demonstrate the correlation between ideal and real PS sequence with Pearson correlation coefficients of $|r|_{\Delta\varphi_{12}} = 0.99$ and $|r|_{\Delta\varphi_{13}} = 0.99$. The few uncorrelated, isolated measurement points seen in the plot result from induced phase jumps due to the phase ambiguity at zero temporal intensity in the offset phase extraction procedure. Again, the automated extraction has some convergence problems for isolated cases that were not removed manually on purpose, but these are not relevant when using the fully recovered electric field for simulating 2D spectra.

Figure 4.6 (c) depicts the extracted delays from the real PS sequences for one particular section of 175 measurement steps. These steps encode 175 different three-pulse sequences with temporal delays between τ, $t = 76 - 97$ fs, out of the whole multidimensional spectroscopy data set. For measurement steps 9522−9697, the increase of the t delay (dark green) from $t = 76$ fs to $t = 96$ fs in steps of 4 fs is reconstructed while inter-pulse delay τ stays constant at $\tau = 96$ fs. The gray line shows the expected data point evolution from ideal PS sequences. After delay t reaches 96 fs, the τ delay is decreased in 4 fs steps down to $\tau = 76$ fs, while t stays constant at $t = 96$ fs.

This time delay scanning behavior reflects our so-called “quadratic delay scan-

ning scheme". The benefit of this delay scanning scheme is to recreate, in case of unexpected abortion of the experiment, a complete quadratic time map, containing all coherence-time combinations up to the current value, which can be Fourier transformed into a 2D spectrum having the same frequency resolution on both frequency axes. This "quadratic scanning" is preferred to a more conventional approach in which one coherence time is scanned completely for all time steps before proceeding by one time step in the other coherence time.

From a systematic analysis of the extracted delays between ideal and real PS sequence of 7582 measurement steps, root-mean-square deviation (RMSD) between real PS and ideal PS delays of $\tau_{\mathrm{RMSD}} = 1.5$ fs, $t_{\mathrm{RMSD}} = 1.3$ fs are determined, which is below the 4 fs delay increment and for this reason ensures temporal ordering of the constituent pulses outside of the pulse-overlap region. Note that the fit accuracy of the extracted delays τ, t can be quantified from the 95 %-confidence bounds of the absolute times t_1, t_2, t_3 (defined in Eq. (4.3.5)) using Gaussian error propagation. The distribution of the extracted fit accuracies (not shown) exhibits for both delays τ, t a maximum at 0.2 fs and a FWHM of ~ 0.2 fs.

As seen in Fig. 4.6 (c), the adjusted pulse-delay configuration stays unchanged for 16 measurement steps before one delay is either increased or decreased. Over the course of these 16 measurement steps the phase cycling of the pulse sequence is carried out as emphasized by the orange box in Fig. 4.6 (c). The applied $1 \times 4 \times 4$ phase cycling changes the phases of the second and third pulse in four steps of 0.5 rad/π. Their experimental characterization is shown in the zoomed-in region of Fig. 4.6 (d). The reconstructed temporal relative phases $\Delta\varphi_{12}$ (dark blue) and $\Delta\varphi_{13}$ (light blue) for all 16 phase-cycling steps (PC steps) are presented during a certain time delay configuration $\tau = 84$ fs and $t = 96$ fs.

Pulse 3 is first phase-cycled from $\Delta\varphi_{13} = 0$ rad/π to 1.5 rad/π in 0.5 rad/π steps, while the relative phase between pulse 1 and 2, $\Delta\varphi_{12}$, stays constant around 0 rad/π. During phase-cycling (PC) steps 5 to 8, pulse 3 is again phase-cycled from 0 rad/π to 1.5 rad/π, while $\Delta\varphi_{12}$ stays constant around 0.5 rad/π. This procedure is continued until $\Delta\varphi_{12}$ and $\Delta\varphi_{13}$ reach 1.5 rad/π which corresponds to the last PC step. The reconstructed phase-cycling scheme is in qualitative agreement with the expected ideal relative phases (horizontal gray lines) of the $1 \times 4 \times 4$ phase-cycling scheme [70]. The systematic comparison of 7582 relative phases, similar to the exemplary subset from Fig. 4.6 (d), between real PS sequence and ideal PS sequence results in deviations of $\Delta\varphi_{12_{\mathrm{RMSD}}} = 0.19$ rad/π and $\Delta\varphi_{13_{\mathrm{RMSD}}} = 0.08$ rad/π. This quantifies the precision or deviation of the phase-cycling scheme for the real PS sequences.

In a next step, a systematic comparison of the three maximum intensity values is carried out for all reconstructed and fitted real PS sequences with respect to the corresponding ideal PS sequences outside of the pulse overlap region. This reveals

that the maximum intensity of the first pulse is systematically reduced. This effect is quantified by averaging the relative deviations between real PS and ideal PS sequences for the data set, which results in $\overline{\frac{\Delta I_1}{I_1}} = -38$ %. The statistic deviations are determined by the standard deviation of $\overline{\frac{\Delta I_1}{I_1}}$ resulting in $\sigma_{\overline{\frac{\Delta I_1}{I_1}}} = 11$ %. For the maximum intensity of the middle and last pulses, only small systematic deviations $\overline{\frac{\Delta I_2}{I_2}} = -3$ %, $\overline{\frac{\Delta I_3}{I_3}} = -4$ % and, with respect to the first pulse comparable, statistic deviations $\sigma_{\overline{\frac{\Delta I_2}{I_2}}} = 11$ % and $\sigma_{\overline{\frac{\Delta I_3}{I_3}}} = 11$ % are disclosed. No further systematic variations of the individual maximum intensity values $I_{1,2,3}$ are observed.

Finally, the impact of the systematic variations of $I_{1,2,3}$ on the scaling of the (rephasing) signal contribution in a 2D spectrum is investigated. At fourth order in perturbation theory (in the case of population-detected methods), the signal results from four electric-field interactions and scales therefore with $S_{\mathrm{reph}} \propto \sqrt{I_1} \cdot \sqrt{I_2} \cdot \sqrt{I_2} \cdot \sqrt{I_3} \propto I^2$. Note that in our current three-pulse and phase-cycling scheme, the second pulse interacts twice [70]. The I^2 scaling of S_{reph} is analyzed as a function of both delays τ and t resulting in a 2D delay map. The plotted I^2 signal is averaged for each delay combination over all 16 phase-cycling steps and the whole averaged delay map is normalized with respect to its global mean value. Hence, in the ideal case, assuming no $I_{1,2,3}$ variations, one would expect a structureless I^2 delay map of value 1.0.

The experimental results using the maximum intensity values $I_{1,2,3}$ extracted from the real PS sequences are depicted in Fig. 4.6 (e). Since the extraction of maximum intensity crucially depends on the uniqueness of the three Gaussian fits, our analysis is restricted further to pulse delays $\tau, t \geq 36$ fs to avoid interference effects of temporally overlapping pulses. The deviation from the ideal case scenario is seen in Fig. 4.6 (e) and quantified by an overall root-mean-square fluctuation of $I^2_{\mathrm{real\ PS_{RMSD}}} = 5$ %. Note that the graphical representation emphasizes deviations because the color range extends only from 0.9 to 1.1. The fluctuation exhibits a delay-related systematic, especially at delays $\tau, t = 64$ fs and $\tau, t = 92$ fs (decreased $I^2_{\mathrm{real\ PS}}$) as well as $\tau, t = 48$ fs and $\tau, t = 100$ fs (increased $I^2_{\mathrm{real\ PS}}$).

To investigate the origin of the systematic deviations of Fig. 4.6 (e), the pulse energy of the unshaped pulse is monitored simultaneously with the SI measurements and the multidimensional spectroscopy experiment, using a linear photodiode (PD) as an integrating detector. Due to the long integration time of our photoemission electron microscope (Elmitec, AC-PEEM) [1], the overall measurement time of this particular experiment is ~ 67 h and as a consequence prone to long-term pulse-energy drifts of the NOPA system.

This raises the question if the deviations of Fig. 4.6 (e) result from NOPA drifts of the input beam rather than systematic pulse-shaping variations of $I_{1,2,3}$.

For comparison, the photodiode reference measurement is presented in Fig. 4.6 (f). To generate this map, the squared pulse energy of the unshaped reference pulse is plotted for the same delay combinations and phase-cycling steps as in Fig. 4.6 (e), again averaged over the 16 phase-cycling steps, normalized as described above, and plotted in the same color bar range. Figure 4.6 (f) reveals analogous scaling fluctuations around the ideal case value of $I^2_{\text{ref PD}} = 1.0$. Comparing Fig. 4.6 (e) and (f) shows that the overall scale of the fluctuation of the reference pulse, $I^2_{\text{ref PD}_{\text{RMSD}}} = 2$ %, is smaller than that observed in the SI-extracted data, $I^2_{\text{real PS}_{\text{RMSD}}} = 5$ %, and that the deviation from 1.0 slowly decreases for larger delays. However, the delay-related systematics are very similar in both maps. As seen from this comparison the deviations observed in Fig. 4.6 (e) are mainly caused by long-term pulse-energy drifts of the NOPA system and not by systematic pulse-shaper imperfections.

In summary, this section analyzed and quantified the pulse-shaping precision of three-pulse sequences with respect to specific parameters that are relevant in 2D spectroscopy and compared real and ideal pulse-shaping behavior systematically for a full data set of time delay and relative phase variations. The impact of deviations from the ideal case on simulated 2D spectra is investigated in the next section.

4.5. Effect of the complete reconstructed multipulse sequence on simulated 2D spectra

To investigate whether deviations in time delays, relative phases, and maximum intensities of the real PS sequence, as quantified in Fig. 4.6, influence the 2D spectrum in population-based collinear multidimensional spectroscopy, purely absorptive 2D spectra are simulated while using the experimentally characterized electric fields for each scanning step as simulation input.

The collective system response after optical excitation is described by a density-matrix approach whose full time evolution was given by the Lindblad quantum master-equation, taking into account system–bath interactions like decoherence and dissipation as introduced in Sec. 2.4. Solving this equation enables the determination of the off-diagonal elements of the density matrix ρ, known as system coherences, as well as of diagonal elements corresponding to the populations of the system. For illustration, a notional system is chosen but typical simulation parameters for molecular pure-dephasing times [253] and coupling strength [254] are employed to model, in a first example, the fluorescence emission of a homogeneous molecular dimer.

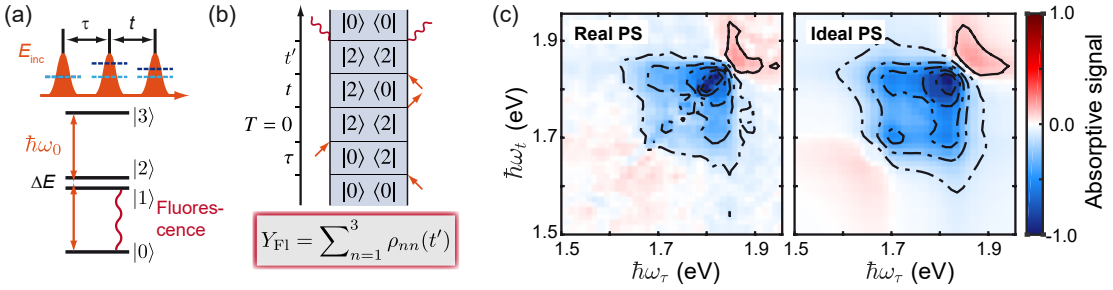

Figure 4.7 – Simulated nonlinear fluorescence 2D spectra with real and ideal pulse sequences. (a) Three-pulse excitation sequence E_{inc} (red) and quantum four-level system, modeling fluorescence from a molecular dimer. The energy distance between the ground-state level $|0\rangle$ and the doubly excited level $|3\rangle$ is $2\hbar\omega_0$ with ω_0 describing the center frequency of the incoming pulse sequence E_{inc}. The two singly excited levels $|1\rangle$ and $|2\rangle$ exhibit a Davydov splitting of ΔE (detailed description see main text). (b) Exemplary double-sided Feynman diagram (DSFD) illustrating a rephasing pathway. To simulate 2D spectra, the fluorescence yield Y_{Fl} is calculated by summing over excited-state populations. (c) Simulated absorptive 2D spectra (real parts) using experimentally determined fields for each scanning step (Real PS) or idealized pulse sequences (Ideal PS). Adapted with permission from Ref. [2] © Optica Publishing Group.

In Fig. 4.7 (a) the simulated level scheme of the dimer in the exciton basis is depicted [255]. The energy difference between the ground-state level $|0\rangle$ and the two-exciton state $|3\rangle$ (with both molecules simultaneously excited), was chosen in this example as $2\hbar\omega_0$, with $\hbar\omega_0 = 1.755$ eV and central frequency $\omega_0 = 2.67$ fs^{-1} of the exciting three-pulse sequence (red). The one-exciton states $|1\rangle$ and $|2\rangle$ describe superpositions of one molecule in the ground state and the other molecule in the excited state. The symmetric Davydov energy-splitting around $\hbar\omega_0$ is modelled by $-\Delta E/2$ and $+\Delta E/2$, where ΔE is related to the coupling strength between the individual molecules [255]. Note that the coupling strength is defined such that the resulting Davydov splitting ΔE is within the spectral width ($\Delta E_{\mathrm{FWHM}} = 150$ meV) of our unshaped pulse spectrum. The individual transition dipole moments, pure-dephasing and dissipation times defining the system are given in Sec. 4.6. Since the fluorescence signal decays on a nanosecond time scale, which is much larger than the summed maximum delays (≈ 250 fs) of the exciting pulse sequence, an infinite dissipation time for the $|1\rangle \rightarrow |0\rangle$ transition was chosen.

2D spectra are calculated using the experimentally characterized electric fields E_{inc} (red), for each scanning step at corresponding time delays τ, t and relative

phases (blue dashed) corresponding to the $1 \times 4 \times 4$ phase-cycling scheme as displayed in Fig. 4.7 (a). Extraction of, e.g., the rephasing signal contribution (or others) via phase-cycling allows us to monitor the temporal evolution of the system via different pathways through the various states of the density matrix. These different pathways can be visualized by DSFDs, of which an exemplary one is depicted in Fig. 4.7 (b) for one particular rephasing pathway. DSFDs can be analogously derived for non-rephasing and other signal contributions.

To calculate the fluorescence yield Y_{Fl} (red) of the molecular-dimer system, the time-domain electric fields from either the reconstructed real PS pulse sequence or the ideal PS pulse sequence are used as exciting fields and the density matrix $\rho(t)$ is propagated by the Lindblad equation [155]. The detection signal Y_{Fl} is defined by summing over the excited-state populations of the density matrix $\rho(t')$ after time $t' \gg \tau + T + t$ as shown in Fig. 4.7 (b). Since a three-pulse basis is utilized, the population time is $T = 0$ fs. Finally, the presented absorptive spectrum is obtained by adding the real part of the rephasing and non-rephasing spectra after inverting the sign of the ω_τ axis for the rephasing spectrum [167].

In previous work, pulse-shaper imperfections had to be taken into account in fluorescence-detected two-dimensional micro-spectroscopy and time-domain artifacts were corrected by subtracting low-excitation-power time-domain maps from high-excitation-power maps before phase cycling [207]. Here, the impact of pulse-shaper imperfections by explicit measurement of all involved electric fields is analyzed.

A detailed description of the simulation procedure of fluorescence detected 2D spectra is given in Sec. 4.6. It should be noted here, that a significant signal contribution along the diagonal of the simulated rephasing time-domain map is observed as depicted in Fig. 4.9, similar to the time-domain artifact discussed in aforementioned experimental data [207], using either the ideal PS reconstructed or real PS reconstructed pulse sequences. The amplitude of this "diagonal artifact" is significantly increased in case of the real PS sequences. On that account, our simulation results are corrected following the earlier approach [207] as described in detail in Sec. 4.6. The rephasing and non-rephasing contributions are then extracted by the corresponding phase-cycling scheme, followed by 2D Fourier transformation.

Figure 4.7 (c) presents the corrected purely absorptive spectrum using the reconstructed time-domain structure of the real PS (left) and the ideal PS pulse sequences (right). The corresponding rephasing and non-rephasing 2D spectra and corrected time-domain maps can be found in App. D, respectively. Both absorptive spectra show the same characteristic features like diagonal and off-diagonal peak positions, line shapes and relative signal amplitudes. The position of the diagonal peaks correlates with the eigenenergies of the one-exciton states $|1\rangle$ and $|2\rangle$ (see Sec. 4.6) and the energy difference between the diagonal peaks of the here simu-

lated homogeneous dimer system corresponds to the Davydov splitting ΔE. The off-diagonal peaks appear due to the nonzero exitonic coupling $J = \Delta E/2$ between the one-exciton states $|1\rangle$ and $|2\rangle$ [255]. The small signal distortion along the diagonal in the Real PS spectrum originates from a small leftover of the time-domain artifact (see Fig. 4.9) resulting from the small pulse-shaper imperfections quantified in Fig. 4.6. The dominating negative sign of the absorptive signal within the spectral region covered by the laser pulse spectrum ($\Delta E = 1.63 - 1.86$ eV foot-to-foot) reflects the dominating fourth-order field interaction with the corresponding sign in the perturbation expansion (see Eq. (2.3.21) and Eq. (2.3.24)).

Note that the small deviations between the real and ideal PS sequences do not significantly change the features in the obtained corrected 2D spectra. It is true from this study that the small deviations of the real PS sequences discussed in Sec. 4.4 lead to increased time-domain artifacts which affect the resulting 2D spectrum. However, these distortional effects can be sufficiently minimized by a "high-minus-low excitation-power" correction, which in turn facilitates the correct interpretation of the resulting 2D spectrum. Nonetheless, if one desires to simulate experimental data as accurately as possible, one can use the fully characterized fields as an input to 2D simulations, potentially along with corrections for *geometric* signal distortion [232–235].

As a second example, the impact of experimentally characterized pulse sequences on electron photoemission experiments is analyzed, as depicted in Fig. 4.8. The sample-dependent work function is chosen to be significantly larger than the energy of the interacting photons $\hbar\omega_0 = 1.755$ eV, thus making multiphoton photoemission the detection signal.

The efficiency of multiphoton photoemission is in general lower compared to single-photon photoemission. The latter can be realized using a separate ionization pulse at sufficiently high photon energy or work-function reduction via Cs evaporation [256]. Here multiphoton photoemission is investigated because the relevant interaction order is higher in nonlinearity than in the case of the fluorescence example, providing a qualitatively different response. In particular, nonlinear photoelectron emission, as depicted in Fig. 4.8 (a, green), from a plasmonic Au nanoslit sample is simulated, which was previously investigated [6], after optical excitation with the same experimentally determined fields $E_{\mathrm{inc}}(t')$ as in the first example.

The work function of gold varies between $4.6 - 5.6$ eV depending on the crystallographic surface orientation and the amount of carbon coverage [42]. Due to strong plasmonic field enhancement [145, 257] of $E_{\mathrm{loc}}(t')$, the possibility of multiphoton photoemission at high nonlinear order $N > 3$ is significantly increased [6] meaning that at photon energies of $\hbar\omega_0 = 1.755$ eV six or more field interactions

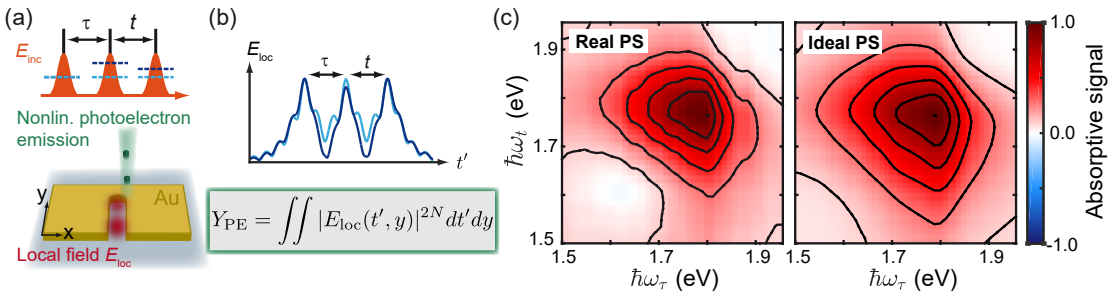

Figure 4.8 – Simulated multiphoton electron emission 2D spectra with real and ideal pulse sequences. (a) The same exciting three-pulse sequences $E_{\mathrm{inc}}(t')$ as for the simulations in Fig. 4.7 were used to simulate nonlinear photoemission (green) 2D spectra for a plasmonic gold nanoslit sample. (b) The local electric field $E_{\mathrm{loc}}(t')$, generated by $E_{\mathrm{inc}}(t')$, depends on the actual time delays and phases and consequently alters the nonlinear photoemission yield Y_{PE}. The nonlinearity is set to $N = 4.2$ corresponding to a dominating four-photon photoemission process. (c) Simulated absorptive 2D spectra (real parts) obtained from Y_{PE} using experimentally determined fields for each scanning step (Real PS) or idealized pulse sequences (Ideal PS). Adapted with permission from Ref. [2] © Optica Publishing Group.

take place to generate photoemitted electrons via at least a three-photon process.

The spatially resolved response function of the plasmonic nanoslit, which is retrieved from FDTD simulations (FDTD Solutions, Lumerical Inc.), enables the calculation of the local electric field $E_{\mathrm{loc}}(t')$ [6]. Figure 4.8 (b) exemplarily shows the resulting momentary local electric field $E_{\mathrm{loc}}(t')$ using an idealized spectral response $R(\omega)$ modeled by two Lorentzians motivated by Sec. 2.3.4

$$R(\omega) = A_1 \frac{\frac{\Delta_1}{2}\pi}{(\omega-\omega_1)^2 + (\frac{\Delta_1}{2})^2} + A_2 \frac{\frac{\Delta_2}{2}\pi}{(\omega-\omega_2)^2 + (\frac{\Delta_2}{2})^2}, \tag{4.5.1}$$

with idealized response parameters: amplitude $A_1 = 5$, $A_2 = 60$ (arbitrary units), spectral widths $\Delta_1 = 0.02$ fs^{-1}, $\Delta_2 = 0.05$ fs^{-1} (FWHM), and individual resonance frequencies $\omega_1 = \omega_0 - 0.08$ fs^{-1}, $\omega_2 = \omega_0 + 0.1$ fs^{-1} with respect to the central frequency $\omega_0 = 2.67$ fs^{-1} of the excitation pulse sequence. For calculating $E_{\mathrm{loc}}(t')$ (see Eq. (2.2.10)), as depicted in Fig. 4.8 (b), the response $R(\omega)$ is normalized with respect to its maximum value and two excitation pulse sequences at two consecutive phase-cycling steps (light and dark blue) and at one particular time-delay combination τ, t are applied.

The nonlinear local photoemission yield is defined by Eq. (2.2.11) as the time-integrated local intensity to the power of N. The measured, spatially resolved, power-law dependence of the local photoemission yield was fitted with an $N = 4.2$

dependence (not shown). Thus, the PEEM yield depends on the fourth power of the excitation pulse intensity hence suggesting that the photoemission process is dominated by a four-photon process. The same order of nonlinearity N has been used in our simulation to model photoemission. The nonlinear photoemission detection signal Y_{PE} is calculated for each pulse sequence separately. Y_{PE} corresponds to the time-integrated nonlinear local photoemission yield, which in a last evaluation step is spatially integrated along the long slit axis covering only the local electric field spot at the open-end termination (shaded red in Fig. 4.8 (a)) within the nanoslit.

Fig. 4.8 (c) presents the simulated absorptive 2D spectra for the experimentally determined (left) and the ideal sequence (right). The absorptive spectra are obtained, just as described for the fluorescence example, from the corresponding rephasing and non-rephasing spectra. The positive sign of the signal in the absorptive spectra can be explained by a dominating signal contribution resulting from higher perturbation order, compared to the case of the fluorescence signal simulations, e.g., eight electric-field interactions. Note that in contrast to the fluorescence 2D spectra simulations, it is not necessary to perform the "high-minus-low excitation-power" correction procedure, because no signal contribution along the diagonal of the rephasing time-domain map is seen (see App. D).

Both spectra depicted in Fig. 4.8 (c) display the same triangular-shaped signal with a maximum around the central frequency of the pulse spectrum corresponding to $\hbar\omega_0 = 1.755$ eV. The small deviations between the real and the ideal pulse sequences, quantified in Sec. 4.4 and Fig. 4.6, do not significantly influence the resulting absorptive spectra in this example. Minor variations are visible in the rephasing and non-rephasing spectra as reported in App. D. Note that the slightly smaller 2D line shape in case of the real PS as compared to the ideal case results from a slower decay along τ, t of the time-domain signal depicted in Fig. D.1 (e) and (f). This slower decay of the time-domain signal might in fact be related to the quantified small deviations of the inter-pulse delays ($\tau_{\mathrm{RMSD}} = 1.5$ fs, $t_{\mathrm{RMSD}} = 1.3$ fs) between the real and ideal PS.

Hence, the impact of signal artifacts due to non-perfect pulse shaping is decreased as compared to the fluorescence case (for which the described power correction procedure has been carried out). The improved robustness against pulse-shaper imperfections results if the detection signal is dominated by signal contributions from higher-order interactions. In this case, the enhanced nonlinear scaling of the sample signal contribution with respect to the optical exciting fields dominates more easily the systematics of the phase-cycled time-domain maps, whereas the diagonal signal artifact, due to pulse shaper imperfections, is strongly suppressed (see Sec. 4.6). This decreased sensitivity to imperfect pulse shaping is especially beneficial for multiphoton photoemission spectroscopy [1] or multiphoton coherent

two-dimensional electronic mass spectrometry [163].

In the present particular example and implementation, ideal and real pulse sequences are quite similar which is a sign of the stability of the experiment and validity of the pulse-shaper design and calibration procedure. However, depending on the particular setup, wavelength regime, investigated quantum system, scanning range, data acquisition procedure and many other parameters, the outcome of such a pulse-shape analysis might be different and the deviations might be more severe. Examples for origins of imperfections are: pointing fluctuations of the laser that might lead to intensity fluctuations at the sample and time–frequency shifts after wavelength conversion; fluctuations of the spectral intensity and phase of the laser source; unstable frequency conversion in NOPA, hollow-core fiber or other filamentation processes; temperature variations at the pulse-shaper element leading to drifts in the generated pulse shapes; unintended pulse-shape modifications when approaching the available "maximum time window" of the pulse shaper; effects of space–time coupling on the pulse structure depending on the optical resolution versus pixel size of the pulse-shaper element; and other effects.

In general, the magnitude and relevance of such deviations for 2D spectra and particular signal contributions is not known beforehand. The presented method characterizes all deviations experimentally, taking into account all sources of deviation within one procedure. In both investigated cases of fluorescence or photoelectron emission, and also in other measurement modalities using either population-based or coherent-field detection, it is possible to use the fully characterized electric fields of each data acquisition scanning step to calculate 2D spectra with the precise experimental pulse shapes. This facilitates a direct comparison between theory and experiment.

4.6. Simulation of phase-cycled 2D time-domain maps

Simulations of phase-cycled 2D time-domain maps are performed using both the reconstructed real PS and the ideal PS sequences. Based on the corresponding uncut reconstructed temporal intensity $I^j_{\mathrm{Sh}}(t)$ and phase $\varphi^j_{\mathrm{Sh}}(t)$, corresponding to the exemplary data shown in Fig. 4.4 (g), the optical excitation is modeled by the real-valued electric field $E^j_{\mathrm{inc}}(t)$ for a certain measurement step j defined as

$$E^j_{\mathrm{inc}}(t) = \frac{A}{2}\sqrt{\frac{I^j_{\mathrm{Sh}}(t)}{I^1_{\mathrm{Sh,\,max}}(t)}}\mathrm{e}^{i\omega_0 t - i\varphi^j_{\mathrm{Sh}}(t)} + \mathrm{c.c.}, \tag{4.6.1}$$

and normalized to the maximum field value $I^1_{\mathrm{Sh,\,max}}(t)$ of the fully overlapping

pulse sequence at the first phase-cycling step. A is an amplitude scaling factor that is adjusted in case of the fluorescence simulations such that for optical excitation with the fully overlapping pulse sequence at the first phase-cycling step, $I^{1}_{\mathrm{Sh,\,max}}(t)$, a maximum of 10 % depopulation of the molecular dimer ground-state occurs during the whole simulation process. For this condition an amplitude scaling factor of $A = 2.7 \times 10^{-4}$ atomic units (a.u.) is determined. In case of the FDTD-based simulations of multiphoton photoemission, A is set to $A = 1$.

To simulate the fluorescence signal for the molecular dimer, discussed in the main manuscript, the Lindblad quantum master-equation [155] is numerically solved,

$$\frac{\partial \rho(t)}{\partial t} = -\frac{i}{\hbar}\Big[\hat{\mathrm{H}}^{j}(t), \rho(t)\Big] + \sum_{k} \frac{1}{T_k}\Big(\mathcal{L}_k \rho(t) \mathcal{L}_k^{\dagger} - \frac{1}{2}\mathcal{L}_k^{\dagger}\mathcal{L}_k \rho(t) - \frac{1}{2}\rho(t)\mathcal{L}_k^{\dagger}\mathcal{L}_k\Big), \quad (4.6.2)$$

for the time evolution of the density matrix $\rho(t)$, in which certain Lindblad terms for each transition k consider population-relaxation and pure-dephasing effects via Lindblad operators $\mathcal{L}_k \in \{\mathcal{L}_k^{\mathrm{rel}}, \mathcal{L}_k^{\mathrm{deph}}\}$ and individual time constants $T_k \in \{T_{1,k}, T^{*}_{2,k}\}$, respectively.

The Hamilton operator $\hat{\mathrm{H}}^{j}(t) = \hat{\mathrm{H}}_0 + \hat{\mathrm{H}}^{j}_{\mathrm{int}}(t)$ consists of a time-independent part $\hat{\mathrm{H}}_0$ describing the homogeneous molecular-dimer system in the exciton basis as seen in Fig. 4.7 (a),

$$\hat{\mathrm{H}}_0 = 0\,|0\rangle\langle 0| + \left(\hbar\omega_0 - \frac{\Delta E}{2}\right)|1\rangle\langle 1| + \left(\hbar\omega_0 + \frac{\Delta E}{2}\right)|2\rangle\langle 2| + 2\hbar\omega_0\,|3\rangle\langle 3|\,, \quad (4.6.3)$$

and a time-dependent part $\hat{\mathrm{H}}^{j}_{\mathrm{int}}(t)$ taking into account the interaction with the optical excitation field $E^{j}_{\mathrm{inc}}(t)$ at measurement step j via

$$\hat{\mathrm{H}}^{j}_{\mathrm{int}}(t) = E^{j}_{\mathrm{inc}}(t) \cdot \sum_{m \neq n} \gamma_{mn}\Big(|m\rangle\langle n| + |n\rangle\langle m|\Big). \quad (4.6.4)$$

Here, γ_{mn} corresponds to the transition dipole element between the electronic states $|m\rangle$ and $|n\rangle$, with values: $\gamma_{31} = 1$ a.u. (atomic units) and $\gamma_{20} = 1$ a.u. for the $|1\rangle \leftrightarrow |3\rangle$ and $|0\rangle \leftrightarrow |2\rangle$ transitions whereas the transition dipole moments for the $|2\rangle \leftrightarrow |3\rangle$ and $|0\rangle \leftrightarrow |1\rangle$ transitions are slightly decreased to $\gamma_{32} = 0.9$ a.u. and $\gamma_{10} = 0.9$ a.u., respectively.

The individual time constants T_k for the dissipative and dephasing terms are set as follows: The simulated pure-dephasing times T_2^{*} are defined by $T_2^{*} = 100$ fs for the $|2\rangle \rightarrow |1\rangle$ transition, $T_2^{*} = 30$ fs for the $|3\rangle \rightarrow |0\rangle$ transition and $T_2^{*} = 60$ fs for all remaining transitions. To model the fluorescence emission process,

the dissipation time T_1 of the $|1\rangle \rightarrow |0\rangle$ transition is set to be infinite and the dissipation times for all other transitions is chosen to be $T_1 = 100$ fs.

Equation 4.6.2 is solved taking into account the excitation field $E^j_{\mathrm{inc}}(t)$ for each measurement step j (see Eq. (4.6.1)) and the fluorescence Y_{Fl} is calculated by summing over the non-ground-state populations

$$Y_{\mathrm{Fl}} = \sum_{n=1}^{3} \rho_{nn}(t'), \tag{4.6.5}$$

with the selected detection time $t' = 500$ fs ensuring that t' is larger than the summed pulse sequence delays, $t' > \tau + T + t$. Y_{Fl} is calculated for each delay combination and every phase-cycling step of our 16-fold phase-cycling scheme ($1 \times 4 \times 4$). As a result, 16 different time-domain maps are obtained $T_i(\tau, t)$ with phase-cycling index i.

To apply phase cycling, these time maps are multiplied by their individual weighting factors $w_i(\beta, \gamma, \Delta\varphi^i_{12}, \Delta\varphi^i_{13})$ depending on the chosen signal-contribution parameters β, γ , e.g., $\beta = 2, \gamma = -1$ for rephasing or $\beta = 0, \gamma = -1$ for non-rephasing (see Sec. 2.3.5 or [70] for details), and the relative phases $\Delta\varphi^i_{12}, \Delta\varphi^i_{13}$ are taken into account as analyzed in Sec. 4.4. Consequently, a phase-cycled time-domain map $T_{\mathrm{PC}}(\tau, t)$ is given by

$$T_{\mathrm{PC}}(\tau, t) = \frac{\sum_{i=1}^{16} T_i(\tau, t) w_i(\beta, \gamma, \Delta\varphi^i_{12}, \Delta\varphi^i_{13})}{1 \times 4 \times 4}, \tag{4.6.6}$$

with weighting factors determined by $w_i(\beta, \gamma, \Delta\varphi^i_{12}, \Delta\varphi^i_{13}) = \mathrm{e}^{-i(\beta\Delta\varphi^i_{12} + \gamma\Delta\varphi^i_{13})}$.

In case of the simulated molecular dimer fluorescence, the resulting rephasing time-domain map $T_{\mathrm{PC}}(\tau, t)$ exhibits for both the real PS pulse sequences (Real PS, Fig. 4.9 (a)) and the ideal PS pulse sequences (Ideal PS, Fig. 4.9 (b)) an unexpected signal contribution along the diagonal. Note that the absolute signal amplitude of this "diagonal artifact" in the rephasing time-domain map is significantly increased if the real PS pulse sequences are used as compared to the ideal PS case. As a result, the signal pattern seen in Fig. 4.9 (b) for small delays $\tau, t < 50$ fs , which is referred to as the nonlinear-response signal, is not observed in Fig. 4.9 (a).

In general, a reliable separation of the nonlinear response from the linear signal contribution has to be ensured. In collinear excitation geometries, this can be achieved with phase cycling. In order for this to work, the nonlinear signal needs to be above a certain signal level [207] such that the dynamic range of the detector is sufficient at a given signal-to-noise level. Here the separation between the nonlinear response signal and the "diagonal artifact" in the rephasing time-domain map is obtained at a certain optical excitation amplitude by simulating the fluorescence signal for different values of A in Eq. (4.6.1).

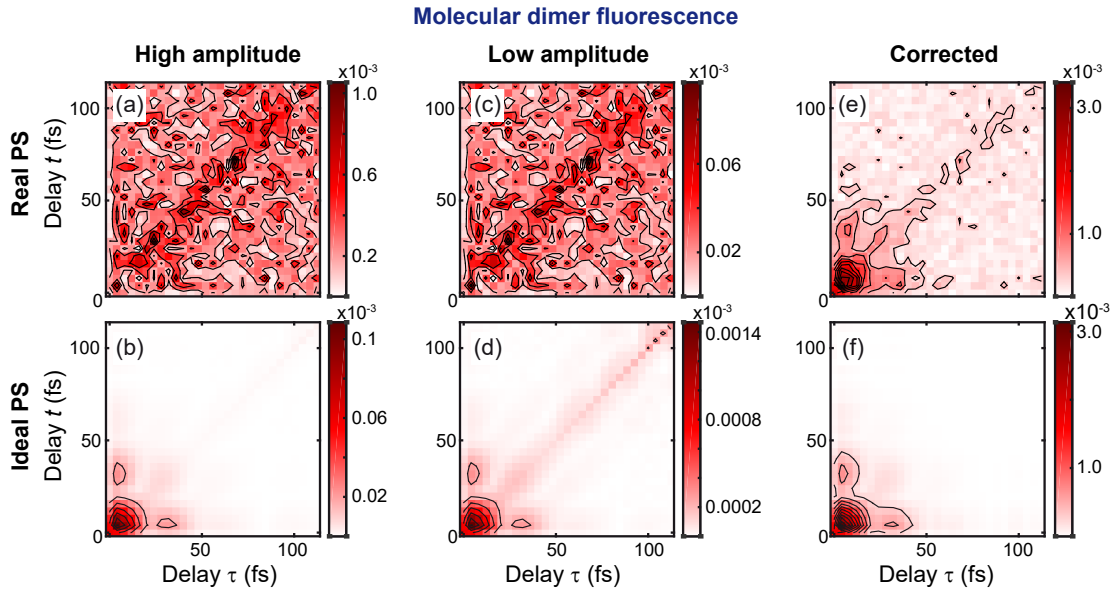

Figure 4.9 – High amplitude and low amplitude simulated rephasing time-domain maps for nonlinear signal separation. (a) Real pulse shaper (PS) and (b) ideal PS rephasing time-domain maps at optical excitation amplitude $A = 2.7 \times 10^{-4}$ a.u. corresponding to 10 % ground-state depopulation. (c) Real PS and (d) ideal PS rephasing time-domain maps as in (a) and (b) but with lower optical excitation amplitude $A = 8 \times 10^{-5}$ a.u. corresponding to 1 % ground-state depopulation. (e) Real PS and (f) ideal PS rephasing time-domain maps after performing the correction procedure described in the text. Adapted with permission from Ref. [2] © Optica Publishing Group.

In the case of small A , i.e., only very weak perturbation of the system by an optical excitation, the nonlinear response is either strongly decreased due to its nonlinear scaling with the excitation amplitude A or it is not visible at all in the phase-cycled time-domain map. Comparing with results obtained for larger A allows separation of the different contributions. Contributions with linear scaling between the high-amplitude and the low-amplitude phase-cycled time-domain map can be identified as signal artifacts introduced, e.g., by the imperfections in the pulse-sequence generation quantified in Sec. 4.4.

In Fig. 4.9 (c) and (d) the same simulations as in Fig. 4.9 (a) and (b) are presented using a reduced overall excitation field amplitude $A = 8 \times 10^{-5}$ a.u. (see Eq. (4.6.1)) for the real PS and ideal PS pulse sequences without changing the time-domain structure of the pulse sequences. In case of the low-field-amplitude excitation (column “Low amplitude” in Fig. 4.9), the ground state is depopu-

lated by only 1 % of its initial population corresponding to a regime of weak perturbation, whereas the ground state is depopulated by 10 % in the high-field-amplitude case with $A = 2.7 \times 10^{-4}$ a.u. (column "High amplitude" in Fig. 4.9). Note that a diagonal artifact is observed in all cases, i.e., "High-amplitude" and "Low-amplitude" for both real PS and ideal PS, but in varying magnitudes. For the real PS map at low amplitude (Fig. 4.9 (c)), the absolute signal is decreased to about 10 % of the High-amplitude map signal (Fig. 4.9 (a)), whereas for the ideal PS map with the reduced optical excitation amplitude A (Fig. 4.9 (d)), the absolute signal decreases much stronger to about 0.01 % of the high-amplitude map (Fig. 4.9 (c)). This is already a first indication of a different scaling behavior of the dominating signals between real PS and ideal PS time-domain maps.

The high-amplitude map for the real PS (Fig. 4.9 (a)) is still dominated by the diagonal artifact and the nonlinear-response signal cannot be distinguished. In case of the ideal PS high-amplitude map (Fig. 4.9 (b)) the diagonal artifact is strongly decreased compared to the real PS high-amplitude map (Fig. 4.9 (a)) and the nonlinear-response signal dominates over the diagonal artifact. Comparing the ideal PS low-amplitude map (Fig. 4.9 (d)) and the ideal PS high-amplitude map (Fig. 4.9 (b)) reveals that the nonlinear signal is reduced but still visible and that the diagonal artifact relative to the nonlinear signal is increased. As a result, a different signal scaling with respect to excitation amplitude of these two signals is observed and verifies our signal assignment.

The fact that a diagonal artifact is observed at all in the phase-cycled ideal PS maps indicates that besides an imperfect pulse-sequence generation also the asymmetric spectrum or a not perfectly flat spectral or temporal phase might lead to the observed diagonal signal which has to be investigated systematically but is beyond the scope of this thesis.

This diagonal artifact significantly influences the 2D spectra obtained after 2D Fourier transformation of the rephasing time-domain map. The different excitation amplitude scaling of the nonlinear response signal and the diagonal artifact allows an extraction of the nonlinear signal. To correct our simulations, a correction procedure [207] is applied by using the high-amplitude and low-amplitude simulations in the following way: The time-domain maps of the Real PS and Ideal PS of both low-amplitude and high-amplitude simulations are normalized for each phase-cycling step $T_i(\tau, t)$ with respect to their individual mean signal outside of the pulse overlap region ($\tau, t > 40$ fs). Then the normalized low-field-amplitude time-domain maps are subtracted from the normalized high-field-amplitude time-domain maps. From the resulting 16 corrected time-domain maps, the rephasing and non-rephasing contributions are extracted by the corresponding phase cycling, as described by Eq. (4.6.6).

The resulting corrected phase-cycled time-domain maps are shown in Fig. 4.9

(e) for the real PS and in Fig. 4.9 (f) for the ideal PS. As seen by comparing the corrected phase-cycled time maps with the uncorrected time maps (Fig. 4.9 (a-d)), a significant reduction of the diagonal artifact signal for both used pulse sequences is observed. Further, the signal contribution visible for the ideal PS simulation in the delay regime $\tau, t < 50$ fs is now also revealed for the real PS. In App. D the corrected time-domain maps for the rephasing and non-rephasing signal contributions of the simulated dimer fluorescence are presented and described in detail. From this analysis it is concluded that for the simulated dimer fluorescence signal, the deviations between the real and the idealized pulse sequence, as quantified in Sec. 4.4, lead to an increase of the "diagonal artifact" in the simulated rephasing time-domain maps. This "diagonal artifact" is reduced by the correction procedure outlined in Fig. 4.9.

For the simulation of the time-domain maps of multiphoton photoemission from plasmonic nanoslits, the corresponding electric field $E^{j}_{\mathrm{inc}}(t)$ in temporal domain was used for optical excitation. Instead of the real-valued field as given in Eq. (4.6.1), however, the complex-valued $E^{+,j}_{\mathrm{inc}}(t)$ is employed here, containing the positive-frequency part of the spectrum only, i.e., the "c.c." term in Eq. (4.6.1) is omitted, and transformed to the spectral domain by Fourier transformation,

$$E^{+,j}_{\mathrm{inc}}(\omega) = \int E^{+,j}_{\mathrm{inc}}(t)\mathrm{e}^{i\omega t}\mathrm{d}t, \tag{4.6.7}$$

with

$$E^{+,j}_{\mathrm{inc}}(\omega) = \begin{cases} E^{j}_{\mathrm{inc}}(\omega) & \text{for } \omega \geq 0, \\ 0 & \text{for } \omega < 0. \end{cases} \tag{4.6.8}$$

In the spectral domain, the negative-frequency part $E^{-,j}_{\mathrm{inc}}(\omega) = \left(E^{+,j}_{\mathrm{inc}}(-\omega)\right)^{*}$ is added to generate the full complex-valued spectral electric field

$$E^{j}_{\mathrm{inc}}(\omega) = E^{+,j}_{\mathrm{inc}}(\omega) + E^{-,j}_{\mathrm{inc}}(\omega). \tag{4.6.9}$$

The spatially resolved response of the plasmonic nanoslit is calculated by FDTD simulations only for positive frequencies,

$$R^{+}(\omega, y) = \begin{cases} R(\omega, y) & \text{for } \omega \geq 0, \\ 0 & \text{for } \omega < 0. \end{cases} \tag{4.6.10}$$

Therefore, the full FDTD response $R(\omega, y) = R^{+}(\omega, y) + R^{-}(\omega, y)$ is constructed by adding the negative-frequency part, generated by $R^{-}(\omega, y) = \left(R^{+}(-\omega, y)\right)^{*}$.

The local field $E^j_{\mathrm{loc}}(t, y)$ for each measurement step is then determined by multiplying the full FDTD response, $R(\omega, y)$, with the full excitation laser field in the spectral domain, $E^j_{\mathrm{inc}}(\omega)$, followed by inverse Fourier transformation back to the time domain [6]. Furthermore, the nonlinear photoemission yield is defined as

$$Y_{\mathrm{PE}} = \int\int |E_{\mathrm{loc}}(t', y)|^{2N} \mathrm{d}t' \mathrm{d}y, \tag{4.6.11}$$

with the order of nonlinearity N of the multiphoton photoemission process. Here the nonlinearity is set to $N = 4.2$ as explained in Sec. 4.5. Calculating Y_{PE} for every measurement step leads to the phase-cycled time-domain maps plotted in Fig. D.1 (e–h), highlighted with a green background between panels. Note that, in contrast to the molecular dimer fluorescence simulation, no high-field-amplitude minus low-field-amplitude correction is necessary to perform. A detailed comparison is found in App. D.

From that comparison results that for the photoemission signal, the deviations between the reconstructed pulse sequence and the idealized pulse sequence do not lead to significant changes in the simulated time-domain maps. Further, no diagonal artifact is observed in the rephasing time-domain maps. Both observations can be explained with the fact that the multiphoton photoemission signal scales in a highly nonlinear fashion with the excitation intensity (here $N = 4.2$ compared to $N = 2$ in the fluorescence case), and for this reason this nonlinear signal contribution already dominates over the diagonal artifact at the chosen excitation amplitude.

Further, the analysis suggests that the appearance of the diagonal artifact might be connected to a non-perfect suppression of linear signal contributions via phase-cycling. This would at least explain the absence of the diagonal artifact in the case of the photoemission signal, where no linear signal contribution is present at all due to the work function of the sample, which allows only nonlinear emitted electrons with the optical excitation applied. Since it is not necessary to perform a diagonal artifact correction for the multiphoton photoemission simulations, it is concluded that the highly nonlinear photoemission signal is less sensitive to the quantified deviations between the real PS and ideal PS pulse sequences.

4.7. Conclusion

This chapter described a measurement procedure for fully characterizing the electric field of femtosecond multipulse sequences, in intensity and phase, for each individual scanning step of pulse shaper-assisted collinear multidimensional spectroscopy. Employing Fourier-transform spectral interferometry (FTSI), the char-

acterization was carried out simultaneously with the actual spectroscopy experiment. This means that the real shape of the pulse sequence was reconstructed for each measurement step and thus can be used in simulations. This procedure is more accurate than using idealized pulses and more accurate than using one experimentally determined pulse shape that is, however, incorrectly assumed to be the same for all pulses of the excitation sequence and all measurement steps.

The precise electric-field reconstruction, carried out in a fully automated fashion, is beneficial to verify and improve pulse-shaper calibration and correction methods. In our specific case, the analysis provided information on the accuracy of relevant multipulse parameters achieved with a specific pulse-shaper implementation. Deviations between real and ideal pulse-shaper sequences were quantified outside of the temporal pulse-overlap regime.

The accuracies of inter-pulse delays were determined to be $\tau_{\mathrm{RMSD}} = 1.5$ fs, $t_{\mathrm{RMSD}} = 1.3$ fs for the coherence times, and relative phases between individual pulses were found to have accuracies of $\Delta\varphi_{12\,\mathrm{RMSD}} = 0.19\ \mathrm{rad}/\pi$ and $\Delta\varphi_{13\,\mathrm{RMSD}} = 0.08\ \mathrm{rad}/\pi$. The extracted maximum intensities of the pulses constituting a real PS sequence exhibited a systematically decreased maximum intensity of the first pulse of $\overline{\frac{\Delta I_1}{I_1}} = -38$ %, small systematic deviations of the second and third pulse of $\overline{\frac{\Delta I_2}{I_2}} = -3$ %, $\overline{\frac{\Delta I_3}{I_3}} = -4$ %, and statistical deviations of about $\sigma_{\frac{\Delta I_1}{I_1},\frac{\Delta I_2}{I_2},\frac{\Delta I_3}{I_3}} = 11$ % compared to the constituent ideal PS pulses. Note that a systematically smaller intensity of any of the pulses in relation to the others is irrelevant at a given order of perturbation theory because the absolute intensities of the participating pulses factor out of the response-function convolution integral and only affect the overall magnitude of the signal, not the shape of resulting 2D spectra. Systematic variations in the scaling of the nonlinear rephasing signal S_{reph} were related to intensity variations and explained by long-term pulse-energy drifts of the NOPA system, and not due to pulse-shaping imperfections.

Further, the impact of the complete experimental pulse shapes on signal features in 2D spectra were simulated for two exemplary systems: first, the fluorescence signal of a molecular dimer-system, and second, the nonlinear photoemission signal from a plasmonic nanoslit sample. In both cases, it was concluded that with the quantified deviations between real and ideal pulse sequences, very similar characteristic 2D spectral features resulted, such as peak positions and line shapes in purely absorptive 2D spectra. In the case of fluorescence detection, additional corrections by a low- and high-field-amplitude simulation had to be applied. Note that it has been found that this correction procedure is not necessary when highly nonlinear signals, as in multiphoton photoemission, are detected.

The precise magnitude of deviations between real and ideal pulse-shaper se-

quence will vary from setup to setup depending on implementation details. Independent of that, the general method demonstrated here, i.e., automated FTSI on each individual pulse sequence, can be used for the precise simulation of obtained experimental spectra with the real applied pulse shapes.

This approach can be applied in a straightforward manner also to other pulse-shaping methods, such as those based on acousto-optic modulators within $4f$-setups or acousto-optic programmable dispersive filters. While pulse-shaping artifacts will likely be different in those cases, the automated characterization, in parallel with the 2D spectroscopic experiment, will allow taking into account the correct electric fields in all simulation and interpretation efforts, and improve the reliability when comparing theoretical and experimental spectra. This procedure eliminates a possible source of disagreement and improves the confidence levels for comparison and interpretation.

CHAPTER

FIVE

DETECTION OF A PLASMON-POLARITON QUANTUM WAVE PACKET

While the previous chapter focused on the experimental procedure (FTSI) to characterize the optical excitation pulse sequences utilized in a particular 2D nanoscopy experiment which is performed simultaneously. The following chapter addresses the actually acquired 2D nanoscopy data and its interpretation in particular. Analysis of the detected spatially resolved nonlinear plasmon-polariton-assisted electron emission from a plasmonic gold nanoslit resonator reveals that the probed plasmon-polariton mode has to be treated as a plasmon-polariton quantum wave packet.

In the last decades, plasmon polaritons became paramount for tailored nanoscale light–matter interaction, and extensive research has been conducted to monitor [258, 259] and manipulate their spatial [260] and spatio-temporal dynamics [261]. These dynamics result from the superposition of various plasmon-polariton modes, i.e., classical wave packets. Beyond this classical picture, plasmon-polariton modes are treated as quasiparticles [35, 262] and they are considered essential for the realization of future nanoscale quantum functionality [263–266]. Implementing and demonstrating such functionality requires access to the quasiparticle's quantum state to monitor and manipulate its corresponding quantum wave-packet dynamics in Hilbert space.

Here, the local detection of such nanoscale plasmon-polariton quantum wave packets is reported using plasmon-polariton-assisted electron emission as signal in coherent 2D nanoscopy [28]. The observation of a quantum coherence oscillating at the third harmonic of the plasmon-polariton frequency is traced back to the superposition of energetically non-adjacent plasmon-polariton occupation number

states and is hence a direct fingerprint of the quantum wave packet.

Beyond demonstrating the existence of a plasmon-polariton quantum wave packet via the coherence between certain occupation number states and providing an improved model for plasmon-assisted electron emission processes, the results presented in this chapter open pathways towards time-dependent probing and manipulating of coupled quantum states and dynamics on the nanoscale.

The chapter is structured as follows: After briefly emphasizing the different definitions in classical and quantum plasmonics in Sec. 5.1, the developed quantum model is introduced in Sec. 5.2. Subsequently, Sec. 5.3, Sec. 5.4, and Sec. 5.5 present the experimental results and simulations. Section 5.6 addresses the theoretical modeling based on the FDTD approach, whereas in Sec. 5.7 the origin and in Sec. 5.8 the experimental manifestation of the observed signal contributions are discussed, followed by the experimental parameters in Sec. 5.9 and the detailed description of the developed quantum model in Sec. 5.10. Section 5.11 summarizes the obtained results.

Note that App. E and App. F provide additional information on the quantitative comparison of 2D spectra and its usefulness as a feedback approach, and a critical analysis of the presumed influence of linear and nonlinear polarizations on the electron emission, respectively. The presented results are published in Ref. [3].

5.1. From classical plasmonics to quantum plasmonics

Plasmon polaritons generated by metallic nanostructures or metal–dielectric interfaces enable nanoscale localization of electromagnetic fields and consequently are of great interest for nanoscopic light–matter interaction.

A plasmon-polariton mode is the collective oscillation of electrons in metals at a specific frequency *and* a corresponding electromagnetic near field. The plasmonic nanostructure forms a cavity resonator which allows, in contrast to free propagating waves, only solutions of the wave equation at distinct eigenfrequencies which depend on the mathematical boundary conditions of the resonator and thus its particular geometry [267]. The associated solutions for the electromagnetic field are standing waves which indeed oscillate in time but whose peak-amplitude profiles do not move in space. The individual standing-wave solutions differ in the number of stationary field nodes. Each standing wave describes an eigenmode of the resonator and one particular eigenmode is here referred to as *mode*. The localization of this modes within the nanoresonator results in general in the su-

perposition of multiple modes due to the optical excitation by spectrally broad laser pulses. In this case, a superposition of such modes forms a classical wave packet whose dynamics being fully covered by classical electrodynamics as has been extensively investigated over the last decades [258, 259].

Switching from classical to quantum physics, plasmon polaritons act as bosonic reservoirs [268]. Analogous to cavity quantum electrodynamics, each plasmon-polariton mode can be represented as a quantum harmonic oscillator (QHO) [269, 270]. Key observations in quantum plasmonics [263, 271, 272] such as plasmon-assisted entangled-state transmission [35], squeezed-state propagation [273], plasmonic quantum interferences [274], and plasmon-polariton entanglement [275] rely on this quantized description of plasmon polaritons. Up to now, probing of these nanoscale quantum processes at room temperature relied completely on analyzing in-going and out-going far-field photon modes, and quantum tomography had been applied merely to the photon–plasmon conversion process [276, 277] rather than to the quantum state of the plasmon polariton itself. But developing and characterizing more advanced integrated nanoscale quantum devices requires methods to spatially resolve, characterize, and eventually to manipulate, the plasmon-polariton quantum state itself.

Recently, the change in quantum statistics of a plasmonic system has been demonstrated, which offers a promising outlook for tailoring photon statistics deterministically by plasmonic near fields [278]. This approach still relies on in-going and out-going far-field photon modes.

Here, 2D nanoscopy [28] is applied, using plasmon-polariton-assisted electron emission [140, 279] as a signal channel, to detect and spatially resolve quantum coherences of the plasmon-polariton quantum state $|\Psi\rangle$ of a plasmonic nanoslit resonator, where $|\Psi\rangle$ may be described as a superposition of occupation number (Fock) states $|p\rangle$ of the QHO with p representing the number of plasmon-polariton quanta. In this sense, $|\Psi\rangle$ represents a quantum wave packet.

The classical polarization of the plasmonic near field is obtained as the expectation value $\langle\Psi|\,(\mathrm{b}+\mathrm{b}^\dagger)\,|\Psi\rangle$, where $\mathrm{b}^\dagger$ and b are the bosonic creation and annihilation operators of plasmon-polariton excitations, respectively. It oscillates at specific plasmon-polariton frequency ω_{pp}. The presented 2D spectroscopy technique is sensitive to quantum coherences of the plasmon-polariton quantum wave packet oscillating at harmonics $n\omega_{\mathrm{pp}}$ of the fundamental ω_{pp}, with $n \in \mathbb{N}$. In contrast to the classical polarization, these coherences contain information about the off-diagonal elements of the density matrix $|\Psi\rangle\langle\Psi|$ of the plasmon polariton and accordingly about the quantum state $|\Psi\rangle$ of the plasmon polariton.

In the following, experimental evidence is presented for the detection of quantum coherences with $n = 3$, which implies a coherent superposition of at least two non-adjacent Fock states separated by three quanta $\hbar\omega_{\mathrm{pp}}$ in energy. Although

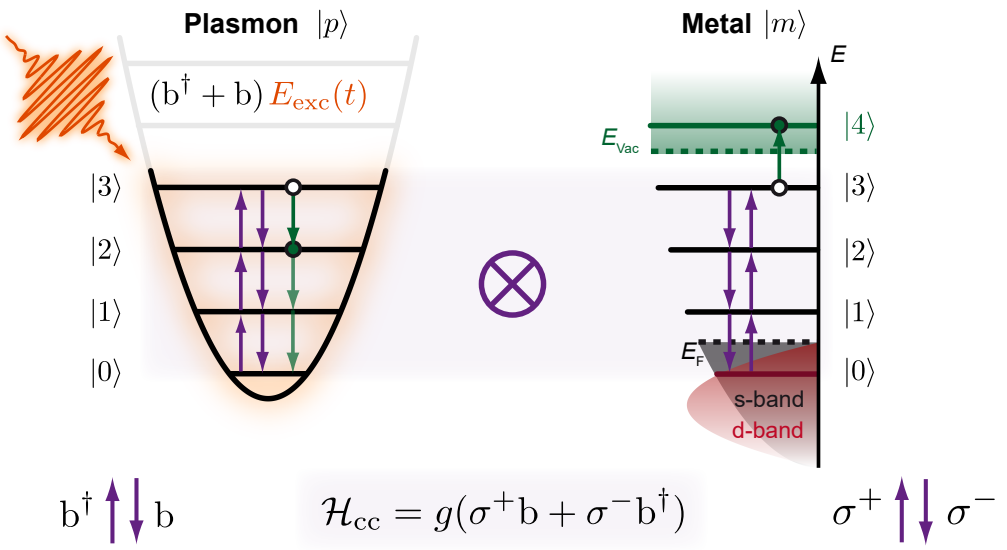

Figure 5.1 – Quantum model of plasmon-polariton-assisted multi-quantum electron emission from a plasmonic resonator. A quantized harmonic oscillator (left) driven by the external light field $E_{\mathrm{exc}}(t)$ (orange) is coherently coupled (purple) to metal states (right) describing the single-electron excitation steps. The coupling term $\mathcal{H}_{\mathrm{cc}}$ in the Hamiltonian (bottom) and the related creation and annihilation operators are described in the text. A unidirectional population transfer (green arrows) models the final electron emission step. Adapted from Ref. [3] with permission from Springer Nature.

this coherence only allows insight into a single off-diagonal element of $|\Psi\rangle\langle\Psi|$, the associated superposition of two stationary states, i.e., Fock states, is already sufficient evidence for the existence of a plasmon-polariton quantum wave packet, even if not all elements of the density matrix for the plasmon polariton are known.

5.2. Quantum model of plasmon-polariton-assisted electron emission

The investigation of the plasmon-polariton quantum state $|\Psi\rangle$ by means of 2D nanoscopy requires the development of a model that describes the coupling of laser-excited plasmonic eigenstates to *sequentially* excited single-electron states, which finally results in the emission of an electron. A sketch of our quantum model is displayed in Fig. 5.1.

It features a bosonic harmonic oscillator (left) representing a single plasmon-

polariton mode with a population relaxation time of T_1. The driving of the oscillator is modeled by a classical optical field $E_{\mathrm{exc}}(t)$ and the plasmon harmonic oscillator is coherently coupled to a multilevel fermionic ladder representing the single-particle electron excitations in the metal. Transitions between the individual number states $|p\rangle$ are taken into account within the plasmonic subsystem (Fig. 5.1, left) as indicated by creation and annihilation operators of plasmon polaritons. These transitions are coherently coupled (purple arrows, Fig. 5.1) to transitions between the single-particle electron states $|m\rangle$, using the coupling Hamiltonian $\mathcal{H}_{\mathrm{cc}} = g(\sigma^+ \mathrm{b} + \sigma^- \mathrm{b}^\dagger)$ in rotating-wave approximation, where g is the coupling constant and σ^+ and σ^- are rising and lowering operators, respectively, in the fermionic ladder. Note that modeling the excitation dynamics in a metal system making use of discrete states separated by the plasmon energy $\hbar\omega_{\mathrm{pp}}$ is a common approach in literature [38].

The value of g is in our case an effective value accounting for the fact that a continuum of states in the metal system was reduced in our model treatment to a multilevel system with a finite number of states. The value of g was chosen small enough to avoid unphysical hybridization effects between metal and plasmon states.

This metal multilevel system (Fig. 5.1, right) is further chosen to reflect the work function of the metal used in the actual experiment (Au) which is expressed in the fact that all states $|m\rangle$, with exception of the highest one, are bound states. The fermionic part of the model captures possible multi-quantum excitation pathways in the metallic band structure as well as the electron-emission channel, which in the present example is realized by placing the highest-energy state above the vacuum energy E_{Vac}, i.e., in the present case $E_{|4\rangle} > E_{\mathrm{Vac}}$. In addition, to mimic the excitation processes of electrons from both the s-band (grey-shaded area) and the d-band (red-shaded area) in Au [32] the electronic ground state $|0\rangle$ is placed 1.6 eV below the Fermi energy E_{F}.

For state $|m = 4\rangle$, i.e., the detected signal, coherent coupling to the plasmon polariton is neglected, and instead the final electron-emission process is modeled as a unidirectional incoherent energy transfer (Fig. 5.1, green arrows). In this emission process, which is described in detail in Sec. 5.10, the annihilation of a plasmon polariton transfers an electron from the energetically highest intermediate state of the metal, in our particular case $|m = 3\rangle$, to the electron emission state with energy $E > E_{\mathrm{Vac}}$, here $|m = 4\rangle$, whose population then serves as the detection signal in our model.

5.3. Characterizing the spectral properties of a plasmonic nanoresonator

The plasmonic nanoslit resonators were fabricated on a 32 nm thick, chemically synthesized, single-crystalline Au microplate [131] by FIB milling. The single-crystalline character improves the FIB fabrication quality and reduces scattering of surface plasmons where structural defects occur [132]. The microplates were positioned on an Au hole mask for both the FIB fabrication process and the 2D nanoscopy experiments, such that a large part of the microplate was located on a flat glass substrate. This approach enables preparation of plasmonic nanostructures on a low-refractive-index material, which reduces the substrate impact on surface-plasmon properties while at the same time providing the sample conductance required for FIB milling as well as PEEM [6].

Fig. 5.2 (top left) shows the spatially resolved electron yield experimentally retrieved by PEEM, for single-pulse excitation of a plasmonic Au nanoslit resonator on a SiO_2 substrate, which is schematically depicted in the bottom left panel. The locally enhanced emission reflects the plasmon-polariton-assisted multi-quantum electron emission process and thus serves to map the near-field distribution of the plasmon-polariton mode. Excitation by multipulse sequences of three ultrashort laser pulses, temporally separated by systematically varied time delays τ and t, provides spectral resolution and allows correlating the pump and the probe energy [20].

This information is accessible via 2D Fourier transformation with respect to the time delays τ and t of the detected PEEM images [1]. Correlations between pump ($\hbar\omega_\tau$) and probe energies ($\hbar\omega_t$) are revealed as peaks in the so obtained 2D spectrum. In the present case, these correlations are dominated by the plasmon-polariton resonance, and thus the most intense peak in the exemplarily shown 2D spectra (Fig. 5.2, top right) is located on the diagonal with $\hbar\omega_\tau = \hbar\omega_t$ and reflects the resonance frequency ω_{pp} of the plasmon-polariton mode weighted with the excitation spectrum.

From a quantum mechanical point of view, the localization of the spectral signature at $\hbar\omega_\tau$ and $\hbar\omega_t$ in a 2D spectrum means that the investigated system is in a coherent superposition during the time interval τ as well as t and that these coherences oscillate at the corresponding frequency. This approach will become important when the obtained measurement data is analyzed in the picture of the plasmon polariton as a quantum object. At this stage, it is important to note that the measured 2D nanoscopy spectra and the corresponding cross sections, the latter are depicted in the bottom right in Fig. 5.2, reveal that the upper emission hot spot is only marginally affected by the interference effects of adjacent quasinormal

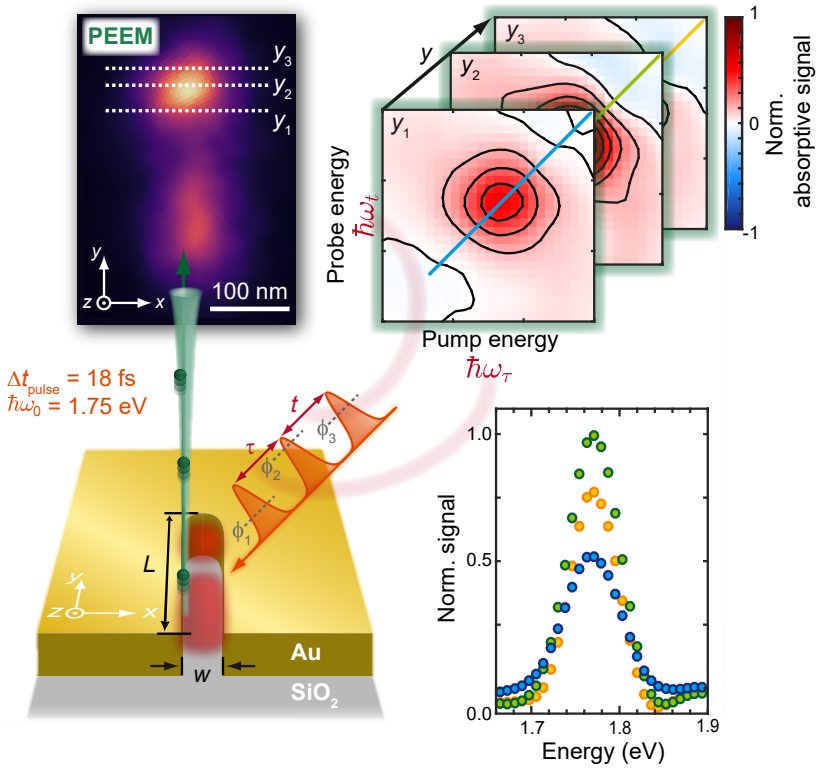

Figure 5.2 – Experimental scheme to detect plasmon-polariton-assisted multi-quantum electron emission from a plasmonic nanoslit by 2D nanoscopy. Photoemission electron microscopy (PEEM) is used to detect temporally and spatially resolved plasmon-polariton-assisted multi-quantum electron emission (green) from a resonantly excited plasmonic near-field mode (red) in a gold nanoslit resonator (bottom left) with slit length $L = 290$ nm and width $w = 23$ nm, as characterized by scanning electron microscopy (SEM) described in detail in Sec. 5.6. The electron emission yield pattern obtained for single-pulse excitation is shown as a false-color plot (upper left). For 2D nanoscopy, PEEM patterns are recorded with an excitation pulse sequence (orange) consisting of three pulses with pulse durations $\Delta t_{\mathrm{pulse}} = 18$ fs, interpulse delays τ, t, and a particular phase-cycling scheme (grey dashed lines). Three exemplary purely absorptive 2D spectra are shown (upper right, normalized to the overall maximum signal, with contour lines corresponding to the color bar ticks) for the vertical positions y_1, y_2, and y_3 and averaged along the horizontal x axis (white dashed lines). Extracted cross sections (bottom right) along the diagonal (light blue, green and yellow lines) reveal a spatially homogeneous spectral response. Adapted from Ref. [3] with permission from Springer Nature.

modes [6]. This can be deduced from the Lorentzian-like line shapes of the cross

sections, where the spectral position is independent of the spatial position within the hot spot. Note that the small deviations from a purely Lorentzian line shape seen in Fig. 5.2, bottom right, are expected for the applied excitation scheme with population time T set to zero [29, 280]. Therefore, the plasmonic near field of the plasmonic nanostructure under investigation can be confidently modeled as a single spatially homogeneous Lorentzian resonator with $\hbar\omega_{\mathrm{pp}} = 1.77 \pm 0.01$ eV, in agreement with our model (Fig. 5.1).

5.4. Measured and simulated 2D spectra of plasmon-polariton-assisted multi-quantum electron emission

To investigate the quantum coherences of the plasmon-polariton quantum state $|\Psi\rangle$ the absolute "rephasing" signal obtained via phase cycling [70] is analyzed. Details about the phase-cycling scheme are provided in Sec. 5.9. Because of the spatially homogeneous spectral response of the electron emission, the electron yield is spatially integrated within the region of interest (ROI) covering the upper emission "hot spot" of the nanoslit resonator, as depicted in Fig. 5.3 (a) (grey ROI).

The resulting 2D spectrum (Fig. 5.3 (b), left panel labeled "PEEM") shows again a dominant diagonal peak corresponding to the plasmon-polariton frequency ω_{pp} weighted by the excitation spectrum (Fig. 5.3 (b), top left). In contrast to the purely absorptive 2D spectra of Fig. 5.2, the peak now has a "cross-like" shape, i.e., it has horizontal and vertical protrusions. Surprisingly, two additional "off-diagonal" peaks, denoted in the figure as "3Q", appear in the 2D spectrum at spectral positions clearly outside the range of the excitation spectrum. In coherent 2D spectroscopy, the origin of these 3Q peaks can be traced back to the occurrence of quantum coherences oscillating at the third harmonic of the plasmon-polariton frequency ω_{pp}, i.e., the 3Q peaks result from the superposition of eigenstates separated by an energy of $3\hbar\omega_{\mathrm{pp}}$.

Usually, the spectroscopic signature of a coherence oscillating during the time interval τ and t is observed at its oscillation frequency in a 2D spectrum, i.e.,at spectral positions $\hbar\omega_\tau$ and $\hbar\omega_t$, respectively. In the presented case these spectral positions are far outside of the experimentally accessible spectral window, which is limited by the Nyquist criterion.

However, here the oscillation is undersampled with a discrete delay step size of $\delta t = \delta\tau = 4$ fs so that due to aliasing effects the corresponding signal peaks are back-folded into the low-frequency range covered by the 2D spectrum. Without

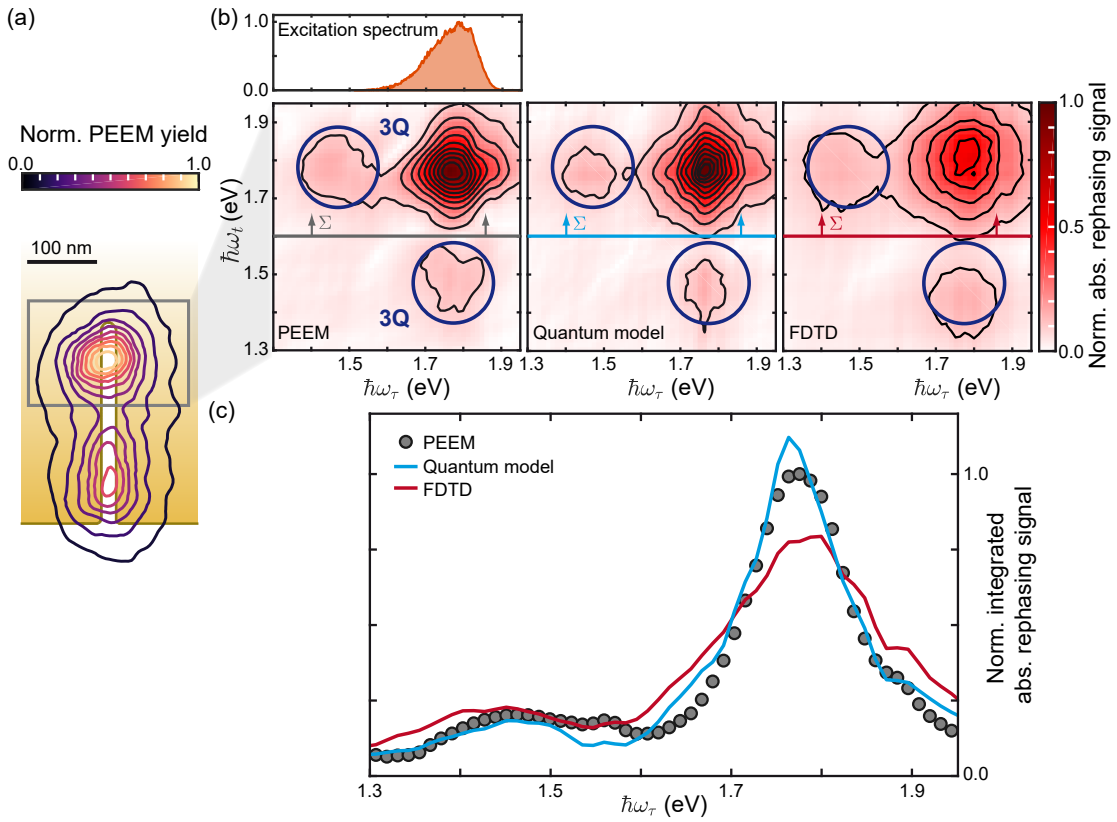

Figure 5.3 – Comparison of measured and simulated rephasing 2D spectra of plasmon-polariton-assisted multi-quantum electron emission. (a), Normalized photoemission electron microscopy (PEEM) yield (contour lines) of the nanoslit resonator for excitation with $\tau = t = 0$ fs and $\varphi_{1,2,3} = 0$ with the ROI used for evaluating 2D spectra shown as a grey rectangle. (b), Absolute-value rephasing 2D spectra as measured by 2D nanoscopy via PEEM (left panel), simulated with the quantum model of Fig. 5.1 (middle panel), and simulated via the finite-difference time-domain (FDTD) method (right panel). The experimental excitation spectrum is shown on top of the left panel. FDTD-based calculations rely on the locally enhanced plasmonic fields and assume instantaneous nonlinear emission. The simulated spectra are based on measured excitation pulse sequences, i.e., for each delay and phase setting the actual excitation field was measured using FTSI [2]. The measured 2D spectrum is normalized to the peak maximum. Both simulated spectra are scaled individually to minimize their integrated root-mean-square deviation with respect to measured 2D spectrum. For further analysis, each 2D spectrum is spectrally integrated (symbolized by "Σ") for each $\hbar\omega_\tau$ value along the high-energy part of the $\hbar\omega_t$ axis starting at $\hbar\omega_t = 1.6$ eV (colored horizontal lines). (c), Spectral high-energy integrations along $\hbar\omega_t$, i.e., projections onto the $\hbar\omega_\tau$ axis, with colors corresponding to the measured (grey circles) and simulated (blue line: quantum model, red line: semiclassical FDTD model) 2D spectra from (b). The curves of the respective simulation models are scaled by the same factor determined by normalizing the PEEM data to its maximum value. Reproduced from Ref. [3] with permission from Springer Nature.

aliasing, one of the 3Q peaks occurs at $\hbar\omega_\tau = 5.31$ eV and $\hbar\omega_t = 1.77$ eV, while the other one is located at $\hbar\omega_\tau = 1.77$ eV and $\hbar\omega_t = 5.31$ eV, as explained in detail in Sec. 5.8. The first peak mentioned describes a system that is initially in a superposition of eigenstates that are separated by an energy of $3\hbar\omega_{\mathrm{pp}}$ during the coherence time τ, and is then brought into a superposition of eigenstates that are separated by $\hbar\omega_{\mathrm{pp}}$ during the coherence time t by the interaction with the central pulse of the multipulse sequence, and vice versa for the other 3Q peak. In nonlinear spectroscopy, this system dynamic is often visualized in terms of DSFDs, as shown in Fig. 5.7 in Sec. 5.7 for the 3Q peaks.

To analyze the measured 2D spectrum, quantum dynamics simulations have been performed based on the proposed quantum model (for details see Sec. 5.10) and the results are compared to 2D spectrum simulations based on a widely applied semiclassical FDTD model of plasmon-assisted electron emission [146]. Note that a detailed description of the obtained simulation results based on the FDTD approach can be found in Sec. 5.6.

The corresponding 2D spectra are shown in the middle and right panels of Fig. 5.3 (b), respectively. To compare the spectral features of the quantum model and the measured spectrum, their RMSD was minimized by varying an overall scaling factor of the signal amplitude, the plasmon energy $\hbar\omega_{\mathrm{pp}}$, and the plasmon population relaxation time constant T_1. The best match was obtained for $\hbar\omega_{\mathrm{pp}} = 1.766 \pm 0.001$ eV and $T_1 = 11 \pm 1$ fs. The signal amplitude ratio between the diagonal peak and the 3Q peaks as well as the "cross-like" line shape of the experimental 2D spectrum are well reproduced by our quantum model. This is further visualized in Fig. 5.3 (c) by integrating the 2D spectra along $\hbar\omega_t$: The proposed quantum model (blue) captures both the linewidth and the signal ratio between diagonal peak and 3Q peaks of the experiment (grey circles).

By contrast, the 2D spectrum calculated using a widely applied model of plasmon-assisted electron emission [146] (Fig. 5.3 (b), right) fails to reproduce the measured 2D spectrum (Fig. 5.3 (b), left). In this common model, the local field, as induced by the respective multipulse sequences of the coherent 2D spectroscopy method, is calculated via a FDTD-derived local response function (see Sec. 5.6). Matching the observed nonlinearity of the emission yield intensity dependence, the signal is obtained as a time integral of the eighth power of the local field. Here, the nanoslit parameters $L = 282$ nm and $w = 23$ nm produced the best match to the measured spectrum. Although the geometrical parameters determined in this way agree very well with the nominal values of the experimental geometry (see Fig. 5.5), the calculated 2D spectrum significantly deviates from the measured 2D spectrum. In contrast to the quantum model, neither the "cross-like" peak shape, nor the peak widths or the peak ratio between diagonal peak and 3Q peaks is well reproduced. The difference in peak ratio and width becomes particularly clear when integrating

the FDTD 2D spectrum along $\hbar\omega_t$ (Fig. 5.3 (c), red), which clearly deviates from experiment (Fig. 5.3 (c), grey circles).

5.5. Physical origin of 3Q signal contributions

Surprisingly, as observed in Fig. 5.3 (b), the semiclassical local-field approach (FDTD) also generates 3Q signal peaks. In coherent 2D spectroscopy of quantum systems such as molecules, these peaks result from the superposition of eigenstates separated by three times the energy of the fundamental transition. In order to assess the appearance of 3Q peaks in the measured 2D spectrum, it is therefore necessary to elucidate the origin of these signals in both the quantum and the semiclassical model.

Again, starting by discussing the quantum model: The decisive point for interpreting the 3Q peaks in the quantum model is the fact that the energy spacing of adjacent levels is $\hbar\omega_{\mathrm{pp}}$. Therefore, the coherence must be assigned to the superposition of energetically non-adjacent eigenstates of the system. Here, the coherence is specifically assigned to the superposition of occupation number states of the QHO representing the plasmon polariton, i.e., the presence of a plasmon-polariton quantum wave packet. To prove this conjecture, Fig. 5.4 presents a comparison of the full quantum model (top row) and a truncated quantum model that represents the plasmon polariton as a pure two-level system (bottom row). The observation is that only the full model, depicted in Fig. 5.4 (a), recovers the experimentally observed 3Q peaks in the simulation, as seen in Fig. 5.4 (b). In the truncated model, presented in Fig. 5.4 (d), these peaks are largely suppressed, as shown in Fig. 5.4 (e). The 3Q peaks also remain for the full model in the case of an idealized, unstructured excitation spectrum, as depicted in Fig. 5.4 (c). Note that the small 3Q peaks for the two-state model in the idealized case, seen in Fig. 5.4 (f), stem from small coherent signals arising in the multi-level metal excitation due to the short but finite pure-dephasing time of $T_2^* = 4$ fs. These contributions become only evident for Gaussian pulses without noise.

Since the multi-quantum (3Q) coherence peaks vanish when truncating the Hilbert subspace of the plasmon polariton in the simulation, it is deduced that the experimentally observed spectroscopic feature of the 3Q coherence allows us to access off-diagonal elements of the density matrix describing the plasmon-polariton Hilbert subspace, which is embedded in the full Hilbert space of the coupled plasmon-polariton–metal system. In the subspace of the plasmon polariton, the 3Q coherence connects non-adjacent occupation number states, which contain crucial information for the reconstruction of the quantum state of the plasmon polariton.

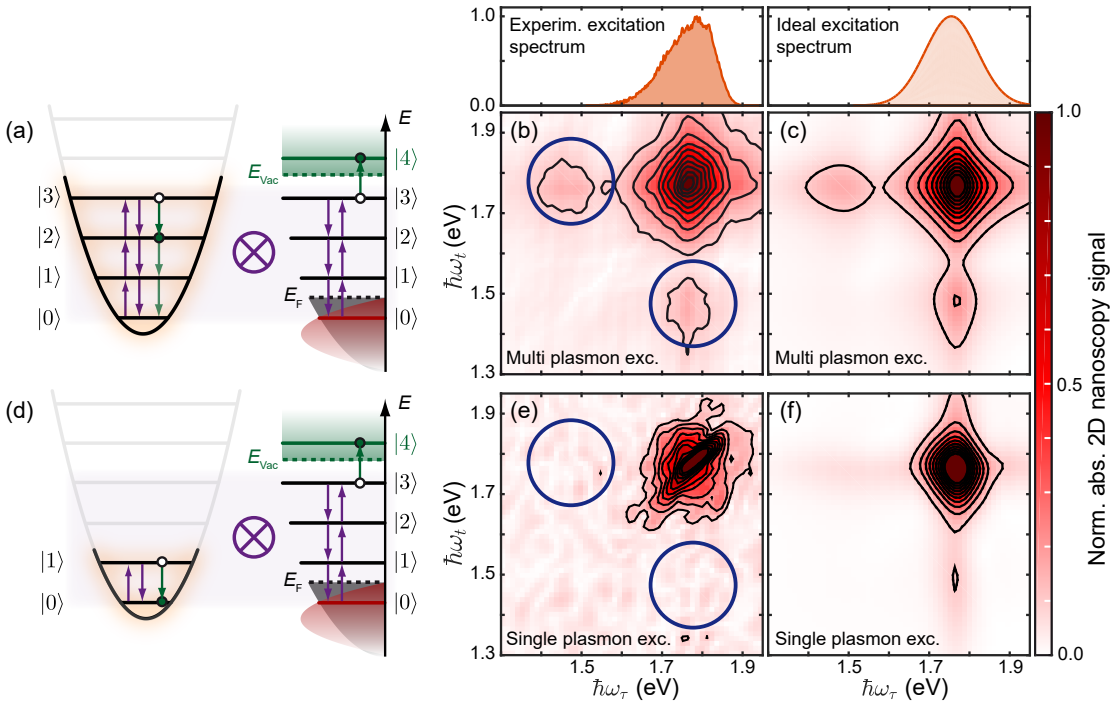

Figure 5.4 – Impact of $3\omega_{pp}$ quantum coherences of the plasmon polariton on the rephasing 2D spectrum. (a), Quantum model featuring multi-plasmon-polariton coherences. (b), (c), Corresponding simulated rephasing 2D spectrum based on experimentally used multipulse sequences (b) and using idealized Gaussian multipulse sequences (c). Experimental and idealized excitation spectra are depicted on top of (b) and (c), respectively. (d), Truncated two-state QHO model which only allows for single plasmon-polariton excitations. (e), (f), Resulting simulated rephasing 2D spectra using experimental multipulse sequences (e) and idealized Gaussian multipulse sequences (f). The Gaussian pulses with central frequency $\hbar\omega_0^{\text{Ideal}} = 1.755$ eV and pulse duration $\Delta t_{\text{pulse}}^{\text{Ideal}} = 18$ fs match closely the pulses used in the experiment. All spectra were rescaled to minimize the RMSD with respect to the measured 2D spectrum (see Fig. 5.3 (b)). Note that the numerically required truncation of the QHO in the full model calculation has no impact on the simulated 2D spectra. Reproduced from Ref. [3] with permission from Springer Nature.

For the sake of completeness, note that small imperfections in the multipulse sequence actually used in the experiment generate an artifact in the diagonal peak [2, 207] that is most pronounced in the truncated model simulation, as depicted in Fig. 5.4 (e), but also slightly affects the simulated spectrum based on the full quantum model (Fig. 5.4 (b)). However, this does not change the main conclusion

that the presented experimental method allows to access components of the quantum state from the plasmon polariton. In addition, it should be emphasize here that the plasmon polariton behaves as a harmonic oscillator and a modification of the quantum statistics of the plasmon polariton via pulsed driving can thus be neglected. Finally, it was made sure that the numerically required truncation of the harmonic quantum oscillator in the full model calculation does not have an impact on the simulated 2D spectra.

To assign the origin of the 3Q peaks in the semiclassical FDTD model, it is essential to consider the nonlinearity of the signal generation. In the FDTD model the nonlinearity of the electron yield is introduced by taking the time integral of the eighth power of the local field (see Sec. 5.6). This generates harmonics $n\omega_{\mathrm{pp}}$, with $n \in \{1, 2, 3, 4\}$, in the nonlinear classical field correlations underlying the 2D spectra, but these harmonics are completely unrelated to plasmon-polariton quantum coherences. The reason for this is that the nonlinear signal generation, i.e., electron emission, is based on a highly simplified physical picture, i.e., the instantaneous absorption of multiple photons in the metal system (see Sec. 2.3.4 for details) without considering intermediate single-electron states which exist in the metallic band structure and dominate plasmon-assisted multi-quantum electron emission [140]. Thus, the 3Q contributions in the FDTD spectrum (Fig. 5.4 (b)) reflect nonlinear classical field correlations of the local field excited by the multipulse sequence, which result from an oversimplified model for multiphoton electron emission from a metal. This model neither reproduces the "cross-like" peak shape of the diagonal peak, nor the peak widths and peak ratios between diagonal peak and 3Q peaks.

In contrast to that, the quantum model takes into account these intermediate single-electron states in the metal system, which exhibit finite population relaxation and ultrashort pure-dephasing times [68], with the latter being responsible for effectively damping the coherences. Furthermore, modeling the plasmon as a quantum harmonic oscillator allows quantized excitation of these single-electron states, and that all constituent parts of the system can be described and understood within the density matrix formalism, which becomes essential when quantum emitters are coupled to the plasmonic mode.

Finally, the impact of a nonlinear plasmon-polariton response is discussed. Classical linear and nonlinear plasmon-polariton fields in combination with nonlinear electron emission might lead, in principle, to multi-quantum coherences in the 2D spectrum. Thus, it is important to check whether the sequential excitation via single-electron states in the metal by classical linear and nonlinear fields could also lead to a 3Q peak in the 2D spectrum. In addition to the excitation of single-electron metal states, localized plasmon-polariton resonances can lead to third-

harmonic generation (THG) inside a metal nanostructure via a nonlinear material polarization [281, 282]. Such THG fields could also give rise to 3Q coherences in the metal by driving the $|m = 0\rangle \rightarrow |m = 3\rangle$ transition. Therefore, an alternative model has been explored in which the polarization of the plasmon polariton, calculated as expectation value of the dipole operator for the plasmon-polariton quantum state and a possible THG component, directly drive the transition between the single-electron states as well as the final electron emission step.

The simulation results confirm that, in principle, a classical nonlinear polarization in the system could give rise to 3Q signal peaks in the 2D spectrum. The detailed investigation is given in App. F. However, using a field-strength ratio between fundamental and THG according to our experimental parameters, it was found that the nonlinear response of the metal contributes well below 1 % to the observed 3Q peaks. Thus, the nonlinear response of the metal can be safely ignored as a competing signal contribution which clearly attributes the observed multi-quantum coherence as signature of a plasmon-polariton quantum wave packet.

5.6. Modeling plasmon-polariton-assisted multi-quantum electron emission based on the semiclassical FDTD approach

In this section the modeling of plasmon-polariton-assisted multi-quantum electron emission from nanoslit resonators based on the local electric near field retrieved from FDTD simulations is described. It is based on the assumption for strongly dephasing systems introduced in Sec. 2.3.4.

Coherent 2D nanoscopy spectra, and hence the corresponding electron emission yields, are modeled starting from the local near-field response function calculated via FDTD simulations [6], in which the geometrical slit parameters are modeled according to scanning electron microscopy (SEM) data, as depicted in Fig. 5.5 (a). The validity of the local near-field calculation is verified by reproducing the characteristic hot-spot electron emission pattern of PEEM experiments, presented in Fig. 5.5 (b), via FDTD simulations of nanoslit resonators (Fig. 5.5 (c)). The simulations are based on slit lengths L obtained from experiment and a specified nonlinearity of the electron emission process of $N = 4$. For the calculation of electron emission patterns shown in Fig. 5.5 (c), the FDTD response function $\mathbf{R}(x, y, z, \nu)$, as introduced in Sec. 2.2.3, is evaluated at $z = 20$ nm, i.e., the Au microplate top surface, along a contour C (Fig. 5.5 (d), blue) that followed in the xy plane the Au edge of the nanoslit at a constant distance of 2 nm in vacuum.

In order to calculate the local near field, the resulting FDTD response $\mathbf{R}_C(x, y, z =$

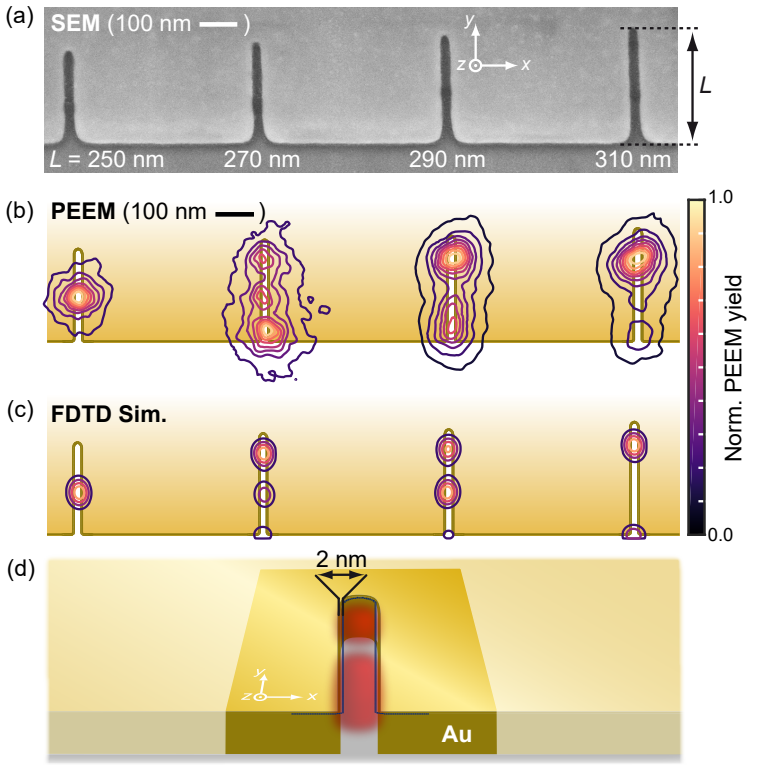

Figure 5.5 – Scanning electron microscopy (SEM) image of four different nanoslit resonators and the corresponding measured PEEM and simulated FDTD yield pattern. (a), SEM image of four different plasmonic nanoslits of length L cut by FIB milling of a gold microplate. (b), Corresponding spatially resolved, and individually normalized, plasmon-polariton-assisted electron emission yield patterns as detected by PEEM. The yield patterns vary depending on the geometrical slit parameters, mainly due to the slit length L. (c), Simulated yield patterns based on the local electric near field retrieved from the FDTD method, assuming a nonlinearity of the electron emission process of $N = 4$. (d), Schematic gold nanoslit (Au) with contour C (blue) located at the Au–vacuum interface in the z direction and following the Au nanoresonator edge at 2 nm distance in vacuum in the xy plane. Along C the FDTD response is evaluated to calculate the local near field $E_C(x, y, t)$ (red shade). Reproduced from Ref. [3] with permission from Springer Nature.

20 nm, ν) is multiplied by the complex-valued single-pulse excitation spectrum and Fourier-transformed to the time domain [6]. Using the resulting near field $\mathbf{E}_C(x, y, t)$, the local nonlinear electron emission yield $Y_C(x, y)$ is calculated via $Y_C(x, y) = \int |\mathbf{E}_C(x, y, t)|^{2N} \mathrm{d}t$, in which the nonlinearity N describes the number of absorbed photons required for the electron emission process.

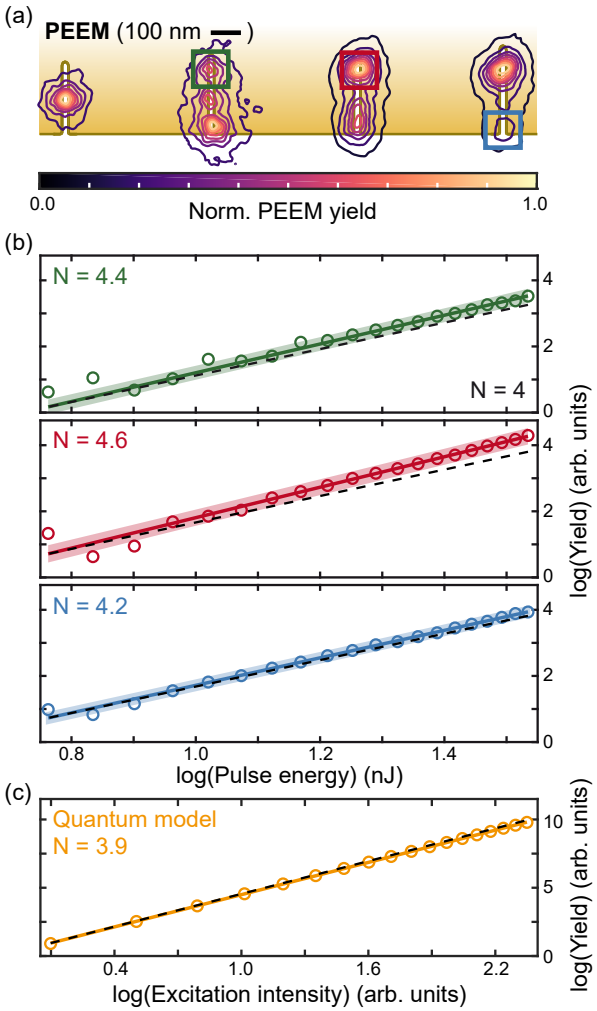

Figure 5.6 – Measured spatially integrated and simulated electron emission yield dependence with respect to excitation pulse energy. (a), Spatially resolved electron emission yield patterns measured by photoemission electron microscopy (PEEM). (b), Electron emission yield (circles) as function of the logarithmic (basis 10) excitation pulse energy. The yield is spatially integrated in the respective region of interest (ROI), which is marked by the colored rectangles in (a). The nonlinearity N in each ROI is determined by the slope of a linear fit of the logarithmic data (colored line), with 95 %-confidence bounds (colored shade). Black dashed lines serve as a guide to the eye and correspond to an $N = 4$ electron emission process. (c), Simulated power law (yellow circles) and linear fit (yellow line) of the time-integrated population in the photoelectron state of the quantum model, as introduced in Sec. 5.2 (four-level quantum harmonic oscillator (QHO)). The same nonlinearity is determined for a quantum model simulation applying a two-level QHO, as discussed in Fig. 5.4. Reproduced from Ref. [3] with permission from Springer Nature.

The nonlinearity of $N \sim 4$ of the electron emission process is determined by recording the spatially resolved yield as a function of excitation pulse energy, in a so-called power law, presented in Fig. 5.6 (b), indicating that the absorption of at least four photons is required to generate one electron. This nonlinearity is larger than expected for threshold electron emission. Based on typical work-function values of Au of about $\Phi \sim 5$ eV, where the exact value depends on the crystallographic surface orientation and the amount of carbon coverage [42], and using a photon energy of $\hbar\omega_0 = 1.75$ eV yields a nonlinearity of $N \sim 3$ for the electron emission process. The deviation of the experimental value is explained by the large amount of d-band electrons, energetically located ~ 2 eV below the Fermi energy [283], which also contribute to the electron emission. A similar assumption has been made in literature for explaining, e.g., the nonlinear electron emission from gold nanotips [284].

To visually compare the simulated local yield $Y_C(x, y)$ with the measured spatially resolved yield pattern (Fig. 5.5 (b)), $Y_C(x, y)$ is convoluted with a two-dimensional Gaussian exhibiting a FWHM of $w_{x,y} = 25$ nm, to mimic a PEEM point-spread function blurring the electron emission pattern and yielding $Y(x, y)$. The resulting simulated 2D yield patterns are shown in Fig. 5.5 (c) for four different nanoslit lengths, i.e., $L_{\mathrm{FDTD}} = 247$ nm, 271 nm, 282 nm, and 302 nm (from left to right). The agreement of the measured hot-spot electron emission pattern (Fig. 5.5 (b)) with the FDTD simulation (Fig. 5.5 (c)) corroborates that the local near field of driven plasmon eigenmodes is the dominant excitation channel of the nonlinear electron emission.

For simulating 2D spectra via the FDTD method, as discussed in Fig. 5.3, the FDTD response is again utilized 2 nm away from the Au surface, along the same nanoslit contour C that is already used for simulating the electron emission pattern. The corresponding electric near field is obtained, as described above, from the multiplication of the local response function $\mathbf{R}_C(x, y, \nu)$ with the complex-valued laser spectrum and subsequent Fourier transformation.

Note that in contrast to the simulation of electron emission patterns, 2D spectroscopy requires a systematic excitation with particular multipulse sequences. These multipulse sequences are generated, in the experiment as well as in the simulation, by manipulating the spectral amplitude and phase of the aforementioned complex-valued laser spectrum to yield the respective combination of inter-pulse temporal delays and relative phases. In particular, the spectral amplitude and phase are reconstructed by FTSI measurements, as described in detail in Ch. 4, and used so that the generated multipulse sequences in the simulation matches those of the actual experiment as closely as possible. The temporal evolution of the local electric field $\mathbf{E}_{C,MP}$ is then determined by these particular multipulse

sequences (MP).

In Sec. 5.4 the nanoslit with length $L_{\mathrm{SEM}} = 290$ nm, shown in Fig. 5.5 (a), is investigated, which exhibits a nanoslit plasmon in resonance with the laser source, i.e., $\omega_{\mathrm{pp}} \sim \omega_0$, where ω_{pp} is the resonance frequency of the plasmon mode and ω_0 the center frequency of the measured laser spectrum. The local nonlinear electron emission yield $Y_{C,MP}(x,y)$ is simulated via $Y_{C,MP}(x,y) = \int |\mathbf{E}_{C,MP}(x,y,t)|^{2N} \mathrm{d}t$, where $N = 4$ is the nonlinearity of the electron emission process [6]. Due to the nanoslits' axial symmetry regarding the y axis, the yield at opposing x positions exhibits equal values at each y position. Consequently, the yield data is merged by averaging the two yield values of opposing x positions for each y position, which results in a line $Y_{MP}(y)$. Subsequently, $Y_{MP}(y)$ is cut and integrated along the y direction with respect to the y dimensions of the ROI depicted in Fig. 5.3. A detailed explanation of the FDTD-based 2D spectrum simulation process, which requires the calculation of $Y_{MP}(y)$ for all systematically varied inter-pulse time delays and relative phases, is described in Sec. 4.6.

The simulated 2D spectrum is then matched to the measured 2D spectrum (Fig. 5.3 (b), left) by fine-tuning of the geometrical parameters of the corresponding nanoslit according to a minimization of the RMSD. In this way the geometrical nanoslit parameters $L_{\mathrm{FDTD}} = 282$ nm and $w_{\mathrm{FDTD}} = 23$ nm have been found, which are in good agreement with the SEM-quantified values, as given in Fig. 5.5 (a). Note that the good agreement of the spectral position of the diagonal peak's signal maximum for the FDTD-based 2D spectrum and the quantified position in the corresponding 2D spectrum of the experiment (both shown in Fig. 5.3 (b)) results from the minimum RMSD optimization.

5.7. Detailed explanation of 3Q signal contributions within the quantum model

This section introduces the eigenstates of our quantum model. In particular, the multipulse-driven dynamics of the corresponding density matrix is translated into the language of DSFDs, which are conveniently utilized in coherent 2D spectroscopy to connect a signal contribution within a 2D spectrum to a particular evolution of the quantum system [166]. This procedure allows to identify the off-diagonal peaks in the measured 2D spectra as a coherent superposition of quantized harmonic oscillator states which represent the plasmon-polariton resonance of the nanoslit structure.

The presented quantum model describes the plasmon-polariton mode of the nanoslit as a QHO with eigenstates $|p\rangle$ and the metallic system of the Au mi-

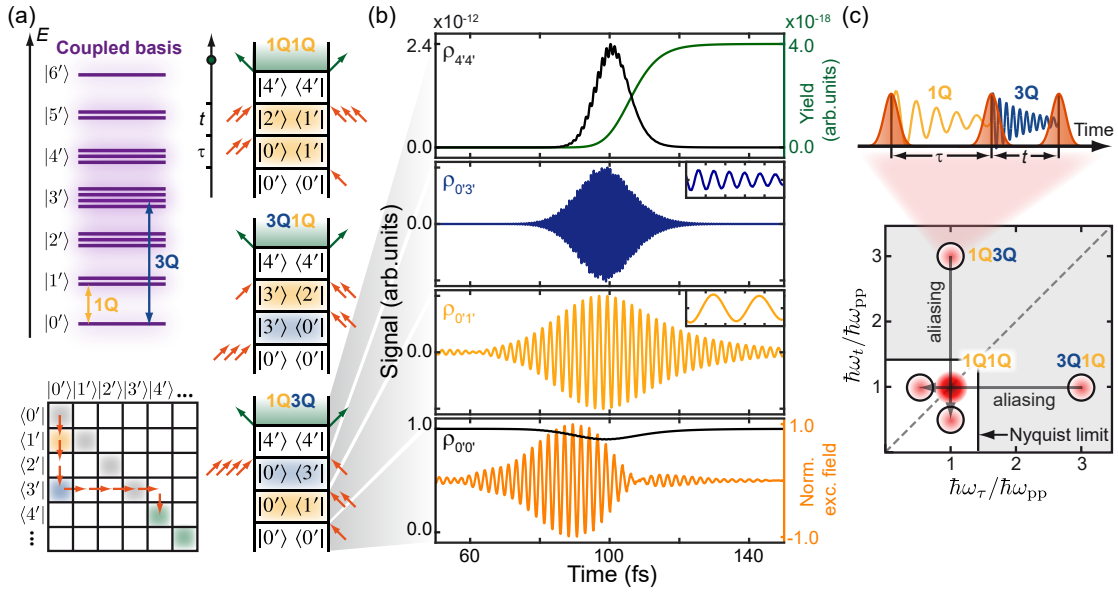

Figure 5.7 – Coupled-basis Liouville pathways and observation of 3Q coherences. (a), Top left, coupled-basis states (purple) with slightly lifted degeneracy and coupled-basis manifolds $|n'\rangle$ with $n \in \{0, ..., 6\}$. Bottom left, an exemplary Liouville pathway which contains multiple optical interactions (orange arrows) and which covers a single-quantum (1Q) coherence (yellow-shaded tile) and a 3Q coherence (blue-shaded tile). This Liouville pathway leads to a 1Q3Q signal contribution. Right column, some possible types of double-sided Feynman diagrams (DSFD) with general time-order indicated by the left black arrow: pure single-quantum (1Q1Q, top) and multi-quantum (3Q1Q, middle, or 1Q3Q, bottom) signal pathways contributing to the detected plasmon-assisted multi-quantum electron emission signal, where the green arrows indicate the unidirectional energy transfer from the plasmon polariton to the electron emission state. (b), Single-pulse-initiated (bottom, orange line) temporal dynamics of particular density matrix elements $\rho_{0'0'}$ (bottom, black line), $\rho_{0'1'}$ (yellow line), $\rho_{0'3'}$ (blue line), and $\rho_{4'4'}$ (top, black line) corresponding to the 1Q3Q DSFD (for details see main text). The slight oscillatory modulation of $\rho_{4'4'}$ is due to the presence of the optical excitation field. The incoherently transferred population to the electron emission state (top, green line) determines the detected electron emission yield. The insets for the second and third panel contain zoomed-in details of the data between 105 and 110 fs. (c), Systematic tuning of inter-pulse delays τ and t (top) enables sampling of 1Q as well as undersampling of 3Q coherences. The resulting single-quantum 2D spectrum (bottom), marked by the white area, features the 1Q1Q signal contribution along the diagonal (dashed line), and the back-folded 3Q peaks emerge next to the diagonal at energies corresponding to the respective aliased frequency axes. Reproduced from Ref. [3] with permission from Springer Nature.

croplate by fermionic single-particle states $|m\rangle$. Due to the weak coherent coupling between these two subsystems, a new set of coupled-basis states is obtained, which are structured in different quasi-degenerate coupled-basis manifolds $|n'\rangle$ with $n \in \{0, ..., 6\}$ (top left, Fig. 5.7 (a)). The number n' is here the sum of quantized excitations of both subsystems, e.g., $n' = 1'$ represents the case in which the plasmon exhibits a single excitation and the electronic system is in its ground state mixed with the case in which the electronic system carries a single excitation and the plasmon is in its ground state.

Since the coupling strength g of the plasmon $|p\rangle$ and the single-electron states $|m\rangle$ is small compared to the plasmon-polariton frequency, the energy degeneracy of each coupled-basis manifold $|n'\rangle$ is only slightly lifted and as a consequence, e.g., $|3'\rangle$ contains four quasi-degenerate states, explicitly depicted in Fig. 5.8. The energy spacing ΔE between adjacent manifolds, e.g., between $|3'\rangle$ and $|2'\rangle$, amounts to $\Delta E \sim \hbar\omega_{\mathrm{pp}}$. Note that each coupled-basis state is a superposition of a certain combination of product states $|pm\rangle$.

As introduced in Fig. 5.1, the excitation field connects adjacent plasmon states $|p\rangle$ and facilitates in this manner transitions between all coupled-basis manifolds $|n'\rangle$. As a consequence of the quasi-degeneracy of the states $|n'\rangle$, the semantic term "transition from $|2'\rangle$ to $|3'\rangle$" is an abbreviated formulation and contains in total twelve different transitions, i.e., connecting each of the three initial states of $|2'\rangle$ with the four different final states of $|3'\rangle$. For the sake of simplicity, the abbreviated manifold formulation $|n'\rangle$ is used in the following as a representative of a specific quantum state of the coupled system, while in the simulation using the quantum model *all* possible states are considered within such a manifold.

The quantum model is based on simulating the collective system response by numerically calculating the full time evolution of the density matrix ρ given by the Lindblad quantum master equation [196, 197] introduced in Sec. 2.4. In the following, this exact solution is treated in the framework of perturbation theory by expanding the density matrix as a power series with respect to the number of electric field interactions [167]. This perturbative approach is justified because of a low depopulation of the ground state, i.e., $|\,|0'\rangle\,|^2 > 0.9$ during the entire system evolution, and it enables us to use the language of DSFDs [166], a common way to visualize excitation pathways in 2D spectroscopy, as briefly introduced in Sec. 2.3.

Due to the high nonlinear dependence of the detected electron emission yield on the laser pulse intensity, the electric field of the multipulse sequence interacts multiple times with the system to reach the final electron emission state. The various combinations of intermediate states between the ground state and the final system state are typically described by so-called Liouville pathways (see Fig. 2.5) through the density matrix ρ. Figure 5.7 (a) (bottom left) exemplarily shows one

possible Liouville pathway. The experimentally determined nonlinearity $N = 4$ of the electron emission process states that the detected electron signal is dominated by Liouville pathways including at least eight field interactions (orange arrows).

In the Liouville pathway presented in Fig. 5.7 (a) (bottom left) a certain amount of the ground-state population (diagonal term $\rho_{0'0'} = |0'\rangle\langle 0'|$) is transferred by the first field interaction (orange arrow pointing down) to a coherence of the coupled-basis states $|1'\rangle$ and $|0'\rangle$ (off-diagonal term $\rho_{0'1'} = |0'\rangle\langle 1'|$). This density matrix element (yellow shade) oscillates with the frequency $\omega_{0'1'} = \frac{E_{|0'\rangle} - E_{|1'\rangle}}{\hbar} = -\frac{\Delta E}{\hbar}$ corresponding to the energy spacing ΔE between the associated manifolds during time interval τ, i.e., the time delay between the first and the second laser pulse of the multipulse sequence, and decays with the dephasing time T_2. It hence reads $\rho_{0'1'} \sim \mathrm{e}^{-i\omega_{0'1'}\tau}\mathrm{e}^{-\frac{\tau}{T_2}}$. The dephasing time T_2 is determined by the population relaxation time T_1 and the pure-dephasing time T_2^* via $\frac{1}{T_2} = \frac{1}{2T_1} + \frac{1}{T_2^*}$. Note that the energy spacing between adjacent coupled-basis manifolds is $\Delta E \sim \hbar\omega_{\mathrm{pp}}$, meaning that the element $\rho_{0'1'}$ oscillates with $-\omega_{\mathrm{pp}}$ during τ.

After the time interval τ, two subsequent field interactions (two down-pointing orange arrows) transfer the coherence $\rho_{0'1'}$ into a coherence $\rho_{0'3'}$ (blue element), oscillating with a frequency $\omega_{0'3'} \sim -3\omega_{\mathrm{p}}$ during a second time interval t, i.e., the time delay between the second and third laser pulse of the multipulse sequence. The most pronounced difference between these two coherences $\rho_{0'1'}$ and $\rho_{0'3'}$ becomes clear when considering their different temporal oscillation frequencies, which is emphasized by calling them one-quantum (1Q) and three-quantum (3Q) coherences, respectively.

To show that the characteristic oscillatory and dephasing behavior of the 1Q and 3Q coherences is also reproduced in the full quantum model, Fig. 5.7 (b) presents the explicit temporal dynamics of the corresponding density-matrix elements of the 1Q3Q pathway (see the DSFD in Fig. 5.7 (a), bottom right). By comparing the time evolution of the $\rho_{0'1'}$ coherence (yellow line) with the electric field oscillations of the driving laser pulse (reconstructed from FTSI, orange line), the expected oscillatory behavior with an oscillation frequency of $\omega_{\mathrm{pp}} \sim \omega_0$ is observed.

The time evolution of the $\rho_{0'3'}$ coherence (blue line) reveals an oscillation frequency three times higher than the $\rho_{0'1'}$ coherence (see the respective insets for details of the oscillation). Note that the density matrix elements are written here in the abbreviated form of the manifolds, e.g., $\rho_{0'3'} = |0'\rangle\langle 3'|$. Actually, the abbreviation $\rho_{0'3'}$ represents, according to the "degeneracy level", four different entries of the density matrix of the simulated quantum model, while $\rho_{0'1'}$ contains two entries. Since the degeneracy is only marginally lifted, the temporal evolution of the density matrix entries, represented by $\rho_{0'3'}$, is almost identical. The same

holds for $\rho_{0'1'}$. Therefore, the respective time traces are added up for illustration in Fig. 5.7 (b).

The detection of emitted electrons requires first of all that the coherence is transferred into a population. This is realized by the remaining five field interactions after time interval t, as depicted in the DSFD (Fig. 5.7 (a), bottom right) by the five remaining orange arrows. Secondly, the total amount of energy contained in the overall system has to overcome the work function. Remember that electron emission is modeled here only via plasmon decay due to the implemented incoherent population transfer, as labeled by the green arrows in Fig. 5.1. From the product states of the coupled basis (Fig. 5.8) it becomes clear that the population states $\rho_{0'0'}$, $\rho_{1'1'}$, $\rho_{2'2'}$, and $\rho_{3'3'}$ (grey diagonal elements in Fig. 5.7 (a), bottom left) do not fulfill the second condition. Only the population states $\rho_{4'4'}$, $\rho_{5'5'}$, and $\rho_{6'6'}$ (green elements in Fig. 5.7 (a), bottom left) are located at an energy above the work function, i.e., $4\hbar\omega_{\mathrm{pp}}$, $5\hbar\omega_{\mathrm{pp}}$, and $6\hbar\omega_{\mathrm{pp}}$, respectively, and for this reason contribute to the detection signal.

The top panel of Fig. 5.7 (b) exemplarily shows the temporal evolution of the $\rho_{4'4'}$ population state (black line) and the effective incoherent population transfer generating the electron emission yield (green line) in the non-perturbative approach.

In general, not only the example shown on the bottom left in Fig. 5.7 (a) has to be taken into account, but every possible Liouville pathway that includes at least eight field interactions and ends in a green-labeled population state. A reduction, and hence a selection, of possible pathways is achieved by using an appropriate phase-cycling scheme. Here a $1 \times 4 \times 4$ phase cycling scheme was applied, i.e., the simulation (and the experiment) have been repeated with 16 different combinations of relative phases between the pulses of the multipulse sequence and added up the respective electron signals with a respective weight, as described in detail in Sec. 2.3.5 and Sec. 4.6.

In Fig. 5.7 (a) (right column) three excitation pathway types are shown that mainly contribute to the plasmon-assisted electron emission signal, visualized by DSFD to emphasize their time structure (black arrow). These pathways give insight into the physical origin of signal peaks in the 2D spectrum and therefore lead to an explanation of the unexpected "off-diagonal" peaks. As seen in the 1Q1Q DSFD (Fig. 5.7 (a), right column), the depicted pathway leads through two different 1Q coherences oscillating with $|\omega_{\mathrm{pp}}|$ during both time intervals τ and t.

By systematically scanning both time delays τ and t between the constituent pulses of the exciting three-pulse sequence (Fig. 5.7 (c), top) the oscillations and the decay of the corresponding density-matrix elements evolving during these intervals are sampled. Based on the different signs and absolute values of the oscillation

frequencies of the sampled coherences, the resulting signal contributions are labeled as the rephasing 1Q1Q contribution, non-rephasing 3Q1Q contribution, and non-rephasing 1Q3Q contribution. The phrases "rephasing" or "non-rephasing" indicate whether the two oscillation frequencies of the coherences within a DSFD exhibit a different sign or the same sign, respectively.

Figure 5.7 (c) connects the acquired knowledge with the measured and simulated 2D spectra and explains how the 3Q coherences emerge in our 2D spectra. The individual oscillation frequencies and dephasing times T_2 characterizing the coherences are represented as signal peak positions and peak line shapes in a 2D spectrum after 2D Fourier transformation of the phase-cycled time-domain data. The peaks corresponding to Liouville pathways including a 3Q coherence appear outside of the experimentally sampled energy window due to a corresponding oscillation frequency higher than the Nyquist frequency (grey-shaded area in Fig. 5.7 (c), bottom). Because of the discrete sampling, these 3Q peaks are back-folded along the energy axis, sampling the 3Q coherence, to the experimentally accessible energy window (white area) and appear as aliased signal peaks shifted along the undersampled energy axis, which results in an "off-diagonal" peak position (see Sec. 5.8 for details).

Using the language of DSFDs, and 2D spectroscopy in general, delivers insight into the constituent coupled-basis states (Fig. 5.8) in our experiments. After diagonalization of the time-independent part of the full Hamilton operator $\mathcal{H}(t)$ as defined in Eq. (5.10.2), the coupled quantum system is described in the coupled basis (Fig. 5.8, left column) by new eigenstates $|n_i'\rangle$ (Fig. 5.8, right column) with index i labeling the quasi-degenerate states within a particular coupled-basis manifold $|n'\rangle$ and shifted eigenenergies (Fig. 5.8, middle column).

The eigenenergies of these states are determined by two contributions: First, the sum of the energy contained in the two individual subsystems, which is in our particular case the same for all contributing states. Since the energy spacing of both uncoupled plasmon states $|p\rangle$ and single-electron states $|m\rangle$ is ΔE, this contribution amounts to multiples of ΔE. The second contribution is an additional shift that depends on the coupling strength g between the corresponding plasmon $|p\rangle$ and single-electron states $|m\rangle$.

Its conversion from atomic units (a.u.) to SI units is achieved by multiplication with the Hartree energy E_h. Since the coupling is weak in our model ($g = 0.0027$ eV) the energy degeneracy of each coupled-basis manifold $|n'\rangle$ (purple states) is only slightly lifted as discussed in detail for Fig. 5.7. This results in an energy spacing between adjacent manifolds of about $\Delta E \sim \hbar\omega_{\mathrm{pp}}$ (orange arrow).

Each coupled-basis state (Fig. 5.8, right column) is a superposition of a certain

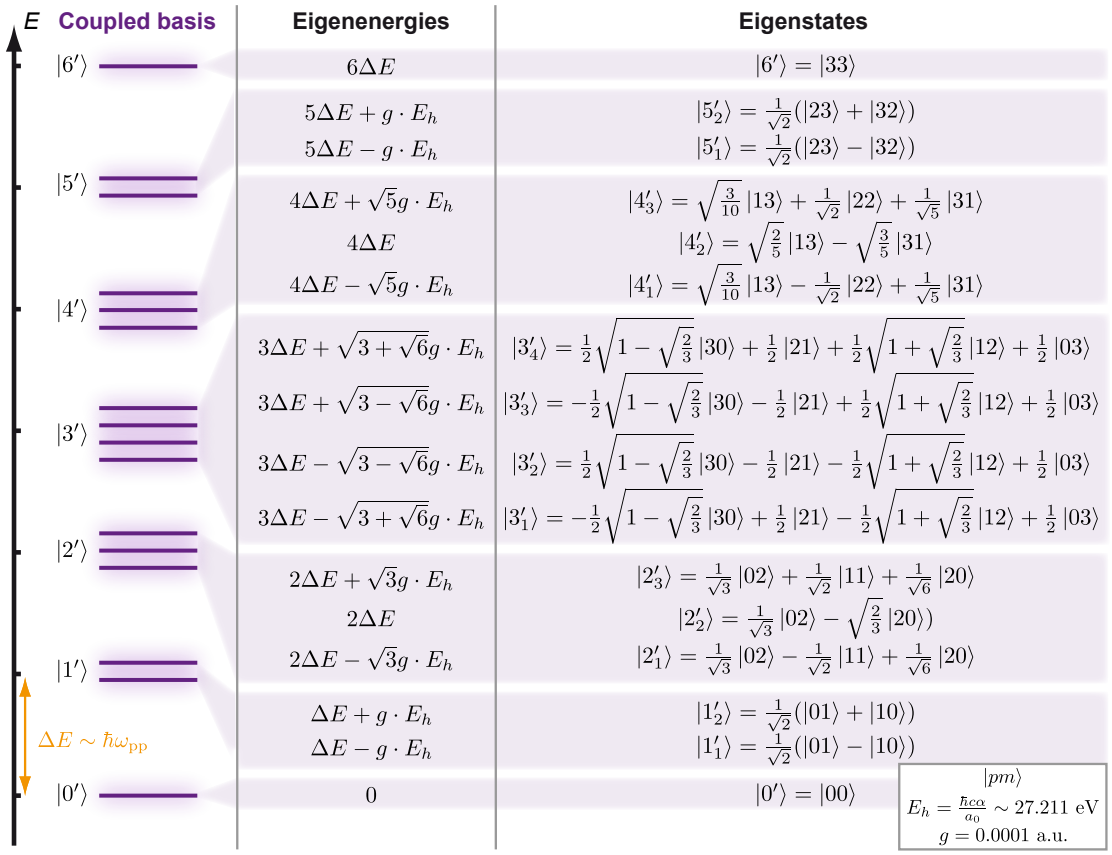

Figure 5.8 – Coupled-basis manifold with complete eigenenergies and eigenstates. Left column: Due to the coherent coupling between the plasmon-polariton states $|p\rangle$ and the electronic states $|m\rangle$, the coupled system is described in a new set of eigenstates (purple). Since the coherent coupling constant g is weak, the degeneracy of each coupled-basis manifold $|n'\rangle$ with $n \in \{0, ..., 6\}$ is only slightly lifted so that adjacent manifolds are energetically separated by $\Delta E \sim \hbar\omega_{\mathrm{pp}}$. Middle column: Eigenenergies for each coupled-basis eigenstate depending on the coupling constant g and the energy splitting ΔE. The constant quantity E_h labels the Hartree energy defined by the fine-structure constant α and the Bohr radius a_0 (bottom right inset). Right column: Coupled-basis eigenstates $|n'_i\rangle$ with $n_i \in \{0, ..., 6\}$, where the index i labels the quasi-degenerate states within a particular manifold. The coupled-basis states are written as superposition of the corresponding product-basis states $|pm\rangle$. Reproduced from Ref. [3] with permission from Springer Nature.

combination of product states $|pm\rangle$. The contribution of each product state $|pm\rangle$ to the corresponding coupled-basis state is given by the individual weighting factor multiplied with $|pm\rangle$ which depends in general, apart from normalization, on the

so called mixing angle θ, as defined, e. g., for two coupled two-level systems [255].

The identification of the measured "off-diagonal" peaks as indicators of coherences between various quantum states reveals that multi-quantum excitations of the QHO play a significant role in the plasmon-assisted multiphoton electron emission process. This interpretation is further verified by the fact that the corresponding multi-quantum peaks disappear in simulated rephasing 2D spectra using only one excitation level in the QHO, as shown in Fig. 5.4.

5.8. Spectral positions of multi-quantum peaks in single-quantum 2D spectra

Based on the experimentally defined pulse-sequence parameters, as defined in Sec. 5.9, e.g., central frequency of excitation spectrum ω_0 and size of delay steps δt, the sampled oscillation frequencies define a certain energy window (white area in Fig. 5.7 (c)) along the $\hbar\omega_\tau$ and $\hbar\omega_t$ axes in the laboratory frame [167]. The upper frequency limit of this window, given by the Nyquist limit, is calculated in the laboratory frame according to $\hbar\omega_{\tau,t}^{\max} = \hbar\omega_0(1-\gamma) + \frac{\hbar\pi}{\delta t} = 1.956$ eV using our sequence parameters $\hbar\omega_0 = 1.755$ eV, delay step size $\delta t = 4$ fs and rotating-frame factor $\gamma = 0.18$ (as introduced in Sec. 5.9).

Since the oscillation frequency ω_{pp} of the 1Q coherences is located within this window, the signal peak corresponding to the 1Q1Q-type of signal pathways (see top right of Fig. 5.7 (a) for the corresponding DSFD) appears along the diagonal of the 2D spectrum (grey dashed line) at energies $\hbar\omega_\tau = \hbar\omega_t = \hbar\omega_{\mathrm{pp}}$. The peaks corresponding to Liouville pathways including a 3Q coherence appear outside of the sampled energy window due to an oscillation frequency higher than the Nyquist limit. These multi-quantum peaks, i.e., the 1Q3Q signal and the 3Q1Q signal, are back-folded along the energy axis via undersampling the 3Q coherence.

Due to the fact that the undersampling takes place directly during the measurement process, the oscillation frequency of a particular signal contribution is (under-)sampled in the partially rotating frame ($\gamma = 0.18$) which is depicted in Fig. 5.9 (b). In this frame a particular signal contribution oscillates at the difference frequency $\Delta\omega_{\tau,t} = \omega_{\tau,t} - \omega_{\mathrm{ref}}$ with $\omega_{\mathrm{ref}} = (1-\gamma)\omega_0$ and laboratory-frame frequency $\omega_{\tau,t}$ [285]. The undersampled signal, originally oscillating in the partially rotating frame at energy $\Delta\hbar\omega_{\tau,t}$, appears at aliased energy $\Delta\hbar\omega_{\tau,t}^{\mathrm{alias}}$ at the corresponding energy axis. The aliased energy is calculated by

$$\begin{aligned} \Delta\hbar\omega_{\tau,t}^{\mathrm{alias}} &= -\Delta\hbar\omega_{\tau,t}^{\max} + |\Delta\hbar\omega_{\tau,t} - \Delta\hbar\omega_{\tau,t}^{\max}| \quad \text{for} \quad \Delta\hbar\omega_{\tau,t} > 0, \\ \Delta\hbar\omega_{\tau,t}^{\mathrm{alias}} &= \Delta\hbar\omega_{\tau,t}^{\max} - |\Delta\hbar\omega_{\tau,t} + \Delta\hbar\omega_{\tau,t}^{\max}| \quad \text{for} \quad \Delta\hbar\omega_{\tau,t} < 0. \end{aligned} \tag{5.8.1}$$

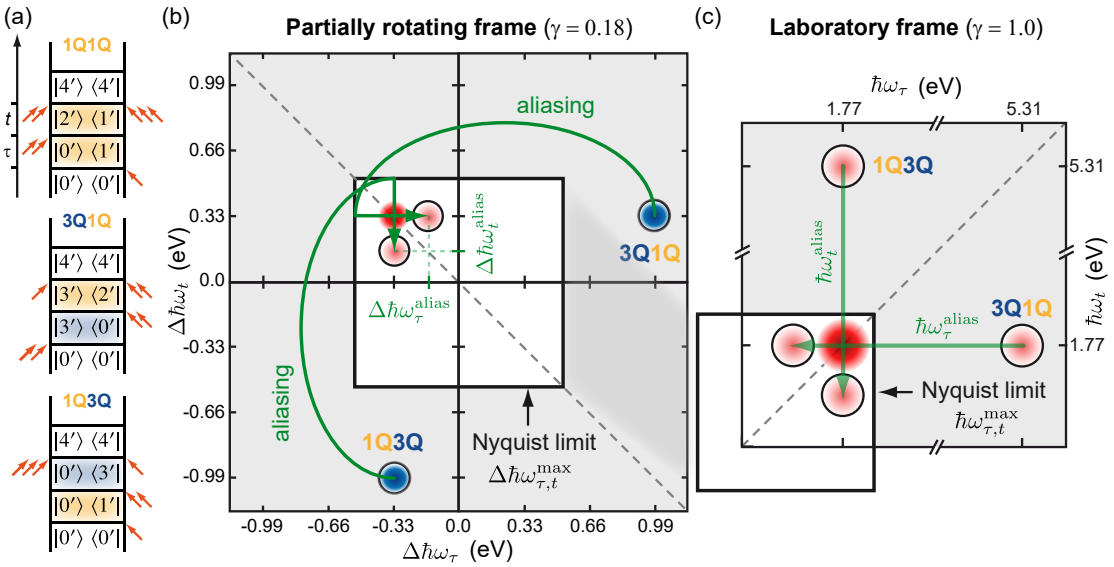

Figure 5.9 – Spectral back-folding of undersampled multi-quantum peaks due to aliasing. (a) From top to bottom, exemplary single-quantum DSFD (1Q1Q) and multi-quantum DSFD (3Q1Q and 1Q3Q), as introduced in Fig. 5.7. (b) Schematic representation of the oscillation frequency, i.e., the spectral position of individual single- and multi-quantum signal contributions in the partially rotating frame, defined by the rotating-frame factor $\gamma = 0.18$. In contrast to the rephasing single-quantum contributions (red), which are unaffected by aliasing, the originally non-rephasing multi-quantum contributions (blue) get back-folded, due to the aliasing effect (green arrows), to the sampled energy window (white area). The edges of the sampled energy window are defined by the corresponding Nyquist limit which results in $\pm\Delta\hbar\omega_{\tau,t}^{\mathrm{max}}$. In our particular case the experimentally undersampled multi-quantum contributions appear at aliased energies $\Delta\hbar\omega_{\tau,t}^{\mathrm{alias}}$ (green, see Eq. (5.8.1)) in the rephasing quadrant (upper left, as defined in Fig. 2.5 (e)). Thus, the originally non-rephasing (blue) multi-quantum contributions are sampled as rephasing (red) contributions at aliased frequencies $\Delta\omega_{\tau,t}^{\mathrm{alias}}$. (c) After flipping of the $\Delta\hbar\omega_{\tau}$-axis, to accomplish an intuitive sign representation of this energy axis, the energies of both axes $\Delta\hbar\omega_{\tau,t}$ within the sampled energy window are transformed to the corresponding oscillation energies $\hbar\omega_{\tau,t}$ in the laboratory frame (see Eq. (5.8.2)). In this frame, the multi-quantum contributions emerge at aliased energies $\hbar\omega_{\tau,t}^{\mathrm{alias}}$ (green) and below the laboratory-frame Nyquist frequency $\hbar\omega_{\tau,t}^{\mathrm{max}}$. Here it should be emphasized that in fact the width of the sampled energy window $2\Delta\hbar\omega_{\tau,t}^{\mathrm{max}} = 1.034$ eV is unaffected by the transformation between frames. Nevertheless, the main information is accumulated in the flipped rephasing quadrant (now upper right) which is emphasized by the chosen data representation as presented, e.g, in Fig. 5.3.

Here, the Nyquist limit of the partially rotating frame $\Delta\hbar\omega_{\tau,t}^{\max}$ (Fig. 5.9 (b), black frame) is determined via $\Delta\hbar\omega_{\tau,t}^{\max} = \frac{\hbar\pi}{\delta t} = 0.517$ eV. Note that for the "non-aliased" case, corresponding to $l = 0$, the sign of the last term in both equations must be inverted. The factor l corresponds to the "amount" of aliasing of the undersampled signal, $l = \text{floor}\left(\frac{\Delta\hbar\omega_{\tau,t}}{\Delta\hbar\omega_{\tau,t}^{\max}}\right)$, where "floor" indicates the largest integer less than or equal to its argument.

In our case the signal leads to peaks that contain contributions of a 3Q coherence at laboratory-frame oscillation frequency $\pm 3\omega_{\text{pp}}$. As a consequence, these signal peaks at energy positions $\Delta\hbar\omega_{\tau,t} = \pm(3 \cdot 0.33)$ eV in the partially rotating frame are back-folded (green arrows) to the sampled energy window, resulting in aliased energy positions $\Delta\hbar\omega_{\tau,t}^{\text{alias}} = \mp 0.04$ eV. Since $l = 1$ the oscillation frequency $\Delta\omega_{\tau,t}$ is aliased once before the back-folded signal appears in the sampled frequency window in the partially rotating frame given by $-\Delta\omega_{\tau,t}^{\max} \leq \Delta\omega_{\tau,t} \leq \Delta\omega_{\tau,t}^{\max}$. Note that in case of the 3Q signals the sign of the aliased energy position is inverted compared to the sign of the oscillation frequency before back-folding. For this reason, originally non-rephasing (blue in Fig. 5.9 (b)) contributions as, e.g., 1Q3Q and 3Q1Q, appear in the energy window of the rephasing (red in Fig. 5.9 (b)) 1Q1Q contribution.

Finally, the aliased energy position along the corresponding energy axis $\hbar\omega_{\tau,t}$ in the laboratory frame, as depicted in Fig. 5.9 (c), is determined by the general transformation equations

$$\begin{aligned} \hbar\omega_{\tau,t}^{\text{alias}} &= |\Delta\hbar\omega_{\tau,t}^{\text{alias}}| + (1-\gamma)\hbar\omega_0 \qquad \text{for} \quad \Delta\hbar\omega_{\tau,t} > 0, \\ \hbar\omega_{\tau,t}^{\text{alias}} &= -\Big(|\Delta\hbar\omega_{\tau,t}^{\text{alias}}| + (1-\gamma)\hbar\omega_0\Big) \quad \text{for} \quad \Delta\hbar\omega_{\tau,t} < 0. \end{aligned} \tag{5.8.2}$$

using the above defined pulse-sequence parameters ($\hbar\omega_0 = 1.755$ eV and $\gamma = 0.18$).

The lower peak below the 1Q1Q peak, emerging at energies $\hbar\omega_\tau = 1.77$ eV and $\hbar\omega_t^{\text{alias}} = 1.48$ eV, is identified as a multi-quantum peak resulting from 1Q3Q signal contributions (DSFD shown in Fig. 5.9 (a), bottom). The peak on the left side of the 1Q1Q peak, located at energies $\hbar\omega_\tau^{\text{alias}} = 1.48$ eV and $\hbar\omega_t = 1.77$ eV, arises from the back-folded 3Q1Q signal contributions (DSFD shown in Fig. 5.9 (a), middle).

5.9. Parameters of the experimental setup

A detailed description of the whole experimental apparatus is found in Ch. 3. Here the individual settings and parameters of the different setup components as used

in the 2D nanoscopy experiments presented in this chapter are briefly summarized.

The NOPA (Riedle group, LMU Munich), pumped by an Yb-doped fiber laser (Amplitude Systèmes, Tangerine HP), was used for frequency conversion and tuned to a central wavelength of about $\lambda_0 = 706$ nm at 1 MHz repetition rate. Laser pulses were pre-compressed by a prism compressor, removing mainly the second-order dispersion, and final compression to a pulse length of $\Delta t_{\mathrm{pulse}} = 18$ fs (extracted from the FWHM, of the intensity autocorrelation function assuming a temporal and spectral Gaussian intensity profile) was achieved by a LCD-based pulse shaper (Jenoptik, SLM-S640d USB). Full pulse characterization was performed using collinear SHG-FROG for the compressed pulses and FTSI for each applied three-pulse sequence, as described in Ch. 4. Pulse sequences were generated by amplitude and phase shaping of the compressed pulse by the same pulse shaper used for compression.

For 2D nanoscopy, the inter-pulse delays τ and t were systematically scanned in a partially rotating frame [190] ($\gamma = 0.18$) from $\tau, t = 0$ to 112 fs with step sizes of $\delta\tau = \delta t = 4$ fs and a $1 \times 4 \times 4$ phase-cycling scheme [70] was performed for each delay combination. The factor γ defines here the reference frequency of the particular frame, $\omega_{\mathrm{ref}} = (1 - \gamma)\omega_0$, and can in principle vary between $\gamma = 0$, where the measurement is performed in the fully rotating frame rotating at the central frequency ω_0 of the exciting pulse train, and $\gamma = 1$, corresponding to the laboratory frame where $\omega_{\mathrm{ref}} = 0$. Since the sampled signal oscillations ω oscillate in the particular frame at the difference frequency $\omega - \omega_{\mathrm{ref}}$, a smaller frequency sampling rate is sufficient in the (partially) rotating frame compared to the laboratory frame, which enables larger time steps $\delta t_{\mathrm{max}} = \frac{\pi}{|\omega - \omega_{\mathrm{ref}}|_{\mathrm{max}}}$.

To avoid space-charge effects of the detected electrons, the sample was irradiated under normal incidence with pulses of ~ 37 nJ energy that were focused to an illumination spot diameter size of ~ 270 µm. The polarization of the excitation pulse sequence was adjusted to be perpendicular to the long slit axis (parallel to the excited dipole mode) of the nanostructure to maximize the emission yield.

The electrons, emitted from a field of view with a diameter of 5 µm, were transferred by our photoemission electron microscope (customized AC-LEEM, ELMITEC Elektronenmikroskopie GmbH) to the detection unit after aberration corrector (AC) by a mirror-type aberration corrector and k-space filtering by a contrast aperture (diameter 60 µm). The detection unit consisted of a chevron-type micro-channel plate (MCP), for electron multiplication, and a phosphor screen, for electron-to-photon conversion, which was imaged by a CCD camera. The micro-channel plate voltage $U_{\mathrm{MCP}} = 1.3$ kV was used to set the gain of each MCP channel acting as a continuous dynode electron multiplier and the screen voltage $U_{\mathrm{Screen}} = 5.6$ kV decelerated the incoming electrons. PEEM images were acquired with 10 s integration time. To compensate for small spatial drifts between mea-

surement steps (within a total measurement time of $\sim$ 67 h), a drift vector was generated from reference images integrated over 100 ms acquisition time and using a single compressed pulse for illumination. Image drift correction was then performed using ImageJ (Version: 1.52a, Plugin: Template Matching).

5.10. Detailed description and parameters of the quantum model

To simulate the electron emission signal, calculations have been preformed to track the time evolution of the density matrix in the product basis $\rho(t) = \rho_{\mathrm{m}}(t) \otimes \rho_{\mathrm{p}}(t)$, where $\rho_{\mathrm{m}}(t)$ and $\rho_{\mathrm{p}}(t)$ represent the density matrix of the metal and plasmon-polariton subsystem, respectively.

5.10.1. Quantum dynamical simulation

The time evolution was tracked by numerically integrating the Lindblad quantum master equation, as introduced in Sec. 2.4, using our own, publicly available, program package for Matlab (QDT: `https://qd-toolbox.org`),

$$\frac{\partial \rho(t)}{\partial t} = -\frac{i}{\hbar}\Big[\mathcal{H}(t), \rho(t)\Big] + \sum_k \gamma_k \Big(\mathcal{L}_k \rho(t) \mathcal{L}_k^\dagger - \frac{1}{2}\mathcal{L}_k^\dagger \mathcal{L}_k \rho(t) - \frac{1}{2}\rho(t)\mathcal{L}_k^\dagger \mathcal{L}_k\Big), \quad (5.10.1)$$

in which the Lindblad terms for explicit transitions k account for population relaxation and pure dephasing between particular states using the corresponding Lindblad operators $\mathcal{L}_k \in \Big\{\mathcal{L}_k^{\mathrm{rel}} = |i\rangle\langle j|, \mathcal{L}_k^{\mathrm{deph}} = |i\rangle\langle i| + |j\rangle\langle j|\Big\}$, where i, j are related to either the individual plasmon-polariton states or the electronic states included in the transition k.

The individual decay rates γ_k are defined in terms of time constants T_k, via $\gamma_k = \frac{1}{T_k}$, where the time constant $T_{1,\mathrm{k}}$ is the population relaxation time connected with a particular transition k and $T_{2,\mathrm{k}}^*$ labels the individual pure-dephasing time between the states i, j contained in the transition k.

The full Hamilton operator $\mathcal{H}(t)$ is given by

$$\mathcal{H}(t) = \mathcal{H}_{\mathrm{e}} + \mathcal{H}_{\mathrm{b}} + \mathcal{H}_{\mathrm{cc}} + \mathcal{H}_{E_{\mathrm{exc}}}(t). \quad (5.10.2)$$

Herein, the time-independent diagonalized Hamilton operators $\mathcal{H}_{\mathrm{e}}$ and $\mathcal{H}_{\mathrm{b}}$ contain the eigenenergies of the electronic states in the metal and the harmonic oscillator states, respectively, of the bosonic plasmon-polariton mode; the Hamiltonian $\mathcal{H}_{\mathrm{cc}}$ describes the coherent coupling between plasmon polariton and single-electron

excitations in the metal; and $\mathcal{H}_{E_{\mathrm{exc}}}(t)$ describes the interaction of the excitation pulse sequence with the bosonic mode. Using creation and annihilation operators $\mathrm{b}^\dagger$ and b, respectively, for the bosonic plasmon polariton, $\mathcal{H}_{\mathrm{b}}$ is given by

$$\mathcal{H}_{\mathrm{b}} = \hbar\omega_{\mathrm{pp}}(\mathrm{b}^\dagger\mathrm{b}), \tag{5.10.3}$$

with the plasmon-polariton resonance frequency ω_{pp}. Note that the eigenstates are the number states $|p\rangle$ defined by

$$\hbar\omega_{\mathrm{pp}}(\mathrm{b}^\dagger\mathrm{b})\,|p\rangle = p\hbar\omega_{\mathrm{pp}}\,|p\rangle\,, \quad (p = 0, 1, 2, 3) \tag{5.10.4}$$

and $\mathrm{b}^\dagger$ and b act on these states as

$$\begin{aligned} \mathrm{b}^\dagger\,|p\rangle &= \sqrt{p+1}\,|p+1\rangle\,, \\ \mathrm{b}\,|p\rangle &= \sqrt{p}\,|p-1\rangle \end{aligned} \tag{5.10.5}$$

The bosonic mode is driven by the external field $E_{\mathrm{exc}}(t)$, whose polarization direction was set, by definition, to be parallel to the excited dipole mode. The related term in the Hamiltonian is then given by [286]

$$\mathcal{H}_{E_{\mathrm{exc}}}(t) = -\sqrt{\frac{\hbar}{2m_0\omega_{\mathrm{pp}}}}(\mathrm{b}^\dagger + \mathrm{b})E_{\mathrm{exc}}(t), \tag{5.10.6}$$

using the electron mass m_0. Note that for each time step in the simulation of reported 2D spectra, individually defined optical driving fields $E_{\mathrm{exc}}(t)$ have been used that varied from step to step. These fields were either determined directly in the experiment for each different excitation sequence using FTSI, as described in Ch. 4, or they were calculated for a sequence of Gaussian pulses using the given relative delays and phases of the three pulses used for excitation.

To describe the excitation pathways in the metal, a multilevel fermionic ladder $\{|0\rangle\,, |1\rangle\,, |2\rangle\,, |3\rangle\}$ was implemented and the free electron state $|4\rangle$ using the time-independent Hamiltonian

$$\mathcal{H}_{\mathrm{e}} = \sum_{m=0}^{4} m\hbar\omega_{\mathrm{pp}}\,|m\rangle\,\langle m|\,. \tag{5.10.7}$$

Within the rotating-wave approximation [167], the coherent coupling term enabling a bidirectional energy exchange between the plasmon-polariton states and the intermediate metal states is given by

$$\mathcal{H}_{\mathrm{cc}} = \sum_{m=1}^{3} g(\sigma_m^+\mathrm{b} + \sigma_m^-\mathrm{b}^\dagger), \tag{5.10.8}$$

featuring the coupling constant g and the fermionic creation and annihilation operators σ_m^+ and σ_m^-, respectively. These operators take into account only single-quantum transitions $|m-1\rangle \rightarrow |m\rangle$ in the case of σ_m^+ and $|m\rangle \rightarrow |m-1\rangle$ in the case of σ_m^-. This results in a coherent coupling between the plasmon-polariton states and the intermediate states of the metal system in which annihilation in the individual subsystems can only drive single-quantum transitions in the other subsystem.

The incoherent unidirectional population transfer needed to correctly model the final electron emission step was adapted from Plenio *et al.* [287]. It simulates the decay of the plasmon mode that in turn drives the final electron emission step with a rate constant $1/T_{\mathrm{inc}}$. The population transfer is described by the Lindblad term

$$L_{\mathrm{inc}}(\rho) = \frac{1}{T_{\mathrm{inc}}}\Big(-\{\mathrm{b}^\dagger\sigma_4^-\sigma_4^+\mathrm{b},\rho\} + 2\sigma_4^+\mathrm{b}\rho\mathrm{b}^\dagger\sigma_4^-\Big). \tag{5.10.9}$$

The curly brackets labeling here the anti-commutator and σ_4^+ and σ_4^- the raising and lowering operators, respectively, connecting only the highest intermediate state $|3\rangle$ with the free-electron state $|4\rangle$. This formulation models the electron-emission process to be driven by the annihilation of a plasmon polariton.

The "detection" signal was simulated using time steps of 0.1 fs for each specific multipulse sequence by calculating the electron emission yield Y, i.e., the population of state $|m=4\rangle$, at a final simulation time of 500 fs chosen such that a stationary population was reached. Note that the simulated 2D spectra are unaffected if the field amplitude of $E_{\mathrm{exc}}(t)$ is increased by an order of magnitude and hence artifacts are excluded due to the truncation of the harmonic oscillator ladder.

5.10.2. Simulation parameters of the quantum model

The plasmon polariton was modeled as a bosonic QHO including 4 levels at an energy spacing of $\Delta E = \hbar\omega_{\mathrm{pp}} = 1.766$ eV (see Fig. 5.1). The energy spacing ΔE and the plasmon-polariton population relaxation time $T_1 = 11$ fs were determined by minimizing the RMSD between simulated and measured 2D spectra, as described in detail in App. E. Note that for the plasmon-polariton mode, dephasing (T_2) is modeled via population relaxation only and an infinite pure-dephasing time T_2^* is assumed (as argued in Sec. 2.2.1), i.e., the plasmon-polariton linewidth was fully determined by T_1.

The energy spacing between the individual intermediate states $|m\rangle$ and the electron emission state $|4\rangle$ in the fermionic ladder system was given by the energy spacing ΔE to match that of the plasmon system. This is due to the fact that the dynamics in the fermionic system are purely driven by the plasmonic system and

thus the energetic spacing of the fermionic ladder system is set by the plasmon-polariton quantum.

The pure-dephasing time of all intermediate states was set to $T_2^* = 4$ fs and set to $T_2^* = 0.5$ fs for the free electron state $|4\rangle$. Note that for the intermediate states this is a conservative upper limit reflecting that metal excitations do in fact occur via a continuum of states which cancels practically all coherence effects in the multi-quantum metal excitation [57].

The population relaxation time T_1 of the intermediate states were adjusted with respect to measurement data [68] and amounted to $T_1^{|1\rangle\rightarrow|0\rangle} = 299$ fs; $T_1^{|2\rangle\rightarrow|1\rangle} = 39$ fs and $T_1^{|3\rangle\rightarrow|2\rangle} = 5$ fs. This is in accordance with Fermi-liquid theory, which states that $T_1 \sim 1/(E - E_\mathrm{F})^2$, where E is the energy of the upper state of a particular transition and E_F is the Fermi energy [68].

Further the intermediate states were not driven directly by the external multi-pulse sequence, but rather by the coherent coupling term $\mathcal{H}_\mathrm{cc}$ (see Fig. 5.1) via the population dynamics of the plasmon polariton. The coherent coupling constant g was fixed to $g = 0.0027$ eV to establish a weak coupling, quantified by relating the resulting energetic splitting $\Delta E_\mathrm{cc} = 2g$ to the FWHM of the optical excitation $\Delta E_\mathrm{exc}^\mathrm{FWHM}$ leading to $\Delta E_\mathrm{cc} = 0.0054$ eV $\ll \Delta E_\mathrm{exc}^\mathrm{FWHM} = 0.137$ eV.

The final electron emission step was modeled by an incoherent unidirectional population transfer [287] driving the excitation $|3\rangle \rightarrow |4\rangle$ from the last intermediate state to the final electron emission state with a transfer rate $1/T_\mathrm{inc} = 1/242$ fs^{-1}. Solving the Lindblad master equation for single-pulse excitation revealed an electron emission yield that depended on the pulse energy to the power of four, as depicted in Fig. 5.6 (c), in agreement with the experimentally observed intensity dependence.

5.11. Conclusion

In conclusion, employing 2D nanoscopy and a newly introduced quantum model for plasmon-assisted multi-quantum electron emission, enables to measure the quantum coherence between plasmon-polariton occupation number states $|p\rangle$ that exhibit an energy difference of $3\hbar\omega_\mathrm{pp}$, i.e., three times the fundamental plasmon energy.

Quantum coherences arising from a superposition of occupation number (Fock) states of *one* particular plasmonic mode must be clearly distinguished from classical plasmonic wave packets, i.e., superpositions of classical oscillations of *different* plasmonic modes; the latter had already been studied intensively using, for example, PEEM [84, 144, 146, 259, 261, 288], but not the former. Detecting a quantum coherence of the superposition of just two stationary states, in this work the Fock

states of the quantized plasmon polariton, is a direct fingerprint of the entire plasmon-polariton quantum wave packet and provides an unprecedented spatially and temporally resolved view on parts of the plasmon-polariton quantum state.

Even though a complete reconstruction of the quantum state of the plasmon polariton is not shown, modeling the plasmon polariton as a quantum harmonic oscillator enables the description of the interaction of all subsystems via their respective annihilation and creation operators. The benefit of this is that the dynamics of all components of the overall system can be described and understood within the framework of the density-matrix formalism. This will become explicitly important in the discussion of the interaction of plasmon polaritons and quantum emitters.

Note that by proper choice of the sampling steps $\delta\tau$ and δt, and a specific phase-cycling scheme [70], coherent 2D spectroscopy becomes sensitive to various quantum coherences, i.e., the various off-diagonal elements of the density matrix of the plasmon polariton that oscillate at multiples of the fundamental plasmon frequency. Interestingly, the photoelectron detection channel relies on the inherent ohmic losses of plasmon polaritons, i.e., Landau damping (see Sec. 2.2), hence a quantum-state reconstruction would also work for dark modes.

Recently, cavity-mode quantum statistics were probed by high-energy free electrons interacting with the cavity field [289]. The here-demonstrated method realizes a similar concept for metal electrons where the detection of quantum coherences now requires time-resolved spectroscopy methods instead of energy-resolved detection used in Ref. [289]. However, the underlying mechanisms are closely related, which suggests that the here-demonstrated method could indeed be extended to not only detect a plasmon-polariton quantum wave packet, but to also reveal the quantum statistics of a particular plasmon-polariton quantum state.

Beyond these utilizations, the quantum model of plasmon-polariton-assisted multi-quantum electron emission developed here could also shed light on the role of plasmon-related nonlinear effects such as plasmon-assisted fragmentation and ionization of clusters [290–292] or the recently demonstrated “non-Einsteinian” plasmoemission component [293–295].

CHAPTER

SIX

SUMMARY AND OUTLOOK

In this work, a versatile multidimensional spectroscopy setup was realized and characterized to detect the temporally- and spatially-resolved nonlinear electron emission from surface systems via coherent two-dimensional (2D) nanoscopy. It was shown that coherent 2D nanoscopy enables to monitor quantum coherences which exist due to superposition of certain quantum states of the investigated sample system. Based on the experimentally achieved and simulated data the time scales, coupling parameters, and transfer mechanisms which determine the preparation process of these quantum states and the ultrafast nonlinear emission process itself were identified and quantified for a nanostructured plasmonic sample.

After a brief introduction of the theoretical concepts of linear and nonlinear electron emission, plasmonics, coherent 2D nanoscopy, and modeling of induced temporal-dynamics in open quantum systems, the experimental apparatus designed and assembled during this thesis was described.

The particular setup is based on a fiber-laser coupled, two-output noncollinear optical parametric amplifier (NOPA) system and offers sub-20 fs laser pulses with broad spectral tunability (effective range $215 - 970$ nm) at 1 MHz repetition rate and pulse energies of $300 - 600$ nJ. The sub-20 fs pulses with spectral components between $600 - 800$ nm were modified in a self-build liquid-crystal display (LCD)-based pulse shaper, whose main task is to generate interferometric-stable multipulse sequences and to systematically and precisely tune the temporal interpulse delays and offset-phases by amplitude- and phase-shaping. This thesis focused in particular on the assembly and quality of the pulse-shaper setup. The applied measurement schemes were discussed to quantify a precise setup align-

ment, Fourier-plane focusing, SLM calibration, and amplitude shaping and thus validated the successful assembly of the setup. The presented proof-of-principle experiments utilized amplitude- and phase-shaped pulse sequences in combination with nonlinear electron emission as a sensitive tool to probe the local response of plasmonic nanoresonators.

Optical excitation of the corresponding sample system, located in ultra-high vacuum (UHV) at room temperature, triggered non-linear electron emission which was spatially-resolved detected via photoemission electron microscopy (PEEM). A brief overview of the customized electron microscope and its additional features was provided, and the quantification of the system's steady-state spatial resolution of < 5 nm and the sample-depended resolvable minimum length scale (here: < 25 nm) was discussed.

It was shown that combining the femtosecond temporal resolution of the optical excitation with the high spatial-resolution of PEEM enables investigation of surface systems by coherent 2D nanoscopy. This technique selectively maps different excitation pathways through various quantum states of the sample, generally allowing to probe changes in the populations and coherences of the density matrix representing the system under study. As demonstrated in this work, this method enabled access to individual superpositions of quantum states directly at the location of the probed system and further allowed to disentangle relevant energy-transfer mechanisms and time scales on the nanoscale.

Prior to the detailed analysis of the nonlinear electron emission process of optically excited plasmonic nanoresonators, this thesis presented a precise quantification of the time-domain structure of the generated pulse sequences based on a performance efficient linear spectral-domain method called Fourier-transform spectral interferometry (FTSI). The complete electric field of each individual pulse sequences was reconstructed and relevant pulse-sequence parameters (maximum intensities, inter-pulse delays and inter-pulse offset-phases) were extracted and systematically compared with the corresponding parameters of idealized pulse-sequences to quantify deviations. The deviations could be traced back to experimental instabilities like systematic NOPA intensity fluctuations or intrinsic pulse-shaping imperfections.

Further, the reconstructed real and ideal pulse sequences were implemented as excitation fields in theoretical simulations of particular 2D spectra. In doing so, the potential effect of real pulse sequences on signal features of the spectral data obtained by fluorescence-based 2D spectroscopy and electron-based 2D nanoscopy was studied. It was shown that the quantified systematic and random deviations only slightly affect the characteristics of the obtained 2D spectra. In case of significant impact on, e.g., the general structure, peak position or linewidth of the

simulated 2D spectra, established corrections were introduced, applied and evaluated. Since the FTSI method allows data acquisition in parallel to a performed experiment, e.g., coherent 2D nanoscopy, the reconstructed pulse sequences were also used in simulations to explain the measured spatially resolved 2D spectra of plasmonic nanoresonators.

The last part of the thesis covered the investigation of the nonlinear electron emission from a plasmonic nanoresonator by 2D nanoscopy and emphasized the application of this technique to disentangle the induced time dynamics and to probe and monitor superpositions of quantum states directly at the nanoscale. The optical excitation generated localized surface plasmon-polaritons in the nanoresonator, whose local field enhancement enables highly nonlinear electron emission. Interestingly, the detailed structure of the spectral features in the measured 2D spectra could not be reproduced using the established semiclassical approach based on the local electric field of the nanoresonator response calculated by an finite-difference time-domain (FDTD)-method. Hence, a new quantum model of the nonlinear electron emission from plasmonic systems were developed and applied in this thesis.

This quantum model treats one single plasmon-polariton mode as an optically driven quantum harmonic oscillator (QHO) and reduces the complicated metallic band-structure to a ladder system of equally-spaced discrete electronic states. The excitation dynamics in the ladder system were only driven by the dynamics of the plasmon-polariton mode which was weakly coupled to the ladder-system in a coherent fashion. Further, the final electron-emission step from a discrete bound-state of the ladder system to the free-electron continuum was modeled by an incoherent unidirectional population transfer triggered by the plasmon-polariton mode.

Following this approach, the good agreement of simulated 2D spectra and measured 2D spectra underlined that the nonlinear electron-emission process in our particular case can be rather viewed as a plasmon-assisted multi-quantum electron emission process with non-instantaneous relaxation times. In contrast, in the semiclassical local-response approach, the relaxation in the metal is considered instantaneous.

The quantum model enabled a clear identification of relevant “classical”, e.g., the population-*relaxation* time of the plasmon-polariton states, and quantum-mechanical parameters like, e.g., electronic level spacings, coupling constants, or *coherence* times of the single electron states in the metal. The implementation of an unbiased feedback approach allowed further the precise determination of these parameters by minimizing the discrepancies between simulated 2D spectra and experimental 2D spectra in an iterative manner. This was demonstrated in this work,

in particular, for the electronic level spacing and the population-relaxation time of the plasmon-polariton. In addition, possible interaction and transfer mechanisms affecting the temporal dynamics of the quantum system under study were verified, e.i., the coherent-coupling mechanism between plasmon-polariton mode and metal and the incoherent unidirectional population transfer. The latter modeled the final step of the nonlinear electron emission process and could be in principle further quantified using the same feedback approach.

Based on the developed quantum model, distinct spectral features of the measured 2D spectra were connected to multi-quantum coherences between plasmon-polariton occupation number states which exhibit an energy spacing corresponding to three times the fundamental plasmon-polariton energy. This superposition of non-adjacent quantum states within one particular plasmon-polariton mode is a direct evidence of a plasmon-polariton quantum wave packet. Note that probing a quantum wave packet has to be distinguished from the established probing of classical plasmon-polariton wave packets, i.e., superpositions of classical oscillations of different plasmonic modes. This evidence underlines the quantum nature of plasmon-polaritons and makes them interesting for designing integrated quantum technologies on the nanoscale used for information processing or sensing.

If the applied optical multipulse excitation based on a three-pulse basis is expanded to a four-pulse basis. The systematic variation of the waiting time T between τ and t, enables investigation of potential changes of selected multi-quantum coherences with time and space. In this way, it can be foreseen that a systematic measurement of these so-called multi-quantum coherences opens pathways to enable spatio-temporal monitoring and eventual manipulation of plasmon-polariton quantum states on the nm scale.

APPENDIX

A

FIRST COHERENT 2D NANOSCOPY OF A PLASMONIC NANOSLIT RESONATOR USING THE PRESENTED EXPERIMENTAL SETUP

Figure A.1 shows the possibilities of using amplitude- and phase-shaped femtosecond pulses generated by the liquid-crystal based pulse shaper to probe the local response of surface systems. The investigated structures are Fabry-Pérot-like plasmonic nanoslit resonators, as exemplary depicted in Fig. A.1 (a). The nanoresonators are cut with defined geometrical length L, width w, and height h into a single-crystalline gold microplate by FIB milling [31, 118, 131]. The spatially resolved emission of electrons (green) is detected within a single nanoslit resonator generated by plasmon-induced local near fields with spatial variations on a sub-10 nm length scale using interferometrically-stable collinear three-pulse sequences with tunable inter-pulse time delays τ, t and controlled relative inter-pulse phase combinations $\varphi_1, \varphi_2, \varphi_3$.

As depicted schematically in Fig. A.1 (a), the spatially resolved photoemission pattern within a different plasmonic nanoslit of geometrical length $L = 320$ nm, $w = 18$ nm, and $h = 32$ nm on a SiO_2 substrate is investigated. The detected spatially resolved photoemission pattern of a single nanoslit under single pulse illumination, i.e., using a three-pulse sequence with zero inter-pulse time delays and relative phases, is presented in Fig. A.1 (b) and reveal again a characteristic two-hot spot electron emission pattern. By measuring the spatially resolved photoemission yield as a function of both time delays and 2D Fourier transforming the obtained two-dimensional dataset along τ and t, a local 2D nanoscopy spectrum is generated.

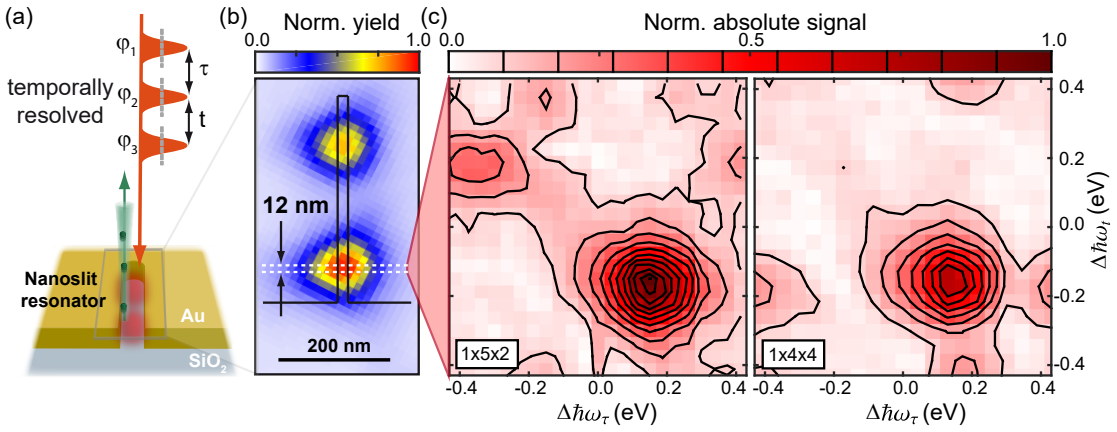

Figure A.1 – Signal-contribution separation by phase-cycling in coherent 2D nanoscopy. (a) Schematic illustration of the coherent 2D nanoscopy experiment to detect the nonlinear photoemission yield (green) of a single plasmonic gold (Au) nanoslit located on a SiO_2 substrate. (b) Laser-induced (660 nm, 19 fs, 56 nJ) photoemission hot-spot pattern of the single nanoslit with $L = 320$ nm, $w = 18$ nm and $h = 32$ nm. (c) Local coherent 2D nanoscopy spectra from an integrated region of interest of 12 nm height, according to the white dashed lines shown in (b), within one hot spot. The absolute-valued part of the photon-echo contribution after 10-fold ($1 \times 5 \times 2$, middle) and 16-fold ($1 \times 4 \times 4$, right) phase cycling is presented. The higher-order signal contribution in the upper left quadrant of the 2D spectrum corresponding to the 10-fold phase cycling is eliminated by the 16-fold phase-cycling scheme. Adapted from Ref. [1], with the permission of AIP Publishing.

As explained in detail in Ch. 2, in contrast to conventional coherent 2D spectroscopy with noncollinear propagation of the exciting pulses and detection of a coherently emitted signal in a phase-matched direction, here, due to our collinear excitation scheme and population-based signal detection (emitted electrons), a certain signal contribution, e.g., the rephasing "photon-echo" contribution, is filtered by using the introduced phase-cycling technique [69, 70, 194].

The home-build pulse shaper imprints for each time delay a combination of different relative inter-pulse phases φ_n with $n \in \{1, 2, 3\}$ on the excitation pulse sequence. To extract exclusively the rephasing photon-echo contribution in a three-pulse basis, for example, a 10-fold phase-cycling scheme ($1 \times 5 \times 2$) has been shown to be sufficient in the case that only up to two field interactions per pulse are present, i.e., higher-order effects can be neglected [70]. Note that this number of field interactions corresponds in fact to a nonlinearity of the photoemission signal of $N \leq 3$, meaning that, if the measured nonlinearity exhibits $N > 3$, additional higher-order signals are expected to be present in the 2D spectrum.

Figure A.1 (c) (left) presents the measured local 2D spectrum which was integrated over a sample ROI with 12 nm height (white dashed lines in Figure A.1 (b)) within a single nanoslit using $1\times5\times2 = 10$-fold phase cycling. The dominant peak of the absolute signal in the lower right quadrant of the 2D spectrum is assigned to the rephasing photon-echo contribution. Since the measurement was performed in a partly rotating frame [153, 190] the energy position of the absolute signal peak in the laboratory reference frame, $\hbar\omega_{\mathrm{lab}}$, with respect to the individual energy axis, is given by Eq. (5.8.2) using $\hbar\omega_0 = 1.88$ eV, as introduced in detail in Sec. 5.8. From this equation it is seen that the dominant peak at $|\Delta\hbar\omega_x| = 0.17$ eV (with $x = \tau, t$) appears within our laser spectrum ($1.79 - 1.99$ eV). The additional signal peak detected in the upper left quadrant ($\Delta\hbar\omega_\tau = -0.39$ eV, $\Delta\hbar\omega_t = +0.22$ eV), is assigned to a signal contribution of higher order which is not suppressed by the 10-fold phase-cycling scheme. The presence of higher-order signals is reasonable in this sample system, taking into account the nonlinear order of the photoemission process of $N = 3.5$.

Since it is expected that a higher phase-cycling scheme suppresses this higher-order contribution [70] an additional three-pulse scan with $1\times4\times4 = 16$-fold phase cycling was performed. The resultant local 2D nanoscopy spectrum integrated from the same spatial position is shown in Figure A.1 (c) (right) and the signal peak assigned to the higher-order contribution in the upper left quadrant is successfully suppressed. In addition to the expected rephasing photon-echo contribution in the lower right quadrant at ($|\Delta\hbar\omega_x| = 0.17$ eV), two weaker signal peaks at higher relative energies can be distinguished. Those are attributed to remaining higher-order contributions specific to the 16-fold phase-cycling scheme and discussed in detail in Ch. 5. To further simplify the 2D spectrum, i.e., to suppress these higher-order signal peaks, a $1 \times 5 \times 4 = 20$-fold phase cycling would be sufficient.

Hence, the possibility to shape femtosecond pulses in amplitude and phase with the implemented pulse shaper extends the PEEM setup to realize spectrally resolved excitation and enables coherent 2D nanoscopy using phase cycling.

APPENDIX

B

TECHNICAL SPECIFICATIONS: PULSE SHAPER

The subsequent table summarizes the most important technical specifications of the pulse-shaper setup conceptualized and assembled during this thesis. All necessary definitions, physical parameters and constants are given in Sec. 3.3.

Calibrated spectral window	$592.88 - 806.15$ nm
SLM transmission	> 75 % for $450 - 1100$ nm
SLM pixel width	$\delta x = 97$ µm
SLM pixel height	$\delta y = 10$ mm
SLM gap width	$\delta x_{\text{gap}} = 3$ µm
Total SLM thickness	$\delta z = 6.02$ mm
Focus size in Fourier plane* (min.)	$2w_{\text{FP}} = 54.88$ µm
Focus size in Fourier plane** (max.)	$2w_{\text{FP}} = 80.48$ µm
Focus length $\sim 2z_{\text{Rayleigh}}$ in Fourier plane* (min.)	12.2 mm
Linear spatial-calibration coeff. (for $\lambda_0 = 700$ nm)	$\alpha = 77.14$ mm $\cdot$ fs
Spatio-temporal coupling velocity	$v_{\text{stc}} = 4.3 \times 10^{-4}$ mm/fs
Tilt angle of shaping axis	$\vartheta = 55.1°$
Fourier plane spectral resolution***	$\delta\omega = 0.0013$ 1/fs
Temporal shaping window*** (min.)	$T = 4$ ps
Setup power throughput without SLM	$P_{\text{out}}/P_{\text{in}} \sim 50$ %
Setup power throughput with SI wedges	$P_{\text{out}}/P_{\text{in}} \sim 25$ %

Setup power throughput without SI wedges	$P_{\mathrm{out}}/P_{\mathrm{in}} \sim 35$ %
VPHG wavelength range	$590 - 810$ nm
VPHG grating constant	$1/d = 935$ l/mm
Polished VPHG thickness	1 mm (each)
VPHG substrat material (AR coated)	Fused silica (each)
VPHG θ_{AOI}	19.04°
VPHG θ_{AOD} (for $\lambda_0 = 700$ nm)	19.04°
VPHG θ_{AOD} (spectral spread)	±6.08°
VPHG power loss (first/second)	10 %/8 %
Polarizer thickness	260 ± 50 µm (each)
Polarizer power loss (first/second)	30 %/20 %
Focal length of CM	$f = -300$ mm (each)

* $\lambda = 592$ nm, $2w_{\mathrm{in}} = 4$ mm

** $\lambda = 806$ nm, $2w_{\mathrm{in}} = 4$ mm

*** linear approximation

Note that the SI wedges correspond to the outcoupling and recombination wedges for the reference pulse used for pulse train reconstruction via Fourier-transform spectral interferometry (FTSI) as discussed in Ch. 4. Further abbreviations used here: spatial light modulator (SLM), volume phase holographic grating (VPHG), anti-reflection (AR), angle of incidence (AOI), angle of diffraction (AOD), and cylindrical mirror (CM).

APPENDIX

C

VERIFICATION OF THE SLM SPECTRAL TRANSFER-FUNCTION

In this chapter, the spectral-interference spectrum measured within the framework of FTSI itself is used to validate that the implemented SLM transfer-function generates multipulse sequences which are conform with the electric field convention used in the nonlinear spectroscopy community.

The theoretical definition of the convention has been carried out together with Dr. Pavel Malý. The software implementation of the specified definitions were checked together with Dr. Stefan Müller and Matthias Nuss for the individual shaping hardware used in the corresponding setups, being an acousto-optic programmable dispersive filter-based pulse shaper (Dazzler, Fastlite) [155] and a different home-built SLM-based $4f$-pulse shaper [207].

This definition of the temporal electric field $E(t)$, describing the individual multipulse sequences which optically excite the particular sample, is according to Ref. [70, 166, 167]

$$\begin{aligned} E(t) &= 2\,\mathrm{Re}\Big[E^{+}(t)\Big], \\ E(t) &= 2\,\mathrm{Re}\Big[E_0(t)\mathrm{e}^{-i\omega_0 t + i\mathbf{k}\cdot\mathbf{r} + i\varphi(t)}\Big]. \end{aligned} \tag{C.0.1}$$

It results from the fact that for noncollinear coherent phase-matched spectroscopy techniques the individual signal components are separated spatially by their individual *propagation direction*. Consequently, an exemplary signal wave vector $\mathbf{k}_s$ is generated by, e.g., $\mathbf{k}_s = -\mathbf{k}_1 + 2\mathbf{k}_2 - \mathbf{k}_3$, corresponding to a rephasing signal contribution (photon-echo) of third order. The signal contribution is labeled by the signs in front of the individual wave vectors $(-1, 2, -1)$.

Following a collinear experimental approach [70], the same signal separation is performed by a certain combination of *offset phases* $\varphi_{1,2,3}$ in the temporal phase $\varphi(t)$ using the phase-cycling technique. With the field definition given in Eq. (C.0.1), the individual signs of the offset phases are the same, as the signs of the phase $\mathbf{k} \cdot \mathbf{r}$ obtained by spatial propagation. Accordingly, by this definition the labeling of the individual signal contribution is chosen to be *equal* $(-\mathbf{k}_1 + 2\mathbf{k}_2 - \mathbf{k}_3 \leftrightarrow -\varphi_1 + 2\varphi_2 - \varphi_3)$.

The validation of the transfer function is performed by examination if certain pulse-shaper introduced time shifts δt of the pulse correspond to the time-shift systematic expected based on the given electric field definition. From the definition it follows that a single pulse with complex-valued amplitude $A(t + \delta t)$, carrier frequency ω_0, additional offset phase φ_0 and arrival time $t = -\delta t$, which means, coming earlier than $t = 0$ is given by

$$E^+(t) = A(t + \delta t)\mathrm{e}^{-i\omega_0(t+\delta t)+i\varphi_0}. \tag{C.0.2}$$

Here higher-order phase terms are neglected and the field is described at position $\mathbf{r} = 0$ for simplicity. The spectral-domain representation is given by the corresponding Fourier transform

$$E^+(\omega) = \int \mathrm{e}^{i\omega t} E^+(t) dt. \tag{C.0.3}$$

If the complex conjugated field definition $E^+(t) = E_0(t)\mathrm{e}^{i\omega_0 t - i\mathbf{k}\cdot\mathbf{r} - i\varphi(t)}$ had been chosen, which also fulfills the nonlinear spectroscopy sign convention, the Fourier transformation to spectral domain would be $E^+(\omega) = \int \mathrm{e}^{-i\omega t} E^+(t) dt$. Based on Eq. (C.0.3), the temporally shifted pulse in spectral domain is given by

$$E^+(\omega) = A(\omega - \omega_0)\mathrm{e}^{-i\omega\delta t}\mathrm{e}^{i\varphi_0}, \tag{C.0.4}$$

and the spectral phase is revealed to be

$$\varphi(\omega) = \varphi_0 - \omega\delta t, \tag{C.0.5}$$

with δt being here a positive number. Therefore, a *negative* slope in the spectral phase corresponds to a pulse arriving at $t = -\delta t$, ergo *earlier*, on a detector.

For this reason, with respect to the electric-field convention, the pulse-shaper transfer function $M(\omega)$ introducing, i.a., a temporal pulse shift by $\pm\delta t$ has to fulfill

$$M(\omega; \delta t, \varphi_0) = \mathrm{e}^{i(\omega\delta t - (1-\gamma)\omega_0\delta t + \varphi_0)}. \tag{C.0.6}$$

The first phase part in the exponential function introduces the temporal shift, while the second phase part enables the transformation to the partially rotating

frame (depending on γ, see Ref. [190]) by adding a δt-dependent phase factor $-(1-\gamma)\omega_0\delta t$. The last phase part finally implements the time-independent offset phase φ_0 being essential for the phase-cycling technique [70]. For this transfer function, a *negative* $\delta t < 0$ results in a *negative spectral-phase slope* and consequently results in a pulse being shifted to *earlier times*.

To verify, whether the *software implemented* spectral transfer function $M(\omega)$ of the home-built SLM-based pulse shaper introduced in Sec. 3.3 is in agreement with the spectral transfer-function resulting from the established field convention as defined in Eq. (C.0.6), the sign of the SLM-induced temporal delay of a single pulse is determined using Fourier-transform spectral interferometry.

Here, the oscillations in the spectral-interference term $S(\lambda)$ are analyzed, as defined in Eq. (4.3.1). These oscillations are determined based on the spectral-interference data acquisition and evaluation procedure discussed in Sec. 4.3.3. Under the assumption that the spectral phase of the unshaped reference pulse $\varphi_{\mathrm{Ref}}(\lambda)$ and the spectral phase of the shaped pulse $\varphi(\lambda)$ are equal before the shaped pulse is temporally shifted, the oscillation frequency of the cosine modulation of $S(\lambda)$ is proportional to the delay τ between both pulses

$$S(\lambda) \sim \cos\Big(-\frac{2\pi c\tau}{\lambda}\Big). \tag{C.0.7}$$

To analyze the sign of the SLM-introduced temporal delay, the temporal positioning of the reference pulse t_{Ref} with respect to the shaped pulse t_{Sh} has to be determined first, before any additional temporal shift δt_{SLM} is applied by the SLM. This procedure is depicted in Fig. C.1 (a). The length of the reference-beam path, as seen in Fig. 4.1 (a), is adjusted by a manual linear delay-stage, which enables a coarse setting of the delay τ_{stage} between the reference pulse (grey) and the signal pulse (orange).

The left graph in Figure C.1 (a) exemplarily depicts the oscillatory modulation of the interference term $S(\lambda)$ (yellow) at a delay-stage position 12.3 mm. The oscillation is characterized by its maximum (red circle) and minimum (blue circle) oscillation amplitude. To further quantify the change of the modulation frequency as a function of the delay-stage position the number of zero-crossings within a fixed wavelength range (green shade) is determined. In Fig. C.1 (a), the different interference terms $S(\lambda)$ are depicted for the corresponding delay-stage positions. Up to a delay-stage position of 12.26 mm the modulation frequency decreases first and increases again for a further increased delay-stage position.

This systematic is more clearly depicted in Fig. C.1 (a) bottom graph. The maximum and minimum oscillation amplitude is monitored by red and blue circles, respectively, to confirm a comparable modulation depth. Note that for large delays

τ_{stage} the modulation depth gets slightly reduced due to the limited resolution of the used spectrometer ($\delta\lambda = 0.11$ nm). The described modulation-frequency systematic is depicted by the green circles labeling the number of oscillation zero-crossings.

From the experimental setup, as presented in Fig. 4.1 (a), it is known that an increasing delay-stage position reduces the beam path of the reference pulse and thus moves this pulse to earlier times with respect to t_{Sh} of the static signal pulse, which is labeled by the red-dashed line in Fig. C.1 (a).

Since the modulation frequency of $S(\lambda)$ is here only proportional to the stage-adjusted delay $\tau = \tau_{\mathrm{stage}}$ between reference and shaped pulse the relative temporal position of reference t_{Ref} and shaped pulse t_{Sh} is clearly identified as indicate in the bottom of Fig. C.1 (a). For delay-stage positions < 12.26 mm the reference pulse is situated at larger times $t_{\mathrm{Ref}} > t_{\mathrm{Sh}}$, which means that the shaped pulse arrives first at a detector, while for positions > 12.26 mm the reverse situation is established with $t_{\mathrm{Ref}} < t_{\mathrm{Sh}}$ leading to the reference pulse being detected first.

To verify now the correct implementation of the spectral transfer function, the reference-pulse's (grey) temporal position is fixed by the manual delay-stage to either one of the two configurations and the shaped pulse (orange) is now shifted in time by δt_{SLM} via the SLM by simply applying a linear spectral-phase as discussed in Eq. (C.0.5). This additional time shift affects the monitored modulation frequency of $S(\lambda)$ since the delay between reference and shaped pulse is now given by

$$\tau = \tau_{\mathrm{stage}} \pm \delta t_{\mathrm{SLM}}, \tag{C.0.8}$$

where the sign of the second term in the equation depends on the two start configurations depicted in Fig. C.1 (b) and (c).

Figure C.1 (b) depicts the configuration, adjusted by fixing the delay-stage position at 12.20 mm, corresponding to the situation that the reference pulse arrives *after* the shaped pulse at the detector. Here the effective delay τ is calculated using a minus sign in Eq. (C.0.8). The reverse situation, meaning that the reference pulse is detected *first*, is realized in Fig. C.1 (c) by setting the delay-stage position to 12.30 mm resulting in a plus sign in Eq. (C.0.8).

As in Fig. C.1 (a), the systematic change of the modulation frequency (green circles) and the maximum modulation depth (red and blue circles) of the spectral interference term $S(\lambda)$ are characterized as a function of the time shift δt_{SLM}. In Fig. C.1 (b) the modulation frequency is increased for negative and decreased for positive time shifts, due to the increased ($-\delta t_{\mathrm{SLM}}$) and decreased ($+\delta t_{\mathrm{SLM}}$) effective delay τ. This is in accordance with the expected performance based on the

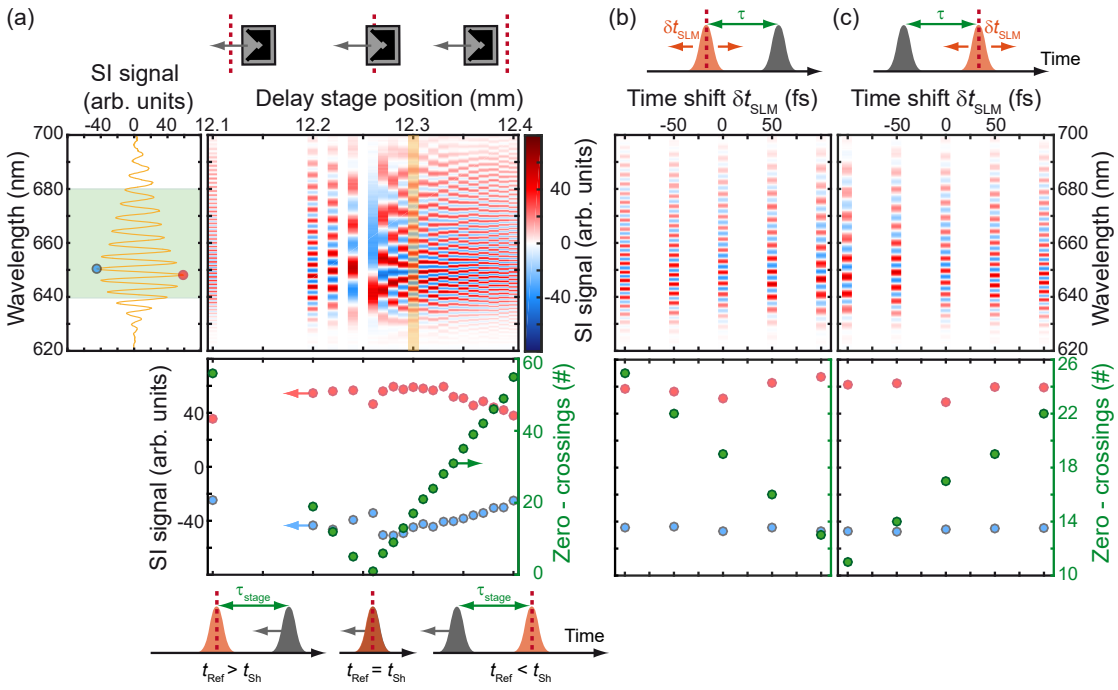

Figure C.1 – Experimental verification of the SLM spectral transfer-function. In (a) the relative temporal positioning of the reference pulse (grey) with respect to the shaped pulse (orange) is determined. Characterization of the modulation frequency (green circles) in a certain wavelength range (green shade) of the spectral-interference term $S(\lambda)$ — exemplary depicted (yellow) for a delay-stage position of 12.3 mm — as function of the manual delay-stage position (induces temporal shift of reference pulse) allows a clear distinction of the different temporal positioning configurations, as depicted on the bottom of (a). Monitoring of individual minimum (blue circles) and maximum (red circles) oscillation amplitudes ensure a sufficient modulation depth at each delay-stage position. (b-c) Applying additional temporal shifts δt_{SLM} (orange arrows) by the SLM in two known and fixed delay-stage configurations, (b) reference pulse arrives last, and (c) reference pulse arrives first, leads to a modulation-frequency systematic (green circles) which reflects the temporal-shift systematic resulting from the established electric-field convention (see main text). This proves that the implemented spectral transfer-function $M(\omega)$ is defined according to the spectral transfer-function resulting from the electric-field convention defined by Eq. (C.0.6).

spectral transfer function resulting from the field convention. An opposite systematic is expected if the start configuration is reversed. This cross check is presented Figure C.1 (c). Here, the modulation frequency decreases for negative and increases for positive time shifts δt_{SLM} and validates again that the implemented

spectral transfer function $M(\omega)$ shapes pulses as expected from the established electric-field convention.

To summarize, the implemented spectral transfer function matches the definition of the spectral transfer function given in Eq. (C.0.6), which is in accordance with the electric-field convention presented in the beginning of this section. This is validated in a simplified shaping configuration, meaning for a single pulse which is temporally shifted by δt in the laboratory frame ($\gamma = 1$) and no offset phase ($\varphi_0 = 0$).

This verification was successfully accomplished for the two most common software implementations in LabView: `GA - initialize PulseTrain.vi` and `PS - Manual Control of Pulse Shaper v2_3 with manual shaper correction.vi` used in several experimental setups in the group.

Note that while the "`PulseTrain.vi`" uses the explicit spectral transfer-function $M(\omega)$, the "`Manual Control.vi`" allows to directly manipulate different coefficients b_n of the Taylor expansion, which approximates the spectral phase $\varphi(\omega)$ around the central frequency ω_0 and is in general given by

$$\varphi(\omega) = \sum_{n=0}^{\infty} \frac{\mathrm{b}_n}{n!}(\omega - \omega_0)^n, \tag{C.0.9}$$

with Taylor coefficients $\mathrm{b}_n = d^n\varphi(\omega)/d\omega^n|_{\omega-\omega_0}$. A detailed description of the physical property of the first Taylor coefficient b_1 can be found in Ref. [212]. Based on the previously described procedure, it is quantified that a *negative* b_1 value results in a pulse shifted to *earlier times*.

From a spectroscopic point of view, the correct realization of the sign convention ensures that the frequency quadrants for the respective contributions in nonlinear 2D spectra can be taken from the literature [70, 166, 167].

APPENDIX

D

COMPLETE TIME- AND SPECTRAL-DOMAIN MAPS USING FTSI-RECONSTRUCTED AND IDEALIZED PULSE SEQUENCES

Shown in Fig. D.1 (a-d) are the corrected time-domain maps for the rephasing, (a) and (b), identical to Fig. 4.9 (e) and (f), respectively, and non-rephasing, (c) and (d), signal contributions highlighted with a blue background between panels. The real pulse shaper (PS) rephasing time-domain map, depicted in Fig. D.1 (a), shows the same damped oscillation along the two delay axis as the ideal PS time-domain map presented in Fig. D.1 (b).

Further, a weak contribution from the diagonal artifact due to a non-perfect correction is still visible on the diagonal in Fig. D.1 (a). Comparing the non-rephasing time-domain maps of the real PS, depicted in Fig. D.1 (c), and the ideal PS (Fig. D.1 (d)) reveals good agreement. Even though the real PS non-rephasing map, presented in Fig. D.1 (c), shows a higher noise level as the ideal PS (Fig. D.1 (d)), systematic oscillations along the delay axes observed in the ideal PS map are also identified in the real PS map.

The phase-cycled time-domain maps simulated for detection of nonlinear photoemission are plotted in Fig. D.1 (e–h), highlighted with a green background between panels. Note that unlike the molecular dimer fluorescence simulation, no high-field-amplitude minus low-field-amplitude correction is necessary to perform. Comparing the rephasing time-domain maps for reconstructed real PS (Fig. D.1 (e)) and ideal PS pulse sequences (Fig. D.1 (f)) shows that the same features and no significant contribution of a diagonal artifact are observed. The same observation is achieved by the analysis of the two non-rephasing maps depicted in Fig. D.1

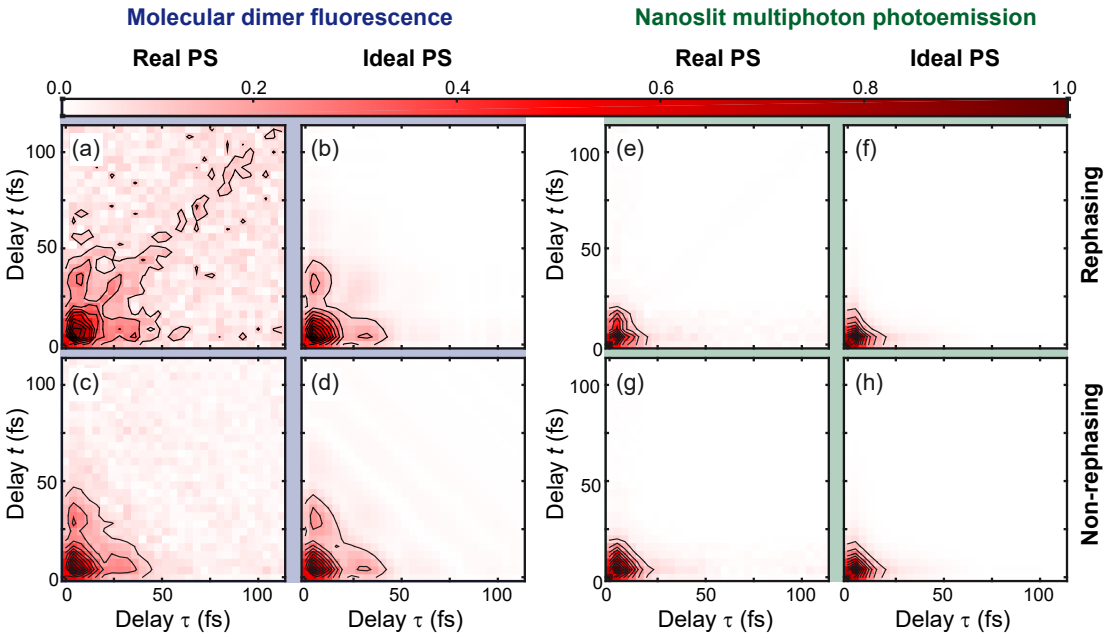

Figure D.1 – Simulated time-domain maps using FTSI-reconstructed pulse sequences (Real PS) and idealized pulse sequences (Ideal PS). (a–d) Dimer fluorescence rephasing real PS (a), rephasing ideal PS (b), non-rephasing real PS (c), and non-rephasing ideal PS (d) maps. (e–h) Nanoslit multiphoton photoemission rephasing real PS (e), rephasing ideal PS (f), non-rephasing real PS (g), and non-rephasing ideal PS (h) maps. Adapted with permission from Ref. [2] © Optica Publishing Group.

(g) and Fig. D.1 (h).

Figure D.2 shows the 2D spectra obtained from 2D Fourier transformation of the time-domain maps presented in Fig. D.1 and discussed in detail in Sec. 4.6. Comparing the real PS and ideal PS spectra of the dimer fluorescence signal, as depicted in Fig. D.2 (a–f) (blue background between panels), shows that the small deviations in the real PS sequences do not modify the energetic positions of either diagonal or off-diagonal peaks. The signal distortion along the diagonal of the real PS rephasing spectrum, shown in Fig. D.2 (a), compared to the ideal rephasing spectrum (Fig. D.2 (b)), results from the residual diagonal artifact contribution (Fig. D.1 (a)) and alters slightly the line shape of the diagonal peaks compared to the ideal PS rephasing spectrum depicted in Fig. D.2 (b).

Nevertheless, the characteristic areas of equal signal sign in the rephasing and non-rephasing signals of the real PS sequence match well the signal-sign areas

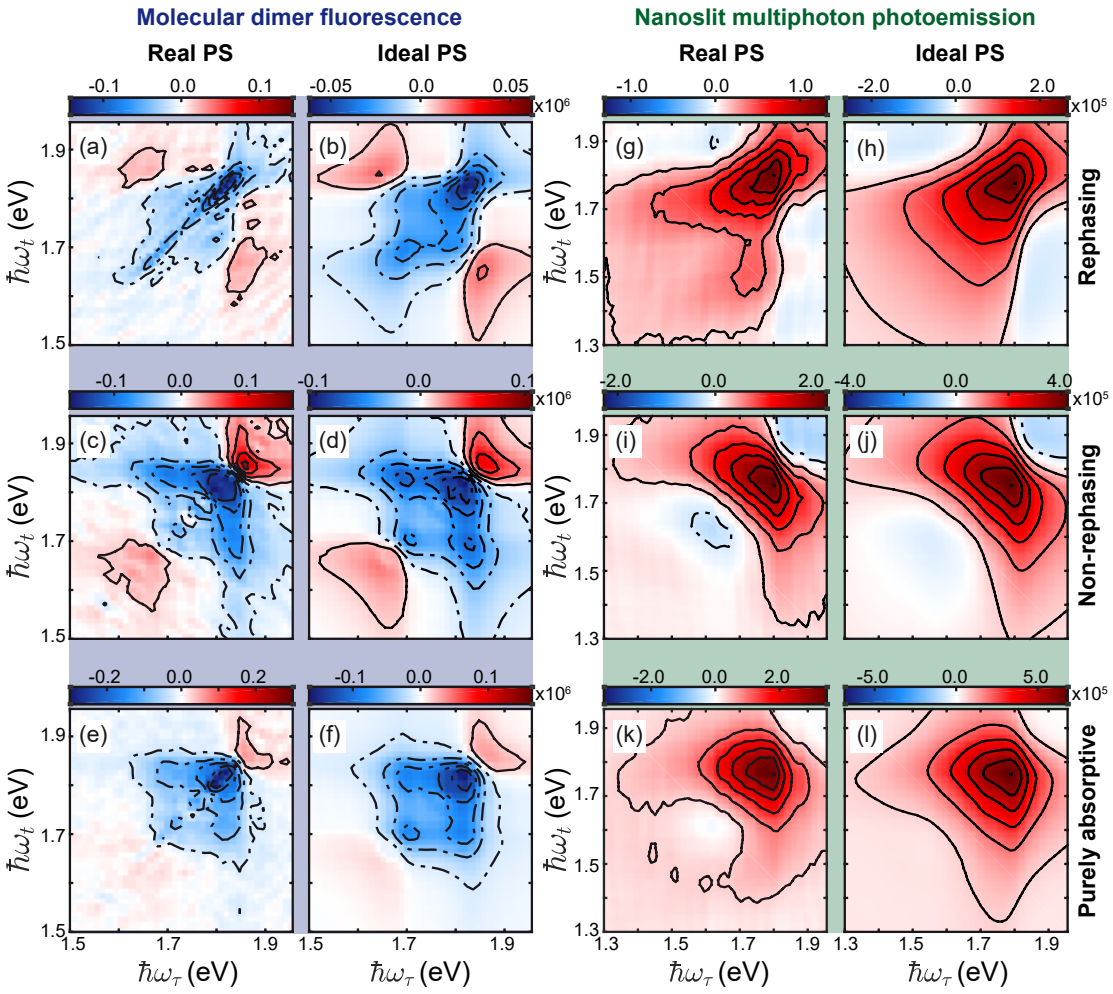

Figure D.2 – Simulated 2D spectra using FTSI-reconstructed pulse sequences (Real PS) and idealized pulse sequences (Ideal PS). The displayed rephasing and non-rephasing 2D spectra for the molecular dimer fluorescence signal (blue) and the nanoslit multiphoton photoemission signal (green) were obtained by 2D Fourier transformation of the time maps shown in Fig. D.1. (a), (b), (g), (h) Real part of the rephasing signal contribution using (a) Real PS and (b) Ideal PS for the fluorescence signal simulation and (g) Real PS and (h) Ideal PS to simulate the photoemission signal; (c), (d), (i), (j) non-rephasing spectrum following an analogous panel labeling systematic. (e), (f), (k), (l) purely absorptive spectra discussed in the main text which follow again an analogous panel labeling systematic. Adapted with permission from Ref. [2] © Optica Publishing Group.

in the corresponding ideal PS spectra. This leads to the result that the main characteristic features of the purely absorptive spectra, depicted in Fig. D.1 (e) and (f), are not significantly distorted by the deviations between real PS and ideal PS pulse sequence, leading to comparable energetic peak positions, relative peak amplitudes, line shapes, and areas of equal signal sign.

The comparison between real PS and ideal PS spectra for nonlinear multiphoton photoemission (Fig. D.2 (g–l), green background between panels) shows slight line-shape modifications in case of the real PS rephasing signal, depicted in Fig. D.2 (g), compared to the ideal PS (Fig. D.2 (h)) due to an increased noise level. This line-shape distortion is not visible in the non-rephasing 2D spectra, Fig. D.2 (i, j). The purely absorptive spectra of the real (Fig. D.2 (k)) and ideal PS sequences (Fig. D.2 (l)) show no significant deviations in the main features, besides the fact of an increased noise level in case of the real PS sequences, as seen in Fig. D.2 (k).

Comparing the purely absorptive spectra of the dimer fluorescence signal, presented in Fig. D.2 (e, f), to the purely absorptive spectra of the nanoslit multiphoton emission signal (Fig. D.2 (k, l)), reveals a changed signal sign in the energetic range covered by the excitation spectrum. The negative signal sign of the molecular dimer fluorescence results from being dominated by fourth-order response signals as exemplarily depicted in Fig. 4.7 (b) in Sec. 4.5, whereas the positive signal sign in case of the nanoslit multiphoton photoemission is an indication that the signal is dominated by a higher-order response signal. Based on the used high nonlinearity of $N = 4.2$, which suggests up to 8 field interactions, an eighth-order response signal would be reasonable.

APPENDIX

E

ROOT-MEAN-SQUARE DEVIATION PROCEDURE FOR QUANTITATIVE 2D SPECTRA COMPARISON

For quantitative comparison of simulated and measured 2D spectra, as presented in, e.g., Fig. 5.4, the signal amplitude values of the simulated spectrum are at first rescaled by a global scaling factor to the measured 2D spectrum labeled with "PEEM" in Fig. 5.3. To determine the optimal scaling factor S the root-mean-square deviation (RMSD) of the corresponding simulated spectrum with respect to the measured spectrum is calculated by

$$\mathrm{RMSD}(S) = \sqrt{\frac{\sum_{i=1}^{n}(S \cdot p_i^{\mathrm{Sim}} - p_i^{\mathrm{PEEM}})^2}{n}}, \tag{E.0.1}$$

with p_i^{Sim} and p_i^{PEEM} being the signal values at individual pixel i of the simulated and measured 2D spectrum, respectively, and n the total number of pixels.

Note that in the presented RMSD analyses each pixel of the whole 2D data, as depicted e.g. in Fig. E.1 (b), are taken into account and limitation of the considered pixels to certain regions of the 2D data do not significantly change the results of the RMSD analyses. This calculation is performed for each varied scaling factor S and the optimal scaling factor is defined at minimal RMSD value.

Figure E.1 (a) depicts the resulting RMSD(S)-curves (green marker) for three exemplary shown 2D spectra which has been simulated based on the local-repsonse approach (FDTD) presented in Sec. 5.6. The three simulations differ in the length L_{FDTD} of the modeled plasmonic nanoresonator. Each curve exhibits a clear minimum at $\mathrm{RMSD}_{\mathrm{min}}$ and thus an individual scaling factor optimized with respect

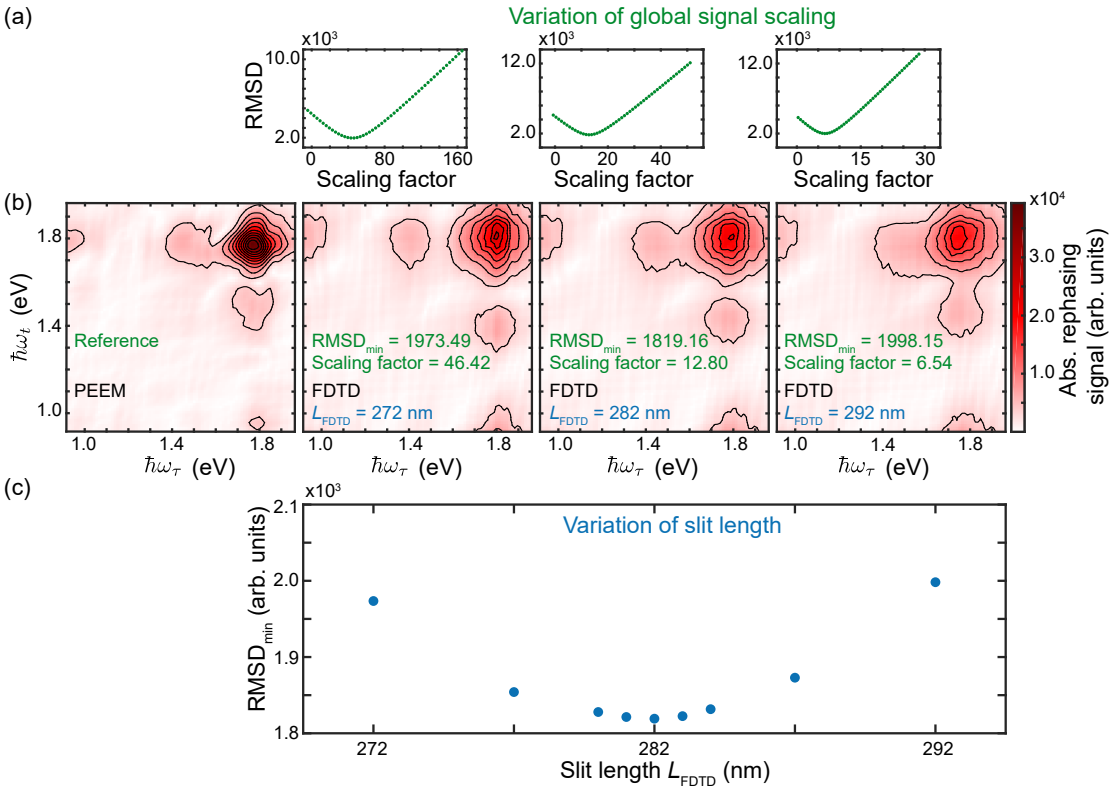

Figure E.1 – Minimal root-mean-square deviation (RMSD) analysis for FDTD-based 2D spectra: Variation of the nanoresonator slit-length. (a), RMSD value versus global signal scaling factor (green) for different exemplary nanoresonator slit length L_{FDTD} = 272 nm, L_{FDTD} = 282 nm and L_{FDTD} = 292 nm (from left to right) as introduced in, e.g., Fig. 5.5. Each RMSD value results from the pixel-wise comparison of the whole simulated 2D spectrum to the measured (PEEM) 2D spectrum. Before each comparison the signal of the simulated spectrum is globally scaled by the individual scaling factor. (b), Starting from left: Measured (PEEM) 2D spectrum which acts as the reference spectrum in this analysis and scaled 2D spectra of exemplary nanoresonator slit lengths L_{FDTD} = 272 nm, L_{FDTD} = 282 nm and L_{FDTD} = 292 nm (labeled in blue). The signal of each spectrum was scaled by the corresponding minimal RMSD scaling factor (labeled in green). (c), Minimal RMSD value from the global signal scaling procedure as function of all simulated slit lengths L_{FDTD} (blue). From this analysis the nanoresonator slit length of best match is obtained by L_{FDTD} = 282 nm at minimal $\mathrm{RMSD}_{\mathrm{min}}$ = 1819.16. The corresponding 2D spectrum is also depicted in Fig. 5.3 (b).

to the measured 2D data.

On the left of Fig. E.1 (b) the measured 2D spectrum (PEEM) is shown, acting

as a reference in this procedure. Then, subsequently (from left to right) follow the simulated 2D spectra at different nanoresonator length $L_{\mathrm{FDTD}} = 272$ nm, $L_{\mathrm{FDTD}} = 282$ nm and $L_{\mathrm{FDTD}} = 292$ nm (blue labels) rescaled with the corresponding optimized scaling factor at minimized RMSD value $\mathrm{RMSD}_{\mathrm{min}}$ (green label). In the individual spectra it is clearly seen that with increased L_{FDTD} the multi-quantum peaks (as defined in Fig. 5.3) are located closer to the single-quantum peak which itself is located along the diagonal ($\hbar\omega_\tau = \hbar\omega_t$) of each 2D spectrum. Comparing the 2D spectrum of shortest nanoresonator length at FDTD = 272 nm to the 2D data at $L_{\mathrm{FDTD}} = 292$ nm shows that the center-of-mass intensity of the single-quantum peak is pulled along the $\hbar\omega_\tau$ axis towards the direction of the multi-quantum peak. Note that an increasing nanoresonator length L_{FDTD} is connected to a red-shift of the Fabry-Pérot resonances of the nanoresonator's spectral response as introduced in Sec. 2.2.2.

As shown in Fig. E.1 (c), plotting of the various $\mathrm{RMSD}_{\mathrm{min}}$ as a function of the tuning parameter of the simulation, here: L_{FDTD} (blue marker) reveals a clear minimum deviation between the rescaled simulated spectra and the measured 2D spectrum at an overall nanoresonator length of $L_{\mathrm{FDTD}} = 282$ nm with $\mathrm{RMSD}_{\mathrm{min}} = 1819.16$. Since this simulation result exhibits best matching with the measured data, this 2D spectrum is used for final comparison as discussed in detail in Sec. 5.4.

In Fig. E.2 and Fig. E.3 the results of the performed RMSD procedure using simulation results based on the developed quantum model (see Sec. 5.10 for details) are presented. The procedure follows the same evaluation steps as described in the previous paragraph for the FDTD-based 2D spectra.

In contrast to employing the slit length L_{FDTD} as a tuning parameter, the energetic level spacing ΔE between the individual QHO states and the electronic ladder-system states is used here in a first optimization step, followed by tuning the population relaxation time T_1 of the plasmon polariton in a second optimization step. Figure E.2 shows the analysis for variation of ΔE at a not optimized relaxation time $T_1 = 7$ fs, while Fig. E.3 depicts the variation of T_1 at optimized level spacing $\Delta E = 1.766$ eV.

Qualitative analysis of the exemplary depicted rescaled 2D spectra labeled as "Quantum model" in Fig. E.2 (b) reveals, that the variation of the level spacing ΔE exhibits the same systematic concerning the spectral positions of the multi-quantum peaks as observed for the FDTD-based simulations, meaning that multi-quantum peaks are shifted closer to the single-quantum peak for decreased (red-shifted) level spacing ΔE. From the complete analysis quantified in Fig. E.2 (c) a best-matching level spacing of $\Delta E = 1.766$ eV with minimal $\mathrm{RMSD}_{\mathrm{min}} = 1116.21$ is determined at fixed plasmon-polariton relaxation time $T_1 = 7$ fs.

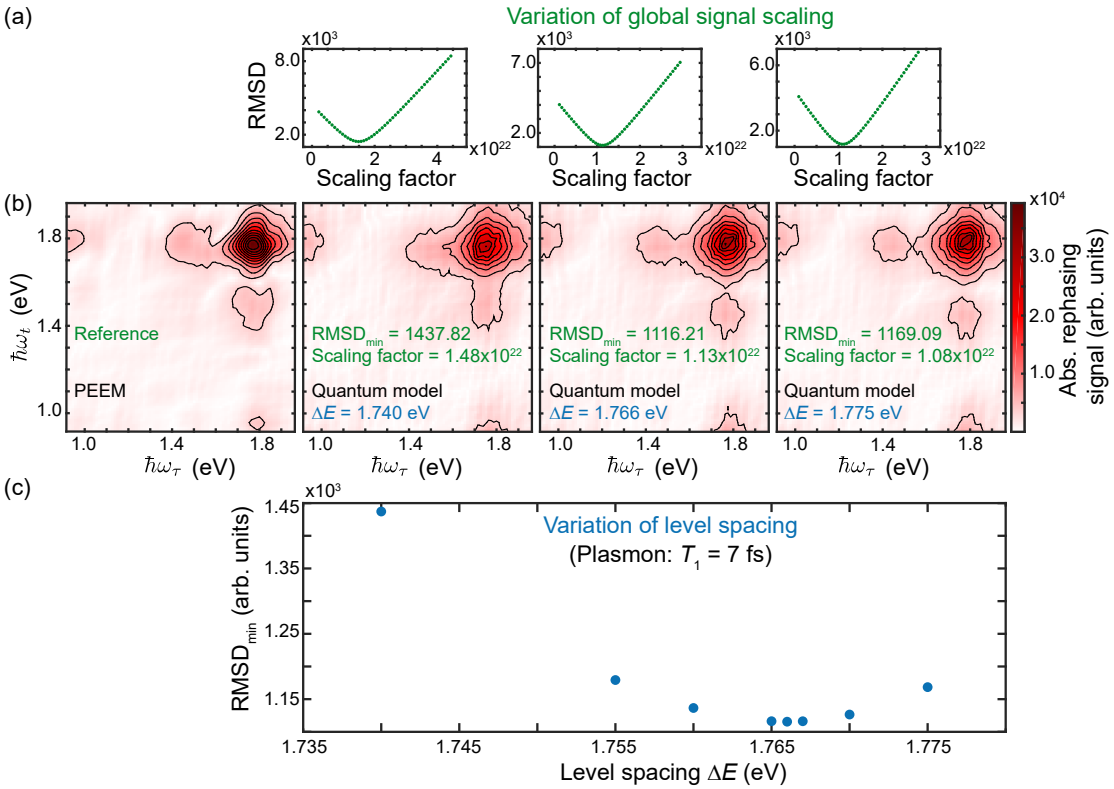

Figure E.2 – Minimal root-mean-square deviation (RMSD) analysis for quantum-model-based 2D spectra: Variation of the enegetic level spacing. (a), RMSD value versus global signal scaling factor (green) for different exemplary level spacings $\Delta E = 1.740$ eV, 1.766 eV and 1.775 eV (from left to right) as introduced in, e.g., Sec. 5.10. Each RMSD value results from the pixel-wise comparison of the whole simulated 2D spectrum to the measured (PEEM) 2D spectrum. Before each comparison the signal of the simulated spectrum is globally scaled by the individual scaling factor. (b), Starting from left: Measured (PEEM) 2D spectrum which acts as the reference spectrum in this analysis and scaled 2D spectra of exemplary level spacings $\Delta E = 1.740$ eV, 1.766 eV and 1.775 eV (labeled in blue). The signal of each spectrum was scaled by the corresponding minimal RMSD scaling factor (labeled in green). (c), Minimal RMSD value from the global signal scaling procedure as function of all simulated energetic level spacings ΔE (blue) for fixed other simulation parameters. In particular, the plasmon-polariton population-relaxation time was set here to $T_1 = 7$ fs. From this analysis the level spacing of best match is obtained by $\Delta E = 1.766$ eV at minimal $\mathrm{RMSD_{min}} = 1116.21$.

In Fig. E.3 the optimized level spacing $\Delta E = 1.766$ eV is kept fix and the plasmon relaxation time T_1 is tuned. This tuning significantly affects the width of

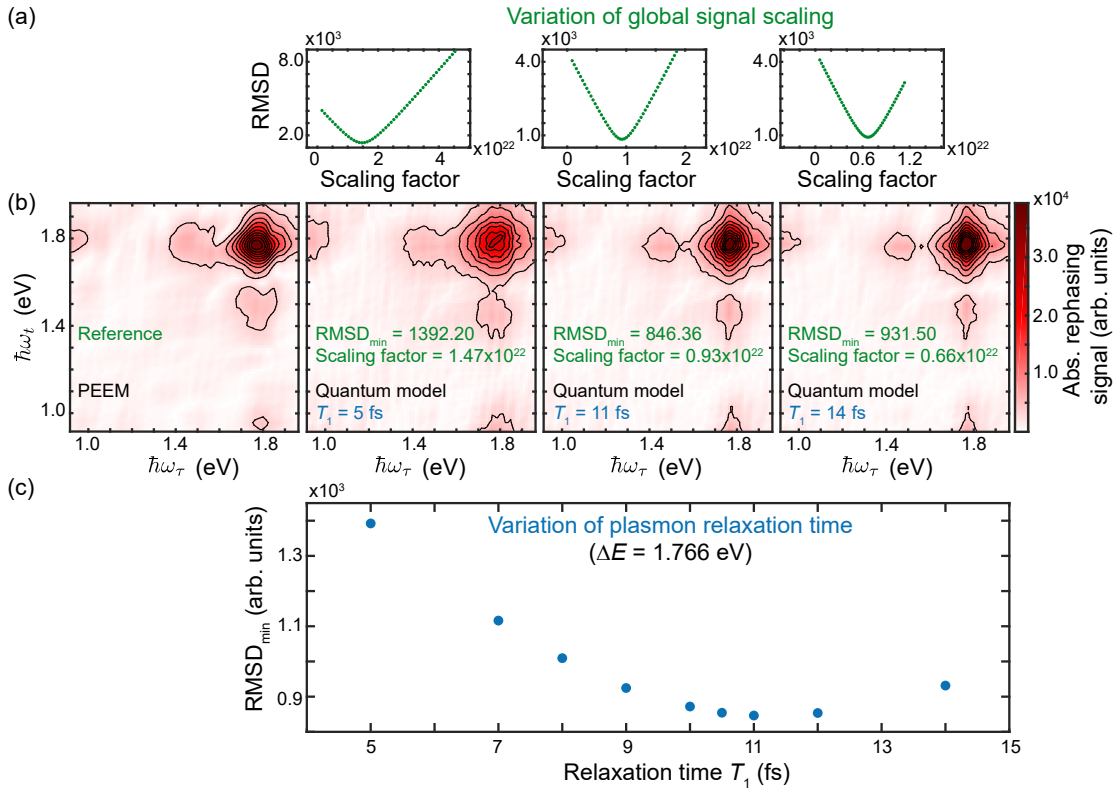

Figure E.3 – Minimal root-mean-square deviation (RMSD) analysis for quantum-model-based 2D spectra: Variation of the plasmon-polariton relaxation time. (a), RMSD value versus global signal scaling factor (green) for different exemplary population-relaxation times $T_1 = 5$ fs, 11 fs and 14 fs (from left to right) as introduced in, e.g., Sec. 5.10. Each RMSD value results from the pixel-wise comparison of the whole simulated 2D spectrum to the measured (PEEM) 2D spectrum. Before each comparison the signal of the simulated spectrum is globally scaled by the individual scaling factor. (b), Starting from left: Measured (PEEM) 2D spectrum which acts as the reference spectrum in this analysis and scaled 2D spectra of exemplary relaxation times $T_1 = 5$ fs, 11 fs and 14 fs (labeled in blue). The signal of each spectrum was scaled by the corresponding minimal RMSD scaling factor (labeled in green). (c), Minimal RMSD value from the global signal scaling procedure as function of all simulated population-relaxation times T_1 (blue) for fixed other simulation parameters. In particular, the energetic level spacing was set here to $\Delta E = 1.766$ eV. From this analysis the plasmon-polariton relaxation time of best match is obtained by $T_1 = 11$ fs at minimal $\mathrm{RMSD_{min}} = 846.36$ at $\Delta E = 1.766$ eV. The corresponding 2D spectrum is also depicted in Fig. 5.3 (b).

the two-dimensional line shape of both the single-quantum and multi-quantum

peaks in the 2D spectrum as seen exemplary for the rescaled 2D spectra depicted in Fig. E.3 (b). An increase of T_1 results here in a decreased width of the individual two-dimensional line shapes. Minimizing the $\mathrm{RMSD}_{\mathrm{min}}$ resulting from the individual scaling-factor variations reveals a best-matching 2D spectrum with respect to the measured 2D data (PEEM) at $T_1 = 11$ fs and $\Delta E = 1.766$ eV with $\mathrm{RMSD}_{\mathrm{min}} = 846.36$. Note that after optimizing T_1 it can be in principle investigated iteratively whether the $\mathrm{RMSD}_{\mathrm{min}}$ can be further decreased by using a different level spacing ΔE or tuning of any additional parameter defining the quantum model. This procedure has been stopped at this iteration point since the obtained $\mathrm{RMSD}_{\mathrm{min}} = 846.36$ is already significantly smaller compared to the FDTD-based result featuring a minimized $\mathrm{RMSD}_{\mathrm{min}} = 1819.16$. Already from the improved RMSD an improved representation of the spectral features in the measured 2D spectrum by the quantum model can be inferred.

The obtained two "best-match" 2D spectra, using either the FDTD-based approach or the developed quantum model, are further compared and discussed in Sec. 5.4.

APPENDIX

F

CONTRIBUTION OF ELECTRON EMISSION DRIVEN BY CLASSICAL LINEAR AND NONLINEAR POLARIZATIONS TO THE 3Q1Q- AND 1Q3Q-SIGNAL

As mentioned in Sec. 5.5, classical plasmon-polariton fields, generated by linear and nonlinear polarizations, in combination with nonlinear electron emission might lead, in principle, to multi-quantum coherences in the 2D spectrum. In the following, it is verified whether nonlinear electron emission driven by either the fundamental plasmon-polariton field or a certain mixture between the fundamental and a plasmon-polariton field due to third-harmonic generation (THG) inside the metal nanostructure significantly contribute to the detected 3Q peaks. In other words, the question is if the 3Q peaks can be unambiguously connected to a multi-quantum coherence or whether some nonlinear polarization in the system could result in such a signal contribution as well.

For answering this, 2D spectra are simulated for the aforementioned excitation scenarios based on a "Classical Plasmon Model" as described in detail below. The conclusion from the resulting spectra is that the nonlinear response of the metal is estimated to contribute well below 1 % to the observed 3Q peaks, and thus can be safely ignore as a competing signal contribution. This strengthens our original claim concerning the quantum origin of the observed wave packet.

There are two sources for system nonlinearities that might affect the system dynamics and lead to a 3Q signal contribution. In principle, a nonlinearity might either arise directly in the excitation in the metal system, i.e., from the nonlinearities of the electron gas, or due to a nonlinear response of the plasmon polariton

itself, i.e., from an anharmonicity of the collective charge motion.

However, in the present case these options can be narrowed down: The 3Q peak is linked to a coherence oscillating with three times the plasmon-polariton frequency. As discussed below, in the metal this coherence is associated with the $|m = 0\rangle \rightarrow |m = 3\rangle$ transition which is most efficiently driven by a field oscillating at the third harmonic, thus at 3ω. Here, m labels the single-electron states in the metal. It is well known that localized plasmon-polariton resonances give rise to third-order nonlinear polarizations that are usually detected in the far field [281, 282]. In particular, it was experimentally demonstrated for gold plasmonic structures that the THG response is dominated by the bulk nonlinear response (electric susceptibility) $\chi^{(3)}$ of the material and not by the surface-induced anharmonicity of the plasmon's collective charge motion [296]. In addition, theoretical work by Wand *et al.* based on time-dependent density-functional theory (TDDFT) for a jellium metal slab showed that, in contrast to SHG, the THG polarization has no significant surface contribution [297]. Based on this the surface-induced anharmonicity of the collective charge motion of the plasmon-polariton is ruled out as a source for THG fields in the present case. Consequently, only the bulk $\chi^{(3)}$ response of gold has to be considered. Boyd *et al.* have summarized the present knowledge about $\chi^{(3)}$ measurements for gold [298]. For short excitation pulses as in our case and a wavelength for which inter-band transitions are negligible, $\chi^{(3)} = 0.2\ \mathrm{nm}^2/\mathrm{V}^2$.

This value is used in connection with FDTD simulations in a first step to determine an upper limit for the ratio between the local THG field, $\mathbf{E}_{\mathrm{THG}}(\mathbf{r}, 3\omega)$, and the local fundamental field, $\mathbf{E}_{\mathrm{fund}}(\mathbf{r}, \omega)$, inside the gold. The local field, $\mathbf{E}_{\mathrm{loc}}(\mathbf{r}, \omega)$, is given by the "local field approach" [299] by

$$\mathbf{E}_{\mathrm{loc}}(\mathbf{r}, \omega) = \mathbf{E}_0(\omega) + \frac{1}{3\epsilon_0}\mathbf{P}(\mathbf{r}, \omega), \tag{F.0.1}$$

with $\mathbf{E}_0(\omega)$ describes the external incident field as it appears in Maxwell's equations, $\mathbf{P}(\mathbf{r}, \omega)$ is the polarization of the material and ϵ_0 the vacuum permittivity. Note that the external incident field can be well approximated as spatially homogeneous on the investigated length scales. In general, $\mathbf{E}_{\mathrm{fund}}(\mathbf{r}, \omega) = \mathbf{E}_{\mathrm{loc}}(\mathbf{r}, \omega)$, but for the argumentation presented here $\mathbf{E}_{\mathrm{fund}}(\mathbf{r}, \omega)$ is calculated from the local field enhancement as defined in Eq. (F.0.3). Nevertheless, according to Eq. (F.0.1) the local THG field, $\mathbf{E}_{\mathrm{THG}}(\mathbf{r}, 3\omega)$, is then obtained by

$$\mathbf{E}_{\mathrm{THG}}(\mathbf{r}, 3\omega) = \frac{1}{3\epsilon_0}\mathbf{P}^{(3)}(\mathbf{r}, 3\omega) = \frac{1}{3}\chi^{(3)}\mathbf{E}^3_{\mathrm{fund}}(\mathbf{r}, \omega), \tag{F.0.2}$$

where $\mathbf{P}^{(3)}(\mathbf{r}, 3\omega) = \epsilon_0\chi^{(3)}\mathbf{E}^3_{\mathrm{fund}}(\mathbf{r}, \omega)$ is the nonlinear polarization generating the

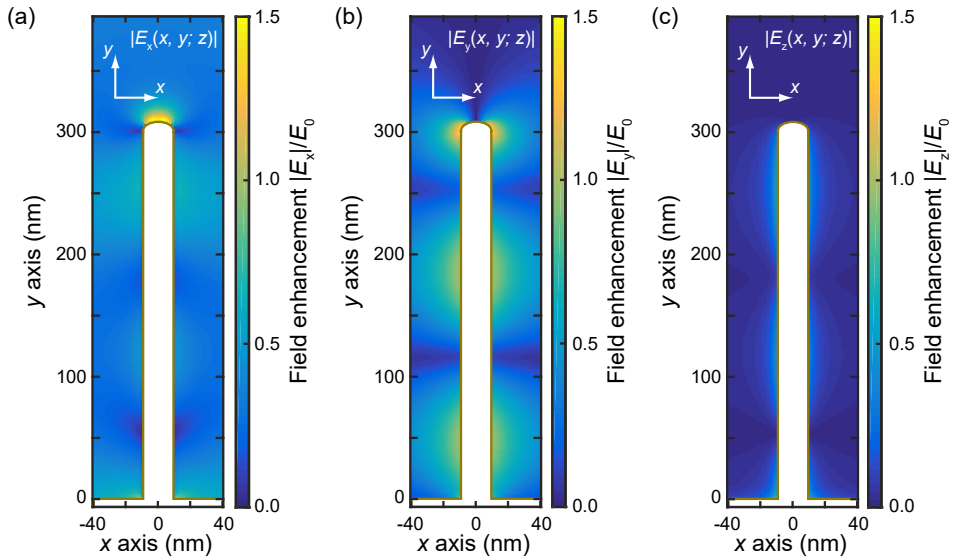

Figure F.1 – Local field enhancement in gold. Local field enhancement depicted for the absolute value of all three polarization directions: $|E_\mathrm{x}(\mathbf{r},\omega_\mathrm{pp})|$ (a), $|E_\mathrm{y}(\mathbf{r},\omega_\mathrm{pp})|$ (b), and $|E_\mathrm{z}(\mathbf{r},\omega_\mathrm{pp})|$ (c) at the plasmon-polariton resonance energy $\hbar\omega_\mathrm{pp} = 1.77$ eV shown in a particular xy plane located at $z = 2$ nm below the upper gold surface, with $E_0(\omega_\mathrm{pp})$ as incident field amplitude. The incident field is a plane wave that is linearly polarized along the x-direction. Note that the strongly enhanced fields at resonant excitation of the nanoslit plasmon polariton exist within the slit and thus are not relevant for the electron emission discussed here. FDTD simulations have been performed by Dr. Matthias Hensen. Adapted from Ref. [3] with permission from Springer Nature.

THG field and $\chi^{(3)}$ the electric susceptibility which has in general tensor properties. In this particular case $\chi^{(3)} = 0.2\ \mathrm{nm}^2/\mathrm{V}^2$ is known from literature [298]. Note that since $\mathbf{E}_\mathrm{THG}(\mathbf{r},3\omega)$ is generated by $\mathbf{E}_\mathrm{fund}(\mathbf{r},\omega)$ in the nanostructure there is no external incident field $\mathbf{E}_0(3\omega)$ oscillating at 3ω and hence the first term on the right hand side of Eq. (F.0.1) vanishes.

The local fundamental field in Eq. (F.0.2) is determined by the linear response of the nanoslit and might be either enhanced or suppressed compared to the external incident field $\mathbf{E}_0(\omega)$. This enhancement or suppression is determined by the local field enhancement factor $f(\mathbf{r},\omega)$ of the nanostructure, as defined in Eq. (2.2.7), which is determined in our case by FDTD simulations. Thus, the local fundamental field is given by

$$\mathbf{E}_\mathrm{fund}(\mathbf{r},\omega) = f(\mathbf{r},\omega)\mathbf{E}_0(\omega). \tag{F.0.3}$$

For simplicity, just scalar quantities are considered here to estimate an upper limit for the THG field strength. In the following, the field enhancement factor is set to $f(\mathbf{r},\omega)=1$. This is justified by FDTD simulation results showing the local field enhancement $f_i(\mathbf{r},\omega=\omega_{\mathrm{pp}})$, with plasmon-polariton resonance frequency ω_{pp}. Here the parameter $i=$ x, y, z is related to the individual three components of the local electric field $\mathbf{E}_{\mathrm{fund}}(\mathbf{r},\omega_{\mathrm{pp}})=(E_{\mathrm{x}}(\mathbf{r},\omega_{\mathrm{pp}}),E_{\mathrm{y}}(\mathbf{r},\omega_{\mathrm{pp}}),E_{\mathrm{z}}(\mathbf{r},\omega_{\mathrm{pp}}))$ in Fig. F.1. According to this data, the spatial distribution of local field enhancement

$$f(\mathbf{r},\omega_{\mathrm{pp}})=\frac{|\mathbf{E}_{\mathrm{fund}}(\mathbf{r},\omega_{\mathrm{pp}})|}{|\mathbf{E}_0(\omega_{\mathrm{pp}})|}=\frac{E_{\mathrm{fund}}(\mathbf{r},\omega_{\mathrm{pp}})}{E_0(\omega_{\mathrm{pp}})}, \tag{F.0.4}$$

barely exceeds 1.

The remaining quantity that needs to be evaluated is the strength of the incident field, $E_0(\omega)$. As an upper limit for $E_0(\omega)$ the peak field amplitude, $E_{0,\,\mathrm{peak}}$, is calculated which is retrieved from the known peak intensity, I_{peak}

$$I_{\mathrm{peak}}=\frac{E_{\mathrm{pulse}}}{\Delta t_{\mathrm{pulse}}A}, \tag{F.0.5}$$

with known laser pulse energy $E_{\mathrm{pulse}}=37$ nJ, pulse duration $\Delta t_{\mathrm{pulse}}=18$ fs and laser spot size at the illuminated sample $A=\pi r^2=\pi(135\ \mu\mathrm{m})^2$. The incident field amplitude $E_{0,\mathrm{peak}}$ is further given by

$$E_{0,\mathrm{peak}}=\sqrt{\frac{2I_{\mathrm{peak}}}{\epsilon_0 nc}}, \tag{F.0.6}$$

with refractive index n of the environment (here $n=1$), the speed of light in vacuum, c, and ϵ_0 the vacuum permittivity as defined in the preamble of this thesis. Using our experimental parameters in Eq. (F.0.5) and Eq. (F.0.6) the incident peak field amplitude results in $E_{0,\mathrm{peak}}=0.15$ V/nm.

With Eq. (F.0.2), Eq. (F.0.3), and $f(\mathbf{r},\omega_{\mathrm{pp}})=1$, the ratio between the THG field and the fundamental field then amounts to (upper limit)

$$\frac{E_{\mathrm{THG}}(\mathbf{r},3\omega_{\mathrm{pp}})}{E_{\mathrm{fund}}(\mathbf{r},\omega_{\mathrm{pp}})}=\frac{1}{3}\chi^{(3)}E_{\mathrm{fund}}^2(\mathbf{r},\omega_{\mathrm{pp}})=\frac{1}{3}\chi^{(3)}E_0^2(\omega_{\mathrm{pp}})=0.0015, \tag{F.0.7}$$

with $E_0(\omega_{\mathrm{pp}})=E_{0,\mathrm{peak}}$. Because of $f(\mathbf{r},\omega_{\mathrm{pp}})=1$, $E_{0,\mathrm{peak}}$ serves also as an upper limit for the local field $E_{\mathrm{fund}}(\omega_{\mathrm{pp}})$ and thus directly appears in Eq. (F.0.7). In most surface regions within the nanoresonator, the local fundamental field is smaller, resulting in an even smaller ratio. Based on the FDTD simulation shown in Fig. F.1 the spatial variation of $E_{\mathrm{THG}}(\mathbf{r},3\omega_{\mathrm{pp}})/E_{\mathrm{fund}}(\mathbf{r},\omega_{\mathrm{pp}})$ inside the gold is retrieved. Fig. F.2 shows the spatial distribution of $|E_{\mathrm{THG}}(\mathbf{r},3\omega_{\mathrm{pp}})|/|E_{\mathrm{fund}}(\mathbf{r},\omega_{\mathrm{pp}})|$

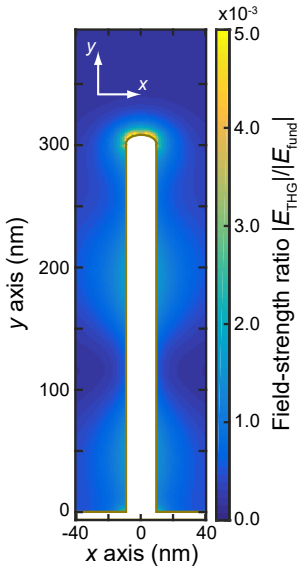

Figure F.2 – Spatially-resolved field strength ratio around the nanoresonator. Depicted are the field strength ratios of the absolute magnitude of the local THG field, $|E_{\mathrm{THG}}(\mathbf{r}, 3\omega_{\mathrm{pp}})|$, and the local fundamental field, $|E_{\mathrm{fund}}(\mathbf{r}, \omega_{\mathrm{pp}})|$, at the plasmon-polariton frequency ω_{pp} for the same xy plane as in Fig. F.1. Since THG only occurs in the gold substrate, the inside of the nanoslit is shown in white. FDTD simulations have been performed by Dr. Matthias Hensen. Adapted from Ref. [3] with permission from Springer Nature.

at the plasmon-polariton frequency ω_{pp}, where $|E_{\mathrm{fund}}(\mathbf{r}, \omega_{\mathrm{pp}})| = |f(\mathbf{r}, \omega_{\mathrm{pp}})|E_{0,\mathrm{peak}}$. The absolute magnitude of the individual scalar field strengths is shown for clarity only.

Having now established that the local THG field is about three orders of magnitude smaller than the local fundamental field, this relative weakness alone is not sufficient to exclude it as a source for the 3Q peak in the nonlinear electron emission process. Thus, this result is now used in a second step to determine the influence of the weak THG component on the corresponding 3Q signal in our 2D spectrum. For this analysis, the introduced quantum model is adapted to allow for direct local field excitation of the metal states, i.e., a driving of the metal excitation (Fig. F.3).

In this excitation scenario the polarization of the plasmon polariton is calculated as an expectation value of the dipole operator for the plasmon-polariton quantum state, instead of considering a coherent coupling between the quantized plasmon-polariton and the metal states as in the quantized plasmon model presented in Fig. 5.1. The resulting quantity is then used as a measure for the time-dependent

local fundamental plasmon-polariton field,

$$E_{\mathrm{fund}}(t') = 2\mathrm{Re}[E^{+}_{\mathrm{fund}}(t')], \tag{F.0.8}$$

where $E^{+}_{\mathrm{fund}}(t')$ is the temporal electric field connected to the positive frequency part of the spectrum. The positive frequency part of the THG field, $E^{+}_{\mathrm{THG}}(t')$, was derived from the fundamental one by taking the third power of the normalized fundamental's complex field and by introducing the amplitude value E_{THG} via

$$E^{+}_{\mathrm{THG}}(t') = E_{\mathrm{THG}}\left(\frac{|E^{+}_{\mathrm{fund}}(t')|}{\max(|E^{+}_{\mathrm{fund}}(t';\tau=0,t=0)|)}\right)^{3} \cdot \mathrm{e}^{i3\varphi(t')}. \tag{F.0.9}$$

Note that here, $|E^{+}_{\mathrm{fund}}(t')|$ is the temporal envelope of the fundamental plasmon-polariton field and $\varphi(t')$ its temporal phase. Special attention must be paid to the term $\max(|E^{+}_{\mathrm{fund}}(t';\tau=0,t=0)|)$. It refers to the peak value of the fundamental plasmon-polariton field that is generated upon single-pulse excitation of the nanoresonator, i.e., the incident multipulse sequence with pulse delays $\tau = 0$ and $t = 0$. Since the impact of THG fields with different relative amplitudes with respect to the fundamental field is investigated, a scaling parameter η is introduced. The THG field amplitude, E_{THG}, can then be set variably according to

$$E_{\mathrm{THG}} = \eta \max(|E^{+}_{\mathrm{fund}}(t';\tau=0,t=0)|) = \eta\, E_{\mathrm{fund}}, \tag{F.0.10}$$

with scaling parameter

$$\eta = \frac{E_{\mathrm{THG}}}{E_{\mathrm{fund}}}. \tag{F.0.11}$$

This parameter describes the ratio of the peak amplitudes of the fundamental plasmon-polariton field and the thus generated THG component upon single-pulse excitation. The time-dependent local THG field, $E_{\mathrm{THG}}(t')$, was retrieved via

$$E_{\mathrm{THG}}(t') = 2\mathrm{Re}[E^{+}_{\mathrm{THG}}(t')], \tag{F.0.12}$$

and finally the total electric field is obtained by

$$E_{\mathrm{tot}}(t') = E_{\mathrm{fund}}(t') + E_{\mathrm{THG}}(t'). \tag{F.0.13}$$

The interaction with the metal system was then driven by the product of the time-dependent field, $E_{\mathrm{tot}}(t')$, with the dipole moment of the metal transitions, $\mu_{m,\,\mathrm{fund}}$. Here, $\mu_{m,\,\mathrm{fund}}$ has the same value for all transitions between adjacent states. Since the excitations in the metal are modeled with broadband single-electron states to mimic a continuum, the numeric value of the dipole moment has

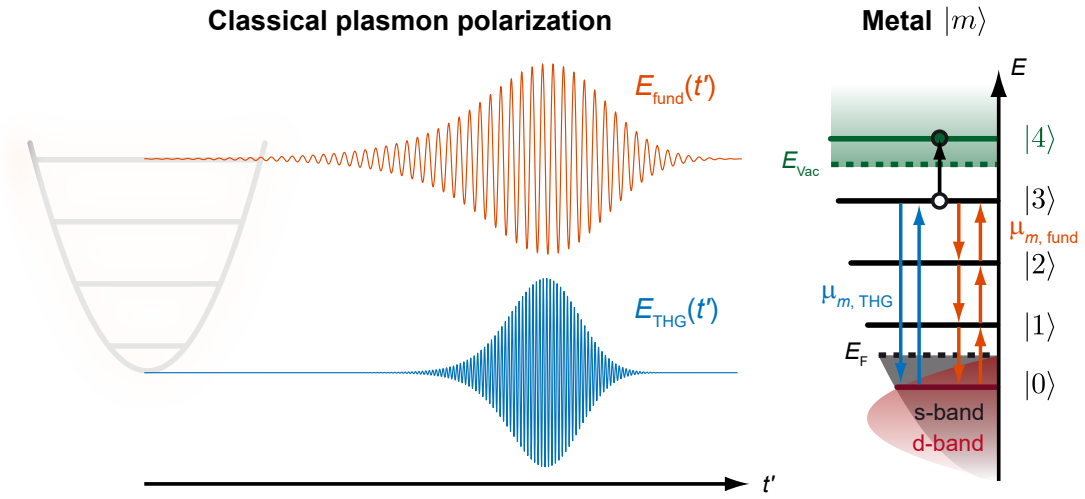

Figure F.3 – Sketch of the Classical Plasmon Model. Blue and orange arrows indicate the dipole coupling for the THG field, $E_{\mathrm{THG}}(t')$, and fundamental field, $E_{\mathrm{fund}}(t')$, respectively, where $\mu_{m,\,\mathrm{THG}} = 10\mu_{m,\,\mathrm{fund}}$. The photoemission step (black arrow) is modeled here in contrast to the quantum model via the Lindblad term L_{PE} according to Eq. (F.0.14). The shaded quantum oscillator on the left illustrates that the classical fields driving the metal are derived from polarization field expectation values of the QHO as described in the text. Adapted from Ref. [3] with permission from Springer Nature.

no physical meaning. Instead, the dipole moment must be adjusted to reproduce an appropriate percentage of the ground-state depopulation in the metal.

In the case where the system is driven exclusively by the fundamental field, the dipole moment $\mu_{m,\,\mathrm{fund}}$ is set such that the ground-state depopulation stayed below 10 %, i.e., an excitation density is chosen close to experimental conditions for plasmon-assisted multi-photon electron emission [56]. Note that somewhat higher excitation levels in gold lead to sample degradation and hence the 10 % depopulation level constitutes an upper level for the metal excitation and thus also limits the metal-related nonlinear response.

For the final excitation step into the photoemission state, the envelope of the total local field, $E_{\mathrm{tot}}(t')$, was used in a Lindblad term which connects the highest lying bound state of the metal system $|m = 3\rangle$ and the photoemission state $|m = 4\rangle$ (see Fig. F.3). The corresponding Lindblad term is given by

$$L_{\mathrm{PE}} = |E^{+}_{\mathrm{tot}}(t')|^2 \Big(\mathcal{L}^{\dagger}_{\mathrm{PE}}\, \rho_{\mathrm{m}}(t')\, \mathcal{L}_{\mathrm{PE}} - \frac{1}{2} \mathcal{L}_{\mathrm{PE}}\, \mathcal{L}^{\dagger}_{\mathrm{PE}}\, \rho_{\mathrm{m}}(t') - \frac{1}{2} \rho_{\mathrm{m}}(t')\, \mathcal{L}_{\mathrm{PE}}\, \mathcal{L}^{\dagger}_{\mathrm{PE}} \Big). \quad \text{(F.0.14)}$$

Here, $\mathcal{L}_{\mathrm{PE}} = |m=3\rangle \langle m=4|$ is the Lindblad jump operator and $\rho_{\mathrm{m}}(t')$ the density matrix of the metal system. The rate constant usual for Lindblad terms was replaced with the squared envelope of the total local field, $|E^{+}_{\mathrm{tot}}(t')|$. Note that compared to the Lindblad terms in Eq. (2.4.3), which model general dehasing processes, the Lindblad term L_{PE} describes a unidirectional population transfer from the bound state $|m=3\rangle$ to the photoemission state $|m=4\rangle$, whereby the measure of population transfer depends on the instantaneous intensity of the local field. The physical units are deliberately disregarded here and it is only ensured that just a small part of the population of $|m=3\rangle$ is transferred to $|m=4\rangle$.

In this way, the signal channel of the developed quantum model (see Fig. 5.1) in which a unidirectional population transfer by means of a Lindblad term is responsible for signal generation is replaced. In contrast to the quantum model, it is not the annihilation of quantized plasmon-polariton excitations that is responsible for the transition from $|m=3\rangle$ to $|m=4\rangle$, but the time-dependent intensity of the classical plasmon-polariton field $|E^{+}_{\mathrm{tot}}(t')|^2$. The increasing classical intensity of the plasmon-polariton field thus has the analogous effect as the increasing population of excited Fock states in the QHO when the intensity of the oscillator's driving field $E_{\mathrm{exc}}(t')$ in the quantum model increases.

The consequence of the fact that $|m=3\rangle$ and $|m=4\rangle$ are only linked via a Lindblad term is that the highest multi-quantum coherence in the metal system, i.e., a coherence between $|m=0\rangle$ and $|m=3\rangle$, oscillates at three times the fundamental frequency. Thus, the appearance of 3Q peaks in the 2D spectrum due to a quantum coherence in the metal alone would be possible in principle. This coherence could either be driven by sequential excitations in the metal via the fundamental field or directly by the THG field generated at the plasmonic nanostructure.

Therefore, the following two cases are now compared: 1) the full quantum model, labeled for better distinguishability "Quantized Plasmon Model" and 2) a five-level metal system, labeled "Classical Plasmon Model", as described in the previous paragraphs. In addition to the detailed description of the Classical Plasmon Model given above, it should be mentioned that the dipole moment for the direct $|m=0\rangle \rightarrow |m=3\rangle$ transition driven by the THG field, $\mu_{m,\,\mathrm{THG}}$, was set to ten times the dipole moment for the transitions driven by the fundamental field, e.g., $|m=0\rangle \rightarrow |m=1\rangle$ transition, $\mu_{m,\,\mathrm{fund}}$, in accordance with the about 100 times larger absorption for THG light in gold compared to the fundamental [300].

The ratio between the maximum field amplitudes $\eta = E_{\mathrm{THG}}/E_{\mathrm{fund}}$ was varied

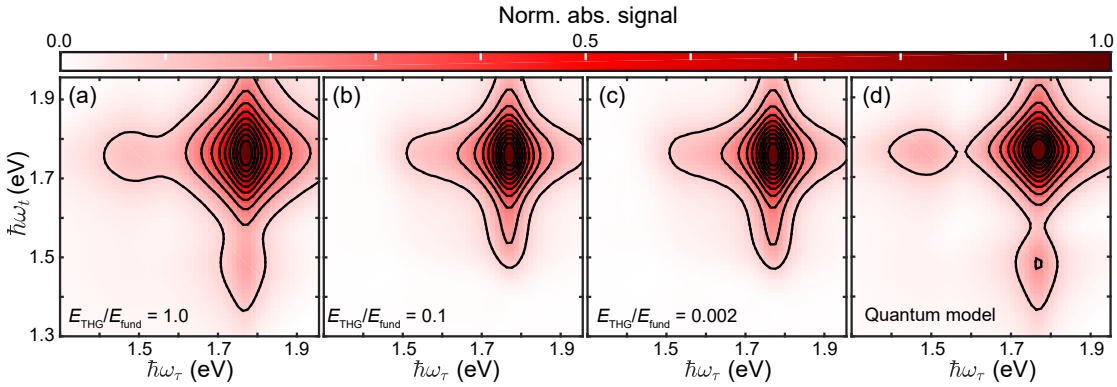

Figure F.4 – Comparison of simulated and normalized 2D spectra for ideal Gaussian excitation pulses. (a-c), Classical Plasmon Model: THG fields of varying relative amplitudes compared to the fundamental local field $E_{\mathrm{THG}}/E_{\mathrm{fund}} = 1.0$ (a), 0.1 (b), and 0.002 (c). (d) Quantized Plasmon Model for comparison. All 2D spectra are normalized to their respective maximum. Reproduced from Ref. [3] with permission from Springer Nature.

in the Classical Plasmon Model to test under which conditions a THG-induced signal would significantly contribute to the 3Q peaks.

The 2D spectra for three different ratios $E_{\mathrm{THG}}/E_{\mathrm{fund}}$ of the Classical Plasmon Model are depicted in Fig. F.4 (a-c), together with the full quantum model and no separate THG-created field, i.e., the Quantized Plasmon Model, in Fig. F.4 (d). In the Classical Plasmon Model, the 3Q peaks are clearly visible at $\hbar\omega_\tau = 1.77$ eV and $\hbar\omega_t = 1.48$ eV as well as at $\hbar\omega_\tau = 1.48$ eV and $\hbar\omega_t = 1.77$ eV if the fundamental field and the THG field exhibit the same amplitude (Fig. F.4 (a)). However, a ratio of $\eta = 1$ would require an enormous frequency conversion efficiency that is far beyond our estimate based on experimental parameters, presented in Eq. (F.0.7). By lowering the amplitude ratio by about one order of magnitude, i.e., $\eta = 0.1$, the 3Q peaks in the 2D spectrum do not only decrease in strength but completely disappear (Fig. F.4 (b)). It is indeed appropriate to speak of a disappearance for this ratio of field strengths, because for an even smaller amplitude ratio of $\eta = 0.002$, no further changes in the line shape of the 2D spectrum can be detected by eye, as depicted in Fig. F.4 (c). Note that the amplitude ratio of $\eta = 0.002$ is within the uncertainties of our estimates, see Eq. (F.0.7), of the expected amplitude ratio for our experimental conditions.

To make the comparison of the 3Q peak strength more quantitative, the difference between 2D spectra of the Classical Plasmon Model is shown using only the fundamental local field $E_{\mathrm{fund}}(t')$ as excitation of the metal system and the

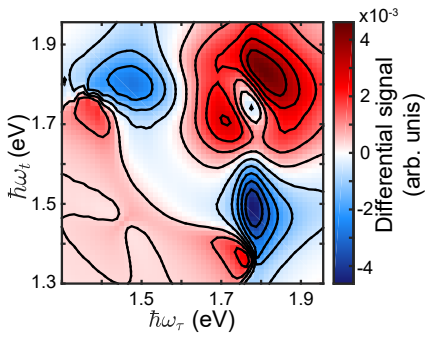

Figure F.5 – Difference 2D spectrum. Difference between the 2D spectrum of Fig. F.4 (b) and the simulated 2D spectrum (not shown) using as well the Classical Plasmon Model, but with a modeled excitation by the fundamental local field $E_{\mathrm{fund}}(t')$ only. The latter was subtracted from the former. Reproduced from Ref. [3] with permission from Springer Nature.

Classical Plasmon Model with both local fundamental $E_{\mathrm{fund}}(t')$ and local THG field $E_{\mathrm{THG}}(t')$ at an amplitude ratio $\eta = 0.1$ in Fig. F.5. The maximum absolute magnitude of the deviation is below 1 % of the maximum peak amplitude. Thus, based on this difference, the THG-induced relative contribution to the 3Q peaks is estimated to be in our experiement well below 1 %. Keep in mind that the actual amplitude ratio due to the bulk THG response is in fact $E_{\mathrm{THG}}/E_{\mathrm{fund}} = 0.0015$, i.e., a much smaller value at which contributions to the 3Q peak in the 2D spectrum are negligible. Accordingly, the Classical Plasmon Model can be neglected as a potential origin of the 3Q peaks in the 2D spectrum.

As discussed already in Sec. 5.5, this vanishingly small contribution from nonlinear polarizations is attributed to the rather short pure-dephasing time of only a few femtoseconds for the intermediate states in the metal. Note that this choice is not arbitrary since it reflects that in a metal the excitation does not occur via discrete levels but via a continuum of states. As it was first reported by Petek's group [57], this cancels practically all coherence effects in the multi-quantum metal excitation. Note that with pure-dephasing times of 4 fs a conservative upper limit is applied. This would correspond to narrow spectral features in the density of states in the unoccupied band structure of gold with about 0.2 eV bandwidth, which are not known of. Note that choosing a significantly shorter pure-dephasing time of 1 fs does not affect the 3Q peak in the 2D spectrum calculated based on the Quantized Plasmon Model.

The observation that transitions driven by nonlinear polarizations have minor impact on plasmon-assisted electron emission is consistent with previous experi-

mental observations. The observation of intermediate-state lifetimes in plasmonic systems in plasmon-assisted two-photon electron emission is clear evidence that the sequential excitation process driven by the fundamental dominates over excitation processes which are driven by harmonics of the fundamental light field [140].

Now that it is shown, via simulations, that the contribution to the 3Q peaks is vanishingly small for linear and realistic THG polarization-driven excitations in the metal system, the potential role of classical SHG fields is briefly discussed because the generation of such fields occurs at a lower order of perturbation theory than THG. In principle, combining a plasmon-polariton-generated SHG field, oscillating at 2ω, and the fundamental plasmon polariton, oscillating at ω, in a sequential excitation process could also give rise to a coherence that oscillates at 3ω and is connected to the superposition of the states $|m = 0\rangle$ and $|m = 3\rangle$ in the Classical Plasmon Model. However, the transition at the fundamental frequency exhibits a dipole moment that is about one order of magnitude lower than that of a transition at the THG frequency (see discussion above). Therefore, the combination of SHG and fundamental fields is even less efficient than direct population of the state $|m = 3\rangle$ by THG fields. Based on this argument, the SHG process is also neglected as a possible source for 3Q coherences.

In summary, the nonlinear response of the metal itself was estimated to contributes well below 1 % to the observed 3Q peak and thus can be safely ignored as a competing signal contribution.

LIST OF ABBREVIATIONS

SiO_2	Silicon-dioxide
1D	One-dimensional
2D	Two-dimensional
2PPE	Two-photon-photoemission
3D	Three-dimensional
AC	Aberration corrector
ACF	Autocorrelation function
Ag	Silver
AOD	Angle of diffraction
AOI	Angle of incidence
Ar	Argon
AR	Anti-reflection
Au	Gold
BBO	β-BaB_2O_4
CCD	Charge-coupled device
CM	Cylindrical mirror
Cs	Caesium
DOS	Density of states
DSFD	Double-sided Feynman diagram
FDTD	Finite-difference time-domain
FIB	Focused-ion-beam
FROG	Frequency-resolved optical gating
FTSI	Fourier-transform spectral interferometry
FWHM	Full-width at half-maximum
GaAs	Gallium arsenide
He	Helium
HeNe	Helium-neon

Hg	Mercury
IR	Infrared
ITO	Indium tin oxide
LCD	Liquid-crystal display
LEED	Low-energy electron diffraction
LEEM	Low-energy electron microscopy
LN_2	Liquid nitrogen
LSP	Localized surface-plasmon polariton
MCP	Micro-channel plate
NIR	Near-infrared
NOPA	Noncollinear optical parametric amplifier
P	Polarizer
Pb	Lead
PC	Phase-cycling
PEEM	Photoemission electron microscopy
PS	Pulse shaper
PSPP	Propagating surface-plasmon polariton
QHO	Quantum harmonic oscillator
RMSD	Root-mean-square deviation
ROI	Region of interest
SCG	Supercontinuum generation
SEM	Scanning electron microscopy
SHG	Second-harmonic generation
SI	Spectral interference
SLM	Spatial light modulator
TDDFT	Time-dependent density-functional theory
THG	Third-harmonic generation
TR-PEEM	Time-resolved photoemission electron microscopy
UHV	Ultra-high vacuum
UV	Ultraviolet
Vc	Voltage count
VIS	Visible
VPHG	Volume phase holographic grating
YAG	Yttrium-aluminium-garnet
Yb	Ytterbium

LIST OF PUBLICATIONS

Parts of this thesis have been published in the following references:

Reference [1]:

B. Huber, S. Pres, E. Wittmann, L. Dietrich, J. Lüttig, D. Fersch, E. Krauss, D. Friedrich, J. Kern, V. Lisinetskii, M. Hensen, B. Hecht, R. Bratschitsch, E. Riedle, and T. Brixner,
Space- and time-resolved UV-to-NIR surface spectroscopy and 2D nanoscopy at 1 MHz repetition rate,
Rev. Sci. Instrum. **90**, 113103 (2019).

Reference [2]:

S. Pres, L. Kontschak, M. Hensen, and T. Brixner,
Coherent 2D electronic spectroscopy with complete characterization of excitation pulses during all scanning steps,
Opt. Express **29**, 4191–4209 (2021).

Reference [3]:

S. Pres, B. Huber, M. Hensen, D. Fersch, E. Schatz, D. Friedrich, V. Lisinetskii, R. Pompe, B. Hecht, W. Pfeiffer and T. Brixner,
Detection of a plasmon-polariton quantum wave packet,
Nat. Phys. (2023). https://doi.org/10.1038/s41567-022-01912-5

The publications listed above have partly been used in this dissertation. The following table itemizes to what extent the different sections of the publications

have been reused at which position in this work. The sources of adapted figures are additionally indicated at the end of the corresponding figure captions.

Publication	Usage	Dissertation
Ref. [1]		
pp. 1–2	text reproduced, modified and extended	pp. 53–54
pp. 2–4	figures adapted; text reproduced, modified and extended	pp. 54–58
pp. 5–7	figures adapted; text reproduced, minor modifications	pp. XVII–XXI
pp. 7–8	figures adapted; text reproduced, minor modifications	pp. 78–82
pp. 11	text reproduced, modified, and extended	pp. 82–85
Ref. [2]		
pp. 1	text reproduced, minor modifications and extended	pp. 85–86
pp. 2–3	text reproduced, minor modifications	pp. 86–88
pp. 3–7	figures adapted; text reproduced, minor modifications	pp. 88–94
pp. 4–5	text reproduced, modified and extended	pp. 75–78
pp. 7–15	figures adapted; text reproduced, minor modifications	pp. 106–117
pp. 15–16	text reproduced, minor modifications and extended	pp. 123–127
SI pp. 1–10	figures adapted; text reproduced, minor modifications	pp. 94–106
SI pp. 11–17	figures adapted; text reproduced, minor modifications	pp. 117–123
SI pp. 18–19	figures adapted; text reproduced, minor modifications	pp. XXIX–XXXIII
Ref. [3]		
pp. 1–3 + pp. 8	figures modified, text reproduced, minor modifications	pp. 127–134
pp. 3–5	figures adapted, text reproduced, minor modifications	pp. 134–140
pp. 5–6	text reproduced, minor modifications	pp. 158–161
pp. 6	text portion reproduced, modified	pp. 161–XVII
pp. 8–9	text reproduced, minor modifications	pp. 153–158
SI pp. 2–8	figures adapted, text reproduced, minor modifications	pp. 140–151
SI pp. 9	figure new; text reproduced, minor modifications	pp. 151–153
SI pp. 10–16	figures adapted or modified; text reproduced, minor modifications	pp. XXXIX–XLIX

Further publications which are not related to this thesis:

Reference [4]:

C. Cremer, R. Kaufmann, M. Gunkel, S. Pres, Y. Weiland, P. Müller, T. Ruckelshausen, P. Lemmer, F. Geiger, S. Degenhard, C. Wege, N.A.W. Lemmermann, R. Holtappels, H. Strickfaden, and M. Hausmann,
Superresolution imaging of biological nanostructures by spectral precision distance microscopy,
Biotechnol. J. **6**, 1037–1051 (2011).

Reference [5]:

B. Huber, M. Hensen, S. Pres, V. Lisinetskii, J. Lüttig, E. Wittmann, E. Krauss, D. Friedrich, B. Hecht, E. Riedle, and T. Brixner,
Time-resolved photoemission electron microscopy of a plasmonic slit resonator using 1 MHz, 25 fs, UV-to-NIR-tunable pulses,
EPJ Web Conf. **205**, 08002 (2019).

Reference [6]:

M. Hensen, B. Huber, D. Friedrich, E. Krauss, S. Pres, P. Grimm, D. Fersch, J. Lüttig, V. Lisinetskii, B. Hecht, and T. Brixner,
Spatial variations in femtosecond field dynamics within a plasmonic nanoresonator mode,
Nano Lett. **19**, 4651–4658 (2019).

Reference [7]:

M. Aeschlimann, T. Brixner, F. Fenner, B. Frisch, P. Folge, M. Hartelt, M. Hensen, T.H. Loeber, W. Pfeiffer, S. Pres, and H. Stiebig,
Direct imaging of photonic band-edge states in golden Vogel spirals using photoemission electron microscopy,
J. Opt. Soc. Am. B: Opt. Phys. **40**, B19–B27 (2023).

BIBLIOGRAPHY

[1] B. Huber, S. Pres, E. Wittmann *et al.*, *Space- and time-resolved UV-to-NIR surface spectroscopy and 2D nanoscopy at 1 MHz repetition rate*, Rev. Sci. Instrum. **90**, 113103 (2019).

[2] S. Pres, L. Kontschak, M. Hensen, and T. Brixner, *Coherent 2D electronic spectroscopy with complete characterization of excitation pulses during all scanning steps*, Opt. Express **29**, 4191–4209 (2021).

[3] S. Pres, B. Huber, M. Hensen *et al.*, *Detection of a plasmon-polariton quantum wave packet*, Nat. Phys. (2023).

[4] C. Cremer, R. Kaufmann, M. Gunkel *et al.*, *Superresolution imaging of biological nanostructures by spectral precision distance microscopy*, Biotechnol. J. **6**, 1037–1051 (2011).

[5] B. Huber, M. Hensen, S. Pres *et al.*, *Time-resolved photoemission electron microscopy of a plasmonic slit resonator using 1 MHz, 25 fs, UV-to-NIR-tunable pulses*, Web Conf. **205**, 08002 (2019).

[6] M. Hensen, B. Huber, D. Friedrich *et al.*, *Spatial variations in femtosecond field dynamics within a plasmonic nanoresonator mode*, Nano Lett. **19**, 4651–4658 (2019).

[7] M. Aeschlimann, T. Brixner, F. Fenner *et al.*, *Direct imaging of photonic band-edge states in golden Vogel spirals using photoemission electron microscopy*, J. Opt. Soc. Am. B: Opt. Phys. **40**, B19–B27 (2023).

[8] M. Schlosshauer, *Decoherence and the quantum-to-classical transition*, The Frontiers Collection (Springer, 2007), 2nd ed.

[9] W. H. Zurek, *Decoherence and the transition from quantum to classical – REVISITED*, arXiv:quant-ph/0306072 (2003).

[10] Z. Yan, *General thermal wavelength and its applications*, Eur. J. Phys. **21**, 625–631 (2000).

[11] P. Collaboration, N. Aghanim, Y. Akrami *et al.*, *Planck 2018 results. VI. Cosmological parameters*, A&A **641**, A6 (2020).

[12] A. Stolow, A. E. Bragg, and D. M. Neumark, *Femtosecond time-resolved photoelectron spectroscopy*, Chem. Rev. **104**, 1719–1758 (2004).

[13] U. Bovensiepen and P. Kirchmann, *Elementary relaxation processes investigated by femtosecond photoelectron spectroscopy of two-dimensional materials*, Laser Photonics Rev. **6**, 589–606 (2012).

[14] S. Backus, C. G. Durfee III, M. M. Murnane, and H. C. Kapteyn, *High power ultrafast lasers*, Rev. Sci. Instrum. **69**, 1207–1223 (1998).

[15] D. Strickland, *Generating High-Intensity Ultrashort Optical Pulses - Nobel Lecture*, (2018).

[16] M. Maiuri, M. Garavelli, and G. Cerullo, *Ultrafast Spectroscopy: State of the Art and Open Challenges*, J. Am. Chem. Soc. **142**, 3–15 (2020).

[17] G. Cerullo and S. De Silvestri, *Ultrafast optical parametric amplifiers*, Rev. Sci. Instrum. **74**, 1–18 (2003).

[18] A. H. Zewail, *Femtochemistry: Atomic-scale dynamics of the chemical bond*, J. Phys. Chem. A **104**, 5660–5694 (2000).

[19] S. Mukamel, *Multidimensional femtosecond correlation spectroscopies of electronic and vibrational excitations*, Annu. Rev. Phys. Chem. **51**, 691–729 (2000).

[20] D. M. Jonas, *Two-dimensional femtosecond spectroscopy*, Annu. Rev. Phys. Chem. **54**, 425–463 (2003).

[21] M. Cho, *Coherent two-dimensional optical spectroscopy*, Chem. Rev. **108**, 1331–1418 (2008).

[22] J. D. Hybl, A. W. Albrecht, S. M. Gallagher Faeder, and D. M. Jonas, *Two-dimensional electronic spectroscopy*, Chem. Phys. Lett. **297**, 307–313 (1998).

[23] P. Hamm, M. Lim, and R. M. Hochstrasser, *Structure of the amide I band of peptides measured by femtosecond nonlinear-infrared spectroscopy*, J. Phys. Chem. B **102**, 6123–6138 (1998).

[24] T. Brixner, I. V. Stiopkin, and G. R. Fleming, *Tunable two-dimensional femtosecond spectroscopy*, Opt. Lett. **29**, 884–886 (2004).

[25] U. Selig, F. Langhojer, F. Dimler *et al.*, *Inherently phase-stable coherent two-dimensional spectroscopy using only conventional optics*, Opt. Lett. **33**, 2851–2853 (2008).

[26] U. Selig, C.-F. Schleussner, M. Foerster *et al.*, *Coherent two-dimensional ultraviolet spectroscopy in fully noncollinear geometry*, Opt. Lett. **35**, 4178–4180 (2010).

[27] S. Biswas, J. Kim, X. Zhang, and G. D. Scholes, *Coherent two-dimensional and broadband electronic spectroscopies*, Chem. Rev. **122**, 4257–4321 (2022).

[28] M. Aeschlimann, T. Brixner, A. Fischer *et al.*, *Coherent two-dimensional nanoscopy*, Science **333**, 1723–1726 (2011).

[29] P. F. Tekavec, J. A. Myers, K. L. M. Lewis *et al.*, *Effects of chirp on two-dimensional Fourier transform electronic spectra*, Opt. Express **18**, 11015–11024 (2010).

[30] L. Lepetit, G. Chériaux, and M. Joffre, *Linear techniques of phase measurement by femtosecond spectral interferometry for applications in spectroscopy*, J. Opt. Soc. Am. B **12**, 2467–2474 (1995).

[31] K. Chen, G. Razinskas, H. Vieker *et al.*, *High-Q, low-mode-volume and multiresonant plasmonic nanoslit cavities fabricated by helium ion milling*, Nanoscale **10**, 17148–17155 (2018).

[32] V. Amendola, R. Pilot, M. Frasconi *et al.*, *Surface plasmon resonance in gold nanoparticles: a review*, J. Phys.: Condens. Matter **29**, 203002 (2017).

[33] S. A. Maier, *Plasmonics: fundamentals and applications* (Springer, Berlin, 2007), 1st ed.

[34] L. Novotny and B. Hecht, *Principles of nano-optics* (Cambridge University Press, Cambridge, 2012), 2nd ed.

[35] E. Altewischer, M. P. van Exter, and J. P. Woerdman, *Plasmon-assisted transmission of entangled photons*, Nature **418**, 304–306 (2002).

[36] M. Fox, *Optical properties of solids*, vol. 3 of *Oxford master series in physics* (Oxford University Press, 2010), 2nd ed.

[37] S. I. Kudryashov, M. Kandyla, C. A. D. Roeser, and E. Mazur, *Intraband and interband optical deformation potentials in femtosecond-laser-excited $\alpha-Te$*, Phys. Rev. B **75**, 085207 (2007).

[38] H. Petek and S. Ogawa, *Femtosecond time-resolved two-photon photoemission studies of electron dynamics in metals*, Prog. Surf. Sci. **56**, 239–310 (1997).

[39] L.-M. Yang, M. Dornfeld, T. Frauenheim, and E. Ganz, *Glitter in a 2D monolayer*, Phys. Chem. Chem. Phys. **17**, 26036–26042 (2015).

[40] N. W. Ashcroft and D. N. Mermin, *Festkörperphysik* (Oldenbourg Wissenschaftsverlag, München, 2012), 4th ed.

[41] C. Kittel, *Introduction to solid state physics* (Wiley John + Sons, 2004), 8th ed.

[42] H. Z. Jooya, X. Fan, K. S. McKay *et al.*, *Crystallographic orientation dependence of work function: carbon adsorption on Au surfaces*, Mol. Phys. **117**, 2157–2161 (2019).

[43] A. Einstein, *Über einen die Erzeugung und Verwandlung des Lichtes betreffenden heuristischen Gesichtspunkt*, Ann. Phys. **322**, 132–148 (1905).

[44] A. Damascelli, *Probing the electronic structure of complex systems by ARPES*, Phys. Scr. **2004**, 61–74 (2004).

[45] B. H. Bransden and C. J. Joachain, *Physics of atoms and molecules* (Pearson Education, 2003), 1st ed.

[46] W. Schattke and M. A. Van Hove, eds., *Solid-state photoemission and related methods* (Wiley-VCH, Weinheim, 2002), 1st ed.

[47] H. Y. Fan, *Theory of photoelectric emission from metals*, Phys. Rev. **68**, 43–52 (1945).

[48] C. N. Berglund and W. E. Spicer, *Photoemission studies of copper and silver: theory*, Phys. Rev. **136**, A1030–A1044 (1964).

[49] P. J. Feibelman and D. E. Eastman, *Photoemission spectroscopy—Correspondence between quantum theory and experimental phenomenology*, Phys. Rev. B **10**, 4932–4947 (1974).

[50] J. H. Bechtel, W. Lee Smith, and N. Bloembergen, *Two-photon photoemission from metals induced by picosecond laser pulses*, Phys. Rev. B **15**, 4557–4563 (1977).

[51] R. Yen, J. Liu, and N. Bloembergen, *Thermally assisted multiphoton photoelectric emission from tungsten*, Opt. Commun. **35**, 277–282 (1980).

[52] J. G. Fujimoto, J. M. Liu, E. P. Ippen, and N. Bloembergen, *Femtosecond laser interaction with metallic tungsten and nonequilibrium electron and lattice temperatures*, Phys. Rev. Lett. **53**, 1837–1840 (1984).

[53] J. Kupersztych and M. Raynaud, *Anomalous multiphoton photoelectric effect in ultrashort time scales*, Phys. Rev. Lett. **95**, 147401 (2005).

[54] A. T. Georges, *Theory of the multiphoton photoelectric effect: A stepwise excitation process*, Phys. Rev. B **51**, 13735–13738 (1995).

[55] A. T. Georges, *Coherent and incoherent multiple-harmonic generation from metal surfaces*, Phys. Rev. A **54**, 2412–2418 (1996).

[56] W. Pfeiffer, C. Kennerknecht, and M. Merschdorf, *Electron dynamics in supported metal nanoparticles: relaxation and charge transfer studied by time-resolved photoemission*, Appl. Phys. A **78**, 1011–1028 (2004).

[57] M. J. Weida, S. Ogawa, H. Nagano, and H. Petek, *Ultrafast interferometric pump–probe correlation measurements in systems with broadened bands or continua*, J. Opt. Soc. Am. B **17**, 1443–1451 (2000).

[58] V. Gasparov and R. Huguenin, *Electron-phonon, electron-electron and electron-surface scattering in metals from ballistic effects*, Adv. Phys. **42**, 393–521 (1993).

[59] W. S. Farm, R. Storz, H. W. K. Tom, and J. Bokor, *Direct measurement of nonequilibrium electron-energy distributions in sub-picosecond laser-heated gold films*, Surf. Sci. **283**, 221–225 (1993).

[60] W. S. Fann, R. Storz, H. W. K. Tom, and J. Bokor, *Electron thermalization in gold*, Phys. Rev. B **46**, 13592–13595 (1992).

[61] G. V. Hansson and R. I. G. Uhrberg, *Photoelectron spectroscopy of surface states on semiconductor surfaces*, Surf. Sci. Rep. **9**, 197–292 (1988).

[62] C. E. Carroll and F. T. Hioe, *Coherent population transfer via the continuum*, Phys. Rev. Lett. **68**, 3523–3526 (1992).

[63] J.-C. Diels and W. Rudolph, *Ultrashort laser pulse phenomena: fundamentals, techniques, and applications on a femtosecond time scale* (Academic Press Inc, Amsterdam, 2006), 2nd ed.

[64] J. Budimir and J. L. Skinner, *On the relationship between T_1 and T_2 for stochastic relaxation models*, J. Stat. Phys. **49**, 1029–1042 (1987).

[65] H. M. Sevian and J. L. Skinner, *T_2 can be greater than $2T_1$*, J. Chem. Phys. **91**, 1775–1782 (1989).

[66] E. Knoesel, A. Hotzel, T. Hertel *et al.*, *Dynamics of photoexcited electrons in metals studied with time-resolved two-photon photoemission*, Surf. Sci. **368**, 76–81 (1996).

[67] C. Suárez, W. E. Bron, and T. Juhasz, *Dynamics and transport of electronic carriers in thin gold films*, Phys. Rev. Lett. **75**, 4536–4539 (1995).

[68] M. Aeschlimann, M. Bauer, S. Pawlik *et al.*, *Transport and dynamics of optically excited electrons in metals*, Appl. Phys. A **71**, 485–491 (2000).

[69] P. Tian, D. Keusters, Y. Suzaki, and W. S. Warren, *Femtosecond phase-coherent two-dimensional spectroscopy*, Science **300**, 1553–1555 (2003).

[70] H.-S. Tan, *Theory and phase-cycling scheme selection principles of collinear phase coherent multi-dimensional optical spectroscopy*, J. Chem. Phys. **129**, 124501 (2008).

[71] C. Sönnichsen, T. Franzl, T. Wilk *et al.*, *Drastic reduction of plasmon damping in gold nanorods*, Phys. Rev. Lett. **88**, 077402 (2002).

[72] R. H. Ritchie, *Plasma losses by fast electrons in thin films*, Phys. Rev. **106**, 874–881 (1957).

[73] E. Rudberg, *Inelastic scattering of electrons from solids*, Phys. Rev. **50**, 138–150 (1936).

[74] C. J. Powell and J. B. Swan, *Origin of the characteristic electron energy losses in aluminum*, Phys. Rev. **115**, 869–875 (1959).

[75] C. J. Powell and J. B. Swan, *Effect of oxidation on the characteristic loss spectra of aluminum and magnesium*, Phys. Rev. **118**, 640–643 (1960).

[76] Y.-Y. Teng and E. A. Stern, *Plasma radiation from metal grating surfaces*, Phys. Rev. Lett. **19**, 511–514 (1967).

[77] E. J. R. Vesseur, J. Aizpurua, T. Coenen *et al.*, *Plasmonic excitation and manipulation with an electron beam*, MRS Bulletin **37**, 752–760 (2012).

[78] S. T. Koev, A. Agrawal, H. J. Lezec, and V. A. Aksyuk, *An efficient large-area grating coupler for surface plasmon polaritons*, Plasmonics **7**, 269–277 (2012).

[79] E. Devaux, T. W. Ebbesen, J.-C. Weeber, and A. Dereux, *Launching and decoupling surface plasmons via micro-gratings*, Appl. Phys. Lett. **83**, 4936–4938 (2003).

[80] S.-K. Kim, H.-S. Ee, W. Choi *et al.*, *Surface-plasmon-induced light absorption on a rough silver surface*, Appl. Phys. Lett. **98**, 011109 (2011).

[81] H. Ditlbacher, J. R. Krenn, N. Felidj *et al.*, *Fluorescence imaging of surface plasmon fields*, Appl. Phys. Lett. **80**, 404–406 (2002).

[82] P. Kahl, S. Wall, C. Witt *et al.*, *Normal-incidence photoemission electron microscopy (NI-PEEM) for imaging surface plasmon polaritons*, Plasmonics **9**, 1401–1407 (2014).

[83] G. Spektor, D. Kilbane, A. K. Mahro *et al.*, *Revealing the subfemtosecond dynamics of orbital angular momentum in nanoplasmonic vortices*, Science **355**, 1187–1191 (2017).

[84] D. Podbiel, P. Kahl, A. Makris *et al.*, *Imaging the nonlinear plasmoemission dynamics of electrons from strong plasmonic fields*, Nano Lett. **17**, 6569–6574 (2017).

[85] A. Bouhelier and G. P. Wiederrecht, *Excitation of broadband surface plasmon polaritons: Plasmonic continuum spectroscopy*, Phys. Rev. B **71**, 195406 (2005).

[86] B. Hecht, H. Bielefeldt, L. Novotny *et al.*, *Local excitation, scattering, and interference of surface plasmons*, Phys. Rev. Lett. **77**, 1889 (1996).

[87] R. Hillenbrand, F. Keilmann, P. Hanarp *et al.*, *Coherent imaging of nanoscale plasmon patterns with a carbon nanotube optical probe*, Appl. Phys. Lett. **83**, 368–370 (2003).

[88] T. Neuman, P. Alonso-González, A. Garcia-Etxarri *et al.*, *Mapping the near fields of plasmonic nanoantennas by scattering-type scanning near-field optical microscopy*, Laser Photonics Rev. **9**, 637–649 (2015).

[89] P. Biagioni, J.-S. Huang, and B. Hecht, *Nanoantennas for visible and infrared radiation*, Rep. Prog. Phys. **75**, 024402 (2012).

[90] K. M. Mayer and J. H. Hafner, *Localized surface plasmon resonance sensors*, Chem. Rev. **111**, 3828–3857 (2011).

[91] M. R. Hasan and O. G. Hellesø, *Dielectric optical nanoantennas*, Nanotechnology **32**, 202001 (2021).

[92] A. J. Haes, C. L. Haynes, A. D. McFarland *et al.*, *Plasmonic materials for surface-enhanced sensing and spectroscopy*, MRS Bulletin **30**, 368–375 (2005).

[93] Y. Xia and N. J. Halas, *Shape-controlled synthesis and surface plasmonic properties of metallic nanostructures*, MRS Bulletin **30**, 338–348 (2005).

[94] V. Amendola and M. Meneghetti, *Size evaluation of gold nanoparticles by UV–vis spectroscopy*, J. Phys. Chem. C **113**, 4277–4285 (2009).

[95] J. Olson, S. Dominguez-Medina, A. Hoggard *et al.*, *Optical characterization of single plasmonic nanoparticles*, Chem. Soc. Rev. **44**, 40–57 (2014).

[96] J. A. Scholl, A. L. Koh, and J. A. Dionne, *Quantum plasmon resonances of individual metallic nanoparticles*, Nature **483**, 421–427 (2012).

[97] J. A. Scholl, A. García-Etxarri, A. L. Koh, and J. A. Dionne, *Observation of quantum tunneling between two plasmonic nanoparticles*, Nano Lett. **13**, 564–569 (2013).

[98] O. Nicoletti, F. de la Peña, R. K. Leary *et al.*, *Three-dimensional imaging of localized surface plasmon resonances of metal nanoparticles*, Nature **502**, 80–84 (2013).

[99] A. C. Atre, B. J. M. Brenny, T. Coenen *et al.*, *Nanoscale optical tomography with cathodoluminescence spectroscopy*, Nat. Nanotechnol. **10**, 429–436 (2015).

[100] A. Losquin, L. F. Zagonel, V. Myroshnychenko *et al.*, *Unveiling nanometer scale extinction and scattering phenomena through combined electron energy loss spectroscopy and cathodoluminescence measurements*, Nano Lett. **15**, 1229–1237 (2015).

[101] P. B. Johnson and R. W. Christy, *Optical constants of the noble metals*, Phys. Rev. B **6**, 4370–4379 (1972).

[102] M. G. Blaber, M. D. Arnold, and M. J. Ford, *A review of the optical properties of alloys and intermetallics for plasmonics*, J. Phys.: Condens. Matter **22**, 143201 (2010).

[103] F. Wang and Y. R. Shen, *General properties of local plasmons in metal nanostructures*, Phys. Rev. Lett. **97**, 206806 (2006).

[104] M. A. Kats, N. Yu, P. Genevet *et al.*, *Effect of radiation damping on the spectral response of plasmonic components*, Opt. Express **19**, 21748–21753 (2011).

[105] X. Li, D. Xiao, and Z. Zhang, *Landau damping of quantum plasmons in metal nanostructures*, New J. Phys. **15**, 023011 (2013).

[106] M. Perner, P. Bost, U. Lemmer *et al.*, *Optically induced damping of the surface plasmon resonance in gold colloids*, Phys. Rev. Lett. **78**, 2192–2195 (1997).

[107] M. L. Brongersma, N. J. Halas, and P. Nordlander, *Plasmon-induced hot carrier science and technology*, Nat. Nanotechnol. **10**, 25–34 (2015).

[108] X. Meng, L. Liu, S. Ouyang *et al.*, *Nanometals for solar-to-chemical energy conversion: from semiconductor-based photocatalysis to plasmon-mediated photocatalysis and photo-thermocatalysis*, Adv. Mater. **28**, 6781–6803 (2016).

[109] A. Brandstetter-Kunc, G. Weick, D. Weinmann, and R. A. Jalabert, *Decay of dark and bright plasmonic modes in a metallic nanoparticle dimer*, Phys. Rev. B **91**, 035431 (2015).

[110] E. J. Heilweil and R. M. Hochstrasser, *Nonlinear spectroscopy and picosecond transient grating study of colloidal gold*, J. Chem. Phys. **82**, 4762–4770 (1985).

[111] C. Reuß, I. L. Shumay, U. Thomann *et al.*, *Control of the dephasing of image-potential states by CO adsorption on Cu(100)*, Phys. Rev. Lett. **82**, 153–156 (1999).

[112] X. Fan, T. Takagahara, J. E. Cunningham, and H. Wang, *Pure dephasing induced by exciton–phonon interactions in narrow GaAs quantum wells*, Solid State Commun. **108**, 857–861 (1998).

[113] C. Voisin, N. Del Fatti, D. Christofilos, and F. Vallée, *Ultrafast electron dynamics and optical nonlinearities in metal nanoparticles*, J. Phys. Chem. B **105**, 2264–2280 (2001).

[114] R. A. Dynich and A. N. Ponyavina, *Effect of metallic nanoparticle sizes on the local field near their surface*, J. Appl. Spectrosc. **75**, 832–838 (2008).

[115] R. Chikkaraddy, B. de Nijs, F. Benz *et al.*, *Single-molecule strong coupling at room temperature in plasmonic nanocavities*, Nature **535**, 127–130 (2016).

[116] K. Santhosh, O. Bitton, L. Chuntonov, and G. Haran, *Vacuum Rabi splitting in a plasmonic cavity at the single quantum emitter limit*, Nat. Commun. **7**, ncomms11823 (2016).

[117] N. Kongsuwan, A. Demetriadou, R. Chikkaraddy *et al.*, *Suppressed quenching and strong-coupling of purcell-enhanced single-molecule emission in plasmonic nanocavities*, ACS Photonics **5**, 186–191 (2018).

[118] H. Groß, J. M. Hamm, T. Tufarelli *et al.*, *Near-field strong coupling of single quantum dots*, Sci. Adv. **4**, eaar4906 (2018).

[119] J. Zhang, W. Zhang, X. Zhu *et al.*, *Resonant slot nanoantennas for surface plasmon radiation in optical frequency range*, Appl. Phys. Lett. **100**, 241115 (2012).

[120] H. U. Yang, R. L. Olmon, K. S. Deryckx *et al.*, *Accessing the optical magnetic near-field through Babinet's principle*, ACS Photonics **1**, 894–899 (2014).

[121] I. M. Hancu, A. G. Curto, M. Castro-López *et al.*, *Multipolar interference for directed light emission*, Nano Lett. **14**, 166–171 (2014).

[122] C. Huck, J. Vogt, M. Sendner *et al.*, *Plasmonic enhancement of infrared vibrational signals: nanoslits versus nanorods*, ACS Photonics **2**, 1489–1497 (2015).

[123] H. Liu, Z. Quan, Y. Cheng *et al.*, *Ultra-compact universal linear-optical logic gate based on single rectangle plasmonic slot nanoantenna*, Plasmonics **16**, 973–980 (2021).

[124] H. Guo, T. P. Meyrath, T. Zentgraf *et al.*, *Optical resonances of bowtie slot antennas and their geometry and material dependence*, Opt. Express **16**, 7756–7766 (2008).

[125] G. Lu, W. Li, T. Zhang *et al.*, *Plasmonic-enhanced molecular fluorescence within isolated bowtie nano-apertures*, ACS Nano **6**, 1438–1448 (2012).

[126] A. Weissman, M. Sukharev, and A. Salomon, *Strong coupling between an inverse bowtie nano-antenna and a J-aggregate*, J. Colloid Interface Sci. **610**, 438–445 (2022).

[127] A. Degiron, H. J. Lezec, N. Yamamoto, and T. W. Ebbesen, *Optical transmission properties of a single subwavelength aperture in a real metal*, Opt. Commun. **239**, 61–66 (2004).

[128] J. Ferreira, M. J. L. Santos, M. M. Rahman *et al.*, *Attomolar protein detection using in-hole surface plasmon resonance*, J. Am. Chem. Soc. **131**, 436–437 (2009).

[129] A. A. Yanik, M. Huang, O. Kamohara *et al.*, *An optofluidic nanoplasmonic biosensor for direct detection of live viruses from biological media*, Nano Lett. **10**, 4962–4969 (2010).

[130] G. Palermo, M. Rippa, Y. Conti *et al.*, *Plasmonic metasurfaces based on pyramidal nanoholes for high-efficiency SERS biosensing*, ACS Appl. Mater. Interfaces **13**, 43715–43725 (2021).

[131] E. Krauss, R. Kullock, X. Wu *et al.*, *Controlled growth of high-aspect-ratio single-crystalline gold platelets*, Cryst. Growth Des. **18**, 1297–1302 (2018).

[132] J.-S. Huang, V. Callegari, P. Geisler *et al.*, *Atomically flat single-crystalline gold nanostructures for plasmonic nanocircuitry*, Nat. Commun. **1**, 150 (2010).

[133] L. Novotny, *Effective wavelength scaling for optical antennas*, Phys. Rev. Lett. **98**, 266802 (2007).

[134] K. S. Yee, *Numerical solution of initial boundary value problems involving Maxwell's equations in isotropic media*, IEEE Trans. Antennas Propag. **14**, 302–307 (1966).

[135] A. Taflove and S. C. Hagness, *Computational electrodynamics: the finite-difference time-domain method* (Artech House, Norwood, MA, 1995), 2nd ed.

[136] J. D. Jackson, *Classical electrodynamics* (Wiley & Sons, 1999), 3rd ed.

[137] D. Bayer, C. Wiemann, O. Gaier *et al.*, *Time-resolved 2PPE and time-resolved PEEM as a probe of LSP's in silver nanoparticles*, J. Nanomater. **2008**, 1–11 (2008).

[138] C. Strüber, *Ultrafast coherent control and multidimensional spectroscopy on the nanoscale*, Ph.D. thesis, Universität Bielefeld (2014).

[139] M. Merschdorf, *Femtodynamics in nanoparticles - The short lives of excited electrons in silver*, Ph.D. thesis, Julius-Maximilians-Universität Würzburg (2002).

[140] M. Merschdorf, C. Kennerknecht, and W. Pfeiffer, *Collective and single-particle dynamics in time-resolved two-photon photoemission*, Phys. Rev. B **70**, 193401 (2004).

[141] S. Ogawa, H. Nagano, H. Petek, and A. P. Heberle, *Optical dephasing in Cu(111) measured by interferometric two-photon time-resolved photoemission*, Phys. Rev. Lett. **78**, 1339–1342 (1997).

[142] U. Höfer, *Time-resolved coherent spectroscopy of surface states*, Appl. Phys. B **68**, 383–392 (1999).

[143] M. Weida, S. Ogawa, H. Nagano, and H. Petek, *Parallel excitation pathways in ultrafast interferometric pump-probe correlation measurements of hot-electron lifetimes in metals*, Appl. Phys. A **71**, 553–559 (2000).

[144] M. Cinchetti, A. Gloskovskii, S. A. Nepjiko *et al.*, *Photoemission electron microscopy as a tool for the investigation of optical near fields*, Phys. Rev. Lett. **95**, 047601 (2005).

[145] A. Kubo, K. Onda, H. Petek *et al.*, *Femtosecond imaging of surface plasmon dynamics in a nanostructured silver film*, Nano Lett. **5**, 1123–1127 (2005).

[146] M. Aeschlimann, M. Bauer, D. Bayer *et al.*, *Adaptive subwavelength control of nano-optical fields*, Nature **446**, 301–304 (2007).

[147] P. Tuchscherer, *A route to optical spectroscopy on the nanoscale*, Ph.D. thesis, Julius-Maximilians-Universität Würzburg (2012).

[148] F. D. Fuller and J. P. Ogilvie, *Experimental implementations of two-dimensional Fourier transform electronic spectroscopy*, Annu. Rev. Phys. Chem. **66**, 667–690 (2015).

[149] C. L. Smallwood and S. T. Cundiff, *Multidimensional coherent spectroscopy of semiconductors*, Laser Photonics Rev. **12**, 1800171 (2018).

[150] W. Wagner, C. Li, J. Semmlow, and W. Warren, *Rapid phase-cycled two-dimensional optical spectroscopy in fluorescence and transmission mode*, Opt. Express **13**, 3697–3706 (2005).

[151] P. F. Tekavec, G. A. Lott, and A. H. Marcus, *Fluorescence-detected two-dimensional electronic coherence spectroscopy by acousto-optic phase modulation*, J. Chem. Phys. **127**, 214307 (2007).

[152] J. R. Widom, W. Lee, A. Perdomo-Ortiz *et al.*, *Temperature-dependent conformations of a membrane supported zinc porphyrin tweezer by 2D fluorescence spectroscopy*, J. Phys. Chem. A **117**, 6171–6184 (2013).

[153] A. K. De, D. Monahan, J. M. Dawlaty, and G. R. Fleming, *Two-dimensional fluorescence-detected coherent spectroscopy with absolute phasing by confocal imaging of a dynamic grating and 27-step phase-cycling*, J. Chem. Phys. **140**, 194201 (2014).

[154] S. Draeger, S. Roeding, and T. Brixner, *Rapid-scan coherent 2D fluorescence spectroscopy*, Opt. Express **25**, 3259–3267 (2017).

[155] S. Mueller, S. Draeger, X. Ma *et al.*, *Fluorescence-detected two-quantum and one-quantum–two-quantum 2D electronic spectroscopy*, J. Phys. Chem. Lett. **9**, 1964–1969 (2018).

[156] V. Tiwari, Y. A. Matutes, A. T. Gardiner *et al.*, *Spatially-resolved fluorescence-detected two-dimensional electronic spectroscopy probes varying excitonic structure in photosynthetic bacteria*, Nat. Commun. **9**, 4219 (2018).

[157] M. Aeschlimann, T. Brixner, D. Differt *et al.*, *Perfect absorption in nanotextured thin films via Anderson-localized photon modes*, Nat. Photonics **9**, 663–668 (2015).

[158] M. Aeschlimann, T. Brixner, M. Cinchetti *et al.*, *Observation of optical coherence in a disordered metal-molecule interface by coherent optical two-dimensional photoelectron spectroscopy*, Phys. Rev. B **105**, 205415 (2022).

[159] G. Nardin, T. M. Autry, K. L. Silverman, and S. T. Cundiff, *Multidimensional coherent photocurrent spectroscopy of a semiconductor nanostructure*, Opt. Express **21**, 28617–28627 (2013).

[160] K. J. Karki, J. R. Widom, J. Seibt *et al.*, *Coherent two-dimensional photocurrent spectroscopy in a PbS quantum dot photocell*, Nat. Commun. **5**, 5869 (2014).

[161] A. A. Bakulin, C. Silva, and E. Vella, *Ultrafast spectroscopy with photocurrent detection: watching excitonic optoelectronic systems at work*, J. Phys. Chem. Lett. **7**, 250–258 (2016).

[162] L. Bolzonello, F. Bernal-Texca, L. G. Gerling *et al.*, *Photocurrent-detected 2D electronic spectroscopy reveals ultrafast hole transfer in operating PM6/Y6 organic solar cells*, J. Phys. Chem. Lett. **12**, 3983–3988 (2021).

[163] S. Roeding and T. Brixner, *Coherent two-dimensional electronic mass spectrometry*, Nat. Commun. **9**, 2519 (2018).

[164] L. Bruder, U. Bangert, M. Binz *et al.*, *Coherent multidimensional spectroscopy of dilute gas-phase nanosystems*, Nat. Commun. **9**, 4823 (2018).

[165] D. Uhl, U. Bangert, L. Bruder, and F. Stienkemeier, *Coherent optical 2D photoelectron spectroscopy*, Optica **8**, 1316–1324 (2021).

[166] S. Mukamel, *Principles of nonlinear optical spectroscopy* (Oxford University Press, New York, 1995), 1st ed.

[167] P. Hamm and M. Zanni, *Concepts and methods of 2D infrared spectroscopy* (Cambridge University Press, New York, 2011), 1st ed.

[168] A. Gelzinis, R. Augulis, V. Butkus *et al.*, *Two-dimensional spectroscopy for non-specialists*, Biochim. Biophys. Acta Bioenerg. **1860**, 271–285 (2019).

[169] T. Brixner, J. Stenger, H. M. Vaswani *et al.*, *Two-dimensional spectroscopy of electronic couplings in photosynthesis*, Nature **434**, 625–628 (2005).

[170] D. Zigmantas, E. L. Read, T. Mančal *et al.*, *Two-dimensional electronic spectroscopy of the B800–B820 light-harvesting complex*, PNAS **103**, 12672–12677 (2006).

[171] N. S. Ginsberg, Y.-C. Cheng, and G. R. Fleming, *Two-dimensional electronic spectroscopy of molecular aggregates*, Acc. Chem. Res. **42**, 1352–1363 (2009).

[172] J. A. Myers, K. L. M. Lewis, F. D. Fuller *et al.*, *Two-dimensional electronic spectroscopy of the D1-D2-cyt b559 photosystem II reaction center complex*, J. Phys. Chem. Lett. **1**, 2774–2780 (2010).

[173] R. D. Mehlenbacher, T. J. McDonough, M. Grechko *et al.*, *Energy transfer pathways in semiconducting carbon nanotubes revealed using two-dimensional white-light spectroscopy*, Nat. Commun. **6**, 6732 (2015).

[174] E. Thyrhaug, K. Žídek, J. Dostál *et al.*, *Exciton structure and energy transfer in the Fenna–Matthews–Olson complex*, J. Phys. Chem. Lett. **7**, 1653–1660 (2016).

[175] J. Dostál, J. Pšenčík, and D. Zigmantas, *In situ mapping of the energy flow through the entire photosynthetic apparatus*, Nat. Chem. **8**, 705–710 (2016).

[176] P. Akhtar, C. Zhang, T. N. Do *et al.*, *Two-dimensional spectroscopy of chlorophyll* a *excited-state equilibration in light-harvesting complex II*, J. Phys. Chem. Lett. **8**, 257–263 (2017).

[177] T. Brixner, R. Hildner, J. Köhler *et al.*, *Exciton transport in molecular aggregates – From natural antennas to synthetic chromophore systems*, Adv. Energy Mater. **7**, 1700236 (2017).

[178] M. Maiuri and J. Brazard, *Electronic couplings in (Bio-) chemical processes*, Top. Curr. Chem. **376**, 10 (2018).

[179] A. Niedringhaus, V. R. Policht, R. Sechrist *et al.*, *Primary processes in the bacterial reaction center probed by two-dimensional electronic spectroscopy*, Proc. Natl. Acad. Sci. U.S.A. **115**, 3563–3568 (2018).

[180] C. C. Jumper, S. Rafiq, S. Wang, and G. D. Scholes, *From coherent to vibronic light harvesting in photosynthesis*, Curr. Opin. Chem. Biol. **47**, 39–46 (2018).

[181] J. Cao, R. J. Cogdell, D. F. Coker *et al.*, *Quantum biology revisited*, Sci. Adv. **6**, eaaz4888 (2020).

[182] J. Sperling, A. Nemeth, J. Hauer *et al.*, *Excitons and disorder in molecular nanotubes: A 2D electronic spectroscopy study and first comparison to a microscopic model*, J. Phys. Chem. A **114**, 8179–8189 (2010).

[183] J. Dostál, F. Fennel, F. Koch *et al.*, *Direct observation of exciton–exciton interactions*, Nat. Commun. **9**, 2466 (2018).

[184] B. Kriete, J. Lüttig, T. Kunsel *et al.*, *Interplay between structural hierarchy and exciton diffusion in artificial light harvesting*, Nat. Commun. **10**, 4615 (2019).

[185] C. Heshmatpour, P. Malevich, F. Plasser *et al.*, *Annihilation dynamics of molecular excitons measured at a single perturbative excitation energy*, J. Phys. Chem. Lett. **11**, 7776–7781 (2020).

[186] B. Kriete, A. S. Bondarenko, R. Alessandri *et al.*, *Molecular versus excitonic disorder in individual artificial light-harvesting systems*, J. Am. Chem. Soc. **142**, 18073–18085 (2020).

[187] P. Malý, S. Mueller, J. Lüttig *et al.*, *Signatures of exciton dynamics and interaction in coherently and fluorescence-detected four- and six-wave-mixing two-dimensional electronic spectroscopy*, J. Chem. Phys. **153**, 144204 (2020).

[188] S. Pawlik, M. Bauer, and M. Aeschlimann, *Lifetime difference of photoexcited electrons between intraband and interband transitions*, Surf. Sci. **377–379**, 206–209 (1997).

[189] P. M. Echenique, J. M. Pitarke, E. V. Chulkov, and A. Rubio, *Theory of inelastic lifetimes of low-energy electrons in metals*, Chem. Phys. **251**, 1–35 (2000).

[190] A. Galler and T. Feurer, *Pulse shaper assisted short laser pulse characterization*, Appl. Phys. B **90**, 427–430 (2008).

[191] C. Kramer, *Investigation of nanostructure-induced localized light phenomena using ultrafast laser spectroscopy*, Ph.D. thesis, Julius-Maximilians-Universität Würzburg (2017).

[192] L. Seidner, G. Stock, and W. Domcke, *Nonperturbative approach to femtosecond spectroscopy: General theory and application to multidimensional nonadiabatic photoisomerization processes*, J. Chem. Phys. **103**, 3998–4011 (1995).

[193] S. Meyer and V. Engel, *Non-perturbative wave-packet calculations of time-resolved four-wave-mixing signals*, Appl. Phys. B **71**, 293–297 (2014).

[194] D. Keusters, H.-S. Tan, and W. S. Warren, *Role of pulse phase and direction in two-dimensional optical spectroscopy*, J. Phys. Chem. A **103**, 10369–10380 (1999).

[195] E. J. Brown, Q. Zhang, and M. Dantus, *Femtosecond transient-grating techniques: Population and coherence dynamics involving ground and excited states*, J. Chem. Phys. **110**, 5772 (1999).

[196] G. Lindblad, *On the generators of quantum dynamical semigroups*, Commun. Math. Phys. **48**, 119–130 (1976).

[197] C. A. Brasil, F. F. Fanchini, and R. d. J. Napolitano, *A simple deduction of the Lindblad equation*, Revista Brasileira de Ensino de Física **35**, 1 (2013).

[198] H.-P. Breuer and F. Petruccione, *The theory of open quantum systems* (Oxford University Press, Oxford, 2002), 1st ed.

[199] T. Kenneweg, *Developement, testing and application of a Matlab quantum dynamics toolbox*, Master's thesis, Universität Bielefeld (2017).

[200] W. H. Press, S. A. Teukolsky, W. T. Vetterling, and B. P. Flannery, *Numerical recipes: The art of scientifc computing.* (Cambridge University Press, 2007), 3rd ed.

[201] E. Wittmann, *Taming optical parametric amplification: Stable few cycle pulses at 210 to 10000 nm from Ti:Sapphire and Yb-based lasers*, Ph.D. thesis, Ludwig-Maximilians-Universität München (2019).

[202] M. Bradler and E. Riedle, *Sub-20 fs μJ-energy pulses tunable down to the near-UV from a 1 MHz Yb-fiber laser system*, Opt. Lett. **39**, 2588–2591 (2014).

[203] C. Schriever, S. Lochbrunner, P. Krok, and E. Riedle, *Tunable pulses from below 300 to 970 nm with durations down to 14 fs based on a 2 MHz ytterbium-doped fiber system*, Opt. Lett. **33**, 192–194 (2008).

[204] A. M. Weiner, *Femtosecond pulse shaping using spatial light modulators*, Rev. Sci. Instrum. **71**, 1929–1960 (2000).

[205] A. Monmayrant, S. Weber, and B. Chatel, *A newcomer's guide to ultrashort pulse shaping and characterization*, J. Phys. B: At. Mol. Opt. Phys. **43**, 103001 (2010).

[206] C. Homann, N. Krebs, and E. Riedle, *Convenient pulse length measurement of sub-20-fs pulses down to the deep UV via two-photon absorption in bulk material*, Appl. Phys. B **104**, 783–791 (2011).

[207] S. Goetz, D. Li, V. Kolb *et al.*, *Coherent two-dimensional fluorescence microspectroscopy*, Opt. Express **26**, 3915–3925 (2018).

[208] C. Homann, C. Schriever, P. Baum, and E. Riedle, *Octave wide tunable UV-pumped NOPA: pulses down to 20 fs at 0.5 MHz repetiton rate*, Opt. Express **16**, 5746–5756 (2009).

[209] P. Baum, S. Lochbrunner, and E. Riedle, *Generation of tunable 7-fs ultraviolet pulses: achromatic phase matching and chirp management*, Appl. Phys. B **79**, 1027–1032 (2004).

[210] A. M. Weiner, *Ultrafast optical pulse shaping: A tutorial review*, Opt. Commun. **284**, 3669–3692 (2011).

[211] F. Träger, ed., *Springer Handbook of lasers and optics* (Springer, Berlin, 2012), 2nd ed.

[212] T. Brixner, *Kohärente Kontrolle von Photodissoziationsreaktionen mit optimal geformten ultrakurzen Laserpulsen*, Diplomarbeit, Julius-Maximilians-Universität Würzburg (1998).

[213] V. Seyfried, *Beobachtung und Kontrolle molekularer Dynamik durch Femtosekundenlaserpulse.* Ph.D. thesis, Julius-Maximilians-Universität Würzburg (1998).

[214] J. Paye and A. Migus, *Space-time Wigner functions and their application to the analysis of a pulse shaper*, J. Opt. Soc. Am. B **12**, 1480–1490 (1995).

[215] M. Wefers and K. Nelson, *Space-time profiles of shaped ultrafast optical waveforms*, IEEE J. Quantum Electron. **32**, 161–172 (1996).

[216] J. Vaughan, T. Feurer, K. Stone, and K. Nelson, *Analysis of replica pulses in femtosecond pulse shaping with pixelated devices*, Opt. Express **14**, 1314–1328 (2006).

[217] Jenoptik, *SLM-S640d SLM-S320d Technische Dokumentation*, (2012).

[218] PHYWE, *Helium-Neon Laser Exp. Descr. LEP 2.6.07 -01*, (2007).

[219] W. Demtröder, *Experimentalphysik, Bd. 2. Elektrizität und Optik* (Springer, Berlin, 2004), 3rd ed.

[220] R. Tromp, J. Hannon, A. Ellis *et al.*, *A new aberration-corrected, energy-filtered LEEM/PEEM instrument. I. Principles and design*, Ultramicroscopy **110**, 852–861 (2010).

[221] E. Bauer, *A brief history of PEEM*, J. Electron. Spectrosc. Relat. Phenomena **185**, 314–322 (2012).

[222] E. Bauer, *Surface microscopy with low energy electrons* (Springer, New York, 2014), 1st ed.

[223] A. B. Pang, T. Müller, M. S. Altman, and E. Bauer, *Fourier optics of image formation in LEEM*, J. Phys.: Condens. Matter **21**, 314006 (2009).

[224] N. M. Buckanie, J. Göhre, P. Zhou *et al.*, *Space charge effects in photoemission electron microscopy using amplified femtosecond laser pulses*, J. Phys. Condens. Matter **21**, 314003 (2009).

[225] F. Haag, T. Eul, P. Thielen *et al.*, *Time-resolved two-photon momentum microscopy—A new approach to study hot carrier lifetimes in momentum space*, Rev. Sci. Instrum. **90**, 103104 (2019).

[226] B. Lv, T. Qian, and H. Ding, *Angle-resolved photoemission spectroscopy and its application to topological materials*, Nat. Rev. Phys. **1**, 609–626 (2019).

[227] E. Brühl, T. Buckup, and M. Motzkus, *Minimization of $1/f^n$ phase noise in liquid crystal masks for reliable femtosecond pulse shaping*, Opt. Express **25**, 23376–23386 (2017).

[228] J. T. Fourkas, W. L. Wilson, G. Wäckerle *et al.*, *Picosecond time-scale phase-related optical pulses: measurement of sodium optical coherence decay by observation of incoherent fluorescence*, J. Opt. Soc. Am. B **6**, 1905–1910 (1989).

[229] K. Lazonder, M. S. Pshenichnikov, and D. A. Wiersma, *Easy interpretation of optical two-dimensional correlation spectra*, Opt. Lett. **31**, 3354–3356 (2006).

[230] D. J. Hoffman and M. D. Fayer, *CLS next gen: Accurate frequency–frequency correlation functions from center line slope analysis of 2D correlation spectra using artificial neural networks*, J. Phys. Chem. A **124**, 5979–5992 (2020).

[231] J. D. Hybl, Y. Christophe, and D. M. Jonas, *Peak shapes in femtosecond 2D correlation spectroscopy*, Chem. Phys. **266**, 295–309 (2001).

[232] M. K. Yetzbacher, N. Belabas, K. A. Kitney, and D. M. Jonas, *Propagation, beam geometry, and detection distortions of peak shapes in two-dimensional Fourier transform spectra*, J. Chem. Phys. **126**, 044511 (2007).

[233] B. Cho, M. K. Yetzbacher, K. A. Kitney *et al.*, *Propagation and beam geometry effects on two-dimensional Fourier transform spectra of multilevel systems*, J. Phys. Chem. A **113**, 13287–13299 (2009).

[234] A. P. Spencer, H. Li, S. T. Cundiff, and D. M. Jonas, *Pulse propagation effects in optical 2D Fourier-transform spectroscopy: Theory*, J. Phys. Chem. A **119**, 3936–3960 (2015).

[235] H. Li, A. P. Spencer, A. Kortyna *et al.*, *Pulse propagation effects in optical 2D Fourier-transform spectroscopy: Experiment*, J. Phys. Chem. A **117**, 6279–6287 (2013).

[236] X. Ma, J. Dostál, and T. Brixner, *Broadband 7-fs diffractive-optic-based 2D electronic spectroscopy using hollow-core fiber compression*, Opt. Express **24**, 20781–20791 (2016).

[237] M. Binz, L. Bruder, L. Chen *et al.*, *Effects of high pulse intensity and chirp in two-dimensional electronic spectroscopy*, Opt. Express **28**, 25806–25829 (2020).

[238] P. Tournois, *Acousto-optic programmable dispersive filter for adaptive compensation of group delay time dispersion in laser systems*, Opt. Commun. **140**, 245–249 (1997).

[239] F. Verluise, V. Laude, Z. Cheng *et al.*, *Amplitude and phase control of ultrashort pulses by use of an acousto-optic programmable dispersive filter: Pulse compression and shaping*, Opt. Lett. **25**, 575–577 (2000).

[240] A. D. Bristow, D. Karaiskaj, X. Dai *et al.*, *A versatile ultrastable platform for optical multidimensional Fourier-transform spectroscopy*, Rev. Sci. Instrum. **80**, 073108 (2009).

[241] D. Brida, C. Manzoni, and G. Cerullo, *Phase-locked pulses for two-dimensional spectroscopy by a birefringent delay line*, Opt. Lett. **37**, 3027–3029 (2012).

[242] M. M. Wefers and K. A. Nelson, *Generation of high-fidelity programmable ultrafast optical waveforms*, Opt. Lett. **20**, 1047–1049 (1995).

[243] N. M. Kearns, R. D. Mehlenbacher, A. C. Jones, and M. T. Zanni, *Broadband 2D electronic spectrometer using white light and pulse shaping: Noise and signal evaluation at 1 and 100 kHz*, Opt. Express **25**, 7869–7883 (2017).

[244] F. Frei, A. Galler, and T. Feurer, *Space-time coupling in femtosecond pulse shaping and its effects on coherent control*, J. Chem. Phys. **130**, 034302 (2009).

[245] D. Brinks, R. Hildner, F. D. Stefani, and N. F. van Hulst, *Beating spatio-temporal coupling: implications for pulse shaping and coherent control experiments*, Opt. Express **19**, 26486–26499 (2011).

[246] L. Wittenbecher and D. Zigmantas, *Correction of Fabry-Pérot interference effects in phase and amplitude pulse shapers based on liquid crystal spatial light modulators*, Opt. Express **27**, 22970–22982 (2019).

[247] C. Froehly, A. Lacourt, and J. C. Viénot, *Time impulse response and time frequency response of optical pupils: experimental confirmations and applications*, Nouvelle Revue d'Optique **4**, 183–196 (1973).

[248] C. Dorrer, N. Belabas, J.-P. Likforman, and M. Joffre, *Experimental implementation of Fourier-transform spectral interferometry and its application to the study of spectrometers*, Appl. Phys. B **70**, 99–107 (2000).

[249] C. Dorrer, N. Belabas, J.-P. Likforman, and M. Joffre, *Spectral resolution and sampling issues in Fourier-transform spectral interferometry*, J. Opt. Soc. Am. B **17**, 1795–1802 (2000).

[250] R. Trebino, *Frequency-resolved optical gating: The measurement of ultrashort laser pulses* (Springer, New York, 2002), 1st ed.

[251] J. Mooney and P. Kambhampati, *Get the basics right: Jacobian conversion of wavelength and energy scales for quantitative analysis of emission spectra*, J. Phys. Chem. Lett. **4**, 3316–3318 (2013).

[252] A. W. Albrecht, J. D. Hybl, S. M. G. Faeder, and D. M. Jonas, *Experimental distinction between phase shifts and time delays: Implications for femtosecond spectroscopy and coherent control of chemical reactions*, J. Chem. Phys. **111**, 10934–10956 (1999).

[253] S. Mueller, J. Lüttig, P. Malý *et al.*, *Rapid multiple-quantum three-dimensional fluorescence spectroscopy disentangles quantum pathways*, Nat. Commun. **10**, 4735 (2019).

[254] P. Malý, J. Lüttig, S. Mueller *et al.*, *Coherently and fluorescence-detected two-dimensional electronic spectroscopy: direct comparison on squaraine dimers*, Phys. Chem. Chem. Phys. **22**, 21222–21237 (2020).

[255] A. V. Pisliakov, T. Mančal, and G. R. Fleming, *Two-dimensional optical three-pulse photon echo spectroscopy. II. Signatures of coherent electronic motion and*

exciton population transfer in dimer two-dimensional spectra, J. Chem. Phys. **124**, 234505 (2006).

[256] D. Thien, P. Kury, M. Horn-von Hoegen *et al.*, *Domain sensitive contrast in photoelectron emission microscopy*, Phys. Rev. Lett. **99**, 196102 (2007).

[257] M. Aeschlimann, T. Brixner, A. Fischer *et al.*, *Determination of local optical response functions of nanostructures with increasing complexity by using single and coupled Lorentzian oscillator models*, Appl. Phys. B **122**, 199 (2016).

[258] N. Rotenberg and L. Kuipers, *Mapping nanoscale light fields*, Nat. Photonics **8**, 919–926 (2014).

[259] M. Dąbrowski, Y. Dai, and H. Petek, *Ultrafast photoemission electron microscopy: imaging plasmons in space and time*, Chem. Rev. **120**, 6247–6287 (2020).

[260] B. Gjonaj, J. Aulbach, P. M. Johnson *et al.*, *Active spatial control of plasmonic fields*, Nat. Photonics **5**, 360–363 (2011).

[261] M. Aeschlimann, M. Bauer, D. Bayer *et al.*, *Spatiotemporal control of nanooptical excitations*, PNAS **107**, 5329–5333 (2010).

[262] R. Kolesov, B. Grotz, G. Balasubramanian *et al.*, *Wave-particle duality of single surface plasmon polaritons*, Nat. Phys. **5**, 470–474 (2009).

[263] M. S. Tame, K. R. McEnery, Ş. K. Özdemir *et al.*, *Quantum plasmonics*, Nat. Phys. **9**, 329–340 (2013).

[264] W. Zhu, R. Esteban, A. G. Borisov *et al.*, *Quantum mechanical effects in plasmonic structures with subnanometre gaps*, Nat. Commun. **7**, 11495 (2016).

[265] P. Vasa and C. Lienau, *Strong light–matter interaction in quantum emitter/metal hybrid nanostructures*, ACS Photonics **5**, 2–23 (2017).

[266] D. Finkelstein-Shapiro, P.-A. Mante, S. Sarisozen *et al.*, *Understanding radiative transitions and relaxation pathways in plexcitons*, Chem **7**, 1092–1107 (2021).

[267] T. Fließbach, *Lehrbuch zur Theoretischen Physik, Bd. 2. Elektrodynamik* (Spektrum, Akad. Verl., Heidelberg, 2008), 2nd ed.

[268] N. Rivera and I. Kaminer, *Light–matter interactions with photonic quasiparticles*, Nat. Rev. Phys. **2**, 538–561 (2020).

[269] C. W. Gardiner and M. J. Collett, *Input and output in damped quantum systems: quantum stochastic differential equations and the master equation*, Phys. Rev. A **31**, 3761–3774 (1985).

[270] S. Franke, S. Hughes, M. K. Dezfouli *et al.*, *Quantization of quasinormal modes for open cavities and plasmonic cavity quantum electrodynamics*, Phys. Rev. Lett. **122**, 213901 (2019).

[271] I. D´Amico, D. G. Angelakis, F. Bussières *et al.*, *Nanoscale quantum optics*, Riv. Nuovo Cim. **42**, 153–195 (2019).

[272] L. Huang, L. Xu, M. Woolley, and A. E. Miroshnichenko, *Trends in quantum nanophotonics*, Adv. Quantum Technol. **3**, 1900126 (2020).

[273] A. Huck, S. Smolka, P. Lodahl *et al.*, *Demonstration of quadrature-squeezed surface plasmons in a gold waveguide*, Phys. Rev. Lett. **102**, 246802 (2009).

[274] R. W. Heeres, L. P. Kouwenhoven, and V. Zwiller, *Quantum interference in plasmonic circuits*, Nat. Nanotechnol. **8**, 719–722 (2013).

[275] S. Fasel, M. Halder, N. Gisin, and H. Zbinden, *Quantum superposition and entanglement of mesoscopic plasmons*, New J. Phys. **8**, 13–13 (2006).

[276] M. Lobino, D. Korystov, C. Kupchak *et al.*, *Complete characterization of quantum-optical processes*, Science **322**, 563–566 (2008).

[277] L. Tang, K. Zheng, J. Guo *et al.*, *Quantum tomography of the photon-plasmon conversion process in a metal hole array*, Opt. Express **27**, 13809–13819 (2019).

[278] C. You, M. Hong, N. Bhusal *et al.*, *Observation of the modification of quantum statistics of plasmonic systems*, Nat. Commun. **12**, 5161 (2021).

[279] J. Lehmann, M. Merschdorf, W. Pfeiffer *et al.*, *Surface plasmon dynamics in silver nanoparticles studied by femtosecond time-resolved photoemission*, Phys. Rev. Lett. **85**, 2921–2924 (2000).

[280] D. Paleček, P. Edlund, E. Gustavsson *et al.*, *Potential pitfalls of the early-time dynamics in two-dimensional electronic spectroscopy*, J. Chem. Phys. **151**, 024201 (2019).

[281] B. Lamprecht, J. R. Krenn, A. Leitner, and F. R. Aussenegg, *Resonant and off-resonant light-driven plasmons in metal nanoparticles studied by femtosecond-resolution third-harmonic generation*, Phys. Rev. Lett. **83**, 4421–4424 (1999).

[282] M. Lippitz, M. A. van Dijk, and M. Orrit, *Third-harmonic generation from single gold nanoparticles*, Nano Lett. **5**, 799–802 (2005).

[283] B. Y. Mueller and B. Rethfeld, *Relaxation dynamics in laser-excited metals under nonequilibrium conditions*, Phys. Rev. B **87**, 035139 (2013).

[284] R. Bormann, M. Gulde, A. Weismann *et al.*, *Tip-enhanced strong-field photoemission*, Phys. Rev. Lett. **105**, 147601 (2010).

[285] S. Yan and H.-S. Tan, *Phase cycling schemes for two-dimensional optical spectroscopy with a pump–probe beam geometry*, Chem. Phys. **360**, 110–115 (2009).

[286] L. O. Castaños and A. Zuñiga-Segundo, *The forced harmonic oscillator: coherent states and the RWA*, Am. J. Phys. **87**, 815–823 (2019).

[287] M. B. Plenio and S. F. Huelga, *Dephasing-assisted transport: quantum networks and biomolecules*, New J. Phys. **10**, 113019 (2008).

[288] A. Kubo, N. Pontius, and H. Petek, *Femtosecond microscopy of surface plasmon polariton wave packet evolution at the silver/vacuum interface*, Nano Lett. **7**, 470–475 (2007).

[289] R. Dahan, A. Gorlach, U. Haeusler *et al.*, *Imprinting the quantum statistics of photons on free electrons*, Science **373**, eabj7128 (2021).

[290] S. Hunsche, T. Starczewski, A. l'Huillier *et al.*, *Ionization and fragmentation of C_{60} via multiphoton-multiplasmon excitation*, Phys. Rev. Lett. **77**, 1966–1969 (1996).

[291] R. Schlipper, R. Kusche, B. von Issendorff, and H. Haberland, *Multiple excitation and lifetime of the sodium cluster plasmon resonance*, Phys. Rev. Lett. **80**, 1194–1197 (1998).

[292] G. F. Bertsch, N. Van Giai, and N. Vinh Mau, *Cluster ionization via two-plasmon excitation*, Phys. Rev. A **61**, 033202 (2000).

[293] M. Reutzel, A. Li, B. Gumhalter, and H. Petek, *Nonlinear plasmonic photoelectron response of Ag(111)*, Phys. Rev. Lett. **123**, 017404 (2019).

[294] A. Li, M. Reutzel, Z. Wang *et al.*, *Plasmonic photoemission from single-crystalline silver*, ACS Photonics **8**, 247–258 (2021).

[295] D. Novko, V. Despoja, M. Reutzel *et al.*, *Plasmonically assisted channels of photoemission from metals*, Phys. Rev. B **103**, 205401 (2021).

[296] D. Wolf, T. Schumacher, and M. Lippitz, *Shaping the nonlinear near field*, Nat. Commun. **7**, 10361 (2016).

[297] M. Wand, A. Schindlmayr, T. Meier, and J. Förstner, *Simulation of the ultrafast nonlinear optical response of metal slabs*, Phys. Status Solidi B **248**, 887–891 (2011).

[298] R. W. Boyd, Z. Shi, and I. De Leon, *The third-order nonlinear optical susceptibility of gold*, Optics Communications **326**, 74–79 (2014).

[299] R. W. Boyd, *Nonlinear optics* (Academic Press, Burlington, 2008), 3rd ed.

[300] P. N. Terekhin, O. Benhayoun, S. T. Weber *et al.*, *Influence of surface plasmon polaritons on laser energy absorption and structuring of surfaces*, Appl. Surf. Sci. **512**, 144420 (2020).

Acknowledgement

Approaching the end of this thesis, I would like to emphasize that the presented work and results have been achieved due to great teamwork, valuable scientific and private discussions and a distinct good sense of humor amongst all. During my time in the group, I had the opportunity to work together with a lot of remarkably inspiring people, I learned from them and hopefully I could teach some things as well. Since I am really grateful for every minute we spent together in lab, at lunch or in private life, I would like to thank some people explicitly in the following.

- **Prof. Dr. Tobias Brixner** for giving me the opportunity to work in this exciting research field, for realizing the financial basis which allowed establishment of the laboratory and the performed experiments, for his inspiring input concerning femtosecond pulse shaping and pulse-characterization techniques and his incentive that I achieve my goals. Moreover, I am thankful for supporting my scientific work and providing me the possibility to visit several national and international conferences.
- **Prof. Dr. Walter Pfeiffer** for his support and discussions concerning the modeling of the plasmon-assisted multi-quantum electron-emission process and his perseverance and encouragement on the long road to the final form of the presented quantum model.
- **Prof. Dr. Bert Hecht** for his support and inspiring input related to the quantum nature of plasmon-polaritons.
- **Prof. Dr. Eberhard Riedle** and **Dr. Emanuel Wittmann** for the design and building of the NOPA system and the instructive time we had together in the Riedle-labs at the LMU in Munich.
- The "Lab4-team", namely **Dr. Matthias Hensen**, **Dr. Victor Lisinetskii**, **Bernhard Huber**, **Daniel Fersch**, **Lysanne Dietrich** and last but not least **Philipp Kessler** for the great time we had in lab, at conferences, and fairs and for all the barriers we broke down together, all the milestones we reached, all the legendary moments, quotes, jokes, topics, and fails inside and outside of the institute and of cause all the scientific and private input.

- **Dr. Matthias Hensen** and **Bernhard Huber** for your enthusiasm, perseverance, honesty and inspiring scientific feedback and discussions. For the introduction to and support in all the different projects that finally led to the presented experiments and results. For all the great memories, common achievements and your reliability in countless private and everyday-work situations.
- **Dr. Victor Lisinetskii** for all his scientific and private support, his physical explanations, valuable coding advice and constructive criticism. I learned a lot from you on so many levels.
- **Dr. Pavel Malý** for his critical questions, inspiring discussions, clear explanations and all the basketball games I lost to him.
- **Dr. Sebastian Götz** for his support and explanations concerning LabView, pulse-shaper artifact-correction strategies and pulse-characterization methods.
- **Ruben Pompe** for his valuable discussions and input concerning the Quantum Dynamical Toolbox (QDT) in Matlab.
- **Daniel Friedrich**, **Philipp Grimm** and **Enno Schatz** for high-quality sample preparation and SEM characterization, fruitful discussions and hilarious evenings at DPG conferences.
- **Dr. Felix Fenner**, **Dr. Benjamin Frisch** and **Dr. Michael Hartelt** for the great moments during many DPG conferences and the inspiring measurement-time in the Kaiserslautern lab during the near-field-control (NFC) collaboration.
- All students I had the pleasure to work with in the lab: **Daniela Brenner**, **Daniel Fersch**, **Maximilian Horn**, **Laura Kontschak** and **Salahudin Smailagic**. Thanks for your smart questions and valuable contributions.
- My former office colleagues **Heiko Hildenbrand**, **Dr. Christian Kramer**, **Dr. Julian Lüttig** and **Dr. Stefan Müller** for the great atmosphere and all the awesome discussions we went through together. Special thanks go to Heiko, who kept the office plant alive as long as possible. My apology to everyone who may be experiencing long-term consequences due to the long storage of deposit bottles.
- **Dr. Matthias Hensen**, **Dr. Simon Draeger** and **Heiko Hildenbrand** for the best New England road trip with countless legendary moments in advance of the Gordon Research Conference and **Dr. Andreas Steinbacher** for the inspiring tour through Cambridge, the MIT labs, and Boston afterwards.

- **Dr. Torsten Franz**, **Florian Schütz**, **Uwe Knipping** and **Dr. Czeslaw Koziol** from ELMITEC GmbH for their patience, motivation and most helpful expertise concerning any issue related to the PEEM.
- **Antje Geissler** and **Peter Gussek** from Jenoptik for their valuable input concerning the construction and specification details of the SLM and the liquid crystals.
- The electronics workshop **Reiner Eck** and **Uwe Reuss** and the members of the mechanics workshop at the IPTC **Wolfgang Liebler**, **Ralf Kohrmann**, **Peter Lang**, **Katharina Wittmann** and **Markus Keller**. Thanks to your individual expertise, spontaneity and inspiration, all the countless small and large problems we faced during the construction phase of the laboratory would not have been solved so efficiently.
- The technical staff **Belinda Böhm**, **Sabine Fuchs**, **Sabine Stahl** and **Ivonne Vollert** for their assistance in several projects, for taking over of all the organizing work and for your warm-hearted nature.
- **Dr. Christoph Brüning** for providing the computational infrastructure at the computation center of the University Würzburg.
- The secretaries **Andrea Gehring**, **Susanne Pfarr**, **Anna Rosenfeldt** and **Sandra Stoudek** for their help regarding any organizational issue and for being such nice and sympathetic persons.
- **Dr. Matthias Hensen** and **Daniel Fersch** for careful proof-reading of this thesis.
- All current and past members of the Brixner work group I had the pleasure to work with: **Stephanie Bachmann**, **Luisa Brenneis**, **Simon Büttner**, **Dr. Jakub Dostál**, **Rebecca Fröhlich**, **Julia Heitmüller**, **Dr. Florian Kanal**, **Niklas Klosterhalfen**, **Dr. Johannes Knorr**, **Dr. Federico Koch**, **Tristan Kopp**, **Julian Kütt**, **Dr. Donghai Li**, **Dr. Yang Li**, **Dr. Xiaonan Ma**, **Bernhard Mahlmeister**, **Katja Mayershofer**, **Dr. Francesc Molins**, **Daniel Müller**, **Matthias Nuss**, **Lea Ress**, **Dr. Sebastian Röding**, **Dr. Stefan Rützel**, **Dr. Sebastian Schott**, **Hans-Peter Solowan**, **Dr. Andreas Steinbacher**, **Daniel Wagner**, **Raphael Wichary**, **Anna Zhitnitsky** and **Thomas Zimmermann**.
- All my friends for making me smile, laugh and escalate.
- My parents **Andrea** and **Axel**, and also my sister **Stefanie**, who have always supported me on my way during the last decades.

- My godchild **Aimée** for her inquisitiveness and for asking the toughest questions.
- My family **Viktoria** and **Frederick** for their optimism and trust, which built me up and encouraged me in so many situations. Together to the next adventure....